University of Reading

An Investigation of the Electronic Structure of Ions in the Liquid Phase Using X-ray Spectroscopic Techniques

Jake M. Seymour

April 2022

Supervised by Dr. Kevin R. J. Lovelock

Submitted in partial fulfilment of the requirements for the degree of
Doctor of Philosophy (PhD) in Chemistry

Declaration

I confirm that the work contained within this thesis is my own unless otherwise indicated. The use of all material from other sources has been properly and fully acknowledged.

As experiments carried out using synchrotron techniques are inherently collaborative, data collection was not purely achieved by myself. Furthermore, all data for neat ionic liquid samples was kindly provided by Dr. Kevin Lovelock. However, all data analysis reported within this thesis was done so independently.

Signed,

Jake Seymour

Acknowledgements

I would like to express my sincere appreciation to everyone that helped me along the way; without whom, the creation of this thesis would not have been possible:

I would first like to thank my first supervisor Kevin Lovelock for his continued guidance, support, and mentorship, throughout my PhD – from whom I have learned a great deal. To my second supervisor Roger Bennett for his beamtime assistance and characteristically honest feedback. To Ekaterina Gousseva, Najaat Alblewi, and Lewis Parker from the Lovelock research group who provided both, help with experimental work, and support throughout this process.

Synchrotron work was aided by Drs. Robert Seidel, Dennis Hein, Garlef Wartner, Claudia Kolbeck, and Wilson Quevedo from BESSY II (Germany), who enabled the collection of all solution X-ray spectroscopy data within this work (Chapters 3 to 6). All neat ionic liquid non-resonant X-ray photoelectron spectroscopy data (primarily Chapter 4) was helpfully collected by Dr. Robert Palgrave. Beyond the work featured within this thesis, I would also like to extend my thanks to Drs. Alex Large, Georg Held, Federica Venturini, Pilar Ferrer Escorihuela, David Duncan, and Shusaku Hayama, from Diamond Light Source (UK), who aided in synchrotron experiment data collection for multiple additional projects.

To my parents and grandparents who encouraged me from a young age to pursue education to the fullest. Finally, I would like to extend a huge thank you to my partner Hannah, whose unwavering encouragement and patience I will be forever grateful for.

Abstract

Ions in solution are ubiquitous within a broad range of chemical applications, *e.g.*, batteries, catalysis, renewable energy production, and aerosols. The physico-chemical properties of each component within solution enables their function within each application, which are in turn determined by their electronic structure. It is well known that solvent-solute interactions influence the electronic structure of each component within solution. However, knowledge of the governing factors, which control how the contributing atomic and molecular orbital energies of solvent and solute species are influenced for liquid phase ions, is heavily lacking. This fact is especially true for solvents other than H_2O. X-ray spectroscopic techniques provide the means to probe the electronic structure of every component in solution. Experiments yield information on how the electronic structure of components in solution are affected upon different chemical changes.

The extent and reasoning as to the influence of solvent identity on the anionic electronic structure was explored (Chapter 3). A strong correlation was found between the anionic molecular orbital energies and solvent Lewis acidity. All anionic molecular orbital energies were affected equally with varying solvent identity; hence, observed solvation effects were stated as non-specific in nature.

For all anion identities measured, destabilisation of the anionic electronic structure upon increasing electrolyte concentration was observed (Chapter 4). Although anion identity was found to influence the extent of anionic destabilisation, the effect of varying anion identity on solvent molecular orbitals was shown to be insignificant.

Varying the concentration of ions in solution was shown to significantly influence the electronic structure of each component (Chapter 5). Both anionic and solvent molecular orbitals were found to decrease in energetic stability with increasing electrolyte concentration. Moreover, a strong linear relationship between core and valence state energies was obtained, once again suggesting that non-specific solvation effects dominate.

The effect of solvent identity on the cationic electronic structure was determined (Chapter 6). Strongly coordinating cations were found to be equally as Lewis acidic within both, aqueous, and organic solvents, in contrast to weakly coordinating cationic species.

Contents

List of figures 1

List of tables 14

1. Introduction 17

- 1.1. Solvent properties 17
  - 1.1.1. Classification and use of solvent species 17
  - 1.1.2. Polarity and polarisability 19
- 1.2. Properties of ionic species 23
  - 1.2.1. Cationic and anionic species 23
  - 1.2.2. Cation-anion interactions 24
  - 1.2.3. Ionic liquids 25
- 1.3. Ions in solution 27
  - 1.3.1. Solvation of solutes 27
  - 1.3.2. Description of bulk electrolyte solutions with varying solute concentration 30
  - 1.3.3. Types of solvent-solute interactions 31
  - 1.3.4. Quantification of solvent-solute interactions 33
  - 1.3.5. Applications of ions in solution 36
- 1.4. Electronic structure 38
- 1.5. The use of X-ray spectroscopy in the probing of ions in molecular solvent 41
- 1.6. Reasoning for ions and solvents studied in this work 49
- 1.7. Aims of current work 51
- 1.8. References 53

2. Spectroscopic methods 61

- 2.1. Non-resonant X-ray photoelectron spectroscopy 65
- 2.2. X-ray absorption spectroscopy 67
- 2.3. Valence resonant X-ray photoelectron spectroscopy 68
- 2.4. Laboratory source X-ray photoelectron spectroscopy setup 70
- 2.5. Synchrotron source photoelectron spectroscopy setup 72
- 2.6. Liquid jet apparatus 74
- 2.7. Data analysis: charge referencing procedures 76
  - 2.7.1. Charge referencing to the E_B(cation) value obtained for dilute ions in H_2O 76
  - 2.7.2. Charge referencing to the E_B(solvent) value obtained for neat solvent 76
  - 2.7.3. Charge referencing for RXP spectra 78
- 2.8. References 79

3. Influence of solvent identity on anionic electronic structure 81

- 3.1. Introduction 82
- 3.2. Spectroscopic methods 85
  - 3.2.1. Sample preparation 85
  - 3.2.2. Synchrotron XPS apparatus 85

- 3.2.3. Laboratory XPS apparatus 86
- 3.3. Results and discussion 87
  - 3.3.1. Changes in anionic atomic charge with varying solvent identity 87
  - 3.3.2. HOVS and LUMO level shifts with varying solvent 98
  - 3.3.3. Relationship between E_B(HOVS) and solvent polarity descriptors 101
  - 3.3.4. Experimental energy level diagram 105
  - 3.3.5. Solvation effect of H_2O versus PC on $[C_4C_1Im][SCN]$ 107
- 3.4. Conclusion and future work 110
- 3.5. References 112

4. Influence of anion identity and concentration on electronic structure 115

- 4.1. Introduction 116
- 4.2. Spectroscopic methods 118
  - 4.2.1. Sample preparation 118
  - 4.2.2. Synchrotron XPS apparatus 118
  - 4.2.3. Laboratory XPS apparatus 119
- 4.3. Results and discussion 120
  - 4.3.1. Changes in anionic atomic charge with varying x_{IL} and anion identity 120
  - 4.3.2. Changes in cationic atomic charge with varying x_{IL} and anion identity 129
  - 4.3.3. Changes in solvent atomic charge with varying anion identity 136
  - 4.3.4. Probing OVSs through valence RXPS 138
- 4.4. Conclusion and future work 140
- 4.5. References 142

5. Influence of aqueous electrolyte concentration on electronic structure 144

- 5.1. Introduction 145
- 5.2. Spectroscopic methods 148
  - 5.2.1. Sample preparation 148
  - 5.2.2. Synchrotron XPS apparatus 148
  - 5.2.3. Laboratory XPS apparatus 148
- 5.3. Results and discussion 149
  - 5.3.1. Changes in anionic and water atomic charge with varying x_{IL} 149
  - 5.3.2. Changes in cationic atomic charge with varying x_{IL} 155
  - 5.3.3. HOVS and LUMO level shifts with varying x_{IL} 156
  - 5.3.4. Core and valence state atomic charge correlations with varying x_{IL} 159
  - 5.3.5. Experimental energy level diagram 160
  - 5.3.6. Evidence for initial state versus final state effects 162
- 5.4. Conclusion and future work 164
- 5.5. References 166

6. Influence of solvent identity on cationic electronic structure 170

- 6.1. Introduction 171
- 6.2. Spectroscopic methods 173
  - 6.2.1. Sample preparation 173
  - 6.2.2. Synchrotron XPS apparatus 173
- 6.3. Results and discussion 174

6.3.1. Changes in cationic atomic charge with varying solvent identity 174
6.4. Conclusion and future work 179
6.5. References 181

7. Conclusion 183

7.1. References 187

8. Appendix 188

8.1. Solution formation parameters 188
8.2. Photoemission peak fitting parameters and subtraction methods 190
8.3. Supplementary information for Chapter 3 192
8.4. Supplementary information for Chapter 4 207
8.5. Supplementary information for Chapter 5 212
8.6. Supplementary information for Chapter 6 227
8.7. References 237

List of figures

Figure 1.1. Examples of the physical properties used to assess solvent polarity: (a) Refractive index (bulk property). (b) Dipole moment (molecular property), where a dipole moment exists in the direction from the δ+ to δ- atom.

Figure 1.2. Orientation of solvent molecules with differing external electric field stimuli: (a) Absence of an electric field. (b) Presence of an electric field. (c) Introduction of a cationic species. Adapted from reference [15].

Figure 1.3. Structure of the 1-butyl-3-methylimidazolium cation, $[C_4C_1Im]^+$, where atoms are numbered according to convention for reference within the current work.

Figure 1.4. The process of solvation: (a) Solvent and solute species exist separately, where solvent-solvent bonds and solute-solute bonds remain intact. (b) Solvent-solvent bonds break to form cavities within the solvent bonding network; solute-solute bonds break. (c) Solute is solvated by the solvent molecules to form a solution.

Figure 1.5. Enthalpy of solution diagram for: (a) Exothermic solvation. (b) Endothermic solvation.

Figure 1.6. The process of increasing the solute concentration of a solution: (a) Regime 1; low solute concentration. (b) Regime 2; medium solute concentration. (c) Regime 3; high solute concentration. (d) Regime 4; pure IL.

Figure 1.7. Structures of probes used in the measurement of each solvent polarity descriptor: (a) Dyes used within the Kamlet-Taft solvent polarity scale. (b) Dyes used within the Catalán solvent polarity scale, where adjacent molecules form homomorphic pairs of dyes.

Figure 1.8. The electronic structure of atomic sulphur presented as an energy level diagram. S 1s, 2s, and 2p are labelled core level orbitals. Valence states are shown at lower E_B and, for the sulphur atom, include the S 3s and S 3p AOs.

Figure 1.9. A simplified schematic of the reported photoelectron peak energy shifts observed with increasing NaI (aq.) concentration, discussed within references [110] and [111].

Figure 1.10. Names and structures of key ions and solvents studied within this work: (a) Cations. (b) Anions. (c) Solvents.

Figure 1.11. A graphic depiction of the roadmap for the current thesis. All chapters are concerned with the use of X-ray spectroscopy within the determination of core and/or valence level E_B values of species in solution. Correlations are then examined alongside solvent polarity scale descriptors (*e.g.,* Kamlet-Taft, Gutmann, and Catalán) to form hypotheses about the molecular level origins of measured E_B variations of solute and solvent.

Figure 2.1. The calculated IMFP curve for elemental samples (orange circle), inorganic compounds (green triangle), and organic compounds (black square), overlaid upon the universal curve (blue).

Figure 2.2. Electronic energy diagram for X-ray photoelectron spectroscopy. (a) ground state. (b) core level photoemission. (c) valence level photoemission. Red circles represent electrons involved within the process. Pink circles represent spectating electrons within the process. Dashed circles represent core hole states. Green arrows represent incident photon energy. Teal arrows represent intra-atomic electron transitions.

Figure 2.3. Electronic energy diagram for X-ray absorption spectroscopy. (a) ground state. (b) X-ray absorption. Red circles represent electrons involved within the process. Pink circles represent spectating electrons within the process. Dashed circles represent core hole states. Green arrows represent incident photon energy. Teal arrows represent intra-atomic electron transitions.

Figure 2.4. Electronic energy diagram for resonant X-ray photoelectron spectroscopy. (a) ground state. (b) X-ray absorption. (c) participator Auger emission. (d) Spectator Auger emission. Red circles represent electrons involved within the process. Pink circles represent spectating electrons within the process. Dashed circles represent core hole states. Green arrows represent incident photon energy. Teal arrows represent intra-atomic electron transitions. Purple arrows represent Auger emission.

Figure 2.5. Experimental apparatus of the lab source XPS setup. The nature of the experiment proceeds from left to right, starting with the generation of X-rays through fluorescence which are subsequently used to irradiate the sample. Electrons ejected through photoemission enter the lens system where they are focussed into a coherent beam. Electron energy spread is reduced within the hemispherical electron analyser, before finally reaching the detector.

Figure 2.6. General diagram of synchrotron Soleil, where 1 = LINAC, 2 = booster ring, 3 = storage ring, 4 = front end, 5 = optics hutch, 6 = experimental hutch, 7 = control cabin. (Copyright © EPSIM 3D/JF Santarelli, Synchrotron Soleil, reproduced with permission).

Figure 2.7. Experimental apparatus of the liquid microjet photoemission experiment. Figure adapted from reference [25].

Figure 2.8. The methodology enabling charge referencing of photoelectron peaks to the vacuum level, as described, requires information gained from two additionally measured XP spectra: (a) The low E_K curve, yielding E_K(cut). (b) The core level XP spectra of the biased sample, yielding E_K(SF).

Figure 3.1. Names and structures of key ions and solvents studied within Chapter 3: (a) Cations, where atoms within $[C_4C_1Im]^+$ are numbered according to convention for reference within the current work. (b) Anions. (c) Solvents.

Figure 3.2. Anionic core level NRXP and valence state NRXP spectra for 0.5 M ($[C_4C_1Im][SCN]$)(solvent), where solvent = H_2O (red), H_2O/EtOH (purple), EtOH (blue), MeCN (green), PC (grey), and for pure $[C_4C_1Im][SCN]$ (orange): (a) N_{anion} 1s. (b) S 2p. All XP spectra for 0.5 M solutions ($[C_4C_1Im][SCN]$)(solvent) were measured at $h\nu$ = 700.0 eV; pure $[C_4C_1Im][SCN]$ XP spectra were measured at $h\nu$ = 1486.6 eV. Dashed lines are intended as a visual aid of the changes in E_B that occur with varying x_{IL}, where lines of the same type have the same gradient. All XP spectra were charge referenced using the methods detailed in Section 2.7.1.

Figure 3.3. E_B against solvent category plots for ($[C_4C_1Im][SCN]$)(solvent), where solvent = H_2O (red), H_2O/EtOH (purple), EtOH (blue), MeCN (green), PC (grey), and for pure $[C_4C_1Im][SCN]$ (orange): (a) $E_B(N_{anion}$ 1s) against solvent. (b) E_B(S $2p_{3/2}$) against solvent. All XP spectra for 0.5 M solutions ($[C_4C_1Im][SCN]$)(solvent) were measured at $h\nu$ = 700.0 eV; pure $[C_4C_1Im][SCN]$ XP spectra were measured at $h\nu$ = 1486.6 eV. All values were charge referenced using the methods detailed in Section 2.7.1.

Figure 3.4. Comparisons between E_B(anion), area ratio, and FWHM ratio for (N_{cation} 1s/N_{anion} 1s) and (S $2p_{3/2}$/S $2p_{1/2}$): (a) FWHM ratio against area ratio for (N_{cation} 1s/N_{anion} 1s), linear trend line with R^2 = 0.68. (b) Area ratio against $E_B(N_{anion}$ 1s) for (N_{cation} 1s/N_{anion} 1s), linear trend line with R^2 = 0.81. (c) FWHM ratio against $E_B(N_{anion}$ 1s) for (N_{cation} 1s/N_{anion} 1s), linear trend line with R^2 = 0.69. (d) FWHM ratio against area ratio for (S $2p_{3/2}$/S $2p_{1/2}$), linear trend line with R^2 = 0.92. (e) Area ratio against $E_B(N_{anion}$ 1s) for (S $2p_{3/2}$/S $2p_{1/2}$), linear trend line with R^2 = 0.50. (f) FWHM ratio against $E_B(N_{anion}$ 1s) for (S $2p_{3/2}$/S $2p_{1/2}$), linear trend line with R^2 = 0.32.

Figure 3.5. Core level and valence state NRXP spectra for 0.5 M (K[SCN])(H_2O) and 0.5 M (K[SCN])(PC): (a) N 1s. (b) S 2p. (c) Valence. (d) K 2p. All XP spectra for 0.5 M (K[SCN])(solvent) were measured at $h\nu$ = 700.0 eV. All XP spectra were charge referenced using the methods detailed in Section 2.7.2.

Figure 3.6. Core level and valence state NRXP spectra for 0.5 M ($Li[NTf_2]$)(H_2O) and 0.5 M ($Li[NTf_2]$)(PC): (a) N 1s, (b) F 1s, (c) S 2p, (d) Li 1s. All XP spectra for 0.5 M ($Li[NTf_2]$)(solvent) were measured at $h\nu$ = 700.0 eV. All XP spectra were charge referenced using the methods detailed in Section 2.7.2.

Figure 3.7. Valence NRXP and N 1s XA spectra for ($[C_4C_1Im][SCN]$)(solvent), where solvent = H_2O (red), H_2O/EtOH (purple), EtOH (blue), MeCN (green), PC (grey), and for pure $[C_4C_1Im][SCN]$ (orange): (a) Valence NRXP spectra. (b) N 1s XA spectra. Dashed lines are intended as a visual aid of the changes in E_B that occur with varying x_{IL}, where lines of the same type have the same gradient. All NRXP spectra for 0.5 M solutions ($[C_4C_1Im][SCN]$)(solvent) were measured at $h\nu$ = 700.0 eV; pure $[C_4C_1Im][SCN]$ NRXP spectra were measured at $h\nu$ = 1486.6 eV. Valence NRXP spectra were charge referenced using the methods detailed in Section 2.7.1.

Figure 3.8. E_B against solvent category plots for ($[C_4C_1Im][SCN]$)(solvent), where solvent = H_2O (red), H_2O/EtOH (purple), EtOH (blue), MeCN (green), PC (grey), and for pure $[C_4C_1Im][SCN]$ (orange): (a) $E_B(HOVS_{anion})$ against solvent where samples of 0.5 M ($[C_4C_1Im][SCN]$)(solvent) were measured at $h\nu$ = 700.0 eV; $[C_4C_1Im][SCN]$ was measured at $h\nu$ = 1486.6 eV. (b) $h\nu(N_{anion}\ 1s \rightarrow \pi^*)$ against solvent. $E_B(HOVS_{anion})$ values were charge referenced using the methods detailed in Section 2.7.1. $h\nu(N_{anion}\ 1s \rightarrow \pi^*)$ values were not subject to charge referencing methods.

Figure 3.9. $E_B(HOVS_{anion})$ against Kamlet-Taft, Gutmann, and Catalán polarity scale descriptors for ($[C_4C_1Im][SCN]$)(solvent), where solvent = H_2O (red), H_2O/EtOH (purple), EtOH (blue), MeCN (green), PC (grey), and for pure $[C_4C_1Im][SCN]$ (orange): (a) $E_B(HOVS_{anion})$ against pure solvent hydrogen bond donor, α_{solv}; R^2 of the dashed line = 0.92. (b) $E_B(HOVS_{anion})$ against pure solvent hydrogen bond acceptor, β_{solv}. (c) $E_B(HOVS_{anion})$ against pure solvent dipolarity-polarisability, π^*_{solv}. (d) $E_B(HOVS_{anion})$ against pure solvent electron acceptor number, AN_{solv}; R^2 of the dashed line = 0.95. (e) $E_B(HOVS_{anion})$ against pure solvent electron donor number, DN_{solv}. (f) $E_B(HOVS_{anion})$ against pure solvent acidity, SA_{solv}; R^2 of the dashed line = 0.92. (g) $E_B(HOVS_{anion})$ against pure solvent basicity, SB_{solv}. (h) $E_B(HOVS_{anion})$ against pure solvent dipolarity-polarisability, SPP_{solv}. $E_B(HOVS_{anion})$ values were charge referenced using the methods detailed in Section 2.7.1.

Figure 3.10. Energy level diagram for ($[C_4C_1Im][SCN]$)(solvent), where solvent = H_2O, H_2O/EtOH, EtOH, PC, and for pure $[C_4C_1Im][SCN]$. $E_B(N_{anion}\ 1s)$ and $E_B(HOVS_{anion})$ values were charge referenced using the methods detailed in Section 2.7.1 (NRXPS) and Section 2.7.3 (RXPS). $E_B(N_{anion}\ \pi^*)$ values were calculated from $E_B(N_{anion}\ 1s)$ minus $h\nu(N_{anion}\ 1s \rightarrow \pi^*)$. All E_B values are reported to 1 decimal place.

Figure 3.11. E_B shift of 0.5 M ($[C_4C_1Im][SCN]$)(solvent), where solvent = H_2O and PC, relative to pure $[C_4C_1Im][SCN]$: (a) $E_B(N_{anion}\ 1s)$. (b) $E_B(S\ 2p_{3/2})$. (c) $E_B(HOVS_{anion})$. All XP spectra for 0.5 M ($[C_4C_1Im][SCN]$)(H_2O) and 0.5 M ($[C_4C_1Im][SCN]$)(PC) were measured at $h\nu$ = 700.0 eV. Charge referencing methods are detailed in Section 2.7.1. All E_B values are reported to 1 decimal place.

Figure 3.12. N 1s valence RXP heat map and valence RXP spectra for ($[C_4C_1Im][SCN]$)(solvent), where solvent = H_2O (red), and PC (grey): (a) N 1s RXPS heat map. (b) $h\nu$ = 402.1 eV subtracted N_{cation} 1s resonant. (c) $h\nu$ = 399.7 eV subtracted N_{anion} 1s resonant. The NRXPS contributions were subtracted using the procedure detailed in Section 8.2. No charge referencing method was applied as spectra were visually shifted to enable a comparative overlay.

Figure 4.1. Names and structures of key ions and solvents studied within Chapter 4: (a) $[C_nC_1Im]^+$ cation studied within the current work, where n = 4 and 8. (b) Anions.

Figure 4.2. Anionic core level NRXP spectra for 0.5 M ($[C_nC_1Im][anion]$)(H_2O) and pure $[C_nC_1Im][anion]$, where anion = $[SCN]^-$, $[N(CN)_2]^-$, $[BF_4]^-$, $[TfO]^-$, Cl^-, and I^-: (a) N_{anion} 1s. (b) B 1s. (c) F 1s. (d) S 2p. (e) Cl 2p. (f) I $3d_{5/2}$. Spectra for samples in aqueous solution were measured at $h\nu$ = 700.0 eV; spectra for samples of pure IL were measured at $h\nu$ = 1486.6 eV. Spectra for aqueous solution and pure IL containing the same solute were vertically offset for clarity. All values were charge referenced using the methods detailed in Section 2.7.1.

Figure 4.3. ΔE_B(anion) from 0.5 M ([C_nC_1Im][anion])(H_2O) to pure [C_nC_1Im][anion], against Kamlet-Taft polarity scale descriptors, and Pearson absolute scale descriptors, where anion = $[BF_4]^-$ (red), $[N(CN)_2]^-$ (purple), $[TfO]^-$ (pink), Cl^- (green), I^- (grey), and $[SCN]^-$ (orange): (a) ΔE_B(anion) against hydrogen bond donor, α_{solv}, $R^2 = 0.81$. (b) ΔE_B(anion) against hydrogen bond acceptor, β_{solv}, $R^2 = 0.86$. (c) ΔE_B(anion) against dipolarity-polarisability, π^*_{solv}, $R^2 = 0.39$. (d) ΔE_B(anion) against absolute electronegativity, χ, $R^2 = 0.57$. (e) ΔE_B(anion) against absolute hardness, η, $R^2 = 0$. ΔE_B(anion) values were calculated from E_B(anion) measured in aqueous solution minus E_B(anion) measured for the pure IL. KT solvent polarity descriptor values used were those of [C_4C_1Im][anion] species from references [22, 23]. Pearson absolute scale descriptor values pertain to those of the neutral atom within brackets on the legend, and were found in reference [18]. Dashed lines represented the linear line of best fit. ΔE_B(anion) values were charge referenced using the methods detailed in Section 2.7.1.

Figure 4.4. Cationic core level NRXP spectra for 0.5 M ([C_nC_1Im][anion])(H_2O) and pure [C_nC_1Im][anion], where anion = $[SCN]^-$, $[N(CN)_2]^-$, $[BF_4]^-$, $[TfO]^-$, Cl^-, and I^-: (a) N_{cation} 1s. (b) C 1s. Spectra for samples in aqueous solution were measured at $h\nu = 700.0$ eV; spectra for samples of pure IL were measured at $h\nu = 1486.6$ eV. Spectra for aqueous solution and pure IL containing the same solute were vertically offset for clarity. All values were charge referenced using the methods detailed in Section 2.7.1.

Figure 4.5. E_B(C_{alkyl} 1s) against E_B(C_{hetero} 1s) for 0.5 M ([C_nC_1Im][anion])(H_2O) and pure [C_nC_1Im][anion], and the comparison of ΔE_B(C_{hetero} 1s – C_{alkyl} 1s) against β_{solv} for pure [C_nC_1Im][anion] and $[C_4C_1Im]^+$ in H_2O, where anion = $[SCN]^-$, $[N(CN)_2]^-$, $[BF_4]^-$, $[TfO]^-$, Cl^-, and I^-: (a) Aqueous solution; the linear line of best fit displayed excluded data points for $[SCN]^-$ and $[N(CN)_2]^-$ and had an $R^2 = 0.64$. (b) Pure IL. (c) Pure IL excluding the data point for H_2O, where the data point for H_2O is obtained from ([C_4C_1Im]Cl)(H_2O); the linear line of best fit displayed excluded data points for $[SCN]^-$ and $[N(CN)_2]^-$ and had an $R^2 = 0.98$. Spectra for samples in aqueous solution were measured at $h\nu = 700.0$ eV; spectra for samples of pure IL were measured at $h\nu = 1486.6$ eV. All values were charge referenced using the methods detailed in Section 2.7.1.

Figure 4.6. The ratio between measured photoelectron peak FWHM values within the C 1s region, C_{alkyl} 1s : C_{hetero} 1s : C^2 1s, for [C_4C_1Im][anion] in aqueous solution (0.5 M) and pure IL, where anion = $[SCN]^-$, $[N(CN)_2]^-$, $[BF_4]^-$, $[TfO]^-$, Cl^-, and I^-.

Figure 4.7. O 1s NRXP spectra and corresponding E_B(O_{liq} 1s) against anion category plot for 0.5 M ([C_4C_1Im][anion])(H_2O), where anion = $[SCN]^-$, $[N(CN)_2]^-$, $[BF_4]^-$, $[TfO]^-$, and I^-: (a) O 1s NRXP spectra; vertically offset for clarity. (b) E_B(O_{liq} 1s) against anion; error bars = ± 0.03 eV. All spectra were measured at $h\nu = 700.0$ eV. All values were charge referenced using the methods detailed in Section 2.7.1.

Figure 4.8. N 1s valence RXP heat map, XA spectra and valence RXP spectra for 0.5 M ($[C_4C_1Im][anion]$)(H_2O), where anion = $[SCN]^-$, $[N(CN)_2]^-$, $[BF_4]^-$, $[TfO]^-$, Cl^-, and I^-: (a) N 1s RXPS heat map. (b) N 1s partial electron yield XA spectra. (c) N 1s valence RXP spectra at $h\nu$ = 402.1 eV; vertically offset for clarity. N 1s valence RXPS heat map was subtracted using the procedure detailed in Section 8.2. N 1s valence RXPS heat map and N 1s valence RXP spectra were charge referenced using the methods detailed in Section 2.7.3. Remaining RXP spectra were shifted to match E_B(N_{cation} 2p) to allow for a clearer visual comparison.

Figure 5.1. Samples measured within Chapter 5, where $([C_4C_1Im][SCN])_x(H_2O)_{1-x}$ was studied at various concentrations, from dilute electrolyte, to concentrated electrolyte. (a) The structure of $[C_4C_1Im][SCN]$, where atoms are numbered according to convention for reference within the current work. (b) A graphic depiction of a dilute electrolyte (left) and a concentrated electrolyte, which is not intended to represent the orientation or arrangement of ions or solvent molecules within solution; red = cation, blue = anion, and solvent (H_2O) = ball and stick structure.

Figure 5.2. NRXPS spectra for $([C_4C_1Im][SCN])_x(H_2O)_{1-x}$, where x_{IL} = 0.01 (red), 0.10 (blue), 0.25 (green) and 1.00 (grey). (a) N_{anion} 1s NRXP spectra. (b) S 2p NRXP spectra. (c) O 1s NRXP spectra. All XP spectra for solutions of $([C_4C_1Im][SCN])_x(H_2O)_{1-x}$, where x_{IL} = 0.01, 0.10, and 0.25, were measured at $h\nu$ = 700.0 eV; pure $[C_4C_1Im][SCN]$ XP spectra were measured at $h\nu$ = 1486.6 eV. Dashed lines are intended as a visual aid of the changes in E_B that occur with varying x_{IL}, where lines of the same type have the same gradient. All values were charge referenced using the methods detailed in Section 2.7.1.

Figure 5.3. Photoemission peak binding energies, E_B, against $([C_4C_1Im][SCN])_x(H_2O)_{1-x}$, where x_{IL} = 0.01 (red), 0.10 (blue), 0.25 (green) and 1.00 (grey). (a) E_B(N_{anion} 1s) against x_{IL}. (b) E_B(S $2p_{3/2}$) against x_{IL}. (c) E_B(O_{liq} 1s) against x_{IL}. All XP spectra for solutions of $([C_4C_1Im][SCN])_x(H_2O)_{1-x}$, where x_{IL} = 0.01, 0.10, and 0.25, were measured at $h\nu$ = 700.0 eV; pure $[C_4C_1Im][SCN]$ XP spectra were measured at $h\nu$ = 1486.6 eV. All values were charge referenced using the methods detailed in Section 2.7.1.

Figure 5.4. Depth profile experiments for E_B(N_{anion} 1s) at varying $h\nu$ (450.0 eV, 500.0 eV, 600.0 eV, 700.0 eV, 850.0 eV, 1000.0 eV, and 1200.0 eV): (a) N_{anion} 1s NRXP spectra at varying $h\nu$. (b) E_B(N_{anion} 1s) against $h\nu$. All XP spectra for solutions of $([C_4C_1Im][SCN])_{0.01}(H_2O)_{0.99}$ were measured at $h\nu$ = 700.0 eV; pure $[C_4C_1Im][SCN]$ XP spectra were measured at $h\nu$ = 1486.6 eV. All values were charge referenced using the methods detailed in Section 2.7.1.

Figure 5.5. Comparisons between E_B(anion), area ratio, and FWHM ratio for (N_{cation} 1s/N_{anion} 1s): (a) FWHM ratio against area ratio for (N_{cation} 1s/N_{anion} 1s). (b) Area ratio against E_B(N_{anion} 1s) for (N_{cation} 1s/N_{anion} 1s). (c) FWHM ratio against E_B(N_{anion} 1s) for (N_{cation} 1s/N_{anion} 1s). All XP spectra for solutions of $([C_4C_1Im][SCN])_x(H_2O)_{1-x}$, where x_{IL} = 0.01, 0.10, and 0.25, were measured at $h\nu$ = 700.0 eV; pure $[C_4C_1Im][SCN]$ XP spectra were measured at $h\nu$ = 1486.6 eV. All values were charge referenced using the methods detailed in Section 2.7.1.

Figure 5.6. NRXPS spectra for $([C_4C_1Im][SCN])_x(H_2O)_{1-x}$, where x_{IL} = 0.01 (red), 0.10 (blue), 0.25 (green) and 1.00 (grey). (a) N_{cation} 1s NRXP spectra. (b) C 1s NRXP spectra. All spectra were measured at $h\nu$ = 700.0 eV. Dashed lines are intended as a visual aid of the changes in E_B that occur with varying x_{IL}. All XP spectra for solutions of $([C_4C_1Im][SCN])_x(H_2O)_{1-x}$, where x_{IL} = 0.01, 0.10, and 0.25, were measured at $h\nu$ = 700.0 eV; pure $[C_4C_1Im][SCN]$ XP spectra were measured at $h\nu$ = 1486.6 eV. All values were charge referenced using the methods detailed in Section 2.7.1.

Figure 5.7. XAS spectra for $([C_4C_1Im][SCN])_x(H_2O)_{1-x}$, where x_{IL} = 0.01 (red), 0.10 (blue), 0.25 (green) and 1.00 (grey). (a) Valence NRXPS for solutions of $([C_4C_1Im][SCN])_x(H_2O)_{1-x}$, where x_{IL} = 0.01, 0.10, and 0.25, were measured at $h\nu$ = 700.0 eV; pure $[C_4C_1Im][SCN]$ XP spectra were measured at $h\nu$ = 1486.6 eV. (b) N_{anion} 1s $\rightarrow \pi^*$ XAS. Dashed lines are intended as a visual aid of the changes in E_B that occur with varying x_{IL}, where lines of the same type have the same gradient. Valence NRXPS values were charge referenced using the methods detailed in Section 2.7.1.

Figure 5.8. Photoemission peak binding energies, E_B, against $([C_4C_1Im][SCN])_x(H_2O)_{1-x}$, where x_{IL} = 0.01 (red), 0.10 (blue), 0.25 (green) and 1.00 (grey). (a) E_B(HOVS) against x_{IL}. (b) $h\nu(N_{anion}\ 1s \rightarrow \pi^*)$ against x_{IL}. All values were charge referenced using the methods detailed in Section 2.7.1.

Figure 5.9. RXPS spectra for $([C_4C_1Im][SCN])_x(H_2O)_{1-x}$, where x = 0.01 (red), 0.10 (blue), 0.25 (green) and 1.00 (grey). (a) N_{cation} 1s at $h\nu$ = 402.1 eV. (b) N_{anion} 1s at $h\nu$ = 399.7 eV. (c) O_{liq} 1s RXPS at $h\nu$ = 535.0 eV. Dashed lines are intended as a visual aid of the changes in E_B that occur with varying x_{IL}, where lines of the same type have the same gradient. All values were charge referenced using the methods detailed in Section 2.7.3.

Figure 5.10. An energy level diagram for $([C_4C_1Im][SCN])_x(H_2O)_{1-x}$, where x_{IL} = 0.01, 0.10, 0.25 and 1.00, constructed from spectroscopic data measured using NRXPS and partial electron yield XAS. All values were charge referenced using the methods detailed in Section 2.7.1 (NRXPS) and Section 2.7.3 (RXPS).

Figure 6.1. Names and structures of key ions and solvents studied within Chapter 6: (a) Cations, where atoms within $[C_4C_1Im]^+$ are numbered according to convention for reference within the current work. (b) Anions. (c) Solvents.

Figure 6.2. Cationic NRXP spectra for 0.5 M (solute)(H_2O) and 0.5 M (solute])(PC), where solute = $[C_4C_1Im][SCN]$, K[SCN], and Li[NTf_2]: (a) N 1s comparison between 0.5 M ($[C_4C_1Im][SCN]$)(H_2O) and 0.5 M ($[C_4C_1Im][SCN]$)(PC). (b) K 2p comparison between 0.5 M (K[SCN])(H_2O) and 0.5 M (K[SCN])(PC). (c) Li 1s comparison between 0.5 M (Li[NTf_2])(H_2O) and 0.5 M (Li[NTf_2])(PC). All spectra were measured at $h\nu$ = 700.0 eV and vertically offset for clarity. All values charge referenced using the methods detailed in Section 2.7.2.

Appendix Figure 8.1. Core and valence state NRXP spectra for pure H_2O (plus 20 mM NaI): (a) O 1s. (b) Valence. All XP spectra were measured at $h\nu$ = 700.0 eV. All XP spectra were charge referenced using the methods detailed in Section 2.7.2.

Appendix Figure 8.2. Core and valence state NRXP spectra for pure EtOH (plus 20 mM NaI): (a) O 1s. (b) C 1s. (c) Valence. All XP spectra were measured at $h\nu$ = 700.0 eV. No charge referencing methods were applied to the NRXP spectra for pure EtOH.

Appendix Figure 8.3. Core and valence state NRXP spectra for pure MeCN (plus 20 mM NaI): (a) N 1s. (b) C 1s. (c) Valence. All XP spectra were measured at $h\nu$ = 700.0 eV. No charge referencing methods were applied to the NRXP spectra for pure MeCN.

Appendix Figure 8.4. Core and valence state NRXP spectra for pure PC (plus 20 mM NaI): (a) O 1s. (b) C 1s. (c) Valence. All XP spectra were measured at $h\nu$ = 700.0 eV. All XP spectra were charge referenced using the methods detailed in Section 2.7.2.

Appendix Figure 8.5. Core and valence state NRXP spectra for 0.5 M ($[C_4C_1Im][SCN]$)(H_2O): (a) C 1s. (b) N 1s. (c) O 1s. (d) S 2p. (e) Valence. All XP spectra were measured at $h\nu$ = 700.0 eV. All XP spectra were charge referenced using the methods detailed in Section 2.7.1.

Appendix Figure 8.6. Core and valence state NRXP spectra for 0.5 M ($[C_4C_1Im][SCN]$)(H_2O/EtOH): (a) C 1s. (b) N 1s. (c) O 1s. (d) S 2p. (e) Valence. All XP spectra were measured at $h\nu$ = 700.0 eV. All XP spectra were charge referenced using the methods detailed in Section 2.7.1.

Appendix Figure 8.7. Core and valence state NRXP spectra for 0.5 M ($[C_4C_1Im][SCN]$)(EtOH): (a) C 1s. (b) N 1s. (c) O 1s. (d) S 2p. (e) Valence. All XP spectra were measured at $h\nu$ = 700.0 eV. All XP spectra were charge referenced using the methods detailed in Section 2.7.1.

Appendix Figure 8.8. Core and valence state NRXP spectra for 0.5 M ($[C_4C_1Im][SCN]$)(MeCN): (a) C 1s. (b) N 1s, where the N_{cation} 1s and N_{anion} 1s photoemission peaks were not reliably fitted without heavy constraints. (c) S 2p. (d) Valence. All XP spectra were measured at $h\nu$ = 700.0 eV. All XP spectra were charge referenced using the methods detailed in Section 2.7.1.

Appendix Figure 8.9. Core and valence state NRXP spectra for 0.5 M ($[C_4C_1Im][SCN]$)(PC): (a) C 1s. (b) N 1s. (c) O 1s. (d) S 2p. (e) Valence. All XP spectra were measured at $h\nu$ = 700.0 eV. All XP spectra were charge referenced using the methods detailed in Section 2.7.1.

Appendix Figure 8.10. N 1s valence RXPS map and spectra for 0.5 M ($[C_4C_1Im][SCN]$)(H_2O): (a) N 1s valence RXPS heat map for 0.5 M ($[C_4C_1Im][SCN]$)(H_2O). (b) Partial electron yield N 1s XA spectra. (c) N 1s valence NRXP spectrum ($h\nu$ = 398.0 eV) and N 1s valence RXP spectra ($h\nu$ = 402.1 eV and $h\nu$ = 399.7 eV), with the valence NRXP contributions subtracted. The NRXPS contributions were subtracted using the procedure detailed in Section 8.2. All RXP spectra were charge referenced using the methods detailed in Section 2.7.3.

Appendix Figure 8.11. N 1s valence RXPS map and spectra for 0.5 M ($[C_4C_1Im][SCN]$)(H_2O/EtOH): (a) N 1s valence RXPS heat map for 0.5 M ($[C_4C_1Im][SCN]$)(H_2O/EtOH). (b) Partial electron yield N 1s XA spectra. (c) N 1s valence NRXP spectrum ($h\nu$ = 398.0 eV) and N 1s valence RXP spectra ($h\nu$ = 402.1 eV and $h\nu$ = 399.7 eV), with the valence NRXP contributions subtracted. The NRXPS contributions were subtracted using the procedure detailed in Section 8.2. All RXP spectra were charge referenced using the methods detailed in Section 2.7.3.

Appendix Figure 8.12. N 1s valence RXPS map and spectra for 0.5 M ($[C_4C_1Im][SCN]$)(EtOH): (a) N 1s valence RXPS heat map for 0.5 M ($[C_4C_1Im][SCN]$)(EtOH). (b) Partial electron yield N 1s XA spectra. (c) N 1s valence NRXP spectrum ($h\nu$ = 398.0 eV) and N 1s valence RXP spectra ($h\nu$ = 402.1 eV and $h\nu$ = 399.7 eV), with the valence NRXP contributions subtracted. The NRXPS contributions were subtracted using the procedure detailed in Section 8.2. All RXP spectra were charge referenced using the methods detailed in Section 2.7.3.

Appendix Figure 8.13. N 1s valence RXPS map and spectra for 0.5 M ($[C_4C_1Im][SCN]$)(MeCN): (a) N 1s valence RXPS heat map for 0.5 M ($[C_4C_1Im][SCN]$)(MeCN). (b) Partial electron yield N 1s XA spectra. (c) N 1s valence NRXP spectrum ($h\nu$ = 398.0 eV) and N 1s valence RXP spectra ($h\nu$ = 400.1 eV), with the valence NRXP contributions subtracted. The NRXPS contributions were subtracted using the procedure detailed in Section 8.2. All RXP spectra were charge referenced using the methods detailed in Section 2.7.3.

Appendix Figure 8.14. N 1s valence RXPS map and spectra for 0.5 M ($[C_4C_1Im][SCN]$)(PC): (a) N 1s valence RXPS heat map for 0.5 M ($[C_4C_1Im][SCN]$)(PC). (b) Partial electron yield N 1s XA spectra. (c) N 1s valence NRXP spectrum ($h\nu$ = 398.0 eV) and N 1s valence RXP spectra ($h\nu$ = 402.1 eV and $h\nu$ = 399.7 eV), with the valence NRXP contributions subtracted. The NRXPS contributions were subtracted using the procedure detailed in Section 8.2. All RXP spectra were charge referenced using the methods detailed in Section 2.7.3.

Appendix Figure 8.15. N 1s valence RXP spectra comparison for 0.5 M ($[C_4C_1Im][SCN]$)(solvent), where solvent = H_2O, H_2O/EtOH, EtOH, MeCN, and PC. (a) N_{cation} 1s valence RXP spectra ($h\nu$ = 402.1 eV), with the valence NRXP contributions subtracted. (b) N_{anion} 1s valence RXP spectra ($h\nu$ = 399.7 eV), with the valence NRXP contributions subtracted. Spectra are vertically offset for clarity. All NRXP spectra were charge referenced using the methods detailed in Section 2.7.3.

Appendix Figure 8.16. N 1s XA spectra comparison for 0.5 M ($[C_4C_1Im][SCN]$)(solvent), where solvent = H_2O, H_2O/EtOH, EtOH, MeCN, and PC. Spectra are vertically offset for clarity and dashed lines are added as a visual aid.

Appendix Figure 8.17. Core and valence state NRXP spectra for 0.5 M ($[C_4C_1Im][N(CN)_2]$)(H_2O): (a) C 1s. (b) N 1s. (c) O 1s. (d) Valence. All XP spectra were measured at $h\nu$ = 700.0 eV. All XP spectra were charge referenced using the methods detailed in Section 2.7.1.

Appendix Figure 8.18. Core and valence state NRXP spectra for 0.5 M ($[C_4C_1Im][BF_4]$)(H_2O): (a) C 1s. (b) N 1s. (c) O 1s. (d) B 1s. (e) F 1s. (f) Valence. All XP spectra were measured at $h\nu$ = 700.0 eV. All XP spectra were charge referenced using the methods detailed in Section 2.7.1.

Appendix Figure 8.19. Core and valence state NRXP spectra for 0.5 M ($[C_4C_1Im]Cl$)(H_2O): (a) C 1s. (b) N 1s. (c) Cl 2p. (d) Valence. All XP spectra were measured at $h\nu$ = 700.0 eV. All XP spectra were charge referenced using the methods detailed in Section 2.7.1.

Appendix Figure 8.20. Core and valence state NRXP spectra for 0.5 M ($[C_4C_1Im]I$)(H_2O): (a) C 1s. (b) N 1s. (c) O 1s. (d) I 3d. (e) Valence. All XP spectra were measured at $h\nu$ = 700.0 eV. All XP spectra were charge referenced using the methods detailed in Section 2.7.1.

Appendix Figure 8.21. Core and valence state NRXP spectra for 0.5 M ($[C_4C_1Im][TfO]$)(H_2O): (a) C 1s. (b) N 1s. (c) O 1s. (d) S 2p. (e) F 1s. (f) Valence. All XP spectra were measured at $h\nu$ = 700.0 eV. All XP spectra were charge referenced using the methods detailed in Section 2.7.1.

Appendix Figure 8.22. Core and valence state NRXP spectra for $([C_4C_1Im][SCN])_{0.01}(H_2O)_{0.99}$: (a) C 1s. (b) N 1s. (c) O 1s. (d) S 2p. (e) Valence. All XP spectra were measured at $h\nu$ = 700.0 eV. All XP spectra were charge referenced using the methods detailed in Section 2.7.1.

Appendix Figure 8.23. Core and valence state NRXP spectra for $([C_4C_1Im][SCN])_{0.10}(H_2O)_{0.90}$: (a) C 1s. (b) N 1s. (c) O 1s. (d) S 2p. (e) Valence. All XP spectra were measured at $h\nu$ = 700.0 eV. All XP spectra were charge referenced using the methods detailed in Section 2.7.1.

Appendix Figure 8.24. Core and valence state NRXP spectra for $([C_4C_1Im][SCN])_{0.25}(H_2O)_{0.75}$: (a) C 1s. (b) N 1s. (c) O 1s. (d) S 2p. (e) Valence. All XP spectra were measured at $h\nu$ = 700.0 eV. All XP spectra were charge referenced using the methods detailed in Section 2.7.1.

Appendix Figure 8.25. Core and valence state NRXP spectra for $([C_4C_1Im][SCN])_{1.00}(H_2O)_{0.00}$: (a) C 1s. (b) N 1s. (c) S 2p. (d) Valence. All XP spectra were measured at $h\nu$ = 700.0 eV. All XP spectra were charge referenced using the methods detailed in Section 2.7.1.

Appendix Figure 8.26. N 1s valence RXPS map and spectra for $([C_4C_1Im][SCN])_{0.01}(H_2O)_{0.99}$: (a) N 1s valence RXPS heat map for $([C_4C_1Im][SCN])_{0.01}(H_2O)_{0.99}$. (b) Partial electron yield N 1s XA spectra. (c) N 1s valence NRXP spectrum ($h\nu$ = 398.0 eV) and N 1s valence RXP spectra ($h\nu$ = 402.1 eV and $h\nu$ = 399.7 eV), with the valence NRXP contributions subtracted. The NRXPS contributions were subtracted using the procedure detailed in Section 8.2. All RXP spectra were charge referenced using the methods detailed in Section 2.7.3.

Appendix Figure 8.27. N 1s valence RXPS map and spectra for $([C_4C_1Im][SCN])_{0.10}(H_2O)_{0.90}$: (a) N 1s valence RXPS heat map for $([C_4C_1Im][SCN])_{0.10}(H_2O)_{0.90}$. (b) Partial electron yield N 1s XA spectra. (c) N 1s valence NRXP spectrum ($h\nu$ = 398.0 eV) and N 1s valence RXP spectra ($h\nu$ = 402.1 eV and $h\nu$ = 399.7 eV), with the valence NRXP contributions subtracted. The NRXPS contributions were subtracted using the procedure detailed in Section 8.2. All RXP spectra were charge referenced using the methods detailed in Section 2.7.3.

Appendix Figure 8.28. N 1s valence RXPS map and spectra for $([C_4C_1Im][SCN])_{0.25}(H_2O)_{0.75}$: (a) N 1s valence RXPS heat map for $([C_4C_1Im][SCN])_{0.25}(H_2O)_{0.75}$. (b) Partial electron yield N 1s XA spectra. (c) N 1s valence NRXP spectrum ($h\nu$ = 398.0 eV) and N 1s valence RXP spectra ($h\nu$ = 402.1 eV and $h\nu$ = 399.7 eV), with the valence NRXP contributions subtracted. The NRXPS contributions were subtracted using the procedure detailed in Section 8.2. All RXP spectra were charge referenced using the methods detailed in Section 2.7.3.

Appendix Figure 8.29. N 1s valence RXPS map and spectra for $([C_4C_1Im][SCN])_{1.00}(H_2O)_{0.00}$: (a) N 1s valence RXPS heat map for $([C_4C_1Im][SCN])_{1.00}(H_2O)_{0.00}$. (b) Partial electron yield N 1s XA spectra. (c) N 1s valence NRXP spectrum ($h\nu$ = 398.0 eV) and N 1s valence RXP spectra ($h\nu$ = 402.1 eV and $h\nu$ = 399.7 eV), with the valence NRXP contributions subtracted. The NRXPS contributions were subtracted using the procedure detailed in Section 8.2. All RXP spectra were charge referenced using the methods detailed in Section 2.7.3.

Appendix Figure 8.30. O 1s valence RXPS map and spectra for pure H_2O: (a) O 1s valence RXPS heat map for pure H_2O. (b) Partial electron yield O 1s XA spectra. (c) O 1s valence NRXP spectrum ($h\nu$ = 532.5 eV) and O 1s valence RXP spectra ($h\nu$ = 536.0 eV and $h\nu$ = 535.0 eV), with the valence NRXP contributions subtracted. The NRXPS contributions were subtracted using the procedure detailed in Section 8.2. All RXP spectra were charge referenced using the methods detailed in Section 2.7.3.

Appendix Figure 8.31. O 1s valence RXPS map and spectra for $([C_4C_1Im][SCN])_{0.01}(H_2O)_{0.99}$: (a) O 1s valence RXPS heat map for $([C_4C_1Im][SCN])_{0.01}(H_2O)_{0.99}$. (b) Partial electron yield O 1s XA spectra. (c) O 1s valence NRXP spectrum ($h\nu$ = 532.5 eV) and O 1s valence RXP spectra ($h\nu$ = 536.0 eV and $h\nu$ = 535.0 eV), with the valence NRXP contributions subtracted. The NRXPS contributions were subtracted using the procedure detailed in Section 8.2. All RXP spectra were charge referenced using the methods detailed in Section 2.7.3.

Appendix Figure 8.32. O 1s valence RXPS map and spectra for $([C_4C_1Im][SCN])_{0.10}(H_2O)_{0.90}$: (a) O 1s valence RXPS heat map for $([C_4C_1Im][SCN])_{0.10}(H_2O)_{0.90}$. (b) Partial electron yield O 1s XA spectra. (c) O 1s valence NRXP spectrum ($h\nu$ = 532.5 eV) and O 1s valence RXP spectra ($h\nu$ = 536.0 eV and $h\nu$ = 535.0 eV), with the valence NRXP contributions subtracted. The NRXPS contributions were subtracted using the procedure detailed in Section 8.2. All RXP spectra were charge referenced using the methods detailed in Section 2.7.3.

Appendix Figure 8.33. O 1s valence RXPS map and spectra for $([C_4C_1Im][SCN])_{0.25}(H_2O)_{0.75}$: (a) O 1s valence RXPS heat map for $([C_4C_1Im][SCN])_{0.25}(H_2O)_{0.75}$. (b) Partial electron yield O 1s XA spectra. (c) O 1s valence NRXP spectrum ($h\nu$ = 532.5 eV) and O 1s valence RXP spectra ($h\nu$ = 536.0 eV and $h\nu$ = 535.0 eV), with the valence NRXP contributions subtracted. The NRXPS contributions were subtracted using the procedure detailed in Section 8.2. All RXP spectra were charge referenced using the methods detailed in Section 2.7.3.

Appendix Figure 8.34. Full N 1s XA spectra comparison for $([C_4C_1Im][SCN])_x(H_2O)_{1-x}$, where x_{IL} = 0.01, 0.10, and 0.25. Spectra are vertically offset for clarity and dashed lines are added as a visual aid.

Appendix Figure 8.35. Full O 1s XA spectra comparison for ([C_4C_1Im][SCN])$_x$(H_2O)$_{1\text{-}x}$, where x_{IL} = 0.01, 0.10, and 0.25. Spectra are vertically offset for clarity and dashed lines are added as a visual aid.

Appendix Figure 8.36. N 1s valence RXP spectra comparison for ([C_4C_1Im][SCN])$_x$(H_2O)$_{1\text{-}x}$, where x_{IL} = 0.01, 0.10, 0.25, and 1.00. (a) N_{cation} 1s valence RXP spectra ($h\nu$ = 402.1 eV), with the valence NRXP contributions subtracted. (b) N_{anion} 1s valence RXP spectra ($h\nu$ = 399.7 eV), with the valence NRXP contributions subtracted. Spectra are vertically offset for clarity. All NRXP spectra were charge referenced using the methods detailed in Section 2.7.3.

Appendix Figure 8.37. O 1s valence RXP spectra comparison within the participator Auger region for ([C_4C_1Im][SCN])$_x$(H_2O)$_{1\text{-}x}$, where x_{IL} = 0.01, 0.10, and 0.25: (a) O 1s valence RXP spectra ($h\nu$ = 536.0 eV), with the valence NRXP contributions subtracted. (b) O 1s valence RXP spectra ($h\nu$ = 535.0 eV), with the valence NRXP contributions subtracted. The NRXPS contributions were subtracted using the procedure detailed in Section 8.2. All RXP spectra were charge referenced using the methods detailed in Section 2.7.3.

Appendix Figure 8.38. Core and valence state NRXP spectra for 0.5 M (K[SCN])(H_2O): (a) C 1s. (b) N 1s. (c) O 1s. (d) S 2p. (e) K 2p. (f) Valence. All XP spectra were measured at $h\nu$ = 700.0 eV. All XP spectra were charge referenced using the methods detailed in Section 2.7.2.

Appendix Figure 8.39. Core and valence state NRXP spectra for 0.5 M (K[SCN])(PC): (a) C 1s. (b) N 1s. (c) O 1s. (d) S 2p. (e) K 2p. (f) Valence. All XP spectra were measured at $h\nu$ = 700.0 eV. All XP spectra were charge referenced using the methods detailed in Section 2.7.2.

Appendix Figure 8.40. Core and valence state NRXP spectra for 0.5 M (Li[NTf_2])(H_2O): (a) C 1s. (b) N 1s. (c) O 1s. (d) S 2p. (e) F 1s. (f) Valence. All XP spectra were measured at $h\nu$ = 700.0 eV. All XP spectra were charge referenced using the methods detailed in Section 2.7.2.

Appendix Figure 8.41. Core and valence state NRXP spectra for 0.5 M (Li[NTf_2])(PC): (a) C 1s. (b) N 1s. (c) O 1s. (d) S 2p. (e) F 1s. (f) Valence. All XP spectra were measured at $h\nu$ = 700.0 eV. All XP spectra were charge referenced using the methods detailed in Section 2.7.2.

Appendix Figure 8.42. N 1s valence RXPS map and spectra for 0.5 M (K[SCN])(H_2O): (a) N 1s valence RXPS heat map for 0.5 M (K[SCN])(H_2O). (b) Partial electron yield N 1s XA spectra. (c) N 1s valence NRXP spectrum ($h\nu$ = 398.0 eV) and N 1s valence RXP spectra ($h\nu$ = 399.7 eV), with the valence NRXP contributions subtracted. The NRXPS contributions were subtracted using the procedure detailed in Section 8.2. All RXP spectra were charge referenced using the methods detailed in Section 2.7.3.

Appendix Figure 8.43. C 1s valence RXPS map and spectra for 0.5 M (K[SCN])(H_2O): (a) C 1s valence RXPS heat map for 0.5 M (K[SCN])(H_2O). (b) Partial electron yield C 1s XA spectra. (c) C 1s valence NRXP spectrum ($h\nu$ = 284.0 eV) and C 1s valence RXP spectra ($h\nu$ = 287.5 eV), with the valence NRXP contributions subtracted. The NRXPS contributions were subtracted using the procedure detailed in Section 8.2. All RXP spectra were charge referenced using the methods detailed in Section 2.7.3.

Appendix Figure 8.44. N 1s valence RXPS map and spectra for 0.5 M (K[SCN])(PC): (a) N 1s valence RXPS heat map for 0.5 M (K[SCN])(PC). (b) Partial electron yield N 1s XA spectra. (c) N 1s valence NRXP spectrum ($h\nu$ = 398.0 eV) and N 1s valence RXP spectra ($h\nu$ = 399.7 eV), with the valence NRXP contributions subtracted. The NRXPS contributions were subtracted using the procedure detailed in Section 8.2. All RXP spectra were charge referenced using the methods detailed in Section 2.7.3.

Appendix Figure 8.45. C 1s valence RXPS map and spectra for 0.5 M (K[SCN])(PC): (a) C 1s valence RXPS heat map for 0.5 M (K[SCN])(PC). (b) Partial electron yield C 1s XA spectra. (c) C 1s valence NRXP spectrum ($h\nu$ = 284.0 eV) and C 1s valence RXP spectra ($h\nu$ = 287.5 eV), with the valence NRXP contributions subtracted. The NRXPS contributions were subtracted using the procedure detailed in Section 8.2. All RXP spectra were charge referenced using the methods detailed in Section 2.7.3.

Appendix Figure 8.46. N 1s valence RXPS map and spectra for 0.5 M (Li[NTf$_2$])(H$_2$O): (a) N 1s valence RXPS heat map for 0.5 M (Li[NTf$_2$])(H$_2$O). (b) Partial electron yield N 1s XA spectra. (c) N 1s valence NRXP spectrum ($h\nu$ = 398.0 eV) and N 1s valence RXP spectra ($h\nu$ = 402.1 eV), with the valence NRXP contributions subtracted. The NRXPS contributions were subtracted using the procedure detailed in Section 8.2. All RXP spectra were charge referenced using the methods detailed in Section 2.7.3.

Appendix Figure 8.47. F 1s valence RXPS map and spectra for 0.5 M (Li[NTf$_2$])(H$_2$O): (a) F 1s valence RXPS heat map for 0.5 M (Li[NTf$_2$])(H$_2$O). (b) Partial electron yield F 1s XA spectra. (c) F 1s valence NRXP spectrum ($h\nu$ = 686.0 eV) and F 1s valence RXP spectra ($h\nu$ = 690.3 eV), with the valence NRXP contributions subtracted. The NRXPS contributions were subtracted using the procedure detailed in Section 8.2. All RXP spectra were charge referenced using the methods detailed in Section 2.7.3.

List of tables

Table 1.1. The classification of common solvent species and their uses within the literature.

Table 1.2. Summary of descriptors and probes used for each quantification method for cation-anion interactions.

Table 1.3. Summary of solvent polarity descriptors and probes used for each quantification method for solvent-solute interactions.

Table 1.4. Quantum numbers used to describe the electronic structure of an atom.

Table 2.1. The photoemission peak identity and E_B value used for charge referencing each sample to the E_B(cation) value obtained for dilute ions in H_2O.

Table 2.2. The photoemission peak identity and E_B value used for charge referencing each sample to the E_B(solvent) value obtained for neat solvent.

Table 2.3. The photoemission peak identity and $h\nu$ value used for charge referencing each sample to the E_B(solvent) value obtained for neat solvent.

Table 3.1. The ten solutions studied within Chapter 3. Concentrations were calculated using parameters listed in Appendix Tables 8.1 to 8.3.

Table 3.2. Experimental binding energies, E_B, recorded by NRXPS for 0.5 M ([C_4C_1Im][SCN])(solvent), where solvent = H_2O, H_2O/EtOH, EtOH, MeCN, PC, and for neat [C_4C_1Im][SCN]. All XP spectra for 0.5 M ([C_4C_1Im][SCN])(solvent) were measured at $h\nu$ = 700.0 eV; neat [C_4C_1Im][SCN] XP spectra were measured at $h\nu$ = 1486.6 eV. All values were charge referenced using the methods detailed in Section 2.7.1. All E_B values are reported to 2 decimal places.

Table 3.3. Experimental area and FWHM ratios of (N_{cation} 1s/N_{anion} 1s) and (S $2p_{3/2}$/S $2p_{1/2}$) recorded by NRXPS for 0.5 M ([C_4C_1Im][SCN])(solvent), where solvent = H_2O, H_2O/EtOH, EtOH, MeCN, PC, and for neat [C_4C_1Im][SCN]. All spectra for 0.5 M ([C_4C_1Im][SCN])(solvent) were measured at $h\nu$ = 700.0 eV; neat [C_4C_1Im][SCN] XP spectra were measured at $h\nu$ = 1486.6 eV.

Table 3.4. Experimental binding energies, E_B, recorded by NRXPS for 0.5 M (solute)(H_2O) and 0.5 M (solute)(PC), where solute = K[SCN] and Li[NTf_2]. All XP spectra for 0.5 M (K[SCN])(solvent) and 0.5 M (Li[NTf_2])(solvent) were measured at $h\nu$ = 700.0 eV. All values charge referenced using the methods detailed in Section 2.7.2. Values are reported to 2 decimal places.

Table 3.5. Experimental binding energies, E_B, recorded by NRXPS for 0.5 M (solute)(H_2O) and 0.5 M (solute)(PC), where solute = [C_4C_1Im][SCN] and K[SCN]. All XP spectra were measured at $h\nu$ = 700.0 eV. All values were charge referenced using the methods detailed in Section 2.7.2. All values are reported to 2 decimal places.

Table 3.6. KT, Gutmann, and Catalán solvent polarity scale descriptor values for H_2O, H_2O/EtOH, EtOH, MeCN, PC, and for neat [C_4C_1Im][SCN]. Valence NRXP spectra used to obtain $E_B(\text{HOVS}_{\text{anion}})$ for samples of 0.5 M ([C_4C_1Im][SCN])(solvent) were measured at $h\nu$ = 700.0 eV, whereas valence NRXP spectra for neat [C_4C_1Im][SCN] was measured at $h\nu$ = 1486.6 eV. All spectra were charge referenced using the methods detailed in Section 2.7.1. KT, and Catalán polarity scale descriptor values were obtained from reference [7] unless otherwise indicated. All values are reported to 2 decimal places.

Table 4.1. The six solutions and six neat ILs studied within Chapter 4. Concentrations were calculated using parameters listed in Appendix Tables 8.1 to 8.3.

Table 4.2. KT α_{solv}, β_{solv}, and π^*_{solv} polarity scale descriptor and Pearson χ and η absolute scale descriptor values for neat [C_4C_1Im][anion] and H_2O included.

Table 4.3. Anionic experimental binding energies, E_B(anion), recorded by NRXPS for 0.5 M ([C_4C_1Im][anion])(H_2O) and neat [C_nC_1Im][anion], where anion = [SCN]$^-$, [$N(CN)_2$]$^-$, [BF_4]$^-$, [TfO]$^-$, Cl$^-$, and I$^-$. Spectra for samples in aqueous solution were measured at $h\nu$ = 700.0 eV; spectra for samples of neat IL were measured at $h\nu$ = 1486.6 eV. All values were charge referenced using the methods detailed in Section 2.7.1. All E_B values are reported to 2 decimal places.

Table 4.4. Experimental binding energies, E_B, recorded by C 1s NRXPS for 0.5 M ([C_nC_1Im][anion])(H_2O) and neat [C_nC_1Im][anion], where anion = [SCN]$^-$, [$N(CN)_2$]$^-$, [BF_4]$^-$, [TfO]$^-$, Cl$^-$, and I$^-$. Spectra for samples in aqueous solution were measured at $h\nu$ = 700.0 eV; spectra for samples of neat IL were measured at $h\nu$ = 1486.6 eV. All values were charge referenced using the methods detailed in Section 2.7.1. All E_B values are reported to 2 decimal places.

Table 5.1. The four solutions studied within Chapter 5. Concentrations were calculated using parameters listed in Appendix Tables 8.1 to 8.3.

Table 5.2. Experimental binding energies, E_B, recorded by NRXPS for ([C_4C_1Im][SCN])$_x$(H_2O)$_{1-x}$, where x = 0.01, 0.10, 0.25 and 1.00. All values were charge referenced using the methods detailed in Section 2.7.1.

Table 5.3. Experimental area and FWHM ratios of (N_{cation} 1s/N_{anion} 1s) and (S $2p_{3/2}$/S $2p_{1/2}$) recorded by NRXPS for $([C_4C_1Im][SCN])_x(H_2O)_{1-x}$, where x_{IL} = 0.01, 0.10, 0.25, and 1.00. All XP spectra for solutions of $([C_4C_1Im][SCN])_x(H_2O)_{1-x}$, where x_{IL} = 0.01, 0.10, and 0.25, were measured at $h\nu$ = 700.0 eV; neat $[C_4C_1Im][SCN]$ XP spectra were measured at $h\nu$ = 1486.6 eV.

Table 6.1. The six solutions studied within Chapter 6. Concentrations were calculated using parameters listed in Appendix Tables 8.1 to 8.3.

Table 6.2. Experimental binding energies, E_B, recorded by NRXPS for 0.5 M (solute)(H_2O) and 0.5 M (solute)(PC), where solute = $[C_4C_1Im][SCN]$, K[SCN], and Li[NTf_2], and the E_B difference between each sample, ΔE_B. All spectra were measured at $h\nu$ = 700.0 eV. All values charge referenced using the methods detailed in Section 2.7.2. All E_B values are reported to 2 decimal places.

Table 6.3. KT and Gutmann-Beckett solvent polarity scale descriptor values for H_2O, and PC. Values for β_{solv} were obtained from reference [10]; values for DN_{solv} were obtained from reference [19].

Table 6.4. Experimental K $2p_{1/2}$ and K $2p_{3/2}$ FWHM values and area ratios of (K $2p_{3/2}$/K $2p_{1/2}$) recorded by NRXPS for 0.5 M (K[SCN])(H_2O) and 0.5 M (K[SCN])(PC). All 0.5 M spectra were measured at $h\nu$ = 700.0 eV.

Appendix Table 8.1. Solute and solvent masses used to produce 100 mL of each solution at the required concentration, measured within the current work.

Appendix Table 8.2. Solute molar mass (M_r) and density (ρ) used to produce each solution measured within the current work.

Appendix Table 8.3. Solvent molar mass (M_r) and density (ρ) used to produce each solution measured within the current work.

Appendix Table 8.4. Constraints used within the peak fitting models for core level X-ray photoelectron spectroscopy (XPS) employed within the current work.

Appendix Table 8.5. The photoemission peak identity and $h\nu$ value of the NRXP spectra used for subtraction of the valence RXPS heat map.

Chapter 1

Introduction

This chapter aims to introduce the overarching topics addressed within this thesis. Solvent properties such as their classification, use, polarity, and polarisability are first examined (Section 1.1). A review of the properties of ionic species is then undertaken, including a comparison between cationic and anionic species, cation-anion interactions and their quantification, and their prevalence within the literature (Section 1.2). Next, a review of ions in solution is carried out, detailing the process of solvation of a solute in molecular solvent (MS), the known theories pertaining to the solvation of solute within bulk MS and at the interface, ion-solvent interactions and their quantification, and the practical uses of ions in solution within the literature (Section 1.3). Following, the concept of *electronic structure* is explored in relation to both the core level, and valence states (Section 1.4). Subsequently, a review of X-ray spectroscopy of ions in MS within the literature is conducted (Section 1.5). Next, the reasoning for the choice of ions and solvents studied within this work was discussed (Section 1.6). Lastly, the aim of the current work is discussed (Section 1.7).

1.1. Solvent properties

1.1.1. Classification and use of solvent species

Uses

A solvent may be defined as a substance in which other materials dissolve to form a solution.[1] Therefore, within a solution at least two components are present: the solvent and the solute, where the solute is the minor component, and the solvent is the major component. The uses of solvents of differing identity and function are vast (Table 1.1). For example, solvents may behave as a reaction medium, whereby dissolution of multiple solutes within a solvent can facilitate their increased reaction rate. Additionally, dissolution can provide a means to study species which would otherwise be too unstable or impractical to measure (or store). Additionally, as the solvent is the major component within a solution, its role as a reactant is very important to consider. For example, solvent-solute interactions occur in almost all solutions. In circumstances where solvent-solute interactions are great, these interactions can lead to the modification of the properties of the solute species. Conversely, where solvent-solute interactions are weak, the solvent may act as a carrier for processes such as liquid chromatography, nuclear magnetic resonance spectroscopy, and mass spectrometry, where it is important that the solvent does not modify the properties of the solute.

Table 1.1. The classification of common solvent species and their uses within the literature, where ML = molecular liquid, EPA = electron pair acceptor, and EPD = electron pair donor.

Solvent	Classification	Use
H_2O	ML; dipolar; EPA/EPD	Key biological solvent[2]
Ethanol	ML; dipolar; EPA/EPD	Organic solvent and biofuel production[3]
Acetonitrile	ML; dipolar; EPD	Solvent for dye-sensitised solar cells[4]
Propylene carbonate	ML; dipolar; EPD	Battery electrolyte[5]
$[C_4C_1Im]X$	IL; ion pairs; EPA/EPD	Lignin decomposition[6, 7]

Classification

The classification of different solvent species can be undertaken based upon a variety of factors. Three methods of classification are discussed herein: based upon chemical bonds, according to physical constants, and according to acid/base behaviour.

Classification according to chemical bonds, where solvents are characterised based upon the type of solvent-solvent bonds present in pure form, is useful for predicting the feasibility of dissolution of a solute in solvent according to greater ease of solvation where similar functional groups are present. Three groups containing differing chemical bonds are used within this method of classification: molecular liquids, atomic liquids, and ionic liquids (ILs). Molecular liquids are solvents which contain covalent bonds, *e.g.*, molecular melts. Atomic liquids are solvents which contain metallic bonds, *e.g.*, liquid mercury. ILs are solvents which contain ionic bonds, *e.g.*, molten salts, ILs.

Classification according to physical constants, where solvents are characterised based upon properties such as cohesive energy density, *ced*, relative permittivity, ε_r, and refractive index, n_D

(these bulk physical properties are discussed in Section 1.1.2), is useful for providing an assessment of solvent polarity and polarisability. For example, the classification according to the molecular physical property dipole moment, μ, is common as it allows for a good description of ion pairing (relevant to later discussion). Solvents are separated into apolar, dipolar, zwitterionic, and ion pairs, where μ increases respectively. Apolar molecules (μ ~ 0 D) allow for the least extent of charge separation for ionic solutes, *e.g.*, cyclohexane. Dipolar molecules (μ ~ 3 - 6 D) allow for a greater extent of charge separation than apolar molecules, *e.g.*, acetone, DMSO, and H_2O. Zwitterionic molecules (μ > 10 D) allow for an increased extent of charge separation than dipolar molecules, *e.g.*, sydnones and zwitterionic amino acids. Lastly, ion pairs contain the greatest extent of charge separation, where cationic and anionic species exist individually in the liquid phase, *e.g.*, ILs.

Classification according to acid/base behaviour, where solvents are characterised based upon the ability of a species to act as an electron pair acceptor (EPA) or an electron pair donor (EPD), according to the description of a Lewis acid/base (more detail in Section 1.3.4), where an EPA is a Lewis acid, and an EPD is a Lewis base. The strength of a donor/acceptor interaction is based upon the size of the overlap between the doubly occupied orbital of the donor and a vacant orbital of the acceptor (Section 1.4).[8, 9] Therefore, this classification is useful within the determination of interactions between solvent and solute species.

1.1.2. Polarity and polarisability

The polarity and polarisability are important properties of a solvent, where the polarity relates to the separation of its electric charge leading to the molecule or its chemical groups having an electric dipole moment, and the polarisability (Equation 1.1) is indicative of the tendency of its electric charge to become distorted due to the influence of a neighbouring species.[1] Polarisability is linked to the refractive index through the Lorentz-Lorenz relation (Equation 1.2), and to the relative permittivity through the Clausius-Mossotti relation (Equation 1.3). The Lorentz-Lorenz law combines the two relations to describe the relationship between the refractive index and the relative permittivity (Equation 1.4). There are many properties used to assess solvent polarity, which are separated into physical and chemical properties. Physical properties are further separated into bulk properties and molecular properties. Physical bulk (macroscopic) properties include cohesive energy density, relative permittivity, and refractive index, whereas molecular (microscopic) properties include dipole moment. Chemical properties include EPA/EPD, and solvatochromic polarity descriptors (Section 1.3.5).

$$\alpha = \frac{\rho}{E} \tag{1.1}$$

α = polarisability ($C \cdot m^2 V^{-1}$)

ρ = electrical dipole moment induced by an electric field

E = electric field strength

$$K\rho = \frac{n^2 - 1}{n^2 + 2} \tag{1.2}$$

K = proportionality factor ($m^3\ kg^{-1}$)

ρ = electrical dipole moment induced by an electric field

n = index of refraction

$$\frac{N\alpha}{3\varepsilon_0} = \frac{\varepsilon_r - 1}{\varepsilon_r + 2} \tag{1.3}$$

N = number density of the molecules (number per cubic meter)

α = polarisability ($C \cdot m^2 V^{-1}$)

ε_0 = permittivity of free space ($V \cdot m^{-1}$)

ε_r = relative permittivity

$$n = \sqrt{\varepsilon_r} \tag{1.4}$$

The cohesive energy density, *ced,* is a measure of the total strength of all solvent-solvent forces within the liquid (Equation 1.5).[10-12] As shown, the *ced* has an inverse relationship with the molecular volume, V_m, which is the volume occupied by one mole at a given temperature and pressure. Therefore, *ced* reflects the absence of solvent-solvent bonds within the vapour phase. However, the *ced* does not consider solvent-solute interactions so is most applicable when these are weak.

$$ced = \frac{\Delta H_{vap} - RT}{V_m} \tag{1.5}$$

ΔH_{vap} = molar enthalpy of vaporisation ($J \cdot mol^{-1}$)

R = gas constant ($mol^{-1} \cdot K^{-1}$)

T = temperature (K)

V_m = molecular volume ($M \cdot \rho$)

The relative permittivity, ε_r, otherwise known as the dielectric constant, is a measure of the ability of a solvent to separate its charges and orient its dipoles.[1] The relative permittivity of a solvent is measured by placing the solvent between two plates of a capacitor. The relationship between the electric field strength between capacitor plates in a vacuum, E_o, and the electric field strength upon the introduction of a solvent, E, is then compared to yield the relative permittivity (Equation 1.6). The relative permittivity ranges between 1.8 (pentane, 293 K) and 191 (*N*-methylacetamide, 305 K), where H_2O is considered a high relative permittivity solvent (ε_r = 80, 293 K).[13]

$$\varepsilon_r = \frac{E_\mathrm{o}}{E} \tag{1.6}$$

E_o = electric field strength between capacitor plates in a vacuum ($V \cdot \mathrm{m}^{-1}$)
E = electric field strength between capacitor plates upon the introduction of a solvent ($V \cdot \mathrm{m}^{-1}$)

The refractive index, n_D, is a measure of the induced polarisability of electrons in a solvent (Figure 1.1a). n_D is the ratio of the speed of light of the sodium D-line (λ = 589 nm) in vacuum, c_o, to its speed in the liquid, c (Equation 1.7). Therefore, n_D generally increases with increasing molar mass and polarisability of the solvent.[1]

$$n_\mathrm{D} = \frac{c_\mathrm{o}}{c} = \frac{\sin\theta}{\sin\phi} \tag{1.7}$$

c_o = speed of light of a specific wavelength in vacuum
c = speed of light in the liquid phase

The dipole moment, μ, yields the polarisation orientation of a molecule (Figure 1.1b). A solvent molecule may be termed either polar or nonpolar, depending upon its dipole moment, which is determined from both, the relative permittivity, and the refractive index. A polar molecule contains an uneven charge distribution due to a greater electron density on one side than the other, inducing a permanent dipole; hence the molecule is susceptible to permanent dipole interactions. In contrast, a nonpolar molecule contains a uniform electron distribution, containing no permanent dipole; hence, the molecule is susceptible to induced dipole interactions. Both permanent and induced dipole interactions will be discussed later (Section 1.3.4).

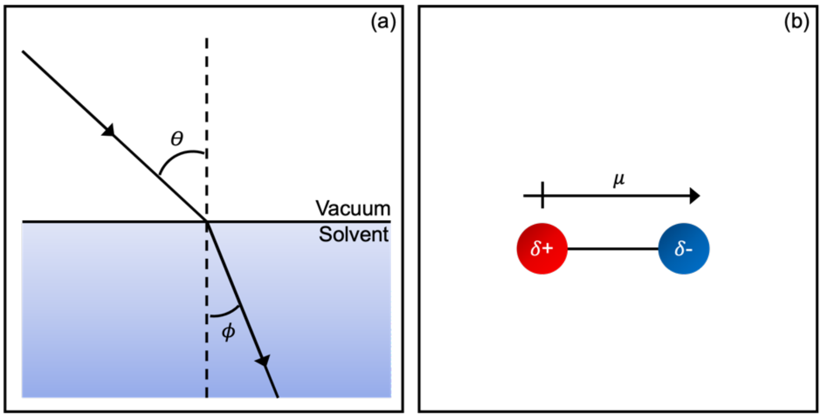

Figure 1.1. Examples of the physical properties used to assess solvent polarity: (a) Refractive index (bulk property). (b) Dipole moment (molecular property), where a dipole moment exists in the direction from the δ+ to δ- atom.

In the pure liquid phase, solvent molecules (excluding liquid crystals) possess a random orientation and movement due to Brownian motion.[14] This random orientation is shown to occur for both polar and nonpolar solvents in the absence of an electric field (Figure 1.2a). Upon the introduction of an electric field, the permanent dipole of polar solvent molecules, and the induced dipole of nonpolar solvent molecules, align (Figure 1.2b). In the presence of an ionic solute species, molecular dipoles of polar solvent molecules orient towards their opposite, attractive charge (Figure 1.2c).

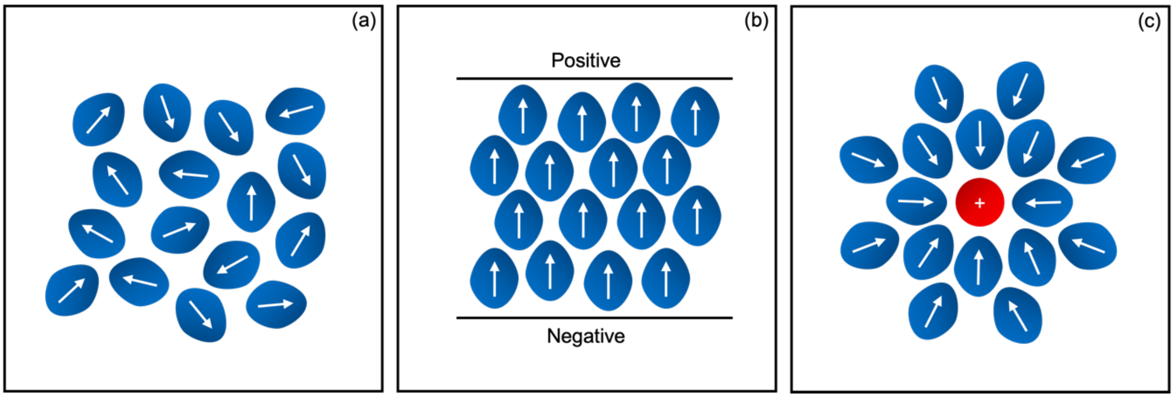

Figure 1.2. Orientation of solvent molecules with differing external electric field stimuli: (a) Absence of an electric field. (b) Presence of an electric field. (c) Introduction of a cationic species. Adapted from reference [15].

1.2. Properties of ionic species

1.2.1. Cationic and anionic species

The ratio between the number of electrons (negatively charged subatomic particles) and protons (positively charged subatomic particles) within an atom, or group of atoms within a molecule, determines the overall charge of the species. Species with an overall excess of either positive or negative charge are termed ‘ions’. For example, a neutral H_2O molecule contains eight protons and eight electrons. Through the addition of a proton to form $[H_3O]^+$, a cation with an overall positive charge is formed. The removal of a proton from H_2O to form $[OH]^-$ results in an excess of negative charge; hence, the species is anionic. Common modes of interaction between ionic species include ionic bonding, and coulombic interactions (Section 1.2.2).

A cation is a species containing an overall positive charge. The electronic structure of singly charged cationic species contain one less electron within their outermost orbital in comparison to their neutral counterparts. Hence, the electron affinity of cations is negative, indicating the favourability of adding an electron to the system. Conversely, ionisation energies are high due to the strong nuclear attraction on the valence electrons. Cationic species possess a unique set of abilities which enables their use in a range of processes. Within electrochemistry, the attraction of a cation to the cathode is exploited for the use in battery systems.[16] Within synthetic chemistry, cations act as electrophilic species due to their electron deficiency, allowing for reactions such as electrophilic addition to occur. Examples of cationic species include Na^+, K^+, and $[C_4C_1Im]^+$.

An anion is a species containing an overall negative charge. In contrast to cations, the electronic structure of singly charged anionic species contain an additional electron within their outermost orbital in comparison to their neutral counterparts. Hence, the electron affinity of anions is positive, reflecting the unfavorability of adding an electron to the system. Ionisation energies are low due to a weak nuclear attraction experienced by the valence electrons, which are screened by the other electrons within the system. Anionic atoms are also useful within a variety of applications due to their contrasting abilities to cations. For example, anions are also used in electrochemistry as the counterion, where they are instead attracted to the anode, facilitating the movement of electrons between electrodes to allow for charging and discharging of batteries. Within synthetic chemistry, anions act as nucleophiles due to their free electron pair or π bond character, allowing for reactions such as those categorised as S_N1 and S_N2.[17] Examples of anionic species include Cl^-, I^-, $[SCN]^-$.

1.2.2. Cation-anion interactions

Cations and anions interact through Coulomb forces. Similarly, ionic solids are held together by electrostatic attraction in ionic bonds.[18] Cations and anions in solution have the ability to act as Lewis acids and bases, respectively, towards other solute species in solution. The indirect quantification of the Lewis acid/base behaviour of ionic species has been attempted through various methodologies (Table 1.2).

Pearson and co-workers used the ground-state electronic energy as a function of the number of electrons, *N*, within a system, calculated through use of density functional theory (DFT), to describe two terms: the absolute electronegativity, χ, and the absolute hardness, η, of a species.[19, 20] The value of the absolute electronegativity of a species indicates the direction of electron transfer within a chemical interaction, where electrons will flow from species with a low value of χ to those of a high value of χ. Therefore, a large value of χ is indicative of a Lewis acid (EPA), and a small value of χ is indicative of a Lewis base (EPD). The value of the absolute hardness relates to the relative energies of the frontier orbitals (Section 1.4) of a species, which indicates the extent of polarisability. Large values of η are indicative of hard species with a large HOMO-LUMO gap. Therefore, hard molecules display low polarisabilities and favour ionic bond formation between species, where an example of a hard base is H_2O, and an example of a hard acid is Li^+. In contrast, small values of η are indicative of soft species with a small HOMO-LUMO gap. Therefore, soft molecules are highly polarisable (large electrostatic repulsion between electrons of relatively similar energies) and favour covalent bond formation between species, where an example of a soft base is I^-, and an example of a soft acid is Ag^+. As a general rule, hard acids are shown to prioritise coordination to hard bases, and soft acids prefer soft bases.[20] One benefit of the Pearson hard and soft acids and bases (HSAB) principle is that no external reference probe is used within the calculation of χ and η, as the number of electrons within a system, *N*, is used. However, as χ and η values are obtained through computational methods, an incomplete description of system experimental parameters can lead to results which are inconsistent with experimental observations.

Gutmann and co-workers (namely Beckett) used two different techniques to describe the ability of a species to act as a Lewis acid or Lewis base, through the descriptors: electron acceptor number, *AN*, and electron donor number, *DN*, respectively.[21, 22] To determine the *AN* of a species, Gutmann utilised the nature of chemical shifts within ^{31}P NMR, which vary in magnitude dependent upon the strength of the interaction between the investigated species and the chemical probe, $Et_3{}^{31}PO$. *AN* is primarily a measure of Lewis acidity, where the greater the value, the greater the ability of a species to accept an electron pair. To determine the *DN* of a species, the negative enthalpy, $-\Delta H^\circ$, for the reaction between the investigated species and the chemical probe, $SbCl_5$, was measured. *DN* is primarily a measure of Lewis basicity, where the greater the value, the greater the ability of a species to donate an electron pair. One benefit of the Gutmann AN/DN scale is that it allows for the rationalisation of Lewis acid/base interactions.[1] However, the Gutmann AN/DN scale is probe dependent, meaning each measured species must be quantified using the same probe for valid comparisons across *AN/DN* values. Additionally, it may be impossible to measure certain species using the standard probes due to alterations of probe or probed species via chemical reactions between the two.

Table 1.2. Summary of descriptors and probes used for each quantification method for cation-anion interactions.

Quantification method	Descriptor	Probe	Technique
Pearson	χ: absolute electronegativity η: absolute hardness	N	DFT
Gutmann	*AN*: acceptor number	$Et_3{}^{31}PO$	^{31}P NMR
	DN: donor number	$SbCl_5$	$-\Delta H^\circ$

1.2.3. Ionic liquids

Ionic liquids (ILs) are substances composed entirely of mobile ions.[23, 24] ILs are commonly composed of bulky organic cations, *e.g.*, $[C_4C_1Im]^+$, paired with smaller inorganic anions, *e.g.*, $[SCN]^-$. The number of potential ILs is vast due to a large quantity of possible cation-anion combinations.[25] Through variation of cation-anion combinations the physicochemical properties of each liquid has been shown to differ, giving rise to the subset of task-specific ILs.[26] However, ionic properties are not superimposable, meaning task-specific ILs may not easily be formed with the favoured properties of their constituent ions.[27] Nevertheless, the majority of ILs are shown to possess the same five common properties:

1. A negligible vapour pressure due to strong ionic character, large electrostatic interactions, and low melting temperatures. When heated to high temperature (between 450 K and 550 K) ILs have been shown to evaporate as ion pairs.[28]
2. A large liquid range due to the existence of a number of different bonding modes, *e.g.*, Coulombic interactions and hydrogen bonding,[29, 30] and a large *ced*.[12]
3. High thermal stability due to a composition of thermally stable ions (although not for all ILs).[31]
4. Good ionic conductivity due to their ionic composition, which favours the solvation of additional ions.[32, 33]
5. High electrochemical stability due to a large electrochemical window.[34-36]

IL nomenclature and the atomic numbering system referred to for the 1-butyl-3-methylimidazolium cation, $[C_4C_1Im]^+$, which features primarily within this work is subsequently explained (Figure 1.3). $[\mathbf{C_4}C_1Im]^+$ is used to denote an alkyl chain with four carbon atoms (butyl), which correspond to C^7, C^8, C^9, and C^{10} atoms. $[C_4\mathbf{C_1}Im]^+$ represents an alkyl group with a single carbon atom (methyl), which corresponds to the C^6 atom. Finally, $[C_4C_1\mathbf{Im}]^+$ is used to signify the presence of the five membered imidazolium ring, which contains three carbon atoms C^2, C^4, and C^5, additional to two nitrogen atoms N^1 and N^3. Resonance is permitted within the imidazolium ring due to the double bond character across both, C^4 and C^5, and N^1, C^2, and N^3. Hence, the cationic positive charge is shown over all atoms within the heterocyclic ring.

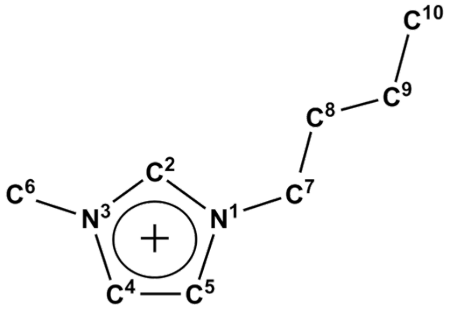

$[C_4C_1Im]^+$

Figure 1.3. Structure of the 1-butyl-3-methylimidazolium cation, $[C_4C_1Im]^+$, where atoms are numbered according to convention for reference within the current work.

1.3. Ions in solution

1.3.1. Solvation of solutes

The solvation of a solute within solvent species results in the formation of a solution.[1] A solution is a homogeneous liquid phase consisting of more than one substance in variable ratios, where the major component is termed the solvent, and the minor component is the solute.[37] Solvation of the solute is achieved through the surrounding of each dissolved molecule or ion by a shell of solvent molecules in reversible chemical combination.[38] The solvation of ions within an aqueous or organic solvent can significantly alter their physicochemical and electronic properties.[39]

The process of solvation is often thermodynamically described by breaking down solvent-solute interactions into the following four steps:[40]

1. Solvent-solvent bonds break to form a cavity within the solvent structure. Cavity creation is both entropically and enthalpically unfavourable (endothermic process, Figure 1.4b).
2. Solute-solute bonds break, leading to the separation of solute species into its constituents, which is also enthalpically unfavourable (endothermic process, Figure 1.4b).
3. Solvent-solute interactions form resulting in the insertion of the solute species into the solvent cavity, which is an enthalpically favourable process (exothermic process, Figure 1.4c).
4. Steps 1 to 3 repeat until complete mixing of solute and solvent species is achieved, which is entropically favourable.

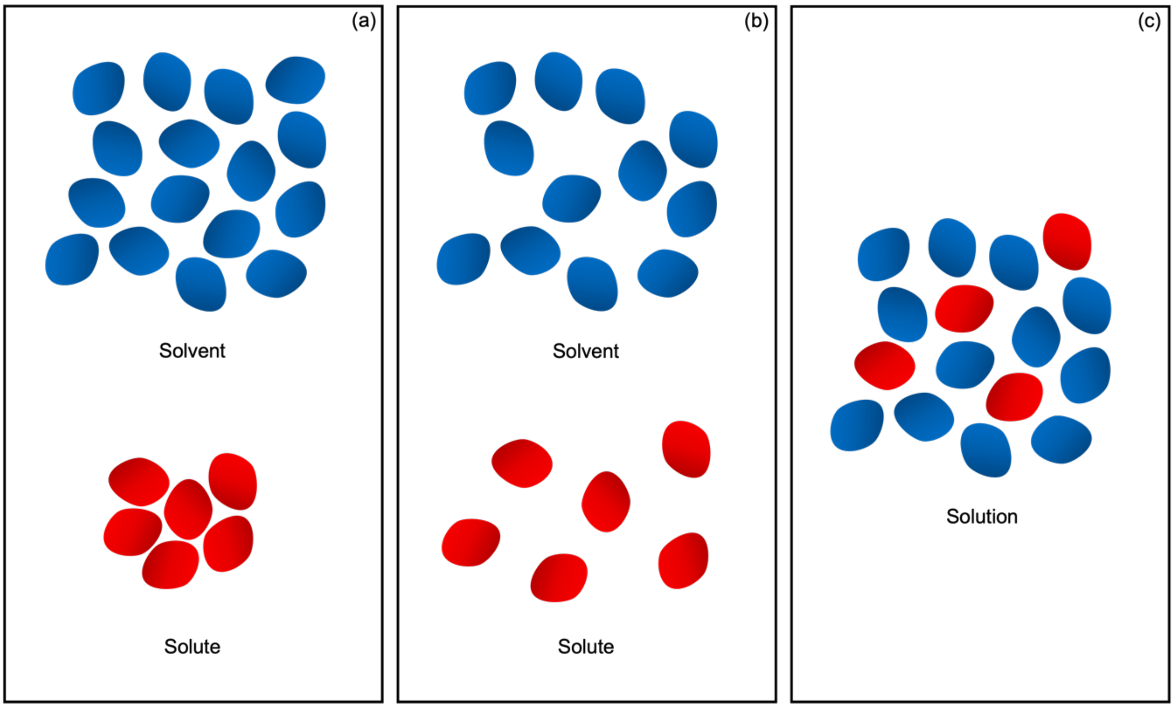

Figure 1.4. The process of solvation: (a) Solvent and solute species exist separately, where solvent-solvent bonds and solute-solute bonds remain intact. (b) Solvent-solvent bonds break to form cavities within the solvent bonding network; solute-solute bonds break. (c) Solute is solvated by the solvent molecules to form a solution.

The overall enthalpy of solution, ΔH_{soln}, can be represented within an enthalpy diagram (Figure 1.5). The enthalpy of solution can be either exothermic, or endothermic (Equation 1.4). The solvation process is exothermic when $\Delta H_{soln} < 0$. In contrast, the solvation process is endothermic when $\Delta H_{soln} > 0$.

$$\Delta H_{soln} = \Delta H_1 + \Delta H_2 + \Delta H_3 \tag{1.4}$$

ΔH_{soln} = enthalpy of solution

ΔH_1 = enthalpy change for the breaking of solvent-solvent bonds (step 1)

ΔH_2 = enthalpy change for the breaking of solute-solute bonds (step 2)

ΔH_3 = enthalpy change for the forming of solvent-solute bonds (step 3)

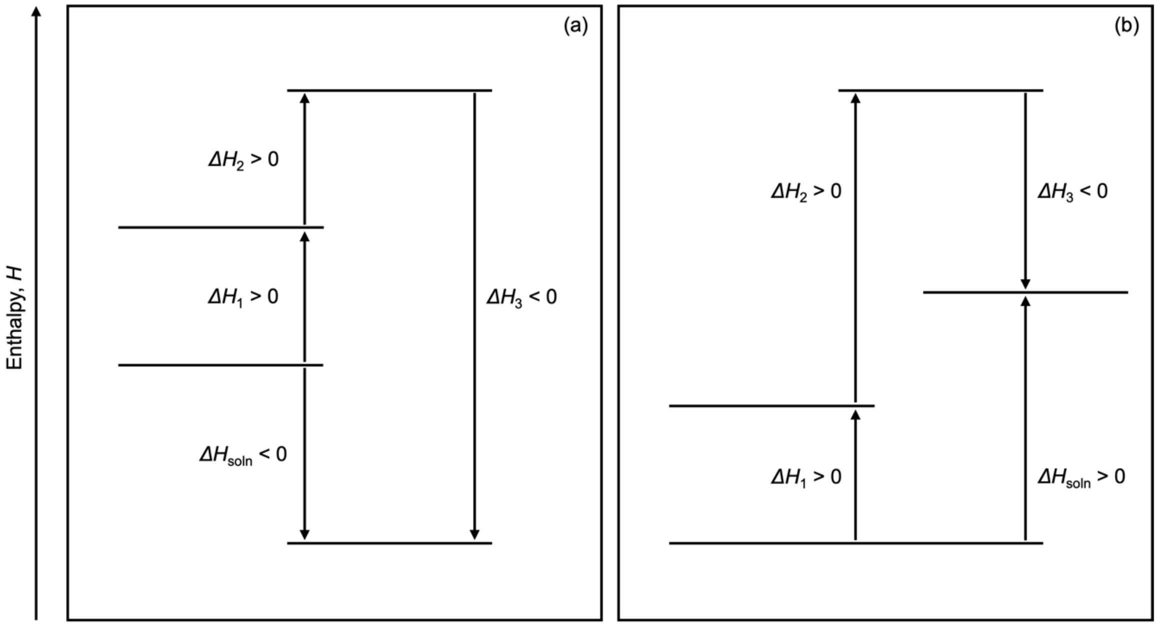

Figure 1.5. Enthalpy of solution diagram for: (a) Exothermic solvation. (b) Endothermic solvation.

The force of interaction between two oppositely charged ions, which indicates the extent of ion pairing in solution, can be predicted in relation to the relative permittivity of the solvent using Coulomb's law (Equation 1.5).[41] Hence, it follows that the greater the relative permittivity of the solvent, the lower the degree of ion pairing in solution is to be expected. This process is termed 'dielectric decrement', whereby ion pairing is screened by high relative permittivity solvents, *e.g.*, H_2O, but permitted to a greater degree within low relative permittivity solvents, *e.g.*, tetrahydrofuran.[10, 42]

$$F \propto \frac{q_1 q_2}{r^2 \varepsilon_{\mathrm{r}}} \tag{1.5}$$

F = force

q_1 = charge on ion 1

q_2 = charge on ion 2

r = distance between the two charges

The Gibbs free energy of solvation, ΔG_S^o, of a mole of ions is calculated from the Born equation (Equation 1.6). ΔG_S^o determines the spontaneity of solvation of an ion in solvent species, where a negative value indicates spontaneous solvation, and a positive value suggests that solvation is nonspontaneous. The Born equation shows that solvation of ions becomes greater with increasing solvent relative permittivity. However, the Born equation treats the solvent as a continuum rather than a collection of individual solvent molecules, neglecting specific solvent-solute interactions (Section 1.3.4).

$$\Delta G_s^o = -\frac{N_A z^2 e^2}{8\pi\varepsilon_o r}\left(1 - \frac{1}{\varepsilon_r}\right) \tag{1.6}$$

N_A = Avogadro's constant

z = charge of ion

e = elementary charge

ε_o = permittivity of free space

1.3.2. Description of bulk electrolyte solutions with varying solute concentration

Varying the amount of solute within solution will lead to a change in the concentration, which is defined by the number of moles per unit volume (M, mol dm^{-3}). An alternative representation of the molar composition of a solution can be defined using the mole fraction, $x_{\text{component}}$, of each constituent, where the mole fraction of a component increases as its concentration in solution increases. As an example, for a solution of IL in H_2O, $x_{\text{IL}} = 0$ signifies pure H_2O, whereas $x_{\text{IL}} = 1$ denotes pure IL.

With increasing x_{IL} in molecular solvent, the degree of ion pairing and liquid phase structure formation has been shown to vary.[43] The process of increasing ionic concentration within molecular solvent has been shown to lead to four distinct concentration regimes (for systems that do not have a miscibility gap, *i.e.,* IL/MS mixtures), from low to high values of x_{IL}:[44]

Regime 1: The concentration of ions in solution is very low (Figure 1.6a). Ions exist in an infinite dilution of solvent molecules, where the population of solvent molecules is higher than needed to complete the primary solvation sheath for the ions. Ions exist in a far lower ratio than MS molecules, *e.g.*, $x_{\text{IL}} = 0.01$ (~0.5 M).

Regime 2: The concentration of ions in solution is greater than during Regime 1 (Figure 1.6b). The population of solvent molecules is just sufficient to complete the primary solvation sheath for the ions. Ions still exist in a lower ratio than MS molecules but with far greater prevalence than Regime 1, *e.g.*, $x_{\text{IL}} = 0.10$ (~2.9 M).

Regime 3: The concentration of ions in solution is greater than during Regime 2 (Figure 1.6c). The primary solvation sheath for ions can no longer be completed due to insufficient solvation population. The Ion:MS ratio is close to equal, e.g., $x_{IL} = 0.25$, (~4.2 M).

Regime 4: Pure IL where cations are solvated by anions and vice versa (Figure 1.6d). In the absence of MS, cation-anion interactions dominate in pure IL, *i.e.*, $x_{IL} = 1.00$, (~5.4 M).

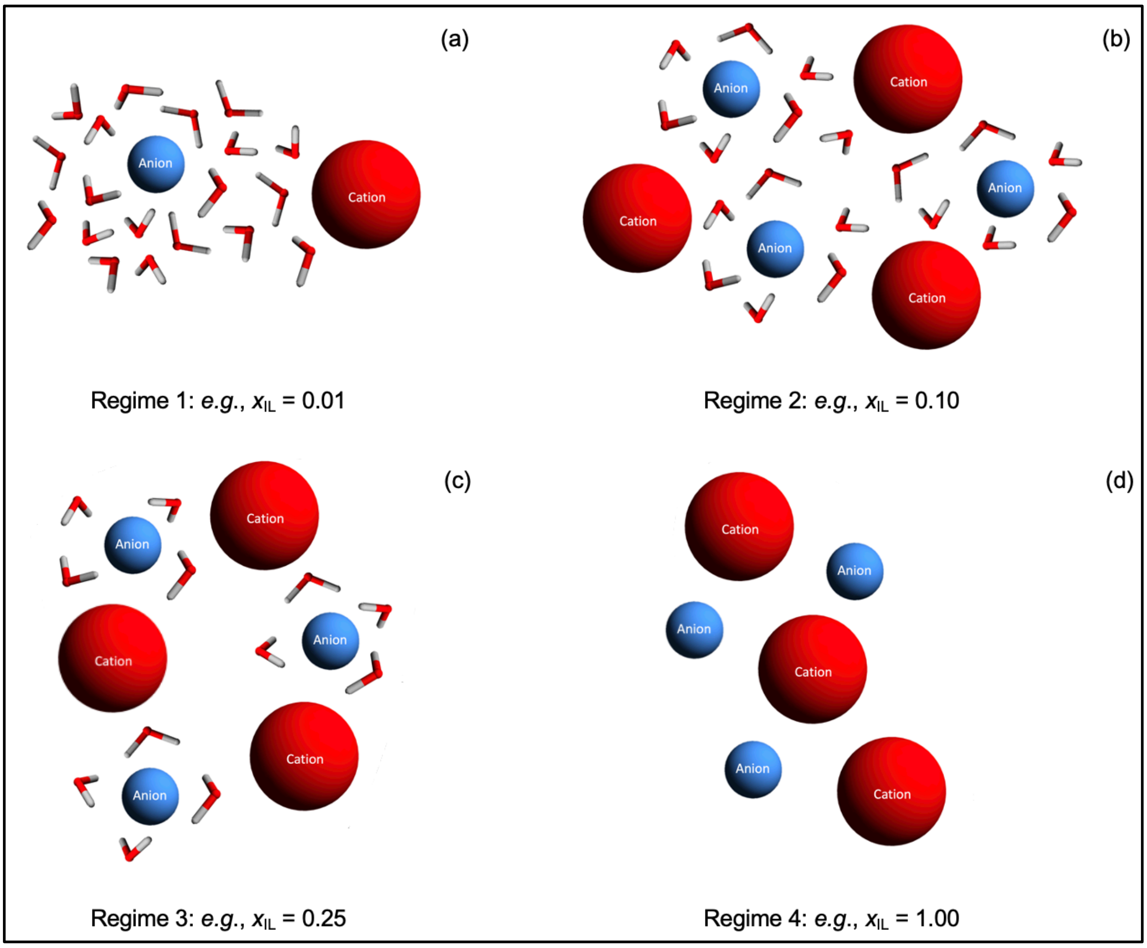

Figure 1.6. The process of increasing the solute concentration of a solution: (a) Regime 1; low solute concentration. (b) Regime 2; medium solute concentration. (c) Regime 3; high solute concentration. (d) Regime 4; pure IL.

1.3.3. Types of solvent-solute interactions

There are many types of solvent-solute interactions which play key roles in determining the physico-chemical and electronic properties of a solution. Differing solvent-solute interactions can be described as either, non-specific or specific.[1] Non-specific solvent-solute interactions are directional, and manifest through induction and dispersion forces, which cannot be completely saturated, *e.g.*, Coulombic interactions between ions. Specific solvent-solute interactions are also directional; however, specific interactions can be fully saturated, *e.g.*, hydrogen bonding. The effect of the solvation environment on the electronic properties of each ion can also be described using specific and non-specific notation, where specific solvation effects affect the electronic properties locally. On the other hand, non-specific solvation effects influence the electronic properties of all electronic environments to an approximate equal degree.

Ion-dipole interactions occur between electrically neutral molecules and ions. If an unsymmetrical charge distribution (permanent dipole moment) exists within a neutral molecule, the introduction of an ionic electric field causes opposing ends of its dipole to orient both attractively towards, and the repulsively away from the electric field (Figure 1.2c). This orientation results in an attractive force between the neutral molecule and an ion. Coulombic interactions are non-specific and are pervasive within solutions of ionic species in dipolar solvents.[1]

Dipole-induced dipole forces occur between a dipolar molecule, containing a permanent dipole moment, and a nonpolar molecule with high polarisability. The permanent dipole moment of the dipolar molecule induces a dipole moment in the nonpolar molecule, resulting in electronic attraction between the neighbouring molecules. Dipole-induced dipole forces are non-specific interactions, which are important within solutions of ionic or dipolar species within a nonpolar solvent.[1]

Instantaneous dipole-induced dipole forces occur between atoms and molecules possessing no permanent dipole, otherwise known as dispersion forces. Through continuous movement of electrons within each atomic or molecular orbital, the probability of an uneven electron distribution existing at any one time is high. The resultant temporary dipole moment can polarise the electrons within neighbouring molecules, resulting in a short-lived, short-range, attractive force between molecules. Instantaneous dipole-induced dipole forces are non-specific interactions, which are the primary mode of interaction between two nonpolar molecules. Dispersion forces exist for all atoms and molecules, where they form the weakest basis for each interaction.[1]

Hydrogen bonding interactions are specific interactions which occur due to a selective set of criteria between hydrogen bond donor species and hydrogen bond acceptor species.[45] Hydrogen bonding takes place between a covalently bound hydrogen atom, and an atom of greater electronegativity, *e.g.*, N, O, S, F.[1] Such interactions may also exist between neutral molecules and ionic species, where anions are particularly good hydrogen bond acceptors. The selective criteria which define a hydrogen bond include its distance, angle, and lone-pair directionality.[29] The strength of hydrogen bonding interactions are known to be approximately ten times stronger than non-specific interaction forces (discussed earlier), due to the small size of the hydrogen atom which can more closely approach a hydrogen bond acceptor species. However, hydrogen bonding interactions are also known to be approximately ten time weaker than covalently bound single bonds. Weak hydrogen bonds are thought to be more electrostatic in nature, whereas strong hydrogen bonds possess a mixture of both, electrostatic and covalent contributions.[1]

Electron-pair acceptor/donor interactions are specific interactions which occur due to the electron transfer from an occupied valence state (OVS) of a donor species to an unoccupied molecular orbital (MO) of an acceptor species, where the energies are sufficiently high and low, respectively, for overlap to occur.[1] Electron pair donor molecules are categorised into n-, σ-, and π-EPDs. The EPD ability of n-EPDs is facilitated through a lone pair of n-electrons on a heteroatom, *e.g.*, R_2O. The ability of σ-EPDs is enabled through an electron pair within an σ-bond, *e.g.*, cyclopropane. Lastly, the ability of π-EPDs is permitted through an electron pair of π-electrons within unsaturated or aromatic compounds, *e.g.*, alkenes. Electron pair acceptor molecules can also be categorised into three types: ν-, σ-, and π-EPAs. The EPA ability of ν-EPAs is due to the high degree of vacancy within the lowest energy orbitals, *e.g.*, metal atoms. The ability of σ-EPAs is due to the presence of a non-bonding σ-orbital, *e.g.*, I_2. Lastly, the ability of π-EPAs is due to the presence of a system of π-bonds, *e.g.*, aromatic compounds. As EPA/EPD interactions can take place between any acceptor/donor species, nine different EPA/EPD combinations exist. Electron transfer is greatest where the ionisation potential of the donor is low, and the electron affinity of the acceptor is high. Therefore, EPA/EPD interactions are closely related to those of Lewis acid/base interactions, where a Lewis acid acts as an EPA, and a Lewis base acts as an EPD.

1.3.4. Quantification of solvent-solute interactions

The ability to reliably predict the feasibility and strength of interaction between solvent-solute species in solution would be a very powerful tool for both, experimental, and computational chemists. Such prediction power would save an experimentalist time and effort during the search for potential methodology improvements, whilst also providing computational chemists with additional parameters to improve upon the accuracy of a computational model. Attempts to quantify the chemical properties responsible for such solvent-solute interactions have been demonstrated through various solvent polarity scales, e.g., Kamlet-Taft (KT), and Catalán.

Kamlet, Taft, and co-workers measured the absorption shifts within UV/Vis spectra of a combination of chemical probe species (Table 1.3, Figure 1.7) which exhibit solvatochromism, to describe the three terms of the KT solvent polarity scale: hydrogen bond donor ability, α, hydrogen bond acceptor ability, β, and dipolarity-polarisability, π^*.[1, 46-49] The hydrogen bond donor ability of a solvent describes the ease with which a solvent molecule yields a proton to facilitate a hydrogen bonding interaction. α has been shown to correlate with Gutmann *AN*, hence can be thought as a measure of solvent Lewis acidity.[50] The hydrogen bond acceptor ability of a solvent describes the ease with which a solvent molecule abstracts a proton to facilitate a hydrogen bonding interaction. β has been shown to correlate with Gutmann *DN*, hence can be thought as a measure of solvent Lewis basicity.[50] The dipolarity-polarisability descriptor demonstrates the movement of π electrons within the solvent molecule, where the π^* descriptor has been shown to correlate with the refractive index of a solvent.[50] One benefit of the KT polarity scale is how it allows for a broad assessment of solvent properties, as evidenced by the correlation of KT values with a range of additional solvent properties. However, limitations arise through probe dependency, where it is not certain that the values obtained for KT scale descriptors, which are a measure of the influence of the solvent on the probed dye species, are applicable to additional solvent-solute interactions.[51]

Similarly to KT, Catalán and co-workers also utilised characteristic absorption shifts within UV/Vis spectra of a combination of chemical probe species (Table 1.3, Figure 1.7) which exhibit solvatochromism, to describe three terms: solvent acidity, *SA*, solvent basicity, *SB*, and solvent dipolarity-polarisability, *SPP*.[52, 53] The probes used to obtain values for each descriptor within the Catalán scale are homomorphic pairs of dyes, allowing for the cancellation of unwanted solvent-solute interaction effects. Values for each Catalán descriptor have been shown to correlate strongly with KT solvent polarity scale descriptors.[54] Therefore, Catalán descriptors, *SA*, *SB*, and *SPP*, also demonstrate the ability of solvent Lewis acidity, Lewis basicity, and dipolarity-polarisability, respectively. One benefit of the Catalán scale over KT is the ability to further separate *SPP* into its constituent contributions, where *SP* describes the solvent polarizability, and *SdP* describes the dipolarity.[53] However, the Catalán scale continues to face the same probe dependency limitation as that discussed for the KT solvent polarity scale.

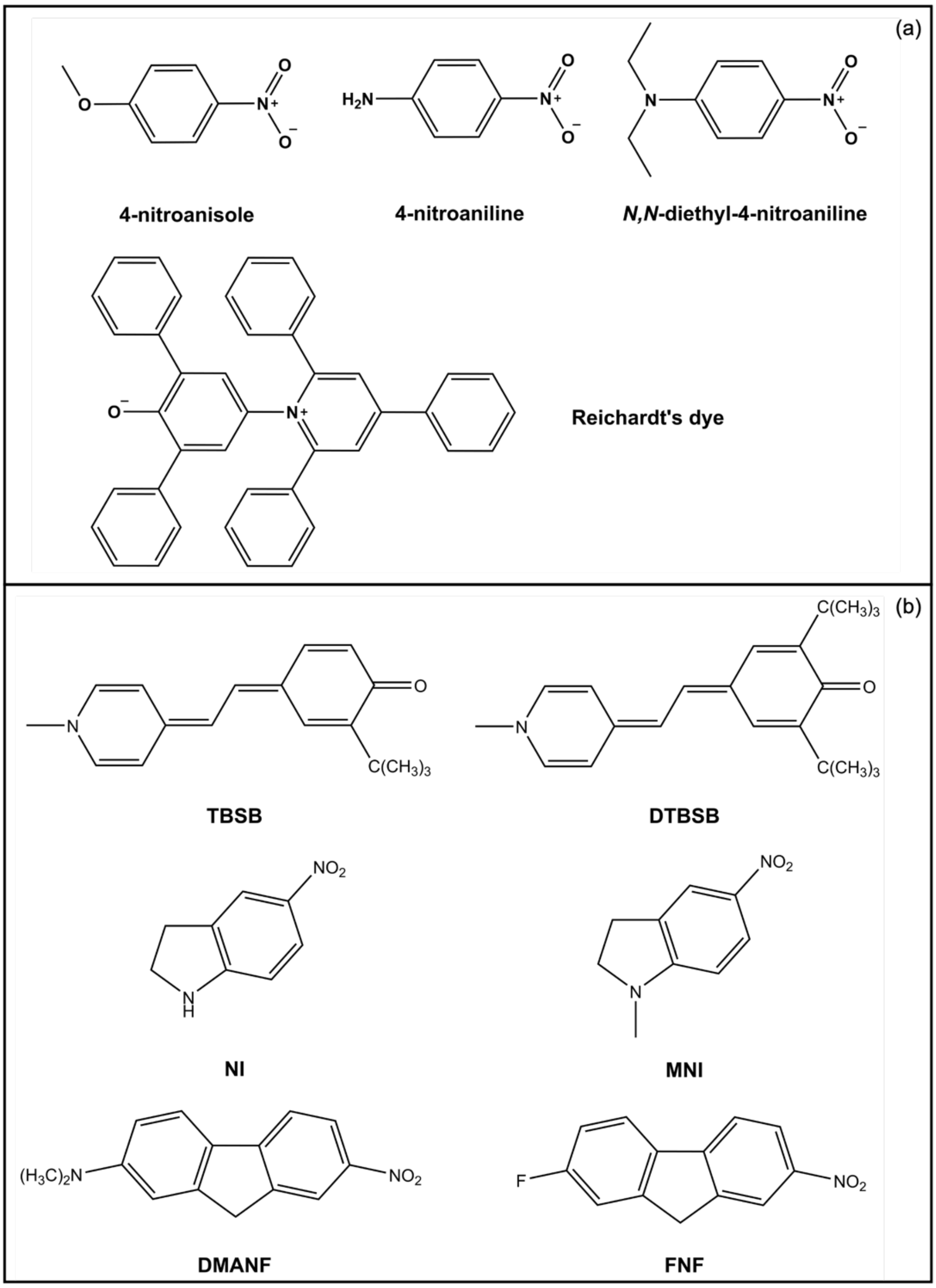

Figure 1.7. Structures of probes used in the measurement of each solvent polarity descriptor: (a) Dyes used within the Kamlet-Taft solvent polarity scale. (b) Dyes used within the Catalán solvent polarity scale, where adjacent molecules form homomorphic pairs of dyes.

Table 1.3. Summary of solvent polarity descriptors and probes used for each quantification method for solvent-solute interactions.

Quantification method	Descriptor	Probe	Technique
Kamlet-Taft	α	4-nitroanisole/Reichardt's dye	UV/Vis
	β	4-nitroaniline/*N*,*N*-Diethyl-4-nitroaniline	UV/Vis
	π^*	p $\rightarrow \pi^*$ and $\pi \rightarrow \pi^*$ transitions for α/β	UV/Vis
Catalán	SA	TBSB + DTBSB	UV/Vis
	SB	NI + MNI	UV/Vis
	SPP	DMANF + FNF	UV/Vis

1.3.5. Applications of ions in solution

The applicability and prevalence of ion-solvent solutions span a range of scientific fields of study. Hence, literature examples of the applications of ions in solution are vast. Therefore, within this section the broad themes of their implementation are discussed, rather than specific comparative examples.

Ions in solution dominate the field of electrochemistry and electrochemical devices, where the movement of electrons in solution is facilitated by the reduction and oxidation of cationic and anionic species.[55, 56] For example, within battery systems a consistent influx of research papers report on new cation-anion-solvent combinations, which allow for higher efficiency at the required voltage for a variety of applications.[16, 57] The increasing popularity of research into water-in-salt batteries look to provide a safer, non-toxic alternative to currently employed battery systems.[16, 58-64] Additional to battery systems, the strong ability of ions to promote the solvation of other ions allows for the electrodeposition of metal species, such as zinc, within metal-IL solutions.[65] Lastly, the use of aqueous ions within electrochemical devices, such as dye-sensitised solar cells, has been proposed.[66] The development of processes which utilise H_2O as a solvent within each electrochemical device is highly attractive due to the subsequent decreased flammability, reduced cost, and reduced negative environmental impact.

The Lewis acid/base ability of ionic species permit several reaction pathways between species in an electrolyte solution. For example, the ability of ions to coordinate with metal centers,[67-72] and the ability of ILs to act as green solvents,[73] lend themselves well to inorganic synthesis.[74] Moreover, the Lewis acidic ability of cationic species, and Lewis basic ability of anionic species in solution afford potential for their application as liquid phase catalysts.[75-79] The reactivity of ions in solution has therefore enabled their employment as components within drug formulation.[80, 81]

Many biological processes require the symbiotic relationship between ions in solution.[82] For example, ions are known to exhibit structural changes in protein molecules when combined in solution, promoting protein refolding and crystallisation.[83] This process is described by the Hofmeister series, in which ion specificity leads to a *salting-in* or *salting-out* effect, depending on the ion present.[84] However, conclusions as to the reasoning of the accepted Hofmeister series remain contentious.

1.4. Electronic structure

The electronic structure of an atom describes the arrangement of electrons within orbitals around a nucleus, which are composed of regions with the highest probability of electron location.[85] At a quantum mechanical level, quantum numbers, n, l, m_l, m_s, are used to describe the shape, position, and energies of the electrons within an atom (Table 1.4). For example, the quantum numbers used to describe the p-electron location within a carbon atom are: $n = 2$; $l = 0, 1$; $m_l = -1, 0, +1$; $m_s = \pm\frac{1}{2}$.

Table 1.4. Quantum numbers used to describe the electronic structure of an atom.

Quantum number	Symbol	Allowed values	Property
Principal	n	Positive integers *e.g.*, 1 = s-orbital	AO size and energy level
Angular momentum	l	Range from 0 to n-1	Shape of the AO
Magnetic	m_l	Range from -l to +l, including 0	AO orientation
Spin	m_s	$\pm\frac{1}{2}$	Electron spin direction

The electronic configuration of an atom is used to describe the distribution of electrons in each AO according to its quantum numbers. For example, the electron configuration of an O^{2-} anion is $1s^2$ $2s^2$ $2p^4$. The rules for filling each subshell within an AO are determined by Hund's rule, the Aufbau principle, and the Pauli exclusion principle.[85] The Aufbau principle states *electrons fill lower energy atomic orbitals before filling higher energy ones*. Hund's rule states that *each orbital in a sublevel is separately occupied before any orbital is doubly occupied*. The Pauli exclusion principle states *that no two electrons in the same atom can have identical values for all four of their quantum numbers*.

Computational techniques afford the ability to assign the formation of molecules to the combination of AOs from each constituent atom to form molecular orbitals (MOs).[86] Of these MOs, the so-called *frontier molecular orbitals* refer to the energetically highest occupied molecular orbitals (HOMOs) and lowest unoccupied molecular orbitals (LUMOs). In 1981, the Nobel Prize for chemistry was won by Fukui for his work on determining the relationship between frontier MOs and the reactivity of each species.[8, 9] Previously, electron density was thought responsible for all chemical interactions. However, Fukui and co-workers computationally probed the role of the highest energy valence orbitals, *i.e.*, the HOMO and LUMO, in chemical reactivity. It was posited that the electron delocalisation between the HOMO and the LUMO was the principle factor in determining the readiness of a chemical reaction, where a larger orbital overlap and smaller energy level separation led to a greater overall stabilisation.[87] During the interaction of the frontier MOs, the HOMO becomes destabilised, while the LUMO becomes more stabilised. The basis of Lewis acidity/basicity follows on from the fundamental principle of HOMO/LUMO interaction. Therefore, understanding the energies involved in the electronic structure of a chemical species is crucial for interpreting and predicting trends in reactivity. Experimental techniques, as opposed to computational methods, do not probe the HOMO level and instead, the energetic position of the highest occupied valence states (HOVSs) are measured. The key principles from Fukui's work are also proven to apply to the experimentally defined behaviour of the HOVSs.[88, 89]

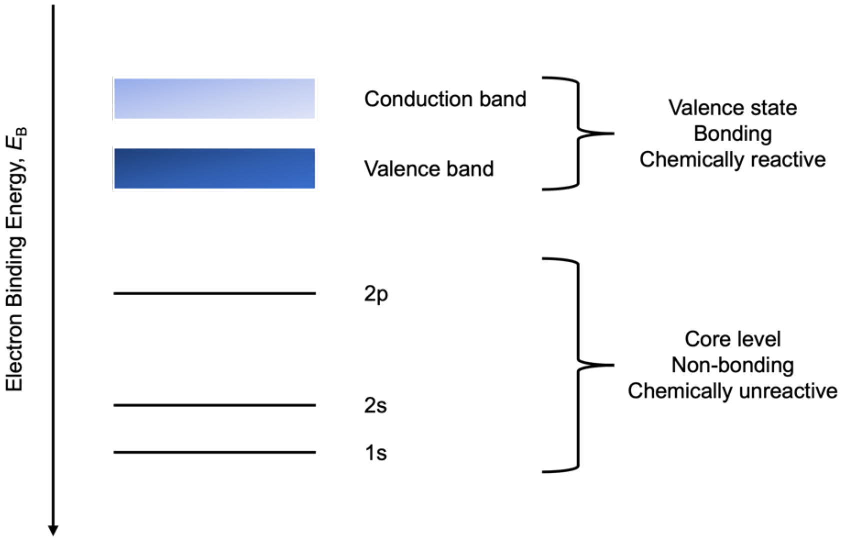

Figure 1.8. The electronic structure of atomic sulphur presented as an energy level diagram. S 1s, 2s, and 2p are labelled core level orbitals. Valence states are shown at lower E_B and, for the sulphur atom, include the S 3s and S 3p AOs.

Each orbital can be further described as either a core or valence state energy level (Figure 1.8). Electrons located within core level orbitals are those located within inner-shell AOs of an atom and experience the greatest nuclear pull attraction as a result. Hence, core level electrons are non-bonding in nature. Conversely, valence state electrons are located within outer-shell MOs and are therefore far more loosely held than their core level counterparts. Hence, valence state orbitals contain key bonding electrons. Within the example for the given electronic configuration of an O^{2-}

anion, the core electrons are located within the 1s and 2s AOs, whereas the valence state electrons are located within the 2p MOs.

1.5. The use of X-ray spectroscopy in the probing of ions in molecular solvent

X-ray spectroscopy is a term used to describe a wide range of techniques, including X-ray photoelectron spectroscopy (XPS), X-ray absorption spectroscopy (XAS), and resonant XPS (RXPS). One subset of X-ray spectroscopy relates to photoelectron spectroscopic techniques, which utilise the photoelectric effect to measure the kinetic energy, E_K, of electrons emitted by photoionisation.[90] As the value of E_K is characteristic to the identity of each element probed, it is used to yield information relating to both, the core level (non-bonding) and valence state (bonding) energies. An introduction to the origin of each spectroscopy and their employment in the probing of ions in molecular solvent is explored below. The mechanisms and technologies through which each of these spectroscopic techniques operate are discussed in greater detail later (Chapter 2).

XPS

XPS was first carried out by Innes and co-workers, who recorded a broad band of emitted electrons as a function of velocity, using a Röntgen X-ray tube (to produce X-rays), Helmholtz coils (to create a controlled magnetic field), an early hemispherical electron analyser (to map electron energies), and photographic plates (as a detector).[91] The broad band of emitted electrons was later refined by researchers such as Moseley, Rawlinson, and Robinson, pre-World War II (WWII).[92, 93] Post WWII, Kai Siegbahn and co-workers from Uppsala (Sweden) developed several significant instrumental improvements, and in 1957 recorded the first examples of high-energy-resolution XP spectra.[94] In 1967, Siegbahn published a comprehensive study of XPS, which he called Electron Spectroscopy for Chemical Analysis (ESCA).[95] Siegbahn later worked in collaboration with engineers from Hewlett-Packard to produce the first commercial monochromatic XPS instrument in 1969.[96] In 1981, Siegbahn received the Nobel Prize in Physics for his contribution to the development of high-resolution electron spectroscopy.[97] The measurement of volatile liquids by XPS is unfeasible using the commercial XPS equipment, due to the requirement for high vacuum for electron detection. However, in 1997, the development of the liquid jet apparatus[98] on synchrotron source XPS instruments allowed for the measurement of volatile liquids, *e.g.*, H_2O,[99-101] further expanding the field of X-ray spectroscopy to liquid-phase research.[102, 103]

The versatility of XPS, and wealth of information gained from XPS experiments has led to its utilisation within the study of a broad range of ionic species in solution. Liquid jet apparatus allowed for the high accessibility of measurement for two classes of species: pure molecular solvent, and solvated species (ions or neutral molecules). This work was highly driven by the Winter research group, who are highly cited within the field. X-ray spectroscopy of aqueous solutions is still a relatively young field (< ~15 years) and therefore, experimental difficulties remain.[104]

The initial studies using liquid jet apparatus focussed on the electronic structure of pure H_2O. Since these initial investigations, the core orbital and valence state contributions and associated energies have been extensively documented. The valence state of pure H_2O was found to contain five characteristic orbital contributions: $1b_1$ (liq), $1b_1$ (gas), $3a_1$, $1b_2$, and $2a_1$, from lowest to highest binding energy, E_B, respectively (Appendix Figure 8.1).[99-101] Special attention is drawn to the electronic position of the $1b_1$ (liq) AO, which is the HOVS of the H_2O molecule. The E_B of the $1b_1$ (liq) for pure H_2O is found to 11.33 ± 0.03 eV.[101] The O 1s core level for pure H_2O is known to be composed of two components: O_{liq} 1s and O_{gas} 1s, at low (538.1 eV) and high E_B, respectively.[100]

The characterisation of pure solvents by X-ray spectroscopy, other than H_2O, within the literature is currently lacking, likely due to the unsuitably high volatility of organic solvents, which causes difficulties for liquid jet experiments. For example, with relevance to the current work, and to demonstrate the difficulty of measuring pure solvents, the characterisation of propylene carbonate (PC) by XPS was carried out at 153 K on an aluminium substrate, rather than as a pure solvent.[105] Moreover, despite the importance of ethanol as an organic solvent, there appears to be no published comprehensive characterisation of its electronic structure through X-ray spectroscopy; instead, ultraviolet photoelectron spectroscopy (UPS) has been used to measure the valence states.[98] As an alternative to pure solvent measurement, the combination of solvent/H_2O solutions, binary solvent mixtures were formed to enable the study of highly volatile solvents. The first study of such highly volatile solvent combinations was through the addition of acetonitrile (MeCN) to H_2O.[106] MeCN was shown to have a stronger affinity for the surface than H_2O; hence, observed E_B shifts were said to be due to the effects of surface dipole orientations. Therefore, the characterisation of the electronic structure of bulk MeCN was unachievable through this methodology. Solvent mixtures containing H_2O_2/H_2O combinations in various ratios were studied to investigate the effect of hydration on the electronic structure of H_2O_2.[107] In contrast to the surface effects observed for MeCN, the observed E_B shift for the H_2O_2 valence states were found due to both, a combination of non-specific electrostatic interactions, and specific interactions between H_2O_2 and H_2O. Within this study, the solute species was H_2O_2, with H_2O acting as the solvent. Therefore, this study may also be applicable to the behaviour of ions in solution, suggesting any E_B shifts may be due to both, non-specific, and specific solvation effects.

The electronic structure of a broad range of ions in (mostly) aqueous solution have been measured through XPS. Through the dissolution of simple salts, such as NaCl in H_2O, the effect of the cationic Na^+ and anionic Cl^- ions on the hydrogen bonding structure of H_2O were probed.[108, 109] Cations were found not to significantly alter the structure of H_2O beyond the first solvation shell, whereas the anion was found to affect the hydrogen bonding network of H_2O to a far greater degree. Similarly, the dissolution of NaI in H_2O, from low (almost pure H_2O) to high (8 M) concentration, was studied by XPS. During an initial investigation of the effect of concentration on valence state energies, Pohl and co-workers observed a large (-0.37 ± 0.06 eV) negative shift in E_B for the $1b_2$ valence state of H_2O, with increasing electrolyte concentration (Figure 1.9, top).[110] In relation to the electronic structure of the solute ions, a very small (-0.15 ± 0.06 eV) negative E_B shift was also observed for the I^- 5p valence state. Hence, the energies of each valence state for the solute and solvent were shown to shift in the same direction, where the $1b_2$ of H_2O shifted twice as much as the I^- 5p. The variable E_B shifts were determined due to an ion-induced disruption of intermolecular electronic interactions. The $1b_1$ (liq) was used as a reference peak, justified by the lack of variation in the E_B with varying concentration through computational calculations. Within a secondary investigation of NaI in H_2O, Credidio and co-workers observed a large change in both, bulk H_2O valence state energies, and solute species electronic structure (Figure 1.9, bottom).[111] The solvent $1b_1$ (liq) and solute I^- 5p electronic state energies were both shown to shift positively by 0.3 eV, indicating a non-specific solvation effect upon increasing electrolyte concentration, where valence states of both species shifted in the same direction by the same magnitude. The study by Credidio provides doubt of the validation of the computational methods used by Pohl, which stated that the $1b_1$ (liq) valence energies were not influenced by concentration effects, in contrast to the observed experimental shift. The direction of the reported E_B shifts are an irrelevant comparison between each study, as the use of charge referencing methodologies varied significantly ($1b_1$ (liq) for Pohl versus cut-off energy for Credidio).

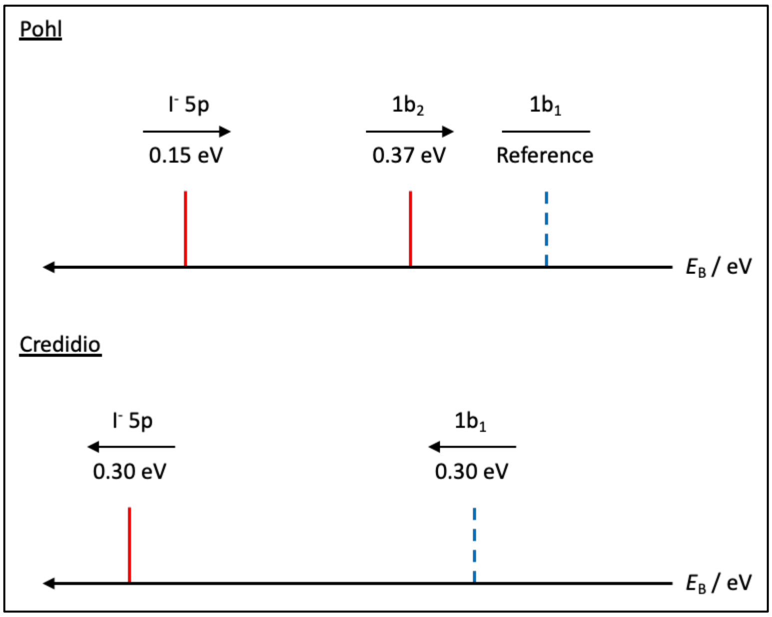

Figure 1.9. A simplified schematic of the reported photoelectron peak energy shifts observed with increasing NaI (aq.) concentration, discussed within references [110] and [111].

Measurement of larger ions in aqueous solution than relatively small, binary salts have also been carried out by XPS. For example, XPS of aqueous solutions of imidazole and its protonated ionic form imidazolium have been achieved, the electronic structure of which is highly applicable to the current work.[112-114] The femto-second timescale of the XPS process allows for the distinction between the protonated and deprotonated nitrogen atoms within the imidazolium cation. The E_B values for the core level and valence states of the imidazolium cation were shown to be greater than that of the neutral imidazole species, which was consistent with the assumed delocalisation of positive charge within the heterocyclic ring of imidazolium. Remarkably, the comparison of the electronic structure of neutral imidazole and cationic imidazolium allowed for the determination of the induced chemical shift due to a single hydrogen bond to be $E_B = + 1.7$ eV. Moreover, the induced chemical shift due to the delocalisation of charge across the heterocyclic imidazolium ring was found to be lower at $E_B = + 1.0$ eV. An additional example of the measurement of a relatively large ionic species in aqueous solution by XPS is the study of acetic acid and its conjugate base, the acetate anion.[115] Solvation effects were shown to shift the E_B of the carboxyl carbon atom -0.7 eV from pure salt to 5 M solution. The observed shift in anionic valence state energy upon solvation in aqueous solution matched that observed in the study by Credidio discussed previously in terms of directional shift but was greater in terms of magnitude. The differing observed E_B magnitudes suggest varying anionic species in solution experience similar solvation effects but to differing degrees.

The electronic structure of Li^+ within multiple battery solvents was carried out by El-Kazzi and co-workers.[116] A difference in core level E_B was observed for both, the Li^+ cation, and corresponding ClO_4^- anion, with varying solvent identity. The change in the ionic electronic structure, demonstrated by a shift in E_B, was explained to be due to the modification of the ionic solvation shell. This study demonstrated the ability of the solvent identity to influence the electronic structure of multiple components in solution, both the solute, and solvent.

The ability to vary the incident photon energy, $h\nu$, during synchrotron XPS experiments allows for variable depth-profiling of the studied solution, from surface (lower $h\nu$) to bulk (higher $h\nu$). The surfactant-like behaviour of Li^+ and K^+ ions have been investigated in aqueous solution.[117] Through probing of different solution depths, Li^+ was found to possess surfactant-like behaviour with a greater affinity for the surface, whereas K^+ did not, residing primarily within the bulk of the solution. The difference in behaviour was cited as due to the resilience of each hydration shell, where Li^+ retained, whereas K^+ lost part of its solvation shell. Further investigations as to the molecular distribution of solute species in solution was carried out for an aqueous solution of trichloroethanol.[118] Using the measured intensity ratios of the liquid phase and gas phase photoelectron peaks, the photoelectron E_K of maximum surface sensitivity was found to be ~100 eV. This study allowed for a benchmark within aqueous liquid jet XPS experiments, with which experimentalists can determine the surface sensitivities of their measurements. Rather than focus on the distribution of molecular species in solution, Mudryk and co-workers monitored changes to the relative electronic structure of solute species with varying $h\nu$ for aqueous solutions of $KMnO_4$ and $NaMNO_4$.[119] This enabled the determination of the extent of bulk versus surface effects within the measured electronic structure of a species. Variable probe depth measurements were carried out at $h\nu$ = 150 eV (surface sensitive) and 800 eV (bulk sensitive), where no change in E_B was observed. The only measured difference in bulk versus surface spectra was an expected variation in relative intensity due to the relative ionisation cross-sections for each AO.

The electronic structure of transition metal (TM) ions have been extensively probed through the dissolution of species in aqueous solution. The first example of XPS measurements of aqueous TMs was published for ruthenium complexes with differing oxidation states,[120] followed by aqueous manganese[121] and aqueous iron[122] at differing oxidation states.

Recently, cutting-edge liquid jet XPS experiments have been used to measure the E_B of solvated electrons. The proof of principle for these experiments was shown through the measurement of liquid ammonia, cooled to 213 K, using liquid jet apparatus.[123] Various alkali metals (Li, Na, and K) were then steadily dissolved in the cooled liquid ammonia, generating excess electrons for measurement in a solvated state.[124] Hydrated electrons were shown to be less reactive, allowing comparisons to be drawn between the relative stability solvated electrons and the relative stability of solvated ions.[125]

XAS

The first XA spectra was observed by de Broglie in 1913, who scattered X-rays through the utilisation of a rotating crystal.[126, 127] X-rays of varying intensities were recorded on a photographic plate, revealing an XA spectra. Over subsequent years, technological advances (Siegbahn and Stenstrom, 1916) and theoretical advances (Kronig, 1931) were made, leading XAS to the method it is today.[126] The experimental XA technique was further advanced through the advent of synchrotron facilities (Chapter 2), such as Diamond Light Source (UK), BESSY II (Germany), Soleil (France), and Elettra (Italy).

The sensitivity of XAS to local solvation environment make it an ideal spectroscopic tool for studying the electronic structure of solutes in solution.[128] However, little work up until now has been published on the effect of solvent identity on ions in solution. The bonding environment within pure H_2O has been extensively studied through XAS, where characteristic XA transitions indicate variations in the local hydrogen bonding network.[103, 128, 129] The XA spectra of pure H_2O can be described by three regions: pre-edge, main-edge, and post-edge. The pre-edge is associated with broken or weakened hydrogen bonds. The main-edge is associated with interstitial H_2O molecules. Finally, the post-edge is associated with strong hydrogen bonds within the H_2O bonding network. Through dissolution of solute in aqueous solution, any variation in edge peak energies can indicate solute effects on the H_2O hydrogen bonding network. Likewise, for XPS of pure solvents, there is unfortunately a lack of literature on assigned peaks within XAS for pure solvents.

To demonstrate the effectiveness of XAS in determining the electronic structure of ionic species in solution a few examples are given. The study of neutral ammonia and cationic ammonium in aqueous solution by XAS was undertaken to determine the mode of bonding between the solute and the solvent species.[130, 131] Through N 1s XAS, NH_4^+ was shown to be weakly hydrogen bond donating with four hydrogen bonds to each solute molecule. In contrast, NH_3 was shown to be strongly hydrogen bond accepting due to the lone pair of electrons on the nitrogen atom. However, despite the presence of hydrogen bonding, charge-transfer was limited due to weak orbital mixing between the solute and solvent, suggesting the ammonium cation to have limited influence over the electronic structure of H_2O. XAS has also been carried out on samples of pure IL to investigate the relationship between the cation and anion in the liquid phase.[132, 133] The N 1s XA spectra of $[C_4C_1Im][SCN]$ was shown to be independent of neighbouring ion solvation environment, suggesting the solvation environment affected the ground state, and excited state, equally. The nitrogen atomic charge for dialkylimidazolium species, *e.g.*, $[C_4C_1Im]^+$, were confirmed to be slightly positively charged and shown not to depend upon the anionic identity, demonstrating intramolecular covalent interactions to be the dominant factor in determining the atomic charge of each nitrogen atom within imidazolium-based species.

RXPS

Resonant X-ray photoelectron spectroscopy (RXPS) is otherwise known as resonant photoelectron spectroscopy (RPES) or resonant Auger electron spectroscopy (RAES) in the literature. RXPS exploits the intensity enhancements measured under resonant conditions to aid in the identification of valence electronic states associated with a specific element, which would otherwise be difficult due to the close overlap of electronic transitions near the Fermi edge.[23, 134-136] Therefore, RXPS is particularly useful for the study of complex systems with large numbers of contributing valence states, such as liquid jet XPS experiments where contributing valence states include all components within a solution.[102]

RXPS has been used for the identification of the AO contributions to the valence state for ILs.[23, 135] Anionic species have been shown to give rise to the HOMO far more often than cationic species. Considering the incredibly high probability of increased Lewis basicity of anions versus cations, this was the expected result. However, it was surprising that the cation ever yielded the HOMO ahead of the anion, as this suggested a greater ease in removing an electron from the cationic species than the anionic species. A subtraction method was demonstrated for removing the non-resonant contributions from the resonant photoelectron peaks of the probed element, allowing for the effective measurement of atom specific XP spectra. Using this method, observed counterion effects were shown to not be due to individual valence states; instead, electrostatic, non-specific interactions affected all valence states. The factors which contribute to the measured strength of the RXPS signal were discussed.[134] Electronegativity of the probed atom was shown to be the primary factor, where a large atomic electronegativity (fluorine) resulted in a small participator Auger to spectator Auger (PA:SA) ratio (discussed in Chapter 2). The secondary factor for determining strength of RXPS signal was bonding type, where atomic π^* valence states showed larger PA:SA intensity than σ^* valence states. The effect of molecular solvation on RXP spectral shapes was also determined, where a strong dependency on covalent bonding was observed, compared to a weak dependency on solvation environment.

1.6. Reasoning for ions and solvents studied in this work

Throughout this work, a large selection of cations, anions, and neutral molecular solvents will be studied by X-ray spectroscopic techniques (Figure 1.10).

Most ions measured within the current work are constituent components within an IL. The ease of handling and purification, air insensitivity, relatively low viscosity, high solubility in a wide range of MSs, and negligible vapour pressure meant ILs were ideal for the experiments herein. Furthermore, the use of ILs allowed for the study of ions across the entire concentration range within the liquid phase – ions in MS to ions in ions. Ions from non-IL species were chosen due to their stability and comparative elements (to the measured ILs), in addition to their high literature significance.

A specific emphasis was placed upon the measurement of one IL in particular – $[C_4C_1Im][SCN]$. The reasoning for this choice was multifaceted. The $[C_4C_1Im]^+$ cation is highly studied within the literature, which the Lovelock research group have published on extensively, including $[C_4C_1Im][SCN]$.[23, 132-135, 137, 138] Concerns during experimental preparation are addressed as $[C_4C_1Im][SCN]$ has a high solubility in a wide range of MSs, is relatively inexpensive, and has low toxicity. $[C_4C_1Im][SCN]$ is ideal for the study of the relationship between the cationic and anionic electronic structure, as $[C_4C_1Im][SCN]$ contains both nitrogen and carbon in both ions, which permits a direct comparison within the same experimental region. Lastly, the $[SCN]^-$ anion has a high biological significance and is an important ligand within the renewable energy sector, both of which benefit from further knowledge of $[SCN]^-$ in solution.[139-142]

The inclusion of both, traditional polar solvents, and non-HBD solvents allowed for the measurement of solvents with a range of differing chemical and physical properties. MSs were chosen to cover a range of HBA/HBD abilities in order to explore whether solvent Lewis acidity/basicity affects the electronic structure of solvated species. Furthermore, MSs were chosen which feature in a range of different academic and industrial applications (Table 1.1).

Lastly, solvent choice was somewhat limited based upon experimental liquid jet method, which requires solvents of low viscosity and low toxicity (due to cleaning requirements and cost).

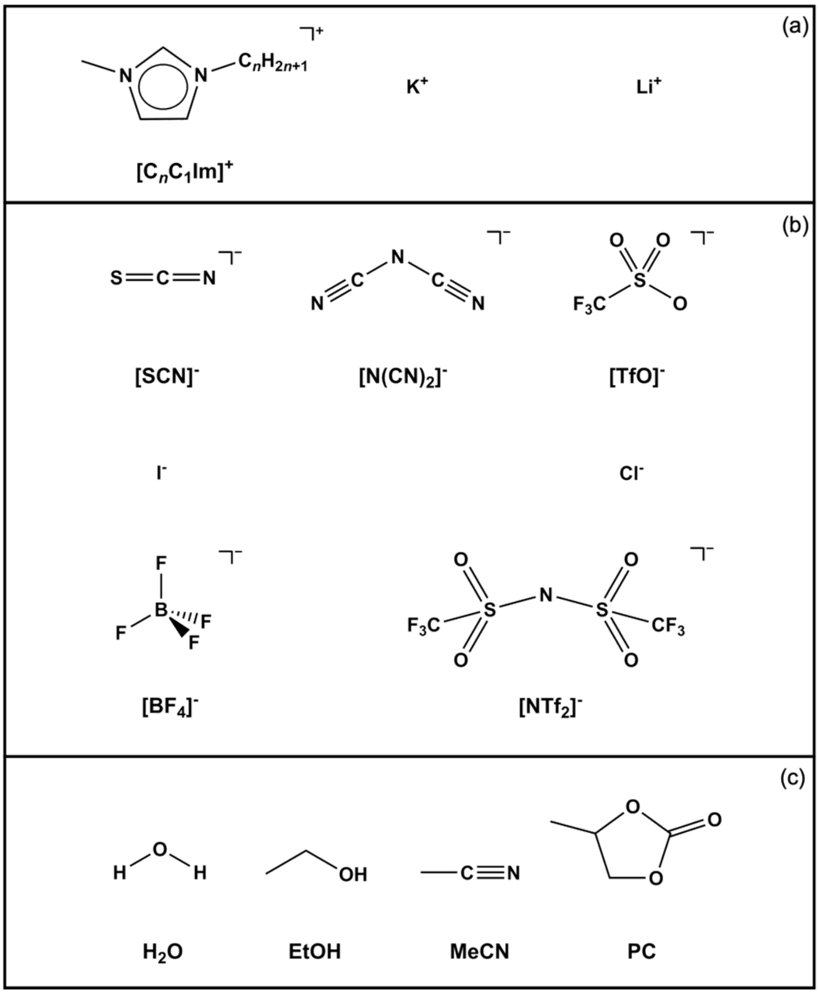

Figure 1.10. Names and structures of key ions and solvents studied within this work: (a) Cations. (b) Anions. (c) Solvents.

1.7. Aims of current work

Within the current work, four results chapters are presented with differing, but complementary questions to be answered in aid of building a picture of the electronic structure of each component within solution (Figure 1.11). Within all chapters, X-ray spectroscopic techniques were utilised in tandem to provide greater insight of the contributing solvation effects which govern component electronic structure variation.

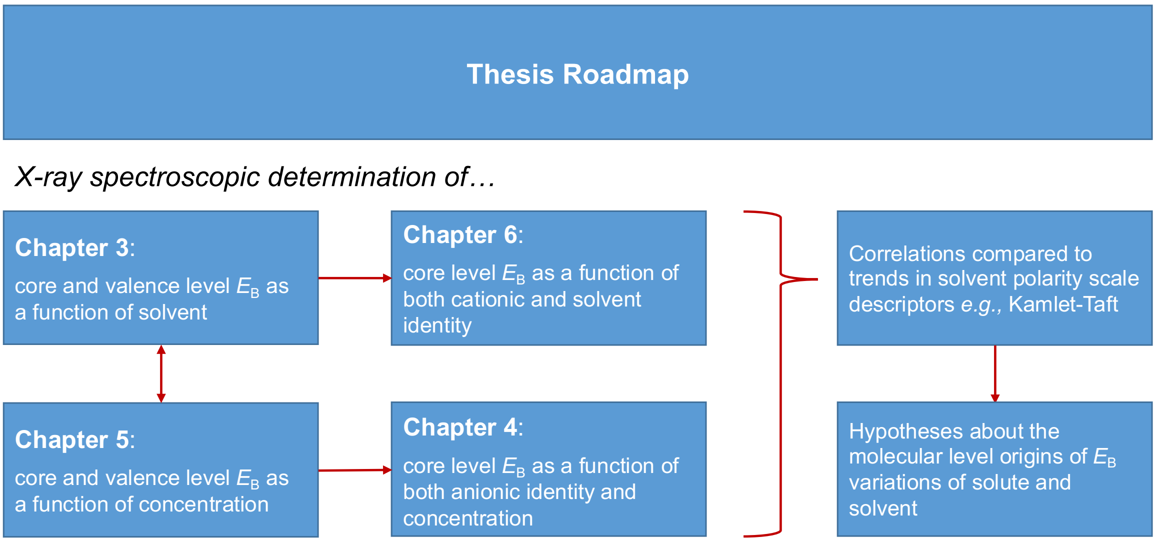

Figure 1.11. A graphic depiction of the roadmap for the current thesis. All chapters are concerned with the use of X-ray spectroscopy within the determination of core and/or valence level E_B values of species in solution. Correlations are then examined alongside solvent polarity scale descriptors (*e.g.,* Kamlet-Taft, Gutmann, and Catalán) to form hypotheses about the molecular level origins of measured E_B variations of solute and solvent.

Chapter 3 addresses the influence of solvent identity on anionic electronic structure. The aim of this chapter is to determine to what extent, and the reasonings for how, solvent identity influences the anionic electronic structure in solution. Within this chapter, an assortment of anionic species and molecular solvents with a diverse selection of physicochemical properties were studied. Such a comprehensive and comparative dataset collected through X-ray spectroscopic techniques has never been carried out to the best of our knowledge. Within Chapter 3, the questions to be answered are: does varying the solvent identity influence the electronic structure of solvated ions? What does the extent of ionic electronic structure changes upon solvation tell us about the nature of the solvent-solute interactions?

Chapter 4 deals with the influence of anion identity and concentration on electronic structure. The aim of this chapter is to determine the effect of varying the anion identity in solution for a large range of anionic species on the electronic structure. Within Chapter 4, the questions to be answered are: is the electronic structure of all anions affected through aqueous solvation? Is the electronic structure of all anions affected equally through aqueous solvation? How is the MS electronic structure affected by the anion identity?

Chapter 5 examines the influence of aqueous electrolyte concentration on electronic structure. The aim of this chapter is to determine the effect of varying the concentration of ions in solution on the electronic structure of each component within solution (cation, anion, solvent). This study focussed on the IL, $[C_4C_1Im][SCN]$, in H_2O at differing mole fractions, from ions in MS (x_{IL} = 0.01, dilute electrolyte) to ions in ions (x_{IL} = 1.00, concentrated electrolyte), with additional measurement of mole fractions marking key IL:MS molecular ratios in between (x_{IL} = 0.10, and 0.25). Within Chapter 5, the questions to be answered are: does varying the concentration of ions in solution affect the electronic structure of each component? Does varying the concentration of ions in solution affect each component equally?

Chapter 6 is entitled: Influence of solvent identity on cationic electronic structure. The aim of this chapter is to determine to what extent, and the reasonings for how, solvent identity influences the cationic electronic structure in solution. Within this chapter, three cationic species, Li^+, K^+, and $[C_4C_1Im]^+$, were studied in both, aqueous solution and propylene carbonate. The electronic structure of $Li[NTf_2]$ solvated by propylene carbonate is of particular relevance to the battery community. Within Chapter 6, the questions to be answered are complementary to those of Chapter 3: does varying the solvent identity influence the electronic structure of solvated ions? What does the extent of ionic electronic structure changes upon solvation tell us about the nature of the solvent-solute interactions?

The overall aim of this work is to obtain molecular level parameters for ionic liquid solvent-solute systems that can be used to validate theoretical predictions of solvent parameters from electronic structure calculations. This will then provide methods for accurate solvent parameter prediction *ab initio*, entirely from (density functional) theory, which will enable users to target and design solvent systems for a specific purpose.

1.8. References

1. C. Reichardt and T. Welton, *Solvents and Solvent Effects in Organic Chemistry*, Wiley, Weinheim, 4th edn., 2011.
2. M. A. Brown, M. Faubel and B. Winter, *Annu. Rep. Prog. Chem., Sect. C*, 2009, **105**, 174-212.
3. A. K. Agarwal, *Prog. Energy Combust. Sci.*, 2007, **33**, 233-271.
4. S. Ito, S. M. Zakeeruddin, R. Humphry-Baker, P. Liska, R. Charvet, P. Comte, M. K. Nazeeruddin, P. Péchy, M. Takata, H. Miura, S. Uchida and M. Grätzel, *Advanced Materials*, 2006, **18**, 1202-1205.
5. J. W. Smith, R. K. Lam, A. T. Sheardy, O. Shih, A. M. Rizzuto, O. Borodin, S. J. Harris, D. Prendergast and R. J. Saykally, *Physical Chemistry Chemical Physics*, 2014, **16**, 23568-23575.
6. A. Brandt, L. Chen, B. E. van Dongen, T. Welton and J. P. Hallett, *Green Chem.*, 2015, **17**, 5019-5034.
7. A. George, A. Brandt, K. Tran, S. Zahari, D. Klein-Marcuschamer, N. Sun, N. Sathitsuksanoh, J. Shi, V. Stavila, R. Parthasarathi, S. Singh, B. M. Holmes, T. Welton, B. A. Simmons and J. P. Hallett, *Green Chem.*, 2015, **17**, 1728-1734.
8. K. Fukui, *Science*, 1982, **218**, 747-754.
9. K. Fukui, *Angew. Chem.-Int. Edit. Engl.*, 1982, **21**, 801-809.
10. Y. Marcus, *Chemical Society Reviews*, 1993, **22**, 409-416.
11. M. R. J. Dack, *Chemical Society Reviews*, 1975, **4**, 211-229.
12. K. R. J. Lovelock, *R. Soc. Open Sci.*, 2017, **4**, 171223.
13. J. Wyman, *Journal of the American Chemical Society*, 1931, **53**, 3292-3301.
14. R. Metzler and J. Klafter, *Physics Reports*, 2000, **339**, 1-77.
15. J. Chipperfield, *Non-Aqueous Solvents*, Oxford University Press, Oxford, 1999.
16. Y. Yamada, *Bulletin of the Chemical Society of Japan*, 2020, **93**, 109-118.
17. Y.-H. Oh, H. B. Jang, S. Im, M. J. Song, S.-Y. Kim, S.-W. Park, D. Y. Chi, C. E. Song and S. Lee, *Org. Biomol. Chem.*, 2011, **9**, 418-422.
18. V. I. Minkin, *Pure and Applied Chemistry*, 1999, **71**, 1919-1981.
19. R. G. Parr and R. G. Pearson, *Journal of the American Chemical Society*, 1983, **105**, 7512-7516.
20. R. G. Pearson, *Inorganic Chemistry*, 1988, **27**, 734-740.
21. U. Mayer, V. Gutmann and W. Gerger, *Monatshefte Fur Chemie*, 1975, **106**, 1235-1257.
22. V. Gutmann, *The Donor-Acceptor Approach to Molecular Interactions*, Plenum Press, New York, 1978.

23. R. M. Fogarty, R. G. Palgrave, R. A. Bourne, K. Handrup, I. J. Villar-Garcia, D. J. Payne, P. A. Hunt and K. R. J. Lovelock, *Physical Chemistry Chemical Physics*, 2019, **21**, 18893-18910.
24. S. Men, K. R. J. Lovelock and P. Licence, *Physical Chemistry Chemical Physics*, 2011, **13**, 15244-15255.
25. K. R. J. Lovelock, I. J. Villar-Garcia, F. Maier, H. P. Steinrück and P. Licence, *Chemical Reviews*, 2010, **110**, 5158-5190.
26. J. J. H. Davis, *Chemistry Letters*, 2004, **33**, 1072-1077.
27. T. Cremer, C. Kolbeck, K. R. J. Lovelock, N. Paape, R. Wölfel, P. S. Schulz, P. Wasserscheid, H. Weber, J. Thar, B. Kirchner, F. Maier and H. P. Steinrück, *Chem.-Eur. J.*, 2010, **16**, 9018-9033.
28. J. P. Armstrong, C. Hurst, R. G. Jones, P. Licence, K. R. J. Lovelock, C. J. Satterley and I. J. Villar-Garcia, *Physical Chemistry Chemical Physics*, 2007, **9**, 982-990.
29. P. A. Hunt, C. R. Ashworth and R. P. Matthews, *Chemical Society Reviews*, 2015, **44**, 1257-1288.
30. P. A. Hunt, *Top. Curr. Chem.*, 2017, **375**, 22.
31. A. Akcay, V. Balci and A. Uzun, *Thermochimica Acta*, 2014, **589**, 131-136.
32. Y. Yoshida, O. Baba, C. Larriba and G. Saito, *Journal of Physical Chemistry B*, 2007, **111**, 12204-12210.
33. S. U. Lee, J. Jung and Y. K. Han, *Chemical Physics Letters*, 2005, **406**, 332-340.
34. S. Kazemiabnavi, Z. C. Zhang, K. Thornton and S. Banerjee, *Journal of Physical Chemistry B*, 2016, **120**, 5691-5702.
35. N. De Vos, C. Maton and C. V. Stevens, *ChemElectroChem*, 2014, **1**, 1258-1270.
36. D. Weingarth, I. Czekaj, Z. F. Fei, A. Foelske-Schmitz, P. J. Dyson, A. Wokaun and R. Kötz, *Journal of the Electrochemical Society*, 2012, **159**, H611-H615.
37. J. G. Calvert, *Pure and Applied Chemistry*, 1990, **62**, 2167-2219.
38. Y. Marcus, *Chemical Reviews*, 2009, **109**, 1346-1370.
39. Y. Marcus, *Ions in Solution and their Solvation*, John Wiley & Sons, 2015.
40. H. Reiss, H. L. Frisch and J. L. Lebowitz, *The Journal of Chemical Physics*, 1959, **31**, 369-380.
41. J. S. Murray and P. Politzer, *WIREs Computational Molecular Science*, 2011, **1**, 153-163.
42. S. Seal, K. Doblhoff-Dier and J. Meyer, *The Journal of Physical Chemistry B*, 2019, **123**, 9912-9921.
43. D. R. MacFarlane, A. L. Chong, M. Forsyth, M. Kar, R. Vijayaraghavan, A. Somers and J. M. Pringle, *Faraday Discussions*, 2018, **206**, 9-28.
44. O. Borodin, J. Self, K. A. Persson, C. S. Wang and K. Xu, *Joule*, 2020, **4**, 69-100.

45. S. C. C. van der Lubbe and C. Fonseca Guerra, *Chemistry – An Asian Journal*, 2019, **14**, 2760-2769.
46. M. J. Kamlet and R. W. Taft, *Journal of the American Chemical Society*, 1976, **98**, 377-383.
47. R. W. Taft and M. J. Kamlet, *Journal of the American Chemical Society*, 1976, **98**, 2886-2894.
48. M. J. Kamlet, J. L. Abboud and R. W. Taft, *Journal of the American Chemical Society*, 1977, **99**, 6027-6038.
49. R. W. Taft, J. L. M. Abboud and M. J. Kamlet, *Journal of the American Chemical Society*, 1981, **103**, 1080-1086.
50. S. Spange, C. Lienert, N. Friebe and K. Schreiter, *Physical Chemistry Chemical Physics*, 2020, **22**, 9954-9966.
51. C. Reichardt, *Chemical Reviews*, 1994, **94**, 2319-2358.
52. J. Catalan, J. Gomez, A. Couto and J. Laynez, *Journal of the American Chemical Society*, 1990, **112**, 1678-1681.
53. J. Catalán, *The Journal of Physical Chemistry B*, 2009, **113**, 5951-5960.
54. J. Catalán and C. Díaz, *Liebigs Annalen*, 1997, **1997**, 1941-1949.
55. M. Armand, F. Endres, D. R. MacFarlane, H. Ohno and B. Scrosati, *Nat. Mater.*, 2009, **8**, 621-629.
56. D. R. MacFarlane, M. Forsyth, P. C. Howlett, J. M. Pringle, J. Sun, G. Annat, W. Neil and E. I. Izgorodina, *Accounts of Chemical Research*, 2007, **40**, 1165-1173.
57. X. L. Dong, Y. G. Wang and Y. Y. Xia, *Accounts of Chemical Research*, 2021, **54**, 3883-3894.
58. L. M. Suo, Y. S. Hu, H. Li, M. Armand and L. Q. Chen, *Nat. Commun.*, 2013, **4**, 9.
59. L. M. Suo, O. Borodin, T. Gao, M. Olguin, J. Ho, X. L. Fan, C. Luo, C. S. Wang and K. Xu, *Science*, 2015, **350**, 938-943.
60. L. M. Suo, O. Borodin, Y. S. Wang, X. H. Rong, W. Sun, X. L. Fan, S. Y. Xu, M. A. Schroeder, A. V. Cresce, F. Wang, C. Y. Yang, Y. S. Hu, K. Xu and C. S. Wang, *Adv. Energy Mater.*, 2017, **7**, 10.
61. X. J. Yan, X. L. Zhao, C. C. Liu, S. P. Wang, Y. J. Zhang, M. Guo, Y. Y. Wang, L. Y. Dai and X. W. Yang, *Journal of Power Sources*, 2019, **423**, 331-338.
62. X. Y. Wu, Y. K. Xu, C. Zhang, D. P. Leonard, A. Markir, J. Lu and X. L. Ji, *Journal of the American Chemical Society*, 2019, **141**, 6338-6344.
63. Y. Yamada, J. H. Wang, S. Ko, E. Watanabe and A. Yamada, *Nat. Energy*, 2019, **4**, 269-280.
64. M. M. Zhang, H. X. Hao, D. X. Zhou, Y. Y. Duan, Y. Wang and H. T. Bian, *J. Phys. Chem. C*, 2020, **124**, 8594-8604.

65. F. M. Rivas-Esquivel, G. M. Brisard, R. Ortega-Borges, G. Trejo and Y. Meas, *Int. J. Electrochem. Sci.*, 2017, **12**, 2026-2041.
66. F. Bella, C. Gerbaldi, C. Barolo and M. Gratzel, *Chemical Society Reviews*, 2015, **44**, 3431-3473.
67. E. J. Smoll, X. M. Chen, L. M. Hall, L. D'Andrea, J. M. Slattery and T. K. Minton, *J. Phys. Chem. C*, 2020, **124**, 382-397.
68. F. Sessa, V. Migliorati, A. Serva, A. Lapi, G. Aquilanti, G. Mancini and P. D'Angelo, *Physical Chemistry Chemical Physics*, 2018, **20**, 2662-2675.
69. J. C. Hamill, J. Schwartz and Y. L. Loo, *ACS Energy Lett.*, 2018, **3**, 92-97.
70. G. Bouhadir and D. Bourissou, in *Chemical Bond Iii: 100 Years Old and Getting Stronger*, ed. D. M. P. Mingos, Springer, New York, 2017, vol. 171, pp. 141-201.
71. R. Hoffmann, S. Alvarez, C. Mealli, A. Falceto, T. J. Cahill, T. Zeng and G. Manca, *Chemical Reviews*, 2016, **116**, 8173-8192.
72. E. Rezabal and T. Schafer, *Physical Chemistry Chemical Physics*, 2015, **17**, 14588-14597.
73. C. J. Clarke, W. C. Tu, O. Levers, A. Brohl and J. P. Hallett, *Chemical Reviews*, 2018, **118**, 747-800.
74. M. Schmeisser and R. van Eldik, *Dalton Trans.*, 2014, **43**, 15675-15692.
75. K. Matuszek, S. Coffie, A. Chrobok and M. Swadźba-Kwaśny, *Catal. Sci. Technol.*, 2017, **7**, 1045-1049.
76. M. Vafaeezadeh and H. Alinezhad, *Journal of Molecular Liquids*, 2016, **218**, 95-105.
77. H. P. Steinrück and P. Wasserscheid, *Catal. Lett.*, 2015, **145**, 380-397.
78. R. L. Vekariya, *Journal of Molecular Liquids*, 2017, **227**, 44-60.
79. T. Welton, *Coordination Chemistry Reviews*, 2004, **248**, 2459-2477.
80. K. S. Egorova, E. G. Gordeev and V. P. Ananikov, *Chemical Reviews*, 2017, **117**, 7132-7189.
81. K. S. Egorova and V. P. Ananikov, *Journal of Molecular Liquids*, 2018, **272**, 271-300.
82. B. Eisenberg, *Physiology*, 2013, **28**, 28-38.
83. C. Schröder, *Top. Curr. Chem.*, 2017, **375**, 25.
84. P. Lo Nostro and B. W. Ninham, *Chemical Reviews*, 2012, **112**, 2286-2322.
85. C. E. Housecroft and E. C. Constable, *Chemistry: an introduction to organic, inorganic and physical chemistry*, Pearson education, 2010.
86. R. S. Mulliken, *Journal of the American Chemical Society*, 1952, **74**, 811-824.
87. L. Salem, *Journal of the American Chemical Society*, 1968, **90**, 543-552.
88. V. R. Koch, L. A. Dominey, C. Nanjundiah and M. J. Ondrechen, *Journal of The Electrochemical Society*, 1996, **143**, 798-803.

89. K. L. Van Aken, M. Beidaghi and Y. Gogotsi, *Angew. Chem. Int. Ed.*, 2015, **54**, 4806-4809.

90. F. A. Stevie and C. L. Donley, *Journal of Vacuum Science & Technology A*, 2020, **38**, 063204.

91. P. D. Innes and J. J. Thomson, *Proceedings of the Royal Society of London. Series A, Containing Papers of a Mathematical and Physical Character*, 1907, **79**, 442-462.

92. H. G. J. Moseley, *Philos. Mag.*, 1913, **26**, 1024-1034.

93. H. R. Robinson, *Philos. Mag.*, 1925, **50**, 241-250.

94. C. Nordling, E. Sokolowski and K. Siegbahn, *Phys. Rev.*, 1957, **105**, 1676-1677.

95. K. Siegbahn, C. Nordling, A. Fahlman, R. Nordberg, K. Hamrin, J. Hedman, G. Johansson, T. Bergmark, S. E. Karlsson, I. Lindgren and B. J. Lindberg, *ESCA: atomic, molecular and solid state structure studies by means of electron spectroscopy*, Almqvist and Wiksells, Uppsala, 1967.

96. M. A. Kelly and C. E. Tyler, *Hewlett-Packard Journal*, 1973.

97. K. Siegbahn, *Science*, 1982, **217**, 111-121.

98. M. Faubel, B. Steiner and J. P. Toennies, *Journal of Chemical Physics*, 1997, **106**, 9013-9031.

99. B. Winter, R. Weber, W. Widdra, M. Dittmar, M. Faubel and I. V. Hertel, *Journal of Physical Chemistry A*, 2004, **108**, 2625-2632.

100. B. Winter and M. Faubel, *Chemical Reviews*, 2006, **106**, 1176-1211.

101. S. Thürmer, S. Malerz, F. Trinter, U. Hergenhahn, C. Lee, D. M. Neumark, G. Meijer, B. Winter and I. Wilkinson, *Chem. Sci.*, 2021, **12**, 10558-10582.

102. R. Seidel, S. Thurmer and B. Winter, *J. Phys. Chem. Lett.*, 2011, **2**, 633-641.

103. T. Fransson, Y. Harada, N. Kosugi, N. A. Besley, B. Winter, J. J. Rehr, L. G. M. Pettersson and A. Nilsson, *Chemical Reviews*, 2016, **116**, 7551-7569.

104. R. Dupuy, C. Richter, B. Winter, G. Meijer, R. Schlögl and H. Bluhm, *The Journal of Chemical Physics*, 2021, **154**, 060901.

105. W. Stickle and T. Stickle, *Surf. Sci. Spectra*, 2014, **21**, 28-34.

106. K. A. Perrine, M. H. C. Van Spyk, A. M. Margarella, B. Winter, M. Faubel, H. Bluhm and J. C. Hemminger, *J. Phys. Chem. C*, 2014, **118**, 29378-29388.

107. S. Thurmer, R. Seidel, B. Winter, M. Oncak and P. Slavíček, *Journal of Physical Chemistry A*, 2011, **115**, 6239-6249.

108. A. P. Gaiduk, M. Govoni, R. Seidel, J. H. Skone, B. Winter and G. Galli, *Journal of the American Chemical Society*, 2016, **138**, 6912-6915.

109. A. P. Gaiduk and G. Galli, *J. Phys. Chem. Lett.*, 2017, **8**, 1496-1502.

110. M. N. Pohl, E. Muchova, R. Seidel, H. Ali, S. Srsen, I. Wilkinson, B. Winter and P. Slavicek, *Chem. Sci.*, 2019, **10**, 848-865.

111. B. Credidio, M. Pugini, S. Malerz, F. Trinter, U. Hergenhahn, I. Wilkinson, S. Thurmer and B. Winter, *Physical Chemistry Chemical Physics*, 2021.

112. B. Jagoda-Cwiklik, P. Slavíček, D. Nolting, B. Winter and P. Jungwirth, *Journal of Physical Chemistry B*, 2008, **112**, 7355-7358.

113. D. Nolting, N. Ottosson, M. Faubel, I. V. Hertel and B. Winter, *Journal of the American Chemical Society*, 2008, **130**, 8150-8151.

114. B. Jagoda-Cwiklik, P. Slavíček, L. Cwiklik, D. Nolting, B. Winter and P. Jungwirth, *Journal of Physical Chemistry A*, 2008, **112**, 3499-3505.

115. J. P. Bruce, K. Zhang, S. G. Balasubramani, A. R. Haines, R. P. Galhenage, V. K. Voora, F. Furche and J. C. Hemminger, *Journal of Physical Chemistry B*, 2021, **125**, 8862-8868.

116. M. El Kazzi, I. Czekaj, E. J. Berg, P. Novak and M. A. Brown, *Topics in Catalysis*, 2016, **59**, 628-634.

117. K. A. Perrine, K. M. Parry, A. C. Stern, M. H. C. Van Spyk, M. J. Makowski, J. A. Freites, B. Winter, D. J. Tobias and J. C. Hemminger, *Proc. Natl. Acad. Sci. U. S. A.*, 2017, **114**, 13363-13368.

118. O. Björneholm, J. Werner, N. Ottosson, G. Öhrwall, V. Ekholm, B. Winter, I. Unger and J. Soderstrom, *J. Phys. Chem. C*, 2014, **118**, 29333-29339.

119. K. D. Mudryk, R. Seidel, B. Winter and I. Wilkinson, *Physical Chemistry Chemical Physics*, 2020, **22**, 20311-20330.

120. R. Seidel, M. Faubel, B. Winter and J. Blumberger, *Journal of the American Chemical Society*, 2009, **131**, 16127-16137.

121. J. Moens, R. Seidel, P. Geerlings, M. Faubel, B. Winter and J. Blumberger, *Journal of Physical Chemistry B*, 2010, **114**, 9173-9182.

122. R. Seidel, S. Thurmer, J. Moens, P. Geerlings, J. Blumberger and B. Winter, *Journal of Physical Chemistry B*, 2011, **115**, 11671-11677.

123. T. Buttersack, P. E. Mason, R. S. McMullen, T. Martinek, K. Brezina, D. Hein, H. Ali, C. Kolbeck, C. Schewe, S. Malerz, B. Winter, R. Seidel, O. Marsalek, P. Jungwirth and S. E. Bradforth, *Journal of the American Chemical Society*, 2019, **141**, 1838-1841.

124. T. Buttersack, P. E. Mason, R. S. McMullen, H. C. Schewe, T. Martinek, K. Brezina, M. Crhan, A. Gomez, D. Hein, G. Wartner, R. Seidel, H. Ali, S. Thurmer, O. Marsalek, B. Winter, S. E. Bradforth and P. Jungwirth, *Science*, 2020, **368**, 1086-+.

125. P. E. Mason, H. C. Schewe, T. Buttersack, V. Kostal, M. Vitek, R. S. McMullen, H. Ali, F. Trinter, C. Lee, D. M. Neumark, S. Thurmer, R. Seidel, B. Winter, S. E. Bradforth and P. Jungwirth, *Nature*, 2021, **595**, 673-+.

126. J. A. van Bokhoven and C. Lamberti, *X-Ray Absorption and X-Ray Emission Spectroscopy: Theory and Applications*, John Wiley & Sons Incorporated, New York, 2016.

127. L. De Broglie, *Nobel lecture*, 1929, **12**, 244-256.

128. J. W. Smith and R. J. Saykally, *Chemical Reviews*, 2017, **117**, 13909-13934.

129. J. A. Sellberg, S. Kaya, V. H. Segtnan, C. Chen, T. Tyliszczak, H. Ogasawara, D. Nordlund, L. G. M. Pettersson and A. Nilsson, *Journal of Chemical Physics*, 2014, **141**.

130. C. Weeraratna, O. Kostko and M. Ahmed, *Molecular Physics*, 2021.

131. M. Ekimova, W. Quevedo, L. Szyc, M. Iannuzzi, P. Wernet, M. Odelius and E. T. J. Nibbering, *Journal of the American Chemical Society*, 2017, **139**, 12773-12783.

132. R. M. Fogarty, R. P. Matthews, C. R. Ashworth, A. Brandt-Talbot, R. G. Palgrave, R. A. Bourne, T. V. Hoogerstraete, P. A. Hunt and K. R. J. Lovelock, *Journal of Chemical Physics*, 2018, **148**, 193817.

133. R. M. Fogarty, R. P. Matthews, M. T. Clough, C. R. Ashworth, A. Brandt-Talbot, P. J. Corbett, R. G. Palgrave, R. A. Bourne, T. W. Chamberlain, T. Vander Hoogerstraete, P. B. J. Thompson, P. A. Hunt, N. A. Besley and K. R. J. Lovelock, *Physical Chemistry Chemical Physics*, 2017, **19**, 31156-31167.

134. J. M. Seymour, E. Gousseva, A. Large, G. Held, D. Hein, G. Wartner, W. Quevedo, R. Seidel, C. Kolbeck, C. J. Clarke, R. Fogarty, R. Bourne, R. Bennett, R. Palgrave, P. A. Hunt and K. R. J. Lovelock, *Faraday Discussions*, 2022.

135. J. M. Seymour, E. Gousseva, A. Large, C. J. Clarke, P. Licence, R. M. Fogarty, D. Duncan, P. Ferrer, F. Venturini, R. A. Bennett, R. G. Palgrave and K. R. J. Lovelock, *Physical Chemistry Chemical Physics*, 2021, **23**, 20957 - 20973.

136. M. H. Richter, W.-H. Cheng, E. J. Crumlin, W. S. Drisdell, H. A. Atwater, D. Schmeißer, N. S. Lewis and B. S. Brunschwig, *Chemistry of Materials*, 2021, **33**, 1265-1275.

137. R. M. Fogarty, R. Rowe, R. P. Matthews, M. T. Clough, C. R. Ashworth, A. Brandt, P. J. Corbett, R. G. Palgrave, E. F. Smith, R. A. Bourne, T. W. Chamberlain, P. B. J. Thompson, P. A. Hunt and K. R. J. Lovelock, *Faraday Discussions*, 2018, **206**, 183-201.

138. I. J. Villar-Garcia, E. F. Smith, A. W. Taylor, F. L. Qiu, K. R. J. Lovelock, R. G. Jones and P. Licence, *Physical Chemistry Chemical Physics*, 2011, **13**, 2797-2808.

139. B. A. Halkier and J. Gershenzon, *Annual Review of Plant Biology*, 2006, **57**, 303-333.

140. Q. Tai, P. You, H. Sang, Z. Liu, C. Hu, H. L. W. Chan and F. Yan, *Nat. Commun.*, 2016, **7**, 11105.

141. P. Chomczynski and N. Sacchi, *Anal. Biochem.*, 1987, **162**, 156-159.

142. M. K. Nazeeruddin, P. Péchy, T. Renouard, S. M. Zakeeruddin, R. Humphry-Baker, P. Comte, P. Liska, L. Cevey, E. Costa, V. Shklover, L. Spiccia, G. B. Deacon, C. A. Bignozzi and M. Grätzel, *Journal of the American Chemical Society*, 2001, **123**, 1613-1624.

Chapter 2

Spectroscopic methods

Throughout this work, three complementary X-ray spectroscopic methods were used: non-resonant X-ray photoelectron spectroscopy (NRXPS), X-ray absorption spectroscopy (XAS), and resonant X-ray photoelectron spectroscopy (RXPS). These X-ray spectroscopic techniques were used in tandem to probe the energies of the occupied core orbitals (OCOs), the occupied valence states (OVSs), and the unoccupied molecular orbitals (UMOs), and thus provided a complete measure of the energetic levels within a chemical system.

Two key physical principles underpin the process of X-ray spectroscopy, which are the quantisation of energy, as described by Max Planck,[1] and the photoelectric effect, as postulated by Albert Einstein.[2] In the former, Planck showed that the energy of electromagnetic waves is quantised, where the excitation energy, E, is equal to the product of the Planck's constant, h, and the frequency of the wave, ν (Equation 2.1).

$$E = h\nu \qquad \textbf{(2.1)}$$

E = excitation energy
h = Planck's constant
ν = frequency

Einstein applied the principle of quantisation to explain the *UV catastrophe* using the photoelectric effect, suggesting criteria must be met before photoemission can take place:[3]

1. The frequency of excitation must be greater than or equal to the threshold level characteristic for each element, regardless of illumination intensity.
2. Upon reaching the required threshold, the number of electrons emitted will be proportional to the intensity of the illumination.
3. The kinetic energy of the emitted electrons is linearly proportional to the frequency of the exciting photons.

From these key principles, the photoemission process can be described. The relationship between the excitation energy, $h\nu$, and the electron kinetic energy, E_K, can be used to calculate the electron binding energy, E_B (Equation 2.2). E_B is a vital parameter within X-ray spectroscopic techniques and allows for the characterisation of individual elements within a chemical species, yielding information on the type of atom and environment from which the electrons are emitted. The photoemission process from excitation to emission is in the order of 10^{-16} seconds, allowing for spectroscopic measurements which are independent of nuclear rearrangement.[4]

$$E_B = h\nu - E_K \tag{2.2}$$

E_B = electron binding energy
$h\nu$ = excitation energy
E_K = electron kinetic energy

Reasoning for measured E_B shifts can be categorised into either initial state effects or final state effects.[5, 6] Initial state effects arise due to any alteration to the ground state of an atom prior to photoemission. For example, the initial state is changed through the formation of additional bonding interactions, which increase the oxidation state of an atom, leading to an increased measured E_B of photoelectrons ejected from the target atom. Within NRXPS experiments, it is generally assumed that initial state effects dominate the reasoning for all chemical shifts of photoelectron peaks present.[3] However, final state effects, which arise due to any alteration to the excited state of an atom after photoemission, may also contribute significantly to the measured E_B. For example, relaxation effects (filling of the core hole post-photoemission) can act to decrease measured E_B. Other types of final state effects include multiplet splitting, where the core hole interacts with unpaired electrons in the outer shell orbitals, and energy loss features such as shake-up peaks, which occur when the outgoing photoelectron loses kinetic energy to excite a valence electron into an unoccupied orbital ($\pi \rightarrow \pi^*$ transition).

The measured area and full width at half maximum (FWHM) of photoemission peaks can provide a semi-quantitative measure of atomic properties within a chemical species. Peak FWHMs are indicative of the core hole lifetime of the element probed, where the core hole lifetime is described by the Heisenberg uncertainty relationship (Equation 2.3). Hence, it is observed that the lesser the core hole lifetime, the greater the peak FWHM within the XP spectra. The core hole lifetime is generally lesser for core level orbitals and greater for valence state orbitals, as the core hole of inner shell orbitals can be filled from outer shell electrons at an increased probability than the reverse scenario.[3] The core hole lifetime also decreases with increasing elemental atomic number, due to an increased probability of core hole filling due to greater valence electron density. Additional contributing factors to photoemission peak FWHM include instrumental resolution (energy spread of the incident X-rays and analyser resolution) and satellite features (vibrational broadening, multiplet splitting, and shake-up satellites). The measured area of photoemission peaks can provide information on the atomic concentration and stoichiometry of each element present. If peak area comparisons are to be made across samples and elements, care must be taken to include the photoionisation cross-section of each element, which greatly influences peak intensity at differing photon energies.[7]

$$\Gamma = h / \tau \qquad \textbf{(2.3)}$$

Γ = intrinsic peak width (eV)
h = Planck's constant (eV·s)
τ = core hole lifetime (s)

During X-ray spectroscopy techniques the measured sample is irradiated with X-rays, which penetrate deep into the sample; however, excited electrons can only travel so far before they are scattered and lose E_K. Therefore, only those electrons that experience minimal energy loss will contribute to the measured photoemission spectra. The process of determining the depth within the sample from which detected photoelectrons originate is calculated quantitatively through inelastic mean free path (IMFP) and sampling depths. As sample type (and thickness) influences the behaviour of photoelectrons, the IMFP is calculated depending on the nature of the material studied. General equations are available for elemental, inorganic, and organic compounds (Equations 2.4 to 2.6, respectively).[8] Over the range of E_K most commonly studied, IMFP is shown to increase with increasing E_K (Figure 2.1). Sampling depth is defined as the depth from which 95 % of the photoemission has taken place and is usually approximated to three times the IMFP.[3, 9]

Elemental (in nm): $\lambda = 538E_{\mathrm{K}}^{-2} + 0.41(\alpha E_{\mathrm{K}})^{0.5}$ **(2.4)**

Inorganic (in nm): $\lambda = 2170E_{\mathrm{K}}^{-2} + 0.72(\alpha E_{\mathrm{K}})^{0.5}$ **(2.5)**

Organic (in mg m^{-2}): $\lambda_{\mathrm{d}} = 49E_{\mathrm{K}}^{-2} + 0.11(E_{\mathrm{K}})^{0.5}$ **(2.6)**

λ = IMFP

E_{K} = electron kinetic energy

α = monolayer thickness

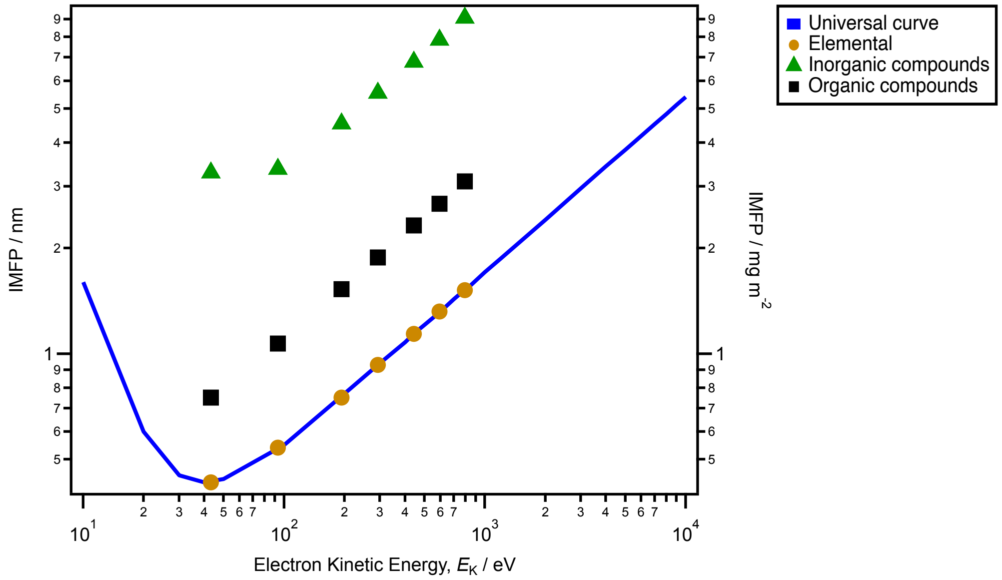

Figure 2.1. The calculated IMFP curve for elemental samples (orange circle), inorganic compounds (green triangle), and organic compounds (black square), overlaid upon the universal curve (blue).

Quantitative values of peak area, FWHM, and crucially E_{B} can be gained through peak fitting parameters (Appendix Table 8.4).

2.1. Non-resonant X-ray photoelectron spectroscopy

During non-resonant X-ray photoelectron spectroscopy (NRXPS), the sample with ground state (GS) electron configuration is loaded into the apparatus (Figure 2.2a). The GS sample is irradiated with X-rays of known photon energy, resulting in the excitation of core level (Figure 2.2b), or valence state electrons (Figure 2.2c) to vacuum, leaving an unstable core hole in its place. The E_K of the ejected photoelectron is measured over the region of interest at low (core level) or high (valence state) energies. Thus, a NRXP spectra is produced for the analysed sample.

The characteristic elemental E_B is calculated from the known $h\nu$ and the measured E_K (Equation 2.2). Due to the influence of nuclear attraction, an electron at proximity to the atomic nucleus (core level electron) will possess a greater E_B than an electron located further away from the nucleus (valence state electron). Therefore, E_B varies with both, the type of atom measured (change in nuclear charge), and the neighbouring atoms bound to the measured atom (alteration of the electron distribution of the measured atom). Changes in E_B, *e.g.*, upon atomic oxidation state variation, are termed binding energy shifts. The measurement of E_B and comparative E_B shifts from NRXP spectra can yield vast information about the chemical system, such as: the elemental identification, information about the molecular environment (oxidation state, interacting species), and aromaticity (shake-up $\pi \rightarrow \pi^*$ transitions).

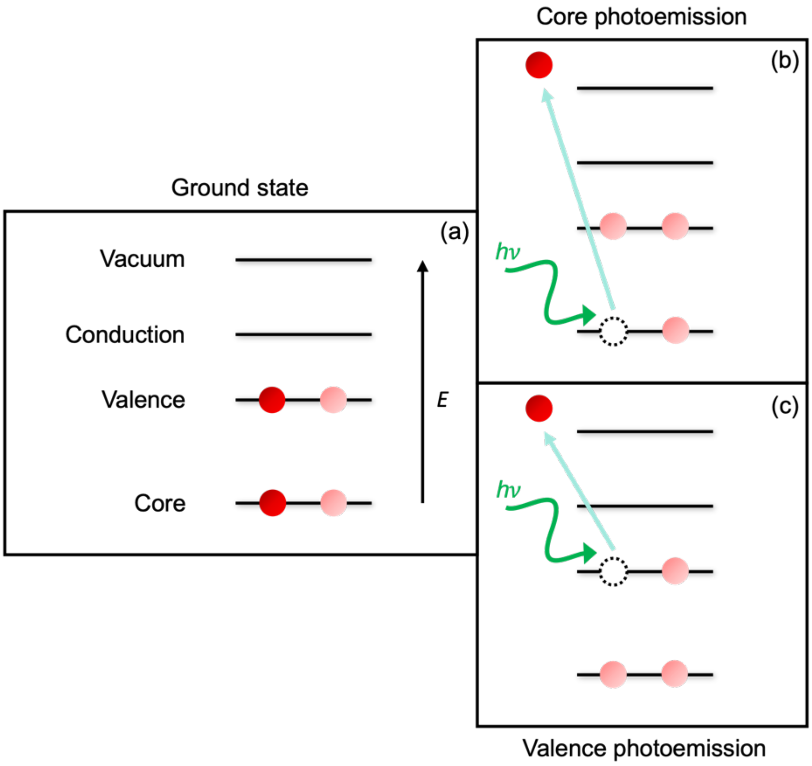

Figure 2.2. Electronic energy diagram for X-ray photoelectron spectroscopy. (a) ground state. (b) core level photoemission. (c) valence level photoemission. Red circles represent electrons involved within the process. Pink circles represent spectating electrons within the process. Dashed circles represent core hole states. Green arrows represent incident photon energy. Teal arrows represent electron ejection to vacuum.

2.2. X-ray absorption spectroscopy

During X-ray absorption spectroscopy (XAS), a sample with GS electron configuration is irradiated by photons of known energy (Figure 2.3a). The incident photon energy is varied throughout the scan. At specific photon energies in the vicinity of a core level binding energy threshold, a photoexcited electron is absorbed into the unoccupied states, resulting in an increased absorption probability, otherwise known as an absorption edge (Figure 2.3b).[10] The increased probability is indicative of the promotion of a ground state electron to an excited state, where typically an occupied core orbital (OCO) to unoccupied molecular orbital (UMO) transition has occurred. The OCO → UMO transition is measured indirectly through either fluorescence yield, or electron yield, both of which arise due to filling of the energetically unstable core hole through electron decay. The method of collecting photoelectrons through use of an electron analyser is termed partial electron yield (PEY), which provides sensitivity to the surface due to the scattering of deeper photoelectrons.[11, 12]

The ability to selectively study each characteristic absorption edge through variation of the incident photon energy range allows XAS to be an element-selective technique. Each absorption edge is known to have a characteristic energy, which is mainly dependent upon the atomic number.[10] XA spectra provide information on the symmetry, geometry, and electronic structure of a species, as XAS probes the complete density of state around the absorbing atom. Therefore, XAS is sensitive to multi-electronic phenomena induced by the excited state; thus, XAS can provide an indication of the influence of final state effects on the system.

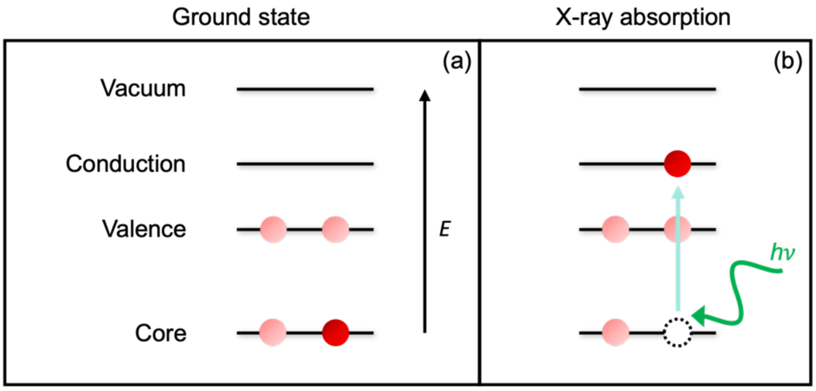

Figure 2.3. Electronic energy diagram for X-ray absorption spectroscopy. (a) ground state. (b) X-ray absorption. Red circles represent electrons involved within the process. Pink circles represent spectating electrons within the process. Dashed circles represent core hole states. Green arrows represent incident photon energy. Teal arrows represent intra-atomic electron transitions.

2.3. Valence resonant X-ray photoelectron spectroscopy

During valence resonant X-ray photoelectron spectroscopy (RXPS), a sample with ground state electron configuration is irradiated by photons of known energy (Figure 2.4a). Valence XP spectra, *i.e.*, E_B = 0 eV to 45 eV, are recorded at stepwise increments of incident photon energy, starting at energies below the absorption edge and continuing through, and above, the absorption edge, *e.g.*, $h\nu$ = 397.0 eV to $h\nu$ = 407.0 eV for the N 1s edge. At specific incident photon energies, known as resonant photon energies, an OCO → UMO transition occurs analogous to the process described in Section 2.2 (Figure 2.4b). The electron decay process necessary to fill the unstable core hole under resonant conditions follows two differing Auger emission processes: participator Auger emission (Figure 2.4c)[13, 14] and spectator Auger emission (Figure 2.4d). At resonant photon energies the valence XP spectra is dominated by electronic contributions from the target element, as a new photon is emitted with the same energy as the incident photon.[10] The electronic process of participator Auger emission and spectator Auger emission differ slightly but offer vastly different physicochemical information.[15]

Participator Auger emission

The decay process leading to participator Auger emission involves the filling of a core hole by an electron located within the conduction band (Figure 2.4c).[16, 17] Hence the electron *participating* is that which was initially excited to the conduction band from ground state during XA. The energy released from the relaxation of the participating electron leads to non-radiative emission of an Auger electron. Participator Auger emission takes place when a strong overlap between the OCO and the core hole exists. Therefore, participator Auger emission peaks appear at E_B positions similar to those of corresponding NRXPS photoemission peaks. Consequently, participator Auger emission provides a very useful tool for identification of unknown peaks within the valence NRXP spectra, particularly those peaks which are otherwise hidden by solvent or surface photoemission peaks.[14, 15]

Spectator Auger emission

The decay process leading to spectator Auger emission involves the filling of a core hole by an electron located within the valence band (Figure 2.4d). Hence the electron *spectating* is that which was initially excited to the conduction band from ground state during XA. Once again, the energy released from the filling of the core hole through electron relaxation leads to non-radiative emission of an Auger electron. However, as the de-excited electron is originally held in the valence band, and the spectating electron still occupies the conduction band, additional screening is provided to the outgoing Auger emission. Therefore, spectator Auger emission peaks appear at E_B positions greater than those of participator Auger emission peaks. Due to the observed screening effect, spectator Auger emission provides a useful tool for probing UMOs localisation and femtosecond electron dynamics.[4] Spectator Auger emission does not feature within the current work, but an explanation is included for completeness.

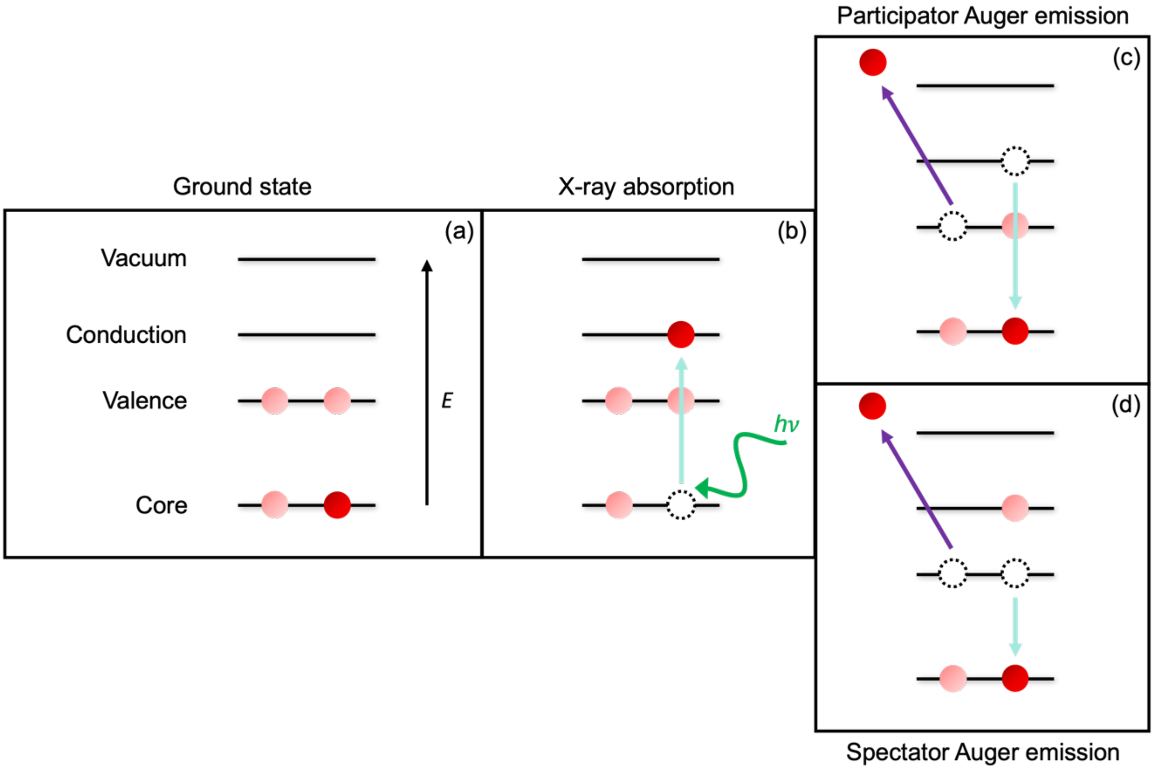

Figure 2.4. Electronic energy diagram for resonant X-ray photoelectron spectroscopy. (a) ground state. (b) X-ray absorption. (c) participator Auger emission. (d) Spectator Auger emission. Red circles represent electrons involved within the process. Pink circles represent spectating electrons within the process. Dashed circles represent core hole states. Green arrows represent incident photon energy. Teal arrows represent intra-atomic electron transitions. Purple arrows represent Auger emission.

2.4. Laboratory source X-ray photoelectron spectroscopy setup

The usefulness of XPS for material characterisation and surface science means lab source XPS systems are readily available within both industrial and educational settings (Figure 2.5). There are three main stages necessary for carrying out lab source XPS: X-ray generation and monochromotisation, sample irradiation, and photoelectron detection.

X-ray generation and monochromotisation

The standard method of X-ray generation is through the process of thermionic emission. Electrons are produced by heating a filament of low work-function material, such as LaB_6. Electrons are then accelerated towards an anodic metal target, such as aluminium or silver, which produces core holes in the metal.[18] The unstable core holes are subsequently filled by electrons in higher lying orbitals, which emit X-ray fluorescence as they decay. The energy of the emitted X-rays is dependent upon the metal target used, *e.g.*, Al Kα = 1486.6 eV. The X-rays produced through fluorescence are un-monochromated, and therefore contain a wide range of energies. The line width of an un-monchromated X-ray source is much larger than that of its monochromated counterpart (Al Kα: 0.85 eV to 0.16 eV, respectively), which would act to reduce overall spectral resolution. Therefore, most lab source XPS systems contain a quartz crystal on a Rowland circle, which allow for constructive interference of the X-rays at the sample spot.[19]

Sample irradiation

The process of sample irradiation takes place within the analysis chamber. Sample X-ray irradiation results in the excitement of electrons within an OCO, which is the first step of all core level X-ray spectroscopic techniques, as described in Sections 2.1 to 2.3. Typical irradiation spot sizes can range between approximately 10 μm to 100 μm, whereas the available sampling area is on the order of centimeters.[19] Excited photoelectrons are ejected to vacuum with E_K equal to the photon energy minus the E_B (Equation 2.2).

Photoelectron detection

A low pressure within the analysis chamber is imperative to photoelectron detection for two reasons:

1. To allow emitted photoelectrons free, unhindered travel to the lens system.
2. To ensure a consistent sample surface, free from additional contaminants.

Hence, ultra-high vacuum (UHV) at a pressure of 10^{-9} mbar is maintained within the analyser chamber using a combination of roughing pumps and turbo pumps. Electrons travel from the analysis chamber through a lens system, which contains both, apertures, and electrostatic lenses. The lens system is employed to focus the photoemitted electrons on to the analyser entrance slit of the hemispherical electron analyser. The hemispherical electron analyser contains an inner hemisphere of net positive charge, which attracts incoming electrons, and an outer hemisphere of net negative charge, which repels incoming electrons. The voltage of the hemispherical analyser can be set to allow more or fewer electrons to travel the length of the analyser through to the detector. This voltage is termed the pass energy, E_{pass}, whereby a larger pass energy allows a greater number of electrons to pass through to the detector; hence, allowing for a greater spectral intensity, while resulting in a lower energy resolution. Finally, the emitted photoelectrons reach the analyser exit plane and are detected. The resultant signal is interpreted by computer software and output as an XP spectrum.

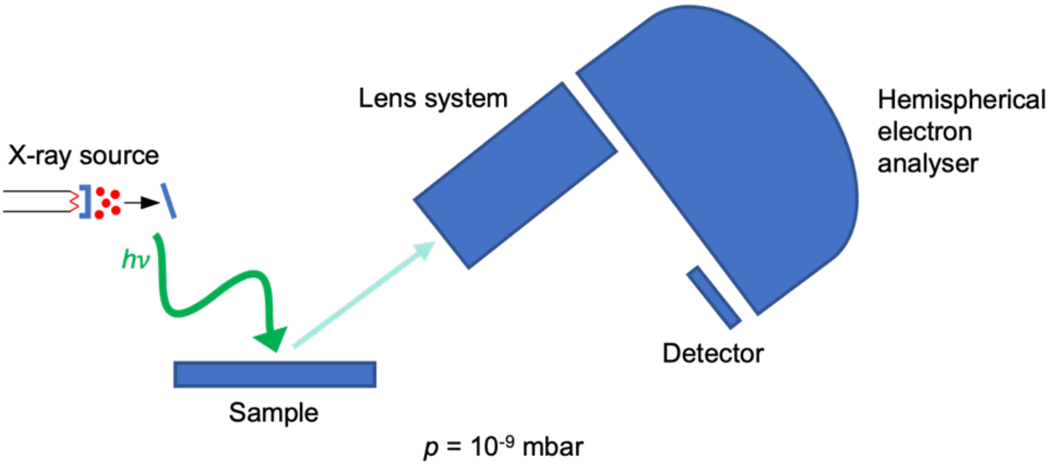

Figure 2.5. Experimental apparatus of the lab source XPS setup. The nature of the experiment proceeds from left to right, starting with the generation of X-rays through fluorescence which are subsequently used to irradiate the sample. Electrons ejected through photoemission enter the lens system where they are focussed into a coherent beam. Electron energy spread is reduced within the hemispherical electron analyser, before finally reaching the detector.

2.5. Synchrotron source photoelectron spectroscopy setup

The use of synchrotron light for X-ray spectroscopy experiments offer benefits far greater than the use of conventional laboratory source XPS systems. For example, synchrotron radiation allows for a tuneable X-ray source, from soft X-rays ($h\nu$ = 0 keV to 2.0 keV), to tender X-rays ($h\nu$ = 2.0 keV to 7.0 keV) to hard X-rays ($h\nu$ = 7.0 eV and above),[20] and high brilliance.[21] Synchrotrons are large (circumference of Diamond Light Source is 562 m), toroidal-shaped machines with a wide range of experimental capabilities (Figure 2.6).[22] Synchrotrons work on the principle that an electron at high speed on a curved trajectory will emit light containing a broad range of wavelengths, one of which is X-ray radiation.[3]

X-ray generation

Similarly to laboratory source XPS systems, electrons are generated through thermionic emission. An electron gun, located within the centre of the synchrotron, uses a heated cathode to generate electrons. Electrons are then accelerated away from the cathodic surface using an anode towards the linear accelerator (linac). The linac increases the energy of the electrons to 100 MeV using radio frequency cavities. Once travelling at high speed, the electrons are transferred to a booster ring where their energy is increased further to 3 GeV through additional use of radio frequency cavities, while maintaining a curved trajectory using bending magnets. From the booster ring, the electrons enter the storage ring, where they are deflected by bending magnets to maintain a closed loop, while simultaneously serving to cause the emission of synchrotron radiation. The storage ring is maintained under UHV conditions to prevent electron scattering. Devices along the storage ring, called undulators and wigglers, contain a series of magnets which cause the electrons to oscillate and consequently radiate energy. The gap between the rows of magnets within undulator devices can be changed to modify the wavelength of X-rays within the beam.

Beamlines

Beamlines appear tangential to the storage ring and are specially equipped to support specific synchrotron techniques, *e.g.*, imaging and microscopy or spectroscopy. Beamlines contain four major sections: the front end, the optics hutch, the experimental hutch, and the control cabin. The front end is where light enters the beamline from the storage ring. The optics hutch contains mirrors and grating necessary for selecting and focussing required wavelengths of light. The experimental hutch contains experimental equipment *e.g.*, the analyser chamber and electron analysis equipment, and where sample mounting takes place during experimentation. Finally, the control cabin is where the scientific team control the experiment from using computer software to manipulate parameters of equipment within the optics and experimental hutches. Many synchrotrons, for example BESSY II (Berlin), do not contain an enclosed optics hutch, experimental hutch, or a control cabin, as soft X-ray is primarily utilised. Instead, the equipment is visible and accessible to all users, and a dosimeter is worn for radiation safety. However, a lead-lined experimental hutch is mandatory when carrying out experiments which utilise hard X-ray radiation.

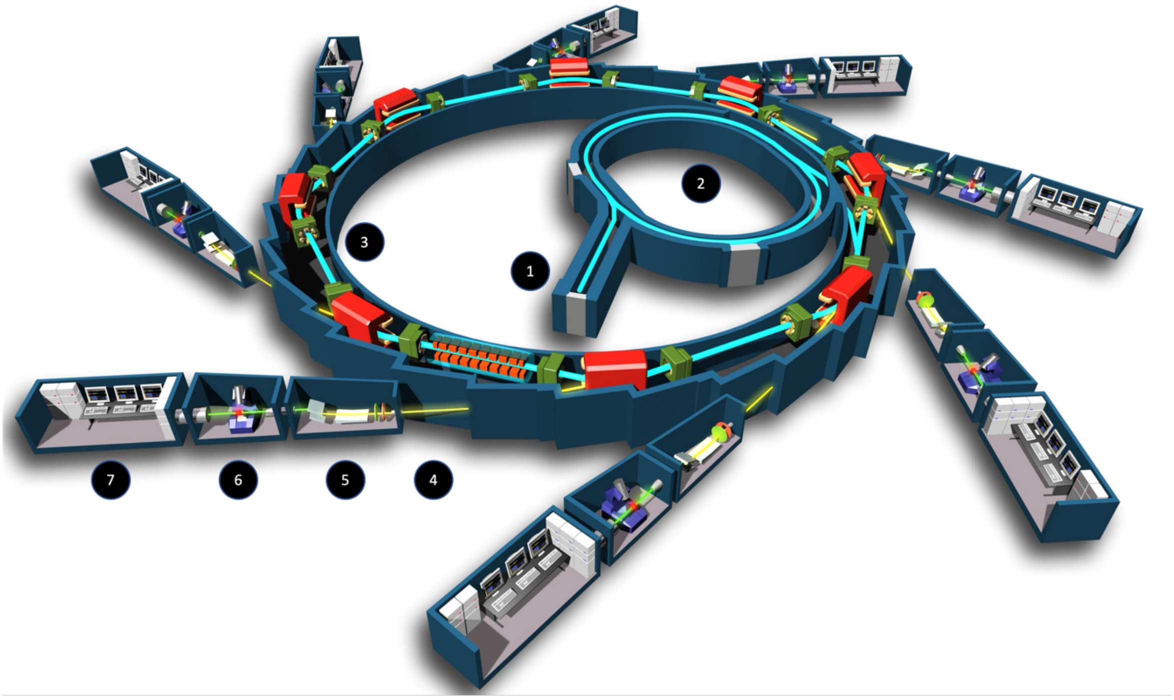

Figure 2.6. General diagram of synchrotron Soleil, where 1 = LINAC, 2 = booster ring, 3 = storage ring, 4 = front end, 5 = optics hutch, 6 = experimental hutch, 7 = control cabin. (Copyright © EPSIM 3D/JF Santarelli, Synchrotron Soleil, reproduced with permission).

2.6. Liquid jet apparatus

The relative ease of carrying out UHV XPS experiments on solid surfaces is apparent due to the large availability and accessibility of both laboratory systems and synchrotron beamlines. However, samples containing molecular liquids, which possess high vapour pressures, cannot be studied under the same UHV conditions due to their relatively high volatilities. Techniques for studying non-aqueous liquids were pioneered by Hans and Kai Siegbahn, where the use of a liquid beam of 0.2 mm diameter allowed for the collection of XP spectra of liquid state samples.[23, 24] Bernd Winter and Manfred Faubel later improved upon the Siegbahn's concept by using a liquid microjet (6 µm).[25, 26] The introduction of near-ambient pressure within the analysis chamber, and differential pumping stages leading to the electron analyser, allowed for the measurement of aqueous samples of relatively high vapour pressure. As the liquid jet apparatus (Figure 2.7) described hereafter was carried out at a synchrotron source (BESSY II, Berlin),[27] X-ray generation and tuning of photon energy will be alike that described in Section 2.5.

Sample loading and irradiation

Samples to be studied are loaded into coiled tubing connected to a high-performance liquid chromatography (HPLC) pump, where the sample flow rate may be manipulated and monitored (in mL / min). Samples are cooled to further reduce evaporation within the analysis chamber and the flow rate varied to enable a stable liquid jet to be attained. The sample is pumped using the HPLC system to the nozzle, which is located within the analysis chamber. The nozzle contains a capillary, which acts to create a laminar flow of liquid, providing a stable surface to irradiate with soft X-rays. Ports accommodating cooling traps (filled with liquid nitrogen) are placed within the analyser chamber to maintain cooling of the sprayed sample.

Photoelectron detection

The skimmer, located above the liquid jet, contains a hole of 100 µm diameter to allow photoemitted electrons entry to the differential pumping unit. Within the differential pumping unit, the photoelectrons pass through apertures to stages of varying pressure, where the pressure decreases from 10^{-4} mbar to 10^{-8} mbar with increasing proximity to the hemispherical analyser. The hemispherical electron analyser and detector are as described in Section 2.4. The advent of the differential pumping unit has allowed for the development of near-ambient pressure XPS systems in synchrotrons around the world, *e.g.*, B07-C at Diamond Light Source, UK.[28]

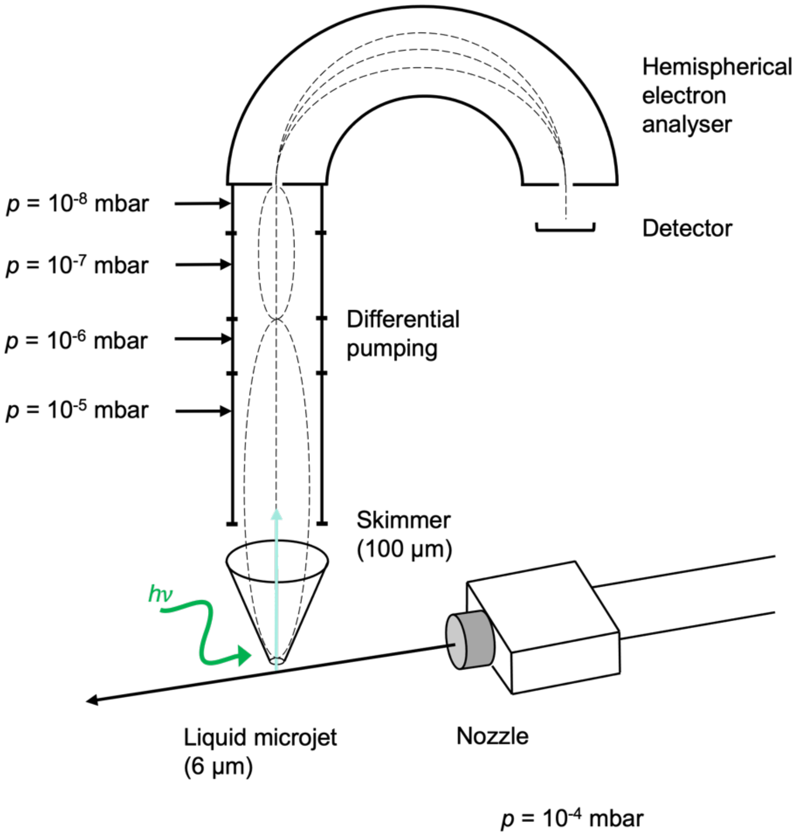

Figure 2.7. Experimental apparatus of the liquid microjet photoemission experiment. Figure adapted from reference [25].

2.7. Data analysis: charge referencing procedures

Variability of the measured E_K for the same sample can be observed due to the large range of experimental parameters discussed (setup, sample ionisation due to photoemission). Hence, charge referencing procedures are employed in order to ensure valid energetic comparisons across all samples. The charge referencing procedures utilised within the current work are detailed in Sections 2.7.1 to 2.7.3, below.

2.7.1. Charge referencing to the E_B(cation) value obtained for dilute ions in H_2O

The literature value of $E_B(O_{liq}$ 1s) for pure H_2O was reported to be 538.1 eV.[26] As solutions at either, a concentration of 0.5 M, or x_{IL} = 0.01, were assumed to contain an infinite dilution of ions in solution, $E_B(O_{liq}$ 1s) was also charge referenced to 538.1 eV. The resultant E_B(cation) value obtained for each solute species was assumed to be representative of that of an ion with zero ion-ion interactions. Therefore, all photoemission peaks for 0.5 M or x_{IL} = 0.01 solutions were charge referenced to the same value of E_B(cation). The identity and value of E_B(cation) used for the charge referencing of each solution are shown (Table 2.1).

Table 2.1. The photoemission peak identity and E_B value used for charge referencing each sample to the E_B(cation) value obtained for dilute ions in H_2O.

Cation species	Photoemission peak	Electron Binding Energy / eV
$[C_4C_1Im]^+$	$E_B(N_{cation}$ 1s)	406.75
K^+	$E_B(K\ 2p_{3/2})$	298.08
Li^+	E_B(Li 1s)	60.54

Spectroscopic regions containing E_B(cation) photoemission peaks were also measured before and after every other region (*e.g.*, N 1s, C 1s, N 1s) to greater aid in the elimination of shifts due to sample charging over time.

2.7.2. Charge referencing to the E_B(solvent) value obtained for pure solvent

Pure solvents (H_2O and PC) were recorded using methodology which allowed for the referencing of each photoelectron peak to the vacuum level, *i.e.*, allowing for the determination of their absolute binding energies.[29, 30] A bias voltage (-50 V) was applied to the liquid microjet, allowing for the removal of any shifts caused due to the process of photoionisation. The XP spectra of the biased sample was measured, yielding the kinetic energy (E_K) of a particular spectral feature, E_K(SF). Additionally, the low E_K curve (lowest E_K required to ionise an electron to vacuum) was measured, E_K(cut). Using both E_K(SF) and E_K(cut), the absolute binding energy of the spectral feature was calculated (Equation 2.7).

$$E_B = h\nu - [E_K(\mathrm{SF}) - E_K(\mathrm{cut})] \qquad \textbf{(2.7)}$$

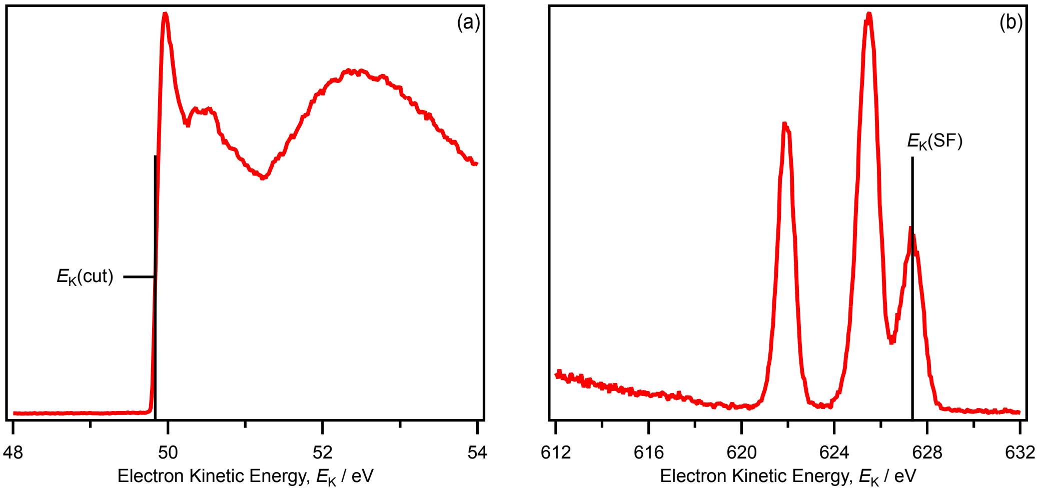

Figure 2.8. The methodology enabling charge referencing of photoelectron peaks to the vacuum level, as described, requires information gained from two additionally measured XP spectra: (a) The low E_K curve, yielding E_K(cut). (b) The core level XP spectra of the biased sample, yielding E_K(SF).

Photoemission peaks were charge referenced to the absolute core level energies of their corresponding pure solvents at the vacuum level (Table 2.2). Solutions at either, a concentration of 0.5 M, or x_{IL} = 0.01, were assumed to contain an infinite dilution of ions in solution. Samples containing H_2O were charge referenced to the vacuum level for E_B(O_{liq} 1s) for pure H_2O.[26] Samples containing PC were charge referenced to the vacuum level for E_B(C_{alkyl} 1s) for pure PC.

Table 2.2. The photoemission peak identity and E_B value used for charge referencing each sample to the E_B(solvent) value obtained for pure solvent.

	Photoemission peak	Electron Binding Energy / eV
H_2O	E_B(O_{liq} 1s)	538.10
PC	E_B(C_{alkyl} 1s)	289.81

The O 1s region or C 1s region, depending on the solvent used (H_2O and PC respectively), was also measured before and after every core level (*e.g.*, O 1s, K 2p, O 1s) to greater eliminate contributions from charging over time.

2.7.3. Charge referencing for RXP spectra

After charge referencing the valence NRXP spectra using the methods detailed within Sections 2.7.1 and 2.7.2, valence RXPS spectra were subsequently charge referenced to the E_B(HOVS) of their corresponding NRXPS valence state by fitting the valence NRXPS[29] measured just below the relevant absorption edge (Table 2.3).

Table 2.3. The photoemission peak identity and $h\nu$ value used for charge referencing each sample to the E_B(solvent) value obtained for pure solvent.

Absorption edge	Valence NRXP energy / $h\nu$
N 1s	398.0
O 1s	532.5
C 1s	284.0
F 1s	686.0

2.8. References

1. M. Planck, The genesis and present state of development of the quantum theory, www.nobelprize.org/prizes/physics/1918/planck/lecture/, (accessed 16 March 2022).
2. A. Einstein, *Ann. Phys.-Berlin*, 1905, **17**, 132-148.
3. J. C. Vickerman and I. S. Gilmore, eds., *Surface Analysis: The Principal Techniques*, John Wiley & Sons, Chichester, 2009.
4. F. Krausz and M. Ivanov, *Rev. Mod. Phys.*, 2009, **81**, 163-234.
5. T. Kirchhuebel, O. L. A. Monti, T. Munakata, S. Kera, R. Forker and T. Fritz, *Physical Chemistry Chemical Physics*, 2019, **21**, 12730-12747.
6. T. L. Barr, E. Hoppe, T. Dugall, P. Shah and S. Seal, *Journal of Electron Spectroscopy and Related Phenomena*, 1999, **98**, 95-103.
7. J. J. Yeh and I. Lindau, *At. Data Nucl. Data Tables*, 1985, **32**, 1-155.
8. M. P. Seah and W. A. Dench, *Surface and Interface Analysis*, 1979, **1**, 2-11.
9. K. W. Kolasinski, *Surface science: foundations of catalysis and nanoscience*, John Wiley & Sons, 2012.
10. J. A. van Bokhoven and C. Lamberti, *X-Ray Absorption and X-Ray Emission Spectroscopy: Theory and Applications*, John Wiley & Sons Incorporated, New York, 2016.
11. G. Hahner, *Chemical Society Reviews*, 2006, **35**, 1244-1255.
12. R. M. Fogarty, R. P. Matthews, M. T. Clough, C. R. Ashworth, A. Brandt-Talbot, P. J. Corbett, R. G. Palgrave, R. A. Bourne, T. W. Chamberlain, T. Vander Hoogerstraete, P. B. J. Thompson, P. A. Hunt, N. A. Besley and K. R. J. Lovelock, *Physical Chemistry Chemical Physics*, 2017, **19**, 31156-31167.
13. J. M. Seymour, E. Gousseva, A. Large, C. J. Clarke, P. Licence, R. M. Fogarty, D. Duncan, P. Ferrer, F. Venturini, R. A. Bennett, R. G. Palgrave and K. R. J. Lovelock, *Physical Chemistry Chemical Physics*, 2021, **23**, 20957 - 20973.
14. R. M. Fogarty, R. G. Palgrave, R. A. Bourne, K. Handrup, I. J. Villar-Garcia, D. J. Payne, P. A. Hunt and K. R. J. Lovelock, *Physical Chemistry Chemical Physics*, 2019, **21**, 18893-18910.
15. J. M. Seymour, E. Gousseva, A. Large, G. Held, D. Hein, G. Wartner, W. Quevedo, R. Seidel, C. Kolbeck, C. J. Clarke, R. Fogarty, R. Bourne, R. Bennett, R. Palgrave, P. A. Hunt and K. R. J. Lovelock, *Faraday Discussions*, 2022.
16. T. Miteva, N. V. Kryzhevoi, N. Sisourat, C. Nicolas, W. Pokapanich, T. Saisopa, P. Songsiririthigul, Y. Rattanachai, A. Dreuw, J. Wenzel, J. Palaudoux, G. Öhrwall, R. Püttner, L. S. Cederbaum, J. P. Rueff and D. Céolin, *J. Phys. Chem. Lett.*, 2018, **9**, 4457-4462.

17. P. A. Brühwiler, O. Karis and N. Mårtensson, *Rev. Mod. Phys.*, 2002, **74**, 703-740.
18. D. Briggs and J. T. Grant, *Surface analysis by Auger and X-ray photoelectron spectroscopy*, SurfaceSpectra, 2012.
19. F. A. Stevie and C. L. Donley, *Journal of Vacuum Science & Technology A*, 2020, **38**, 063204.
20. S. Axnanda, E. J. Crumlin, B. Mao, S. Rani, R. Chang, P. G. Karlsson, M. O. M. Edwards, M. Lundqvist, R. Moberg, P. Ross, Z. Hussain and Z. Liu, *Sci Rep*, 2015, **5**, 9788.
21. M. Patanen, S. Svensson and N. Martensson, *Journal of Electron Spectroscopy and Related Phenomena*, 2015, **200**, 78-93.
22. G. Materlik, T. Rayment and D. I. Stuart, *Philosophical Transactions of the Royal Society A: Mathematical, Physical and Engineering Sciences*, 2015, **373**, 20130161.
23. H. Fellner-Feldegg, H. Siegbahn, L. Asplund, P. Kelfve and K. Siegbahn, *Journal of Electron Spectroscopy and Related Phenomena*, 1975, **7**, 421-428.
24. H. Siegbahn, L. Asplund, P. Kelfve and K. Siegbahn, *Journal of Electron Spectroscopy and Related Phenomena*, 1975, **7**, 411-419.
25. B. Winter and M. Faubel, *Chemical Reviews*, 2006, **106**, 1176-1211.
26. B. Winter, *Nucl. Instrum. Methods Phys. Res. Sect. A-Accel. Spectrom. Dect. Assoc. Equip.*, 2009, **601**, 139-150.
27. R. Seidel, M. N. Pohl, H. Ali, B. Winter and E. F. Aziz, *Review of Scientific Instruments*, 2017, **88**, 073107.
28. G. Held, F. Venturini, D. C. Grinter, P. Ferrer, R. Arrigo, L. Deacon, W. Quevedo Garzon, K. Roy, A. Large and C. Stephens, *J. Synchrot. Radiat.*, 2020, **27**, 1153-1166.
29. S. Thürmer, S. Malerz, F. Trinter, U. Hergenhahn, C. Lee, D. M. Neumark, G. Meijer, B. Winter and I. Wilkinson, *Chem. Sci.*, 2021, **12**, 10558-10582.
30. H. C. Schewe, K. Brezina, V. Kostal, P. E. Mason, T. Buttersack, D. M. Stemer, R. Seidel, W. Quevedo, F. Trinter, B. Winter and P. Jungwirth, *The Journal of Physical Chemistry B*, 2022, **126**, 229-238.

Chapter 3

Influence of solvent identity on anionic electronic structure

Abstract

Solvent-solute interactions are ubiquitous in science due to the wide-ranging implementation of solutions within both, industrial, and academic, processes. Whilst H_2O is the solvent of choice for biological life, many additional solvents are employed every day for a myriad of applications, *e.g.*, batteries and catalysis. Assessing the applicability of each solvent-solute interaction for the desired task individually would be incredibly time consuming. Therefore, solvent polarity scales have been formulated to allow for the categorisation of solvents based upon their solvent-solute interactions, such as Lewis reactivity, to allow for a targeted approach to research. However, experimental knowledge of how a range of solvents with varying polarity scale descriptor values quantitively affect both bonding, and non-bonding, electronic structure energies of ionic solutes remain sparse. In this chapter, the influence of changing solvent identity within 0.5 M (solute)(solvent) solutions on core and valence state electron binding energies is explored. A range of complementary X-ray spectroscopic techniques were utilised, which crucially allowed for the comparison of the highest occupied valence states and lowest unoccupied molecular orbitals of the system. A large range of volatile solvents were measured for the same ionic species by X-ray spectroscopic techniques, which has previously never been achieved. Moreover, solvent species were chosen to represent the entire series of Lewis acidity/basicity abilities. All anionic core and valence state energies were found to be equally influenced by changing solvation environment, which was concluded to be the result of non-specific solvation effects, due to a strong correlation between the energy of the highest occupied valence state and various solvent polarity descriptors relating to solvent Lewis acidity (Kamlet-Taft, Gutmann, and Catalán). Solvents were demonstrated to possess a strong influence over anionic energy levels and hence showed feasibility in the enabling of selective control over solute Lewis acidity/basicity through solvent choice.

3.1. Introduction

Solvent species feature within many important industrial applications, due to their ability to act as both, reaction media for the interaction of two solute species, and chemically inert carriers for the spectroscopic study of solute species. However, during each application it is also crucial to consider the ability of solvent molecules to act as reactants themselves, where solvents can react with solutes (the minor component of a solution)[1] in solution. There are many diverse solvents which react with solutes in different ways through so called solvent-solute interactions. For example, the vital S_N1 reaction within organic chemistry utilises polar solvents to stabilise the transition state.[2] Additionally, solvent-solute interactions can affect the growth rate and crystal shape of metal oxide-based composites[3], and enable control over crystallisation and morphology of perovskites.[4] Specific solvent-solute interactions have also been shown to enhance Lewis reactivity for ionic liquids (ILs).[5] Due to the large solvent diversity, it can be difficult to determine which solvent is best suited within each circumstance. Therefore, research has been conducted to categorise and quantify solvent-solute interactions based upon common solvent properties. One such example of solvent categorisation is that relating to the acid/base behaviour of a species, which has prompted the creation of solvent polarity scales, such as $E_T(30)$[6-8], Kamlet-Taft (KT)[7, 9-12], and Catalán[7, 13]. The aforementioned solvent polarity scales are formulated through the monitoring of the solvatochromic changes observed for dye molecules, such as Reichardt's dye[14], upon the introduction of solvent species, by UV/Vis spectroscopy. Additional non-solvatochromic solvent polarity scales, such as the Gutmann[15, 16] scale, instead utilise nuclear magnetic resonance (NMR) spectroscopy and enthalpy of reaction data. Solvent polarity scales permit the determination of the strength, and the way in which, solvent species interact through electron donation and acceptance of probe molecules; hence, solvent polarity scales describe the Lewis acidity/basicity of the solvent species. KT and Gutmann polarity scale values have been shown to strongly correlate, indicating the strength of using each scale in tandem to describe the solvent-solute interactions within a solution.[17] However, current methods of measuring solvent polarity descriptor values contain an inherent probe dependency, where obtained values primarily provide a measure of the influence of the solvent on the specific dye species used. Therefore, extrapolation of solvent polarity descriptor values to additional solvent-solute interactions may be invalid.[14]

The electronic structure of a species is composed of both, occupied core level orbitals (OCOs), and occupied valence states (OVSs), the latter of which govern the Lewis reactivity of a species.[18] Even though solvent-solute interactions are an important consideration when designing a new chemical system, little experimental research has been carried out to determine how different solvents, across the entire polarity scale range, affect the electronic structure of each species in solution. Through the measurement of the electronic structure of each solute within molecular solvent (MS) by X-ray spectroscopy, the influence of the solvent on the solute species can be thoroughly evaluated, as X-ray spectroscopic methods yield far greater information about the probed system than using solvent polarity scales alone. Furthermore, X-ray spectroscopy provides a means of directly measuring the objective solvent-solute system, rather than applying values obtained for the strength of interaction between solvent and dye species to an unrelated system. Therefore, an important question to be addressed is whether varying the solvent identity can be used to tune OCO and OVS energies in a scale-like manner. If so, through greater understanding of how solvent identity affects OCO and OVS energies, it would be possible to manipulate this factor to aid in the better choice and design of systems which rely upon solvent-solute interactions.

In this chapter, core level non-resonant X-ray photoelectron spectroscopy (NRXPS), valence state NRXPS, X-ray absorption spectroscopy (XAS), and valence resonant XPS (RXPS) were used to measure samples of 0.5 M ([C_4C_1Im][SCN])(solvent), where solvent = H_2O, H_2O/EtOH, EtOH, MeCN and PC, and for the pure ionic liquid (IL) [C_4C_1Im][SCN] (structures of each species used in this chapter are shown in Figure 3.1). Solvents were chosen with a range of KT descriptors, in particular a large range of solvent hydrogen bond donor abilities. The measurement of such a diverse range of solvent identities highlights the novelty of this study, as very few non-aqueous solvents have been studied by X-ray spectroscopy. At a low concentration of ions in molecular solvent (0.5 M), it was assumed that ion-ion interactions were not present and consequently only solvent-solute interactions were probed. Conversely, pure [C_4C_1Im][SCN] provided a measure of pure ion-ion interactions. The listed X-ray spectroscopic techniques were used to compare the size and direction of binding energy, E_B, shifts for each solvent relative to pure [C_4C_1Im][SCN]. Each E_B measurement allowed for the exploration of relationships between E_B(anion) and solvent polarity descriptors. The information gained allowed conclusions to be drawn relating to OCO and OVS energetic shifts, the influence of non-specific versus specific solvation effects, and Initial state versus final state effects. Furthermore, differing solutions containing K[SCN] and Li[NTf_2] within both, aqueous solution, and propylene carbonate (PC) were studied by the same spectroscopic methods to allow for a comparison of the influence of solvent identity on the anionic structure of multiple species.

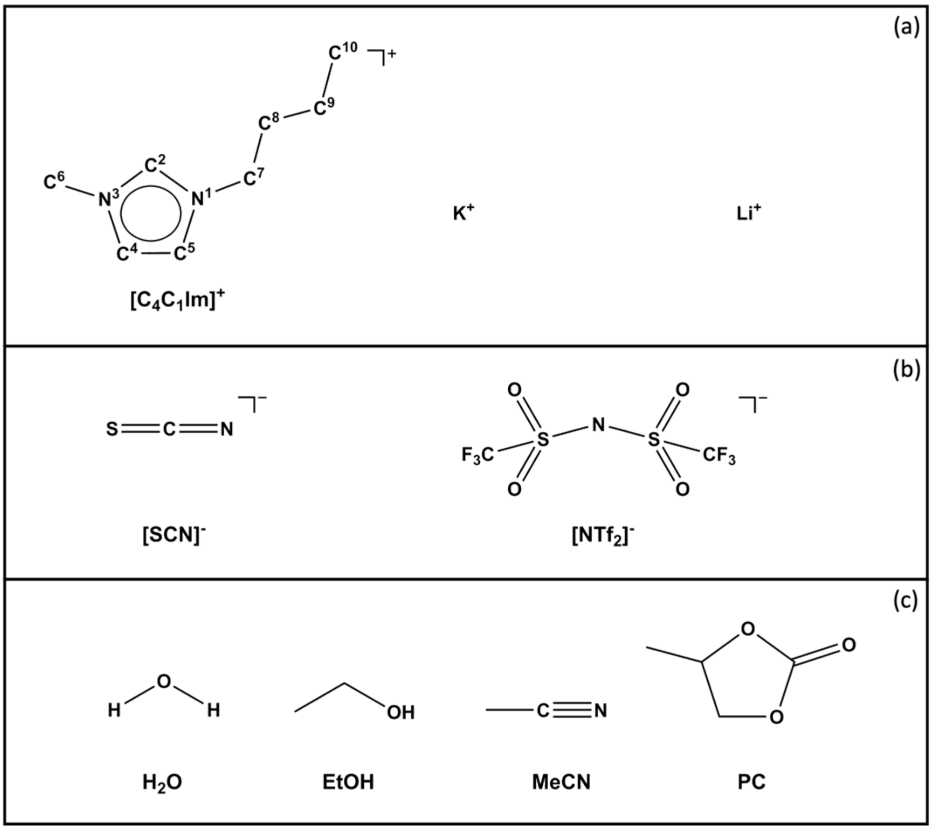

Figure 3.1. Names and structures of key ions and solvents studied within Chapter 3: (a) Cations, where atoms within $[C_4C_1Im]^+$ are numbered according to convention for reference within the current work. (b) Anions. (c) Solvents.

3.2. Spectroscopic methods

3.2.1. Sample preparation

Ethanol (EtOH), acetonitrile (MeCN), and propylene carbonate (PC) were purchased from Sigma-Aldrich, with no further purification or drying prior to use. Highly demineralised H_2O (conductivity ~0.2 μS cm^{-1}) was used for all aqueous solutions. [C_4C_1Im][SCN] was purchased from Iolitec, with no further purification or drying prior to use. K[SCN] and Li[NTf_2] were purchased from Sigma-Aldrich, with no further purification or drying prior to use. [C_4C_1Im][SCN], K[SCN], and Li[NTf_2] were weighed and mixed with a corresponding mass of solvent to achieve a concentration of 0.5 M (Appendix Table 8.1). The corresponding mole fraction, concentration and solute:solvent ratio for each sample are shown (Table 3.1).

Table 3.1. The ten solutions studied within Chapter 3. Concentrations were calculated using parameters listed in Appendix Tables 8.1 to 8.3.

	x_{IL}	x_{solv}	conc. IL/ M	conc. solv / M	solute:solv
[C_4C_1Im][SCN]	100	0	5.4	0	1:0
([C_4C_1Im][SCN])(H_2O)	1	99	0.5	50.3	1:99
([C_4C_1Im][SCN])(H_2O/EtOH)	1	99	0.5		
([C_4C_1Im][SCN])(EtOH)	3	97	0.5	15.6	1:32
([C_4C_1Im][SCN])(MeCN)	3	97	0.5	17.3	1:32
([C_4C_1Im][SCN])(PC)	4	96	0.5	10.8	1:24
(K[SCN])(H_2O)	1	99	0.5	54.1	1:109
(K[SCN])(PC)	4	96	0.5	11.5	1:23
(Li[NTf_2])(H_2O)	1	99	0.5	49.6	1:99
(Li[NTf_2])(PC)	4	96	0.5	10.5	1:21

3.2.2. Synchrotron XPS apparatus

The measurement of pure solvent, 0.5 M ([C_4C_1Im][SCN])(solvent), 0.5 M (K[SCN])(solvent), and 0.5 M (Li[NTf_2])(solvent), where solvent = H_2O, H_2O/EtOH, EtOH, MeCN, or PC, was performed on the U49/2-PGM 1 beamline with SOL^{3}PES end-station at BESSY II (Germany) using liquid-jet apparatus.[19]

XP and RXP spectra were acquired using a Scienta Omicron R4000 HIPP-2 hemispherical electron analyser. The analyser angle was 90.0° horizontal to the plane of polarised light.

RXPS measurements for $[C_4C_1Im][SCN]$ ($x_{IL} = 1.00$) were performed on the I311 beamline at MAX-lab (Sweden). The apparatus used at MAX-lab is explained in reference [20].

3.2.3. Laboratory XPS apparatus

Laboratory–based XPS for the $[C_4C_1Im][SCN]$ was carried out using a Thermo K–alpha spectrometer utilising Al Kα radiation ($h\nu = 1486.6$ eV), as detailed in reference [20].

3.3. Results and discussion

3.3.1. Changes in anionic atomic charge with varying solvent identity

The core level E_B of the anionic components for ([C_4C_1Im][SCN])(solvent), where solvent = H_2O, H_2O/EtOH, EtOH, MeCN, PC, and for pure [C_4C_1Im][SCN], were measured by NRXPS (Figure 3.2). N_{anion} 1s NRXPS showed a single Gaussian peak due to a single N_{anion} environment (Figure 3.2a). A doublet of peaks indicative of spin orbit coupling interactions was observed in the S 2p NRXP spectrum due to a single S_{anion} environment (Figure 3.2b). The N 1s and S 2p NRXP spectra allowed for unobstructed analysis of the anionic electronic structure as there were no overlapping or additional photoelectron peak contributions from other components present within solution. However, an exception arose for 0.5 M ([C_4C_1Im][SCN])(MeCN) where the N 1s NRXP spectra was completely dominated by the solvent photoelectron peaks[21] (Appendix Figure 8.8), preventing accurate and meaningful anionic peak identification; hence N 1s NRXPS was not shown for 0.5 M ([C_4C_1Im][SCN])(MeCN) (Figure 3.2a). All spectra were arranged in order of decreasing E_B (top to bottom): H_2O > H_2O/EtOH > EtOH > [C_4C_1Im][SCN] > MeCN > PC; a trend followed by each core level energy within Figure 3.2.

Through comparison of anionic NRXPS E_B values (Table 3.2, Figure 3.3) it was shown that ΔE_B trends matched for both N_{anion} 1s NRXPS and S 2p NRXPS in differing solvents relative to pure [C_4C_1Im][SCN]. For example, both $\Delta E_B(N_{anion}\ 1s)$ and $\Delta E_B(S\ 2p_{3/2})$ were approximately equal to ~0.1 eV from 0.5 M ([C_4C_1Im][SCN])(H_2O) to 0.5 M ([C_4C_1Im][SCN])(H_2O/EtOH). Due to the nature of the identical energetic shift measured for both anionic components, non-specific solvation effects were concluded as the reasoning for the decreased ΔE_B shift with varying solvation environment, as all anionic OCO energies were shown to shift equally rather than a single OCO energy, which would have instead been indicative of a specific solvation effect. A similar trend was observed through varying the concentration of [C_4C_1Im][SCN] in H_2O, whereby an increase in x_{IL} resulted in a monotonic decrease in both $E_B(N_{anion}\ 1s)$ and $E_B(S\ 2p_{3/2})$ (Chapter 5).

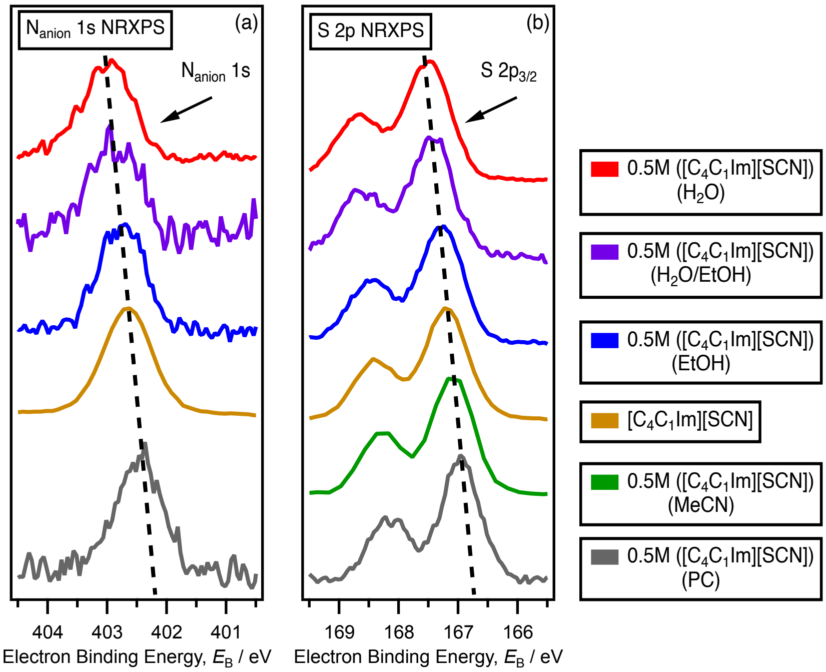

Figure 3.2. Anionic core level NRXP and valence state NRXP spectra for 0.5 M ([C_4C_1Im][SCN])(solvent), where solvent = H_2O (red), H_2O/EtOH (purple), EtOH (blue), MeCN (green), PC (grey), and for pure [C_4C_1Im][SCN] (orange): (a) N_{anion} 1s. (b) S 2p. All XP spectra for 0.5 M solutions ([C_4C_1Im][SCN])(solvent) were measured at $h\nu$ = 700.0 eV; pure [C_4C_1Im][SCN] XP spectra were measured at $h\nu$ = 1486.6 eV. Dashed lines are intended as a visual aid of the changes in E_B that occur with varying x_{IL}, where lines of the same type have the same gradient. All XP spectra were charge referenced using the methods detailed in Section 2.7.1.

Table 3.2. Experimental binding energies, E_B, recorded by NRXPS for 0.5 M ([C_4C_1Im][SCN])(solvent), where solvent = H_2O, H_2O/EtOH, EtOH, MeCN, PC, and for pure [C_4C_1Im][SCN]. All XP spectra for 0.5 M ([C_4C_1Im][SCN])(solvent) were measured at $h\nu$ = 700.0 eV; pure [C_4C_1Im][SCN] XP spectra were measured at $h\nu$ = 1486.6 eV. All values were charge referenced using the methods detailed in Section 2.7.1. All E_B values are reported to 2 decimal places.

	Electron binding energy / eV	
	N_{anion} 1s (± 0.03)	S $2p_{3/2}$ (± 0.06)
0.5 M ([C_4C_1Im][SCN])(H_2O)	403.00	167.53
0.5 M ([C_4C_1Im][SCN])(H_2O/EtOH)	402.91	167.43
0.5 M ([C_4C_1Im][SCN])(EtOH)	402.76	167.27
[C_4C_1Im][SCN]	402.66	167.20
0.5 M ([C_4C_1Im][SCN])(MeCN)		167.09
0.5 M ([C_4C_1Im][SCN])(PC)	402.47	166.96

Although data for pure $[C_4C_1Im][SCN]$ was measured using laboratory XPS apparatus, rather than liquid-jet apparatus used for all samples of 0.5 M ($[C_4C_1Im][SCN]$)(solvent), a linear E_B trend was still observed. A difference in experimental setup should not present a challenge when comparing relatively small E_B shifts as, although intrinsic full width at half maximum (FWHM) values differ between X-ray sources and choice of spectrometer, E_B values should remain independent of peak broadening.[22] Therefore, measuring E_B in this manner while employing the current charge referencing methodology (Section 2.7.1) was demonstrated to provide a valid comparison between data collected on differing X-ray spectroscopic apparatus.

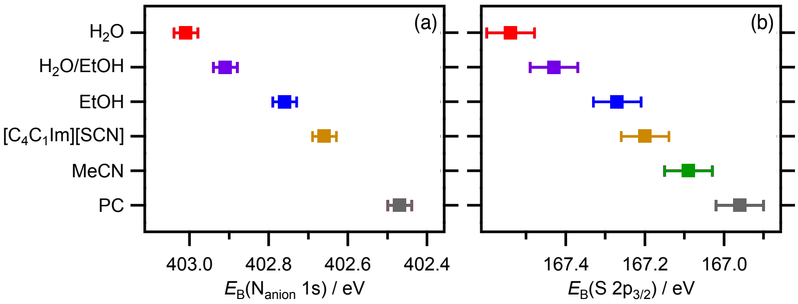

Figure 3.3. E_B against solvent category plots for ($[C_4C_1Im][SCN]$)(solvent), where solvent = H_2O (red), H_2O/EtOH (purple), EtOH (blue), MeCN (green), PC (grey), and for pure $[C_4C_1Im][SCN]$ (orange): (a) $E_B(N_{anion}\ 1s)$ against solvent. (b) $E_B(S\ 2p_{3/2})$ against solvent. All XP spectra for 0.5 M solutions ($[C_4C_1Im][SCN]$)(solvent) were measured at $h\nu$ = 700.0 eV; pure $[C_4C_1Im][SCN]$ XP spectra were measured at $h\nu$ = 1486.6 eV. All values were charge referenced using the methods detailed in Section 2.7.1.

An investigation into preferential solvation effects was carried out through the measurement of 0.5 M ($[C_4C_1Im][SCN]$)(H_2O/EtOH). Both $E_B(N_{anion}\ 1s)$ and $E_B(S\ 2p_{3/2})$ values for 0.5 M ($[C_4C_1Im][SCN]$)(H_2O/EtOH) were shown to be between measurements of each separate solvent, 0.5 M ($[C_4C_1Im][SCN]$)(H_2O) and 0.5 M ($[C_4C_1Im][SCN]$)(EtOH), with a slight bias towards E_B values for 0.5 M ($[C_4C_1Im][SCN]$)(H_2O). This result may suggest a minor preferential solvation of $[C_4C_1Im][SCN]$ by H_2O rather than EtOH. However, the strength of preferential solvation of the anion within the mixture was not strong, suggesting each solvent had an almost equal interaction with the anionic components.[7] This conclusion agrees with literature findings, which showed addition of H_2O to a non-aqueous solution to slightly affect the solute electronic structure, however not as greatly as changing the solvent completely.[23] Variation in photoelectron peak FWHM are commonly used to give an indication as to the number of electronic environments for a specific atom contribute to the observed photoelectron peak, which may differ depending on the number of differently bonded solvent molecules. However, anionic peak FWHM for 0.5 M

([C_4C_1Im][SCN])(H_2O/EtOH) was lower than constituent mono-solvent solutions, yielding no indication of preferential solvation by either H_2O or EtOH solvent molecules (Table 3.3).

The photoelectron peak area and FWHM ratios for measured peaks within the N 1s NRXP spectra, (N_{cation} 1s/N_{anion} 1s), and the S 2p NRXP spectra, (S $2p_{3/2}$/S $2p_{1/2}$), were compared for all possible samples (Table 3.3.). The values used to calculate area ratio reflected the total intensity of electrons within the measurement, due to reported peaks being the sole photoelectron peaks within each region. Therefore, area ratios presented in Table 3.3. were to be considered percentage atomic concentration measurements. Hence, small changes in experimental conditions did not influence relative comparisons between samples.

Table 3.3. Experimental area and FWHM ratios of (N_{cation} 1s/N_{anion} 1s) and (S $2p_{3/2}$/S $2p_{1/2}$) recorded by NRXPS for 0.5 M ([C_4C_1Im][SCN])(solvent), where solvent = H_2O, H_2O/EtOH, EtOH, MeCN, PC, and for pure [C_4C_1Im][SCN]. All spectra for 0.5 M ([C_4C_1Im][SCN])(solvent) were measured at *hν* = 700.0 eV; pure [C_4C_1Im][SCN] XP spectra were measured at *hν* = 1486.6 eV.

	(N_{cation} 1s / N_{anion} 1s)		(S $2p_{3/2}$ / S $2p_{1/2}$)	
	Area	FWHM	Area	FWHM
0.5 M ([C_4C_1Im][SCN])(H_2O)	2.27	1.06	1.69	0.90
0.5 M ([C_4C_1Im][SCN])(H_2O/EtOH)	2.24	1.01	1.62	0.89
0.5 M ([C_4C_1Im][SCN])(EtOH)	2.15	1.07	1.67	0.88
[C_4C_1Im][SCN]	2.21	1.08	1.88	1.00
0.5 M ([C_4C_1Im][SCN])(MeCN)			1.90	1.00
0.5 M([C_4C_1Im][SCN])(PC)	2.04	1.14	1.82	0.94

The relationship between (N_{cation} 1s/N_{anion} 1s) area ratio and FWHM ratio was explored, with a very weak negative correlation (R^2 = 0.68) observed (Figure 3.4a), *i.e.*, a greater FWHM ratio resulted in a lesser area ratio. However, it was noted that the (N_{cation} 1s/N_{anion} 1s) FWHM ratio for all samples were very similar, with the possible exception of 0.5 M ([C_4C_1Im][SCN])(PC). The similarity of each FWHM ratio coupled with the weak correlation between area ratio and FWHM ratio meant there was not much to be gained from this comparison. The relationship between (S $2p_{3/2}$/S $2p_{1/2}$) area ratio and FWHM ratio was also considered, with a very strong positive correlation (R^2 = 0.92) observed (Figure 3.4d), *i.e.*, a greater FWHM ratio resulted in a greater area ratio. This was indicative of the intrinsic relationship between photoelectron peaks which arise due to spin orbit coupling effects.

Photoelectron peak area and FWHM ratios for measured peaks within the N 1s NRXP spectra and S 2p NRXP spectra were compared to $E_B(N_{anion}$ 1s) and E_B(S $2p_{3/2}$), respectively (Figures 3.4b, 3.4c, 3.4d, and 3.4f). The relationship between $E_B(N_{anion}$ 1s) and (N_{cation} 1s/N_{anion} 1s) area ratio yielded a relatively strong positive correlation ($R^2 = 0.81$, Figure 3.4b), *i.e.*, a greater area ratio resulted in a greater $E_B(N_{anion}$ 1s). However, the relationship between $E_B(N_{anion}$ 1s) and (N_{cation} 1s/N_{anion} 1s) FWHM ratio yielded a relatively weak negative correlation ($R^2 = 0.69$, Figure 3.4c), *i.e.*, a greater FWHM ratio resulted in a lesser $E_B(N_{anion}$ 1s). As all measurements were carried out at the same *hν* and therefore at the same probing depth, the measured percentage atomic concentration may be indicative of solute proximity to the surface within solution. For example, the N_{cation} area (representing the position of the cation) was greater than the N_{anion} area (representing the position of the anion) for ([C_4C_1Im][SCN])(H_2O) than ([C_4C_1Im][SCN])(PC), indicating that the cation was located closer to the surface while solvated by water (relative to the anion) than the cation solvated by PC. If this were to be true, the trend of solute proximity to the solution surface would follow: H_2O > H_2O/EtOH > [C_4C_1Im][SCN] > EtOH > PC. With the omission of pure [C_4C_1Im][SCN], which was measured using a different spectrometer and at a different photon energy, and therefore area and FWHM measurements may not be comparable due to a variation in photoionisation cross section, the trend in solute proximity to the solution surface followed that of E_B(anion). This seemed to suggest a surface effect contribution to measured E_B values; however, depth probe measurements disprove this theory (Figure 5.4). Hence, the reduction in N_{anion} area between 0.5 M ([C_4C_1Im][SCN])(H_2O) and 0.5 M ([C_4C_1Im][SCN])(PC) was considered a result of solvent-solute interaction.

In contrast to discussed trends between $E_B(N_{anion}$ 1s) and (N_{cation} 1s/N_{anion} 1s) area ratio and FWHM ratio, the relationship between E_B(S $2p_{3/2}$) and both (S $2p_{3/2}$/S $2p_{1/2}$) area ratio and FWHM ratio yielded very weak correlations, where $R^2 = 0.50$ and $R^2 = 0.32$, respectively (Figures 3.4d and 3.4f).

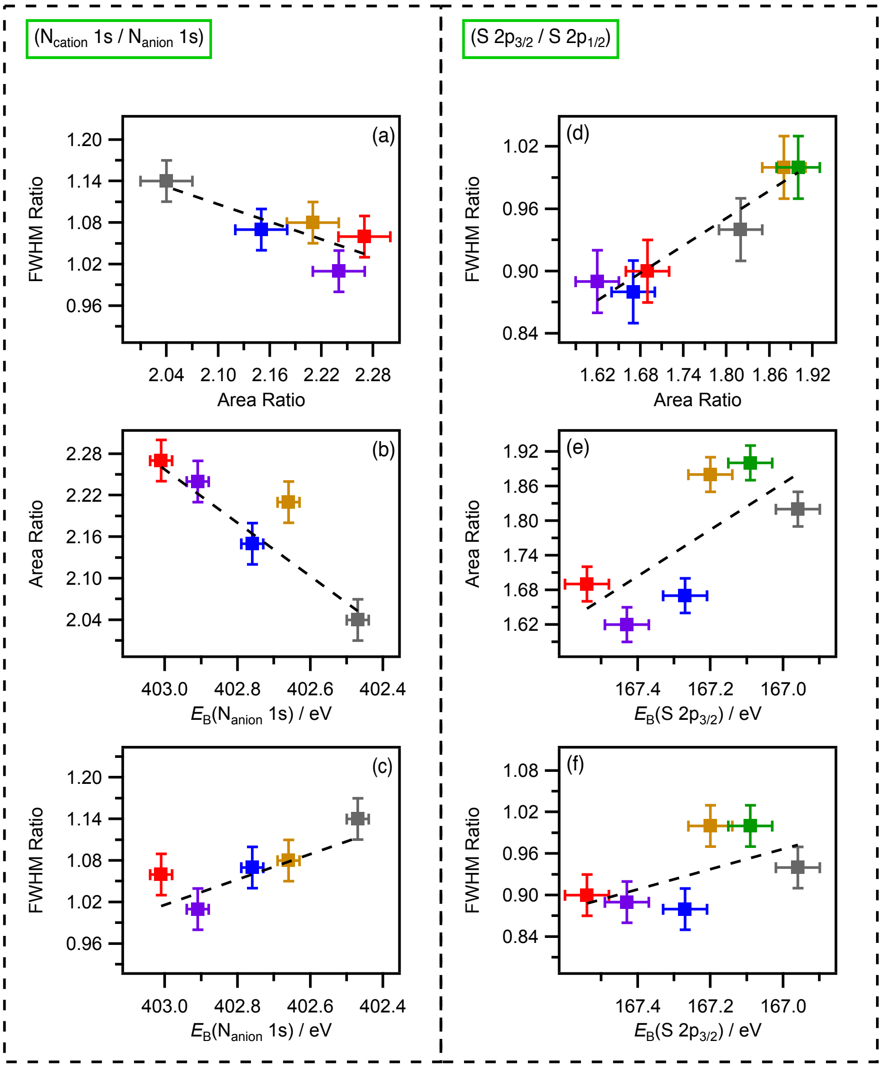

Figure 3.4. Comparisons between E_B(anion), area ratio, and FWHM ratio for (N$_{cation}$ 1s/N$_{anion}$ 1s) and (S 2p$_{3/2}$/S 2p$_{1/2}$): (a) FWHM ratio against area ratio for (N$_{cation}$ 1s/N$_{anion}$ 1s), linear trend line with R^2 = 0.68. (b) Area ratio against E_B(N$_{anion}$ 1s) for (N$_{cation}$ 1s/N$_{anion}$ 1s), linear trend line with R^2 = 0.81. (c) FWHM ratio against E_B(N$_{anion}$ 1s) for (N$_{cation}$ 1s/N$_{anion}$ 1s), linear trend line with R^2 = 0.69. (d) FWHM ratio against area ratio for (S 2p$_{3/2}$/S 2p$_{1/2}$), linear trend line with R^2 = 0.92. (e) Area ratio against E_B(N$_{anion}$ 1s) for (S 2p$_{3/2}$/S 2p$_{1/2}$), linear trend line with R^2 = 0.50. (f) FWHM ratio against E_B(N$_{anion}$ 1s) for (S 2p$_{3/2}$/S 2p$_{1/2}$), linear trend line with R^2 = 0.32.

The OCO and OVS energies for 0.5 M (K[SCN])(H_2O) and 0.5 M (K[SCN])(PC) were measured by NRXPS (Figure 3.5). N 1s NRXP spectra showed one photoelectron peak due to a single N$_{anion}$ electronic environment on [SCN]$^-$ anion, and no nitrogen atoms present in neither the cation nor the solvent (Figure 3.5a). E_B(N$_{anion}$ 1s) was shown to be greater for 0.5 M (K[SCN])(H_2O) than 0.5 M (K[SCN])(PC) (Table 3.4). Valence NRXP spectra was used to probe the E_B(HOVS$_{anion}$), which contained contributions from the N 2p and S 2p OVSs (Figure 3.5b).[20] E_B(HOVS$_{anion}$) was also shown to be greater for 0.5 M (K[SCN])(H_2O) than 0.5 M (K[SCN])(PC). S 2p NRXP spectra were shown to contain two photoelectron peaks with an area ratio of 2:1, due to spin orbit coupling of a single S 2p electronic environment on $[SCN]^-$ anion. E_B(S $2p_{3/2}$) was also shown to be greater for 0.5 M (K[SCN])(H_2O) than 0.5 M (K[SCN])(PC).

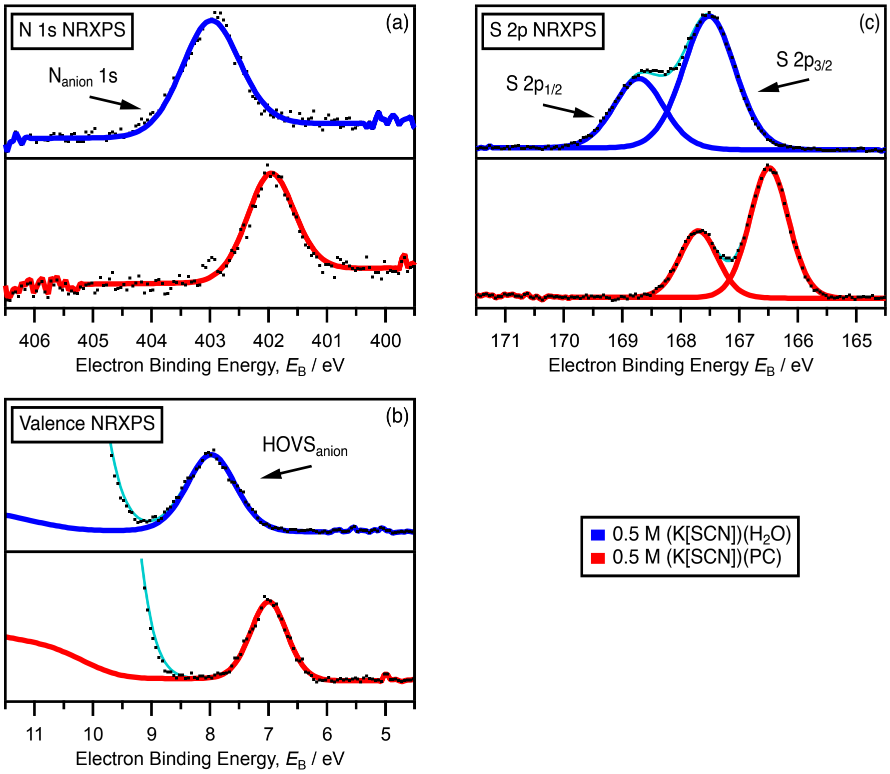

Figure 3.5. Core level and valence state NRXP spectra for 0.5 M (K[SCN])(H_2O) and 0.5 M (K[SCN])(PC): (a) N 1s. (b) S 2p. (c) Valence. (d) K 2p. All XP spectra for 0.5 M (K[SCN])(solvent) were measured at $h\nu$ = 700.0 eV. All XP spectra were charge referenced using the methods detailed in Section 2.7.2.

For all anionic component energies, ΔE_B(anion) was shown to be equal from 0.5 M (K[SCN])(H_2O) to 0.5 M (K[SCN])(PC) (Table 3.4). As the same phenomena was observed for ΔE_B(anion) from 0.5 M ([C_4C_1Im][SCN])(H_2O) to 0.5 M ([C_4C_1Im][SCN])(PC) (Table 3.2), this strengthened the suggestion that non-specific solvation effects resulted in the identical energetic shift of E_B(anion) components. More specifically, nitrogen and sulphur OCOs behave energetically alike with varying solvation environment.

Table 3.4. Experimental binding energies, E_B, recorded by NRXPS for 0.5 M (solute)(H_2O) and 0.5 M (solute)(PC), where solute = K[SCN] and Li[NTf_2]. All XP spectra for 0.5 M (K[SCN])(solvent) and 0.5 M (Li[NTf_2])(solvent) were measured at $h\nu$ = 700.0 eV. All values charge referenced using the methods detailed in Section 2.7.2. Values are reported to 2 decimal places.

	Electron binding energy / eV			
	N_{anion} 1s (± 0.03)	$HOVS_{anion}$ (± 0.03)	S $2p_{3/2}$ (± 0.06)	F_{anion} 1s (± 0.03)
0.5 M (K[SCN])(H_2O)	403.00	7.98	167.52	
0.5 M (K[SCN])(PC)	402.30	7.32	166.81	
0.5 M (Li[NTf_2])(H_2O)	404.33		173.89	693.66
0.5 M (Li[NTf_2])(PC)	403.78		173.29	693.29

The core and valence level energies for 0.5 M (Li[NTf_2])(H_2O) and 0.5 M (Li[NTf_2])(PC) were measured by NRXPS (Figure 3.6). N 1s NRXP spectra showed one photoelectron peak due to a single N_{anion} electronic environment on $[NTf_2]^-$ anion (Figure 3.6a). E_B(N_{anion} 1s) was shown to be greater for 0.5 M (Li[NTf_2])(H_2O) than 0.5 M (Li[NTf_2])(PC) (Table 3.4). F 1s NRXP spectra also showed one photoelectron peak due to a single F_{anion} electronic environment on $[NTf_2]^-$ anion (Figure 3.6b). E_B(F_{anion} 1s) appeared at greater energy for 0.5 M (Li[NTf_2])(H_2O) than 0.5 M (Li[NTf_2])(PC). S 2p NRXP spectra showed two photoelectron peaks with an area ratio of 2:1, due to spin orbit coupling of a single S 2p electronic environment on $[NTf_2]^-$ anion (Figure 3.6c). E_B(S $2p_{3/2}$) was also shown to be greater for 0.5 M (Li[NTf_2])(H_2O) than 0.5 M (Li[NTf_2])(PC).

The NRXP spectra of all anionic components of 0.5 M (Li[NTf_2])(H_2O) and 0.5 M (Li[NTf_2])(PC), E_B(N_{anion} 1s), E_B(S $2p_{3/2}$), and E_B(F_{anion} 1s), decreased from 0.5 M (Li[NTf_2])(H_2O) to 0.5 M (Li[NTf_2])(PC), which was to be expected from previous ([C_4C_1Im][SCN])(solvent) and (K[SCN])(solvent) measurements. However, while the trends in anionic component energies from H_2O to PC were in the same direction for [C_4C_1Im][SCN], K[SCN], and Li[NTf_2], they differed in both size of ΔE_B and absolute E_B position. E_B(N_{anion} 1s) and E_B(S $2p_{3/2}$) were shown to be greater for 0.5 M (Li[NTf_2])(H_2O) than for 0.5 M ([C_4C_1Im][SCN])(H_2O) and 0.5 M (K[SCN])(H_2O), matching reported E_B for corresponding anions within pure ILs.[24, 25] The difference in relative E_B positions indicated that both the nitrogen and sulphur atoms were less electron dense in the $[NTf_2]^-$ anion, due to the greater electron withdrawing ability of the neighbouring O_2CF_3 groups; whereas the nitrogen and sulphur atoms were more electron dense in the $[SCN]^-$ anion due to lesser electron withdrawing from far fewer neighbouring atoms (with lower electronegativities). ΔE_B(N_{anion} 1s) and ΔE_B(S $2p_{3/2}$) were also shown to be greater for K[SCN] than for Li[NTf_2], from solvation in H_2O to solvation in PC.

The difference in observed ΔE_B(anion) may be related to the hydrophilicity and hydrophobicity of each anion, where the $[NTf_2]^-$ anion was more hydrophobic than the $[SCN]^-$ anion due to its poorer ability as a hydrogen bond acceptor.[26] However, the cationic counterion has been shown to alter the hydrophobicity of the anion significantly, perhaps diminishing the rationale behind the conclusion of hydrophilicity and hydrophobicity of each anion.[27] Size and accessibility of the anionic atoms may impact upon anion-solvent interactions as the $[NTf_2]^-$ anion is far larger and bulkier than the $[SCN]^-$ anion. Therefore, each atom of $[SCN]^-$ is arguably more greatly exposed to interaction to the solvent molecules simultaneously.

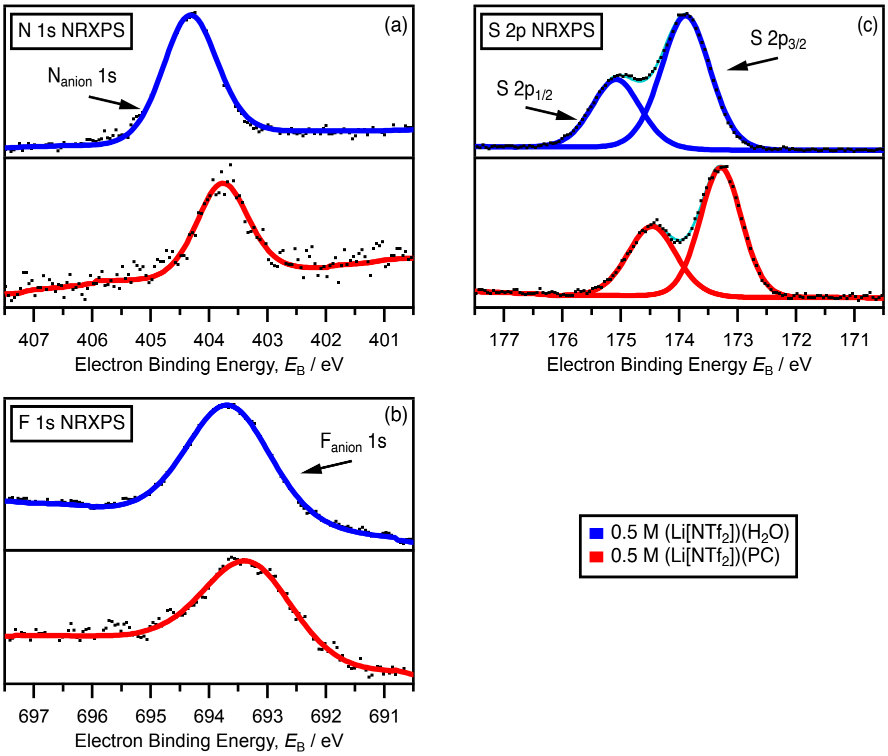

Figure 3.6. Core level and valence state NRXP spectra for 0.5 M $(Li[NTf_2])(H_2O)$ and 0.5 M $(Li[NTf_2])(PC)$: (a) N 1s, (b) F 1s, (c) S 2p, (d) Li 1s. All XP spectra for 0.5 M $(Li[NTf_2])$(solvent) were measured at $h\nu$ = 700.0 eV. All XP spectra were charge referenced using the methods detailed in Section 2.7.2.

All data in Tables 3.2 and 3.4 were charge referenced to an internal cationic reference, *i.e.*, $E_B(N_{cation}$ 1s), $E_B(K\ 2p_{3/2})$, or E_B(Li 1s). The reasoning for the choice of reference peak was due to the assumption that for samples studied at 0.5 M, cation ($[C_4C_1Im]^+$ or K^+) and anion ($[SCN]^-$ or $[NTf_2]^-$) species had no long- or short-range intermolecular interactions with one another. Therefore, when specifically relating to $[C_4C_1Im][SCN]$ and K[SCN], solvent-solute interactions probed were expected to affect E_B(anion) identically in either circumstance, as $[SCN]^-$ was assumed to be within an infinite dilution of molecular solvent. However, using the cation as a charge reference relied heavily upon the cation remaining chemically unreactive towards solvent molecules, with the sole interaction in solution taking place between anion and solvent molecules. As discussed above, ΔE_B(anion) from 0.5 M (K[SCN])(H_2O) to 0.5 M (K[SCN])(PC) was shown to be slightly greater than ΔE_B(anion) observed from 0.5 M ($[C_4C_1Im][SCN]$)(H_2O) to 0.5 M ($[C_4C_1Im][SCN]$)(PC). As $[C_4C_1Im]^+$ and K^+ differed significantly in both size and structure, the two cationic references did not provide comparable E_B(anion) values. Interestingly, E_B(anion) values matched identically for 0.5 M ($[C_4C_1Im][SCN]$)(H_2O) and 0.5 M (K[SCN])(H_2O) where E_B values were charge referenced to the absolute binding energies of pure H_2O. They also matched identically for 0.5 M ($[C_4C_1Im][SCN]$)(PC) and 0.5 M (K[SCN])(PC) where E_B values were charge referenced to the absolute binding energies of pure PC (Table 3.5). Therefore, when comparing E_B for different solutes in solvents, charge referencing to the pure solvent afforded the most reliable comparison. Nevertheless, it was deemed acceptable to charge reference using cationic peaks when comparing E_B values of solutes with the same cation, as E_B values have mutual relative energies; this is common practice used throughout IL XPS literature, where charge referencing to the E_B(C_{alkyl} 1s) is abundant.[24]

Through charge referencing photoemission energies to that of the pure solvent, ΔE_B(N_{anion} 1s) and ΔE_B(S $2p_{3/2}$) for 0.5 M ($Li[NTf_2]$)(H_2O) and 0.5 M ($Li[NTf_2]$)(PC) were shown to be equal, matching the observed relationship between ΔE_B(N_{anion} 1s) and ΔE_B(S $2p_{3/2}$) measured for $[C_4C_1Im][SCN]$ and K[SCN] from H_2O to PC (Table 3.5). Therefore, when varying solvation environment of a solute from H_2O to PC, E_B(N_{cation} 1s) and E_B(S $2p_{3/2}$) were shown to shift by the same value, although the magnitude of this value varied with solute identity. However, ΔE_B(F_{anion} 1s) was shown to be lower from 0.5 M ($Li[NTf_2]$)(H_2O) and 0.5 M ($Li[NTf_2]$)(PC) than either ΔE_B(N_{anion} 1s) or ΔE_B(S $2p_{3/2}$). The lesser ΔE_B(F_{anion} 1s) value may be a consequence of the non-reactivity of fluoride atoms within a C-F bond due to its strength, as in polytetrafluoroethylene.[28] Hence, ΔE_B(F_{anion} 1s) was smaller from 0.5 M ($Li[NTf_2]$)(H_2O) to 0.5 M ($Li[NTf_2]$)(PC) as there are little to no new interactions between fluorine atoms and the differing solvent molecules in solution.

Table 3.5. Experimental binding energies, E_B, recorded by NRXPS for 0.5 M (solute)(H_2O) and 0.5 M (solute)(PC), where solute = [C_4C_1Im][SCN] and K[SCN]. All XP spectra were measured at $h\nu$ = 700.0 eV. All values were charge referenced using the methods detailed in Section 2.7.2. All values are reported to 2 decimal places.

	Electron binding energy / eV			
	N_{anion} 1s (± 0.03)	$HOVS_{anion}$ (± 0.03)	S $2p_{3/2}$ (± 0.06)	F_{anion} 1s (± 0.03)
0.5 M ([C_4C_1Im][SCN])(H_2O)	403.01	8.04	167.54	
0.5 M ([C_4C_1Im][SCN])(PC)	402.00	6.99	166.49	
0.5 M (K[SCN])(H_2O)	402.99	7.97	167.52	
0.5 M (K[SCN])(PC)	401.97	6.99	166.49	
0.5 M (Li[NTf_2])(H_2O)	404.35		173.91	693.68
0.5 M (Li[NTf_2])(PC)	403.78		173.29	693.29

As energetic comparisons made throughout the remainder of this chapter solely feature solutes with the same cation ([C_4C_1Im]$^+$) and anion ([SCN]$^-$], it was deemed acceptable to discuss and compare measured E_B values relative to a fixed internal reference (E_B(N_{cation} 1s) = 406.75 eV).

3.3.2. HOVS and LUMO level shifts with varying solvent

The energies of the highest occupied valence states (HOVSs) and the lowest unoccupied molecular orbitals (LUMOs) of a system can be measured using a combination of valence NRXPS and XAS (Figure 3.7). The energy of the HOVS serves to yield information on the reactivity of key bonding OVSs within a system through donation of electron density (Lewis basicity), whereas the energy of the LUMO gives information as to how readily each component within solution accepts electron density (Lewis acidity).[18]

The HOVS was probed using valence NRXPS (Figure 3.7a). The identity of the $\text{HOVS}_{\text{anion}}$ for $[C_4C_1\text{Im}][\text{SCN}]$ was found to comprise contributions from the N_{anion} 2p and S_{anion} 2p OVSs.[20] The identity of the $\text{HOVS}_{\text{anion}}$ was shown to match in all solvents, demonstrated through the comparison of N 1s RXPS measurements (Figure 3.12b, Appendix Figure 8.15) and density functional theory calculations of the pure solvent.[29] Spectra were arranged in order of decreasing $E_{\text{B}}(\text{HOVS}_{\text{anion}})$ (top to bottom): H_2O > H_2O/EtOH > EtOH > MeCN > PC.

The LUMO was indirectly probed using XAS, which gave information on the energy of an electron transition from an occupied core orbital (OCO) to an UMO, $h\nu(\text{OCO} \rightarrow \text{UMO})$. By varying $h\nu$ it is possible to select for specific OCO → UMO transitions and therefore, XAS is considered an atom specific/selective technique.[20, 29] The N 1s edge (also known as the N K-edge) was probed and yielded two sharp peaks in the XA spectra for each sample of 0.5 M ($[C_4C_1\text{Im}][\text{SCN}]$)(solvent) measured (Appendix Figure 8.16). From the overall similar shape and close match in $h\nu$ of the 0.5 M ($[C_4C_1\text{Im}][\text{SCN}]$)(solvent) XA spectra to that of 0.5 M ($[C_4C_1\text{Im}][\text{SCN}]$)($H_2O$), it was concluded equally that for both transitions the excited electron originated from either the N_{anion} OCO ($h\nu$ = ~399.7 eV) or the N_{cation} OCO ($h\nu$ = ~402.1 eV), assigned to the N_{anion} 1s → π^* and N_{cation} 1s → π^* transitions respectively.[30] The final state of each transition resulted in the occupancy of the π^* UMO, as both the $[C_4C_1\text{Im}]^+$ cation and the $[\text{SCN}]^-$ anion contain π-systems (involving the nitrogen atoms), which have high absorption intensities due to a large absorption cross-section.[29] For samples of 0.5 M ($[C_4C_1\text{Im}][\text{SCN}]$)(solvent), where solvent = H_2O, EtOH, and PC, the ionic rather than solvent π^* UMOs were probed. However, for the solution of 0.5 M ($[C_4C_1\text{Im}][\text{SCN}]$)(MeCN), the solvent not only contained a nitrogen atom, but also contained a π-system about the nitrile group, causing the N 1s XA spectrum to be dominated by the solvent, as it did for the N 1s NRXPS region, (Appendix Figure 8.13). Therefore, the N 1s XA spectrum for 0.5 M ($[C_4C_1\text{Im}][\text{SCN}]$)(MeCN) was not shown. As the HOVS contains purely anionic components, the N_{anion} 1s → π^* transition was shown for clarity of comparison (Figure 3.7b). The identity of the $\mathrm{LUMO}_{\mathrm{anion}}$, $\mathrm{N}_{\mathrm{anion}}$ π^*, was measured to be constant, $h\nu$ = 399.7 ± 0.06 eV, for all solvents.

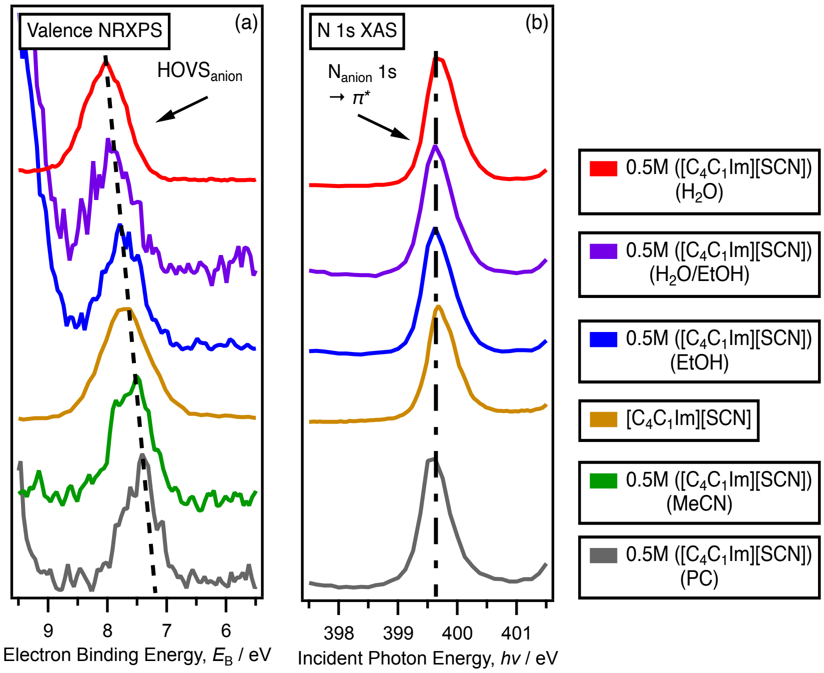

Figure 3.7. Valence NRXP and N 1s XA spectra for ([C_4C_1Im][SCN])(solvent), where solvent = H_2O (red), H_2O/EtOH (purple), EtOH (blue), MeCN (green), PC (grey), and for pure [C_4C_1Im][SCN] (orange): (a) Valence NRXP spectra. (b) N 1s XA spectra. Dashed lines are intended as a visual aid of the changes in E_B that occur with varying x_{IL}, where lines of the same type have the same gradient. All NRXP spectra for 0.5 M solutions ([C_4C_1Im][SCN])(solvent) were measured at $h\nu$ = 700.0 eV; pure [C_4C_1Im][SCN] NRXP spectra were measured at $h\nu$ = 1486.6 eV. Valence NRXP spectra were charge referenced using the methods detailed in Section 2.7.1.

Through comparison of anionic valence NRXPS E_B values it was shown that $E_B(\mathrm{HOVS}_{\mathrm{anion}})$ decreased monotonically from H_2O > H_2O/EtOH > EtOH > [C_4C_1Im][SCN] > MeCN > PC (Figure 3.8a). $\Delta E_B(\mathrm{HOVS}_{\mathrm{anion}})$ was shown to match observed $\Delta E_B(\mathrm{N}_{\mathrm{anion}}\ 1\mathrm{s})$ and $\Delta E_B(\mathrm{S}\ 2\mathrm{p}_{3/2})$ for ([C_4C_1Im][SCN])(solvent) compared to the same change in solvation environment (Figure 3.2). In contrast, $h\nu(\mathrm{N}_{\mathrm{anion}}\ 1\mathrm{s} \rightarrow \pi^*)$ was shown not to change outside the margin of experimental error with varying solvent (Figure 3.8b). Any observed deviation for $h\nu(\mathrm{N}_{\mathrm{anion}}\ 1\mathrm{s} \rightarrow \pi^*)$ could demonstrate variation in the ionic conductivity of the solution.[31] As $h\nu(\mathrm{N}_{\mathrm{anion}}\ 1\mathrm{s} \rightarrow \pi^*)$ represents an energetic transition, no observed change in transition energy, $\Delta h\nu(\mathrm{N}_{\mathrm{anion}}\ 1\mathrm{s} \rightarrow \pi^*) = 0$, indicated that the energy gap between the OCO and the UMO was consistent across all solvents. As $E_B(\mathrm{N}_{\mathrm{anion}}\ 1\mathrm{s})$ was shown to decrease in the order H_2O > H_2O/EtOH > EtOH > [C_4C_1Im][SCN] > MeCN > PC (Figures 3.2a and 3.3a, Table 3.2), it was deduced that the corresponding anionic nitrogen π^* UMO, $\mathrm{N}_{\mathrm{anion}}$ π^*, trended in the same direction by the same magnitude, due to the consistency of $h\nu(\mathrm{N_{anion}}\ 1s \rightarrow \pi^*)$ observed with varying solvent. Furthermore, as $\Delta E_B(\mathrm{N_{anion}}\ 1s)$ and $\Delta E_B(\mathrm{HOVS_{anion}})$ were shown to trend very similarly (Figure 3.3a and Figure 3.8a, respectively), $\Delta E_B(\mathrm{HOVS_{anion}})$ and $\Delta E_B(\mathrm{LUMO_{anion}})$ were also shown to be equal (within experimental error) with varying solvent. Consequently, the ease of removal of an electron from the $[SCN]^-$ $\mathrm{HOVS_{anion}}$, but difficulty of addition of an electron to the $[SCN]^-$ $\mathrm{LUMO_{anion}}$, increased following solvation of $[C_4C_1Im][SCN]$ in H_2O < H_2O/EtOH < EtOH < $[C_4C_1Im][SCN]$ < MeCN < PC. Additionally, the very similar energetic shift for $E_B(\mathrm{HOVS_{anion}})$ and $E_B(\mathrm{LUMO_{anion}})$ with varying solvation environment indicated that the energy gap between the $\mathrm{LUMO_{anion}}$ and $\mathrm{LUMO_{cation}}$ increased from H_2O < H_2O/EtOH < EtOH < $[C_4C_1Im][SCN]$ < MeCN < PC. Similarly, the energy gap between the $\mathrm{HOVS_{anion}}$ and $\mathrm{HOVS_{cation}}$ increased from H_2O < H_2O/EtOH < EtOH < $[C_4C_1Im][SCN]$ < MeCN < PC. Consequently, through varying the electrolyte solvent, HOVS/LUMO energies can be tailored to favour specific requirements (*e.g.,* a greater or lesser ability to undergo redox reactions), much like varying x_{IL} (Chapter 5). Therefore, absolute control of the HOVS/LUMO energies may be obtained through choice of both the solvent and the concentration of electrolyte in solution, in tandem.

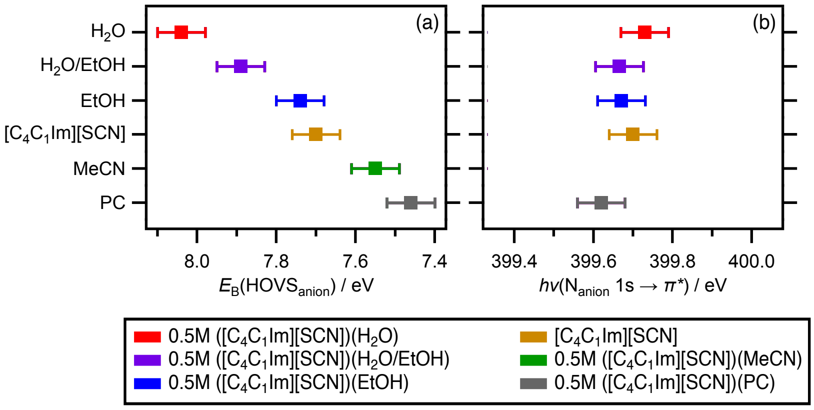

Figure 3.8. E_B against solvent category plots for $([C_4C_1Im][SCN])$(solvent), where solvent = H_2O (red), H_2O/EtOH (purple), EtOH (blue), MeCN (green), PC (grey), and for pure $[C_4C_1Im][SCN]$ (orange): (a) $E_B(\mathrm{HOVS_{anion}})$ against solvent where samples of 0.5 M $([C_4C_1Im][SCN])$(solvent) were measured at $h\nu$ = 700.0 eV; $[C_4C_1Im][SCN]$ was measured at $h\nu$ = 1486.6 eV. (b) $h\nu(\mathrm{N_{anion}}\ 1s \rightarrow \pi^*)$ against solvent. $E_B(\mathrm{HOVS_{anion}})$ values were charge referenced using the methods detailed in Section 2.7.1. $h\nu(\mathrm{N_{anion}}\ 1s \rightarrow \pi^*)$ values were not subject to charge referencing methods.

3.3.3. Relationship between E_B(HOVS) and solvent polarity descriptors

Empirical polarity scales, such as the Kamlet-Taft (KT) scale, are widely applied to give insight into the strength and ability of interaction a solvent may display in solution.[32] Common solvent polarity scale descriptors for each solvent used to produce a 0.5 M solution with [C_4C_1Im][SCN], and pure [C_4C_1Im][SCN], were collated (Table 3.6). KT descriptors for pure solvents include hydrogen bond donor ability, α_{solv}, hydrogen bond acceptor ability, β_{solv}, and dipolarity-polarisability, π^*_{solv}.[7, 9-12] Gutmann descriptors for pure solvents include electron acceptor number, AN_{solv}, and electron donor number, DN_{solv}.[15, 16] Catalán descriptors for pure solvents include solvent acidity, SA_{solv}, solvent basicity, SB_{solv}, and solvent dipolarity-polarisability, SPP_{solv}.[13, 33] All solvent polarity scales provide a measure of both solvent Lewis acidity and solvent Lewis basicity.[17]

Table 3.6. KT, Gutmann, and Catalán solvent polarity scale descriptor values for H_2O, H_2O/EtOH, EtOH, MeCN, PC, and for pure [C_4C_1Im][SCN]. Valence NRXP spectra used to obtain $E_B(\text{HOVS}_{\text{anion}})$ for samples of 0.5 M ([C_4C_1Im][SCN])(solvent) were measured at $h\nu$ = 700.0 eV, whereas valence NRXP spectra for pure [C_4C_1Im][SCN] was measured at $h\nu$ = 1486.6 eV. All spectra were charge referenced using the methods detailed in Section 2.7.1. KT, and Catalán polarity scale descriptor values were obtained from reference [7] unless otherwise indicated. All values are reported to 2 decimal places.

	H_2O	H_2O/EtOH	EtOH	[C_4C_1Im][SCN]	MeCN	PC
$E_B(\text{HOVS}_{\text{anion}})$ / eV	8.04	7.89	7.75	7.70	7.55	7.46
α_{solv}	1.17	0.96[a]	0.86	0.43[b]	0.19	0
β_{solv}	0.47	0.65[a]	0.75	0.71[b]	0.40	0.40
π^*_{solv}	1.09	0.79[a]	0.54	1.06[b]	0.66	0.83
AN^c_{solv}	54.80		37.90		18.90	18.30
DN^c_{solv}	18.0		19.20		14.10	15.10
SA_{solv}	1.062		0.400		0.044	0.106
SB_{solv}	0.025		0.658		0.286	0.895
SPP_{solv}	0.962		0.853		0.895	0.930

[a] Obtained from reference [34].

[b] Obtained from reference [35, 36].

[c] Obtained from reference [37].

A linear correlation between $E_B(\text{HOVS}_{\text{anion}})$ and α_{solv}, AN_{solv}, and SA_{solv}, which are primary descriptors of solvent Lewis acidity, were observed (Figures 3.9a, 3.9d, 3.9f). Out of the three primary descriptors of solvent Lewis acidity, AN_{solv} was shown to reflect the trends in $E_B(\text{HOVS}_{\text{anion}})$

closest, where a single linear line of best fit (R^2 = 0.95) could be drawn through all data points. Moreover, linear trends between E_B(HOVS$_{anion}$) and α_{solv} and SA_{solv} were also strong, where a single linear line of best fit passed within experimental error of each datapoint (both R^2 = 0.92). As both α_{solv} and AN_{solv} trended linearly with E_B(HOVS$_{anion}$), suggesting that the solvent-solute interactions were purely hydrogen bonding in nature would be invalid. Instead, it can be proposed that the solvent acted as a Lewis acid and the anion acted as a Lewis base.

A poor correlation between E_B(HOVS$_{anion}$) and β_{solv}, DN_{solv}, and SB_{solv}, which are primary descriptors of solvent Lewis basicity, was observed for all three solvent polarity scales (Figures 3.9b, 3.9e, 3.9g). E_B(HOVS$_{anion}$) position was therefore not shown to be significantly influenced by the ability of the solvent to act as an electron donor. Hence, solvent Lewis acidity, and not Lewis basicity, was shown to be the dominant factor in determining relative E_B(HOVS$_{anion}$) position.

Protogenic solvents (H_2O and EtOH) were shown to have high values of α_{solv}, AN_{solv}, and SA_{solv}, where H_2O was the most Lewis acidic solvent measured in this work. The structure of H_2O permit a high level of Lewis acidity, through an electronegative oxygen atom, which is covalently bonded to two electron poor hydrogen atoms. Both hydrogen atoms are capable of being 'donated' and accepting electron density from the anionic nitrogen and sulphur atoms of [SCN]$^-$, thus reducing anionic atomic charge and resulting in a greater E_B(HOVS$_{anion}$) relative to pure [C_4C_1Im][SCN]. The second strongest Lewis acidic solvent utilised within this work was EtOH. Analogous to H_2O, EtOH also contains an electronegative oxygen atom, which is covalently bonded to a single electron poor hydrogen atom. Therefore, in contrast to H_2O, only a single hydrogen atom is available for 'donation' and acceptance of electron density from the anionic nitrogen and sulphur atoms of [SCN]$^-$. Consequently, EtOH is less Lewis acidic than H_2O, resulting in a lesser E_B(HOVS$_{anion}$) value than [C_4C_1Im][SCN] solvated by H_2O, but greater than pure [C_4C_1Im][SCN]. The 1:1 molar solution of H_2O/EtOH yielded E_B(HOVS$_{anion}$) and α_{solv} values between the values of each of its constituent solvents, indicating that the influence of H_2O and EtOH on the anion was approximately equal. It was no great surprise that H_2O, EtOH, and a mixture of the two showed a similar relationship between E_B(HOVS$_{anion}$) and Lewis acidity as liquid alcohols resemble water analogues (replacing one hydrogen atom with an alkyl group) and can therefore similarly accommodate excess electrons within cavities of their hydrogen-bonding network.[38] Subsequently, values of AN_{solv} and SA_{solv} for a 1:1 molar solution of H_2O/EtOH can be predicted from the relationship between E_B(HOVS$_{anion}$) and α_{solv} to be ~46 and ~0.72, respectively.

Non-protogenic solvents ([C_4C_1Im][SCN], MeCN, and PC) were shown to have lower values of α_{solv}, AN_{solv}, and SA_{solv}, and can therefore be described as poorer Lewis acids than the protogenic solvents measured in this work. [C_4C_1Im][SCN] has previously been shown to participate in hydrogen bonding at the C^2 position (Figure 3.1a) with the anionic nitrogen and sulphur atoms of [SCN]$^-$.[39] The hydrogen atom at the C^2 position is more electron rich than the hydrogen atoms located on H_2O as carbon is more electropositive than oxygen. Therefore, the hydrogen atom at the C^2 position is less able to accept excess electron density from the anionic nitrogen and sulphur atoms of [SCN]$^-$, thus resulting in a lesser measured E_B(HOVS$_{\mathrm{anion}}$) than for the protogenic solvents, H_2O and EtOH. In contrast to solvents already discussed, the remaining non-protogenic solvents (MeCN and PC) were shown to act to make [C_4C_1Im][SCN] more reactive, *i.e.*, reducing E_B(HOVS$_{\mathrm{anion}}$) for ([C_4C_1Im][SCN])(MeCN) and ([C_4C_1Im][SCN])(PC) below that of pure [C_4C_1Im][SCN]. This was due to MeCN and PC being poorer Lewis acids than pure [C_4C_1Im][SCN], as evidenced by their very low values of α_{solv}, AN_{solv}, and SA_{solv}. Furthermore, a far greater number of solvent molecules than ions (Table 3.1) resulted in solvent-ion interactions which far outnumbered ion-ion interactions in solution. Coupled with the poor Lewis acidity of MeCN and PC, the overwhelming prevalence of MeCN and PC molecules in solution resulted in a lesser E_B(HOVS$_{\mathrm{anion}}$) than pure [C_4C_1Im][SCN], *i.e.*, the solvent molecules prevented the cation from stabilising the anion.

Solvent polarity scales require an internal probe, such as Reichardt's dye,[14] to assess the strength of solvent-solute interactions, as discussed in Chapter 1. The need for an internal probe creates several issues:

1. The measured solvent may react with the internal probe to create a new chemical species, preventing the measurement of solvatochromic effect of the solvent on the probe.
2. Values of acidity/basicity may be probe-dependent, resulting in the need for normalisation across polarity scales.[40]

Core level spectroscopy has the advantage of lacking the requirement of an internal probe species. Therefore, an XPS basicity scale based upon E_B(HOVS$_{\mathrm{anion}}$) position would be universal, without the need to normalise across polarity scales. In addition, data gained through the nature of core level spectroscopy measurements can reveal key information for individual electronic environments such as oxidation state and number of contributing components.

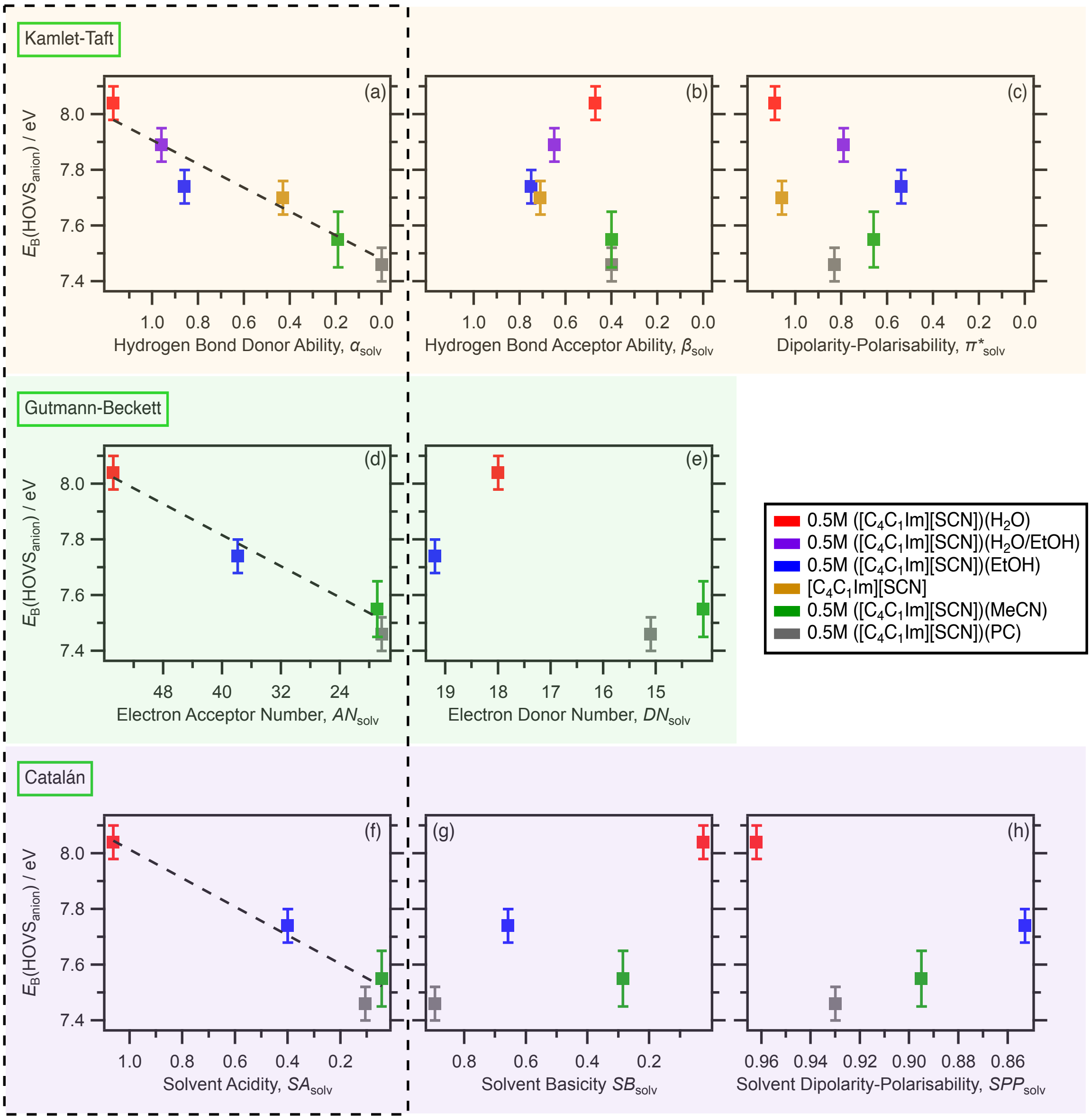

Figure 3.9. $E_B(HOVS_{anion})$ against Kamlet-Taft, Gutmann, and Catalán polarity scale descriptors for ([C$_4$C$_1$Im][SCN])(solvent), where solvent = H_2O (red), H_2O/EtOH (purple), EtOH (blue), MeCN (green), PC (grey), and for pure [C$_4$C$_1$Im][SCN] (orange): (a) $E_B(HOVS_{anion})$ against pure solvent hydrogen bond donor, α_{solv}; R^2 of the dashed line = 0.92. (b) $E_B(HOVS_{anion})$ against pure solvent hydrogen bond acceptor, β_{solv}. (c) $E_B(HOVS_{anion})$ against pure solvent dipolarity-polarisability, π^*_{solv}. (d) $E_B(HOVS_{anion})$ against pure solvent electron acceptor number, AN_{solv}; R^2 of the dashed line = 0.95. (e) $E_B(HOVS_{anion})$ against pure solvent electron donor number, DN_{solv}. (f) $E_B(HOVS_{anion})$ against pure solvent acidity, SA_{solv}; R^2 of the dashed line = 0.92. (g) $E_B(HOVS_{anion})$ against pure solvent basicity, SB_{solv}. (h) $E_B(HOVS_{anion})$ against pure solvent dipolarity-polarisability, SPP_{solv}. $E_B(HOVS_{anion})$ values were charge referenced using the methods detailed in Section 2.7.1.

3.3.4. Experimental energy level diagram

Using data collected from a combination of complementary X-ray spectroscopic methods allowed for the construction of an energy level diagram showing core, valence, and unoccupied energies (Figure 3.10). This enabled easier visual comparison and a clearer overview of the energetic trends within the system. NRXPS gave a direct value for both, $E_B(\mathrm{N_{anion}}\ 1s)$ and $E_B(\mathrm{HOVS_{anion}})$, whereas XAS yielded a transition energy. As $E_B(\mathrm{N_{anion}}\ 1s)$ was known from NRXPS measurements, $E_B(\mathrm{N_{anion}}\ 1s)$ minus $h\nu$ ($\mathrm{N_{anion}}$ 1s → π^*) resulted in $E_B(\mathrm{N_{anion}}\,\pi^*)$.

$\Delta E_B(\mathrm{N_{anion}}\ 1s)$, $\Delta E_B(\mathrm{HOVS_{anion}})$, and $\Delta E_B(\mathrm{N_{anion}}\ \pi^*)$ were shown to be equal as a function of solvent. A similar relationship exists with respect to the concentration, which will be discussed in Chapter 5. The anionic charge density distribution on the solvent molecules is expected to be the determining factor for the measured equal energy shift as a function of solvent. Whether the resultant charge density distribution occurred due to hydrogen bonding, ion-dipole interactions, or any other specific interaction is currently unknown. All atoms in the $[\mathrm{SCN}]^-$ anion were affected by interaction with the most prominent hotspots on the functional group interaction profiles for each solvent molecule.[41] The observation that $E_B(\mathrm{HOVS_{anion}})$, $\mathrm{HOVS_{anion}}$, and $E_B(\mathrm{N_{anion}}\ \pi^*)$, $\mathrm{LUMO_{anion}}$, shifted equally by the same size and direction is of particular importance to the design of electrolyte solutions for functional applications. The apparent importance of both the electrolyte concentration, and the solvent identity in determining the HOVS and LUMO energy levels were therefore both shown to relate to non-specific solvation effects, but to varying degrees:

1. The variation in HOVS and LUMO energy levels through varying the solvent identity was strongly, but not purely, influenced by non-specific solvation effects. This was evidenced through the same observed monotonic energetic shift of all component OCO and OVSs; however, a strong correlation between solvent Lewis acidic polarity scale descriptors, which relate to specific solvation effects, and E_B(anion), and a lack of correlation between E_B(anion) and the relative permittivity of solution suggests that multiple factors must be considered (Chapter 3).
2. The deviation in HOVS and LUMO energy levels through varying electrolyte concentration was dominated by non-specific solvation effects. This was evidenced through a monotonic shift of all component OCO and OVS, and a strong correlation between E_B(anion) and the relative permittivity of solution (Chapter 5).

Anionic photoelectron peak energies for 0.5 M ([C_4C_1Im][SCN])(H_2O/EtOH) were measured at values between those of 0.5 M ([C_4C_1Im][SCN])(H_2O) and 0.5 M ([C_4C_1Im][SCN])(EtOH), which suggested a lack of preferential solvation effects.[7] This effect was shown to extend to HOVS$_{\text{anion}}$ and LUMO$_{\text{anion}}$ energies as E_B(N$_{\text{anion}}$ 1s), E_B(HOVS$_{\text{anion}}$), and E_B(N$_{\text{anion}}$ π*) for 0.5 M ([C_4C_1Im][SCN])(H_2O/EtOH) were also measured between those of 0.5 M ([C_4C_1Im][SCN])(H_2O) and 0.5 M ([C_4C_1Im][SCN])(EtOH). Therefore, preferential solvation affected neither OCOs nor UMOs in a H_2O/EtOH solvent mixture. However, preferential solvation effects may come into play in a situation where two different solvents interact with ions through differing functional groups, *e.g.*, hydroxyl and nitrile.[7, 42] Through knowledge that OCOs, OVSs, and UMOs trend energetically in the same direction by the same magnitude, energy level predictions of an ionic system are possible given a single OCO or OVS measurement. For example, if ([C_4C_1Im][SCN])(MeCN) were added to Figure 3.10 E_B(anion) values would be expected between those of pure [C_4C_1Im][SCN] and ([C_4C_1Im][SCN])(PC), with E_B(N$_{\text{anion}}$ 1s) = 402.6 eV and E_B(N$_{\text{anion}}$ π*) = 2.9 eV, judging from the measurable value of E_B(HOVS$_{\text{anion}}$) (Figure 3.8a, Table 3.6).

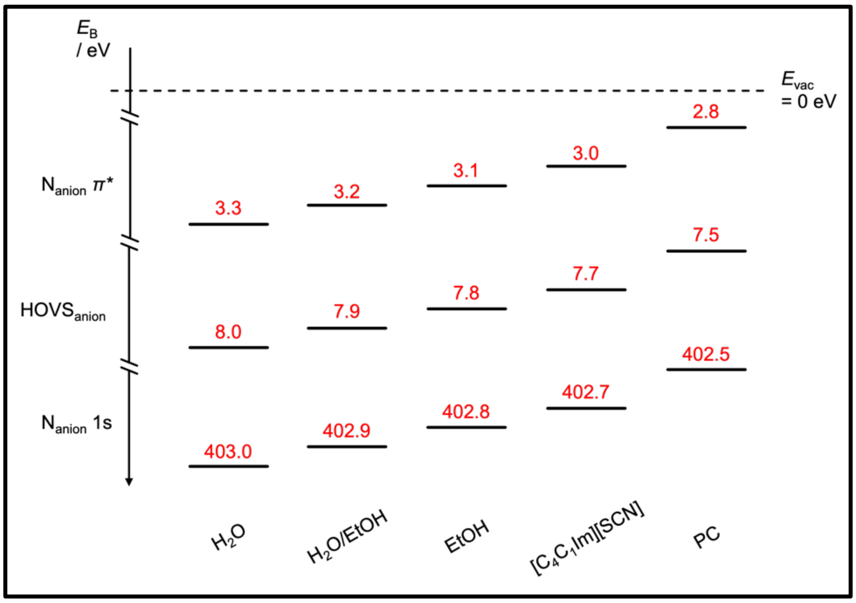

Figure 3.10. Energy level diagram for ([C_4C_1Im][SCN])(solvent), where solvent = H_2O, H_2O/EtOH, EtOH, PC, and for pure [C_4C_1Im][SCN]. E_B(N$_{\text{anion}}$ 1s) and E_B(HOVS$_{\text{anion}}$) values were charge referenced using the methods detailed in Section 2.7.1 (NRXPS) and Section 2.7.3 (RXPS). E_B(N$_{\text{anion}}$ π*) values were calculated from E_B(N$_{\text{anion}}$ 1s) minus $h\nu$(N$_{\text{anion}}$ 1s → π*). All E_B values are reported to 1 decimal place.

3.3.5. Solvation effect of H_2O versus PC on $[C_4C_1Im][SCN]$

Relative to pure $[C_4C_1Im][SCN]$, ΔE_B(anion) was shown to shift both positively and negatively for samples of ($[C_4C_1Im][SCN]$)(solvent) depending upon the molecular solvation environment. The most significant examples of this phenomena occur for $[C_4C_1Im][SCN]$ solvated by H_2O, yielding a positive 0.3 eV E_B shift, and solvated by PC, yielding a negative 0.2 eV E_B shift (Figure 3.11). The reasoning behind the ability of H_2O to increase $E_B(HOVS_{anion})$, and the contrasting ability of PC to decrease $E_B(HOVS_{anion})$, has been shown to correlate strongly with solvent acidity descriptors demonstrated through comparison to various solvent polarity scales. Although solvation of $[C_4C_1Im][SCN]$ by H_2O and PC acted to shift ΔE_B(anion) in opposite directions relative to pure $[C_4C_1Im][SCN]$, $E_B(N_{anion}\ 1s)$, $E_B(S\ 2p_{3/2})$, and $E_B(HOVS_{anion})$ in either molecular solvent were observed to shift in the same direction by the same magnitude (Figures 3.11a-3.11c, respectively). The energetic relationship for all components of E_B(anion) demonstrated the similarity of interaction between the solute and each solvent, regardless of whether $[C_4C_1Im][SCN]$ was solvated by H_2O or solvated by PC. Therefore, non-specific solvation effects were shown to dictate anionic OCO and OVS energetic positions irrespective of the solvent present for all molecular solvents measured throughout this chapter, for both protogenic and non-protogenic classifications.

The surprising ability of PC (and MeCN) to reduce anionic OCO and UMO energies below that of pure $[C_4C_1Im][SCN]$ further demonstrates the powerful ability of solvent choice to allow for tunability of the energies of solvated species to meet functional requirements. Observing strong, linear relationships between solvent acidity and OVS energies can also provide a useful tool for understanding and predicting the energetic behaviour of future solvent-solute interaction. This advance can aid in more targeted experimentation, which would have otherwise been time-consuming and costly.

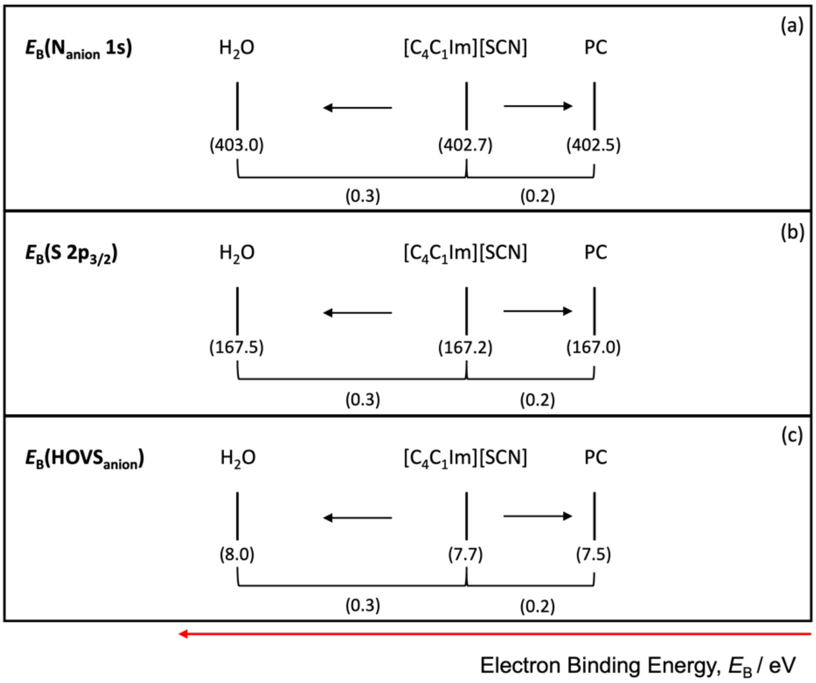

Figure 3.11. E_B shift of 0.5 M ([C$_4$C$_1$Im][SCN])(solvent), where solvent = H_2O and PC, relative to pure [C$_4$C$_1$Im][SCN]: (a) E_B(N$_{anion}$ 1s). (b) E_B(S 2p$_{3/2}$). (c) E_B(HOVS$_{anion}$). All XP spectra for 0.5 M ([C$_4$C$_1$Im][SCN])(H_2O) and 0.5 M ([C$_4$C$_1$Im][SCN])(PC) were measured at $h\nu$ = 700.0 eV. Charge referencing methods are detailed in Section 2.7.1. All E_B values are reported to 1 decimal place.

The measurement of an N 1s valence RXP heat map allowed for the comparison of nitrogen anionic and nitrogen cationic contributions to the valence states for both, 0.5 M [(C$_4$C$_1$Im][SCN])(H_2O) and 0.5 M [(C$_4$C$_1$Im][SCN])(PC) (Figure 3.12a). A horizontal trace at $h\nu$ = 402.1 eV yielded N$_{cation}$ 1s valence RXP contributions, indicated by peaks labelled 1 and 2, where peak 1 showed the N$_{cation}$ 2p contribution to the valence states (HOVS$_{cation}$, Figure 3.12b). A horizontal trace at $h\nu$ = 399.7 eV yielded N$_{anion}$ 1s valence RXP contributions, indicated by peaks 3 to 7, where peak 3 shows the position of the N$_{anion}$ 2p contribution to the valence states (HOVS$_{anion}$, Figure 3.12c). A visual comparison of the peak E_B separation and relative peak intensity of valence RXP spectra for 0.5 M ([C$_4$C$_1$Im][SCN])(H_2O) and 0.5 M ([C$_4$C$_1$Im][SCN])(PC) at the cationic edge, $h\nu$ = 402.1 eV, showed a good overall match (Figure 3.12b). This match continued when comparing valence RXP spectra for the same samples at the anionic edge, $h\nu$ = 399.7 eV, which was far more complex in shape than that of the cationic edge (Figure 3.12c). The similar relative peak intensity and peak E_B separation in the valence RXP spectra, which was shown to be sensitive to changes in covalent intermolecular bonding,[43] indicated no change in bonding type with changing solvent, *i.e.*, both solvents acted as Lewis acids towards the anionic OVSs.[29] This provided further evidence, additional to the identical shifts in all components of E_B(anion), that although H_2O and PC acted to shift E_B(anion) for

($[C_4C_1Im][SCN]$)(solvent) in opposite directions, solvent-solute interactions were similar enough to remain undetected by valence RXPS.

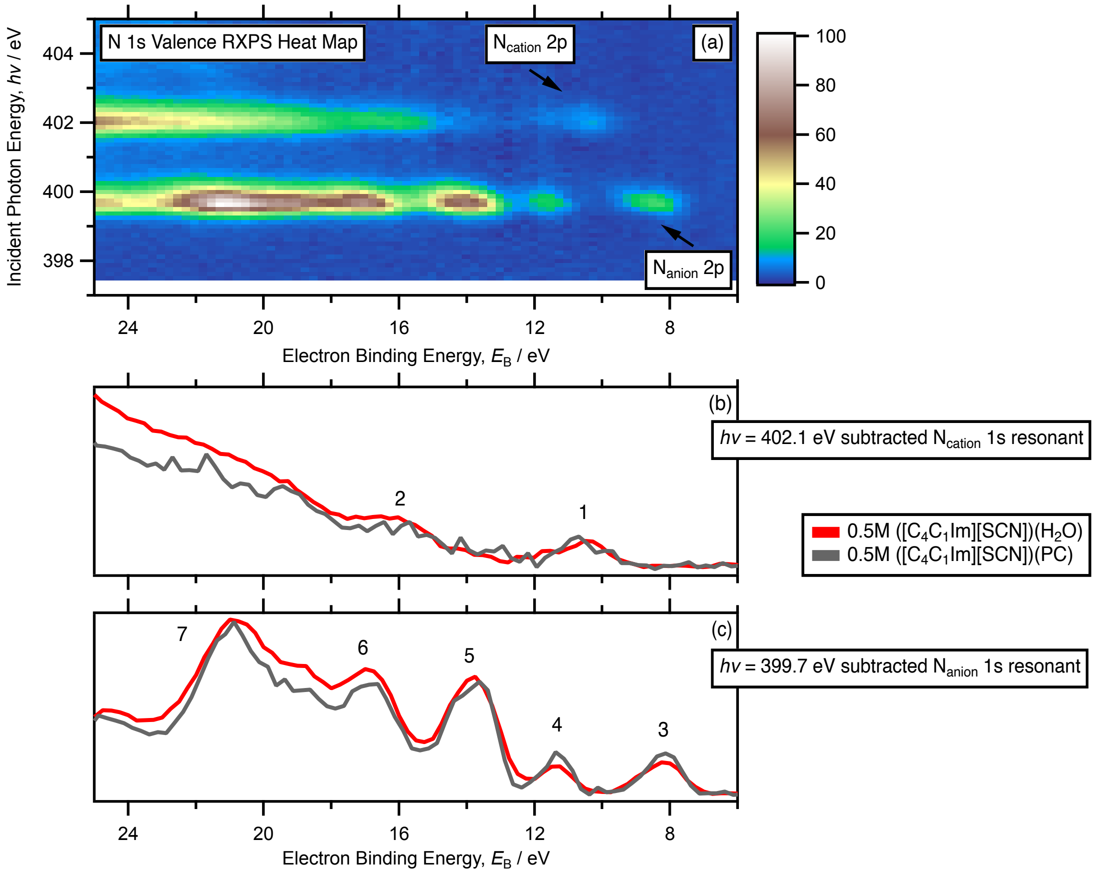

Figure 3.12. N 1s valence RXP heat map and valence RXP spectra for ($[C_4C_1Im][SCN]$)(solvent), where solvent = H_2O (red), and PC (grey): (a) N 1s RXPS heat map. (b) $h\nu$ = 402.1 eV subtracted N_{cation} 1s resonant. (c) $h\nu$ = 399.7 eV subtracted N_{anion} 1s resonant. The NRXPS contributions were subtracted using the procedure detailed in Section 8.2. No charge referencing method was applied as spectra were visually shifted to enable a comparative overlay.

3.4. Conclusion and future work

Throughout this chapter, the effect of varying the molecular solvent identity within samples of 0.5 M ($[C_4C_1Im][SCN]$)(solvent) on the energies of key non-bonding OCO and bonding OVSs was explored. These were further compared to measurements of pure $[C_4C_1Im][SCN]$. To determine the effect of varying solvation environment on different solute species, core and valence NRXP spectra for 0.5 M (K[SCN])(H_2O), 0.5 M (K[SCN])(PC), 0.5 M ($Li[NTf_2]$)(H_2O), and 0.5 M ($Li[NTf_2]$)(PC) were also studied. The comparison between E_B values of many solvent and solute species allowed for a comprehensive investigation of the effect of varying solvent identity on solute electronic structure.

For every 0.5 M ($[C_4C_1Im][SCN]$)(solvent) sample studied, E_B(anion), *i.e.*, E_B(N_{anion} 1s), E_B(S $2p_{3/2}$), and E_B($HOVS_{anion}$), was shown to shift energetically in the same direction by the same magnitude with varying solvent. Likewise, E_B(anion) from 0.5 M (K[SCN])(H_2O) to 0.5 M (K[SCN])(PC) was shown to shift energetically in the same direction as from 0.5 M ($[C_4C_1Im][SCN]$)(H_2O) to 0.5 M ($[C_4C_1Im][SCN]$)(PC). A comparison of measured E_B(anion) values for $[SCN]^-$ containing solutes ($[C_4C_1Im][SCN]$ and K[SCN]) revealed identical energies, giving credence to the rationale that at 0.5 M, cation and anion species have limited long- or short-range intermolecular interactions. ΔE_B(N_{anion} 1s), ΔE_B(S $2p_{3/2}$), and ΔE_B(F_{anion} 1s) from 0.5 M ($Li[NTf_2]$)(H_2O) to 0.5 M ($Li[NTf_2]$)(PC) were also shown to shift in the same direction by the same magnitude, although significantly less than those of $[SCN]^-$ containing species. The observed trend in OCO and OVS energies, categorised under E_B(anion), with varying solvent identity were concluded to occur due to non-specific solvation effects, as the E_B of all OCO and OVSs for a single solute shifted in the same direction by the same magnitude (except for unreactive fluorine OCOs which shifted in the same direction but to a lesser degree). The area ratio and FWHM ratio of the (N_{cation} 1s / N_{anion} 1s) and (S $2p_{3/2}$ / S $2p_{1/2}$) photoemission peaks were compared for all 0.5 M ($[C_4C_1Im][SCN]$)(solvent) combinations. Of most significance, the (N_{cation} 1s / N_{anion} 1s) area ratio was shown to follow the same trend as E_B(anion), where 0.5 M ($[C_4C_1Im][SCN]$)(H_2O) showed the largest area ratio, and 0.5 M ($[C_4C_1Im][SCN]$)(PC) showed the smallest. This was concluded to be a result of solvent-solute interaction, rather than surface vs bulk effects.

Two different charge referencing procedures were demonstrated, where it was shown that valid E_B comparisons were permitted between two significantly different solutes in solvent, (solute)(solvent), when peak energies were charge referenced to pure solvent photoemission peaks. Furthermore, relative solute peak references were permitted for E_B comparisons between two solutes with at least one identical component, *e.g.*, [C_4C_1Im][SCN] and [C_4C_1Im][NTf_2].

Measured E_B(anion) values for 0.5 M ([C_4C_1Im][SCN])(solvent) were shown to possess a clear relationship with the solvent polarity scale descriptors: α_{solv}, AN_{solv}, and SA_{solv}, with the strongest correlation observed between E_B(anion) and AN_{solv}. These descriptors are most indicative of solvent Lewis acidity, strongly suggesting the solvent acts as a Lewis acid towards solute species. The trend between E_B(anion) and Lewis acidic solvent polarity descriptors was applicable to both protogenic and non-protogenic solvents, showing the measured solvent-solute interactions to be electron pair accepting (solvent) and electron pair donating (solute) in nature. Although acting to shift E_B(anion) energetically in different directions relative to pure [C_4C_1Im][SCN], and therefore most likely to display different bonding interaction to the solute, H_2O and PC (protogenic and non-protogenic, respectively) were shown to participate in intermolecular bonding with [C_4C_1Im][SCN] almost identically to one another through visual comparison of valence RXP spectra. Therefore, AN_{solv} is shown to be a useful predictor of E_B(anion).

In future, it is important to test the hypotheses made within this chapter, to instil confidence within the use of Lewis acidic solvent polarity descriptors as a metric for predicting E_B(anion) within a solute-solvent system. For example, the solvent, triethylphosphate (TEP), has the same measured value of α_{solv} as PC but a different value of β_{solv}. Therefore, E_B(anion) shifts for [C_4C_1Im][SCN] solvated by TEP are expected to be similar or equal to those measured for [C_4C_1Im][SCN] solvated by PC. If E_B(anion) values were measured to be similar, this would support the conclusion that solvent polarity descriptors indicative of Lewis acidity were the greatest predictors of E_B(anion). However, if E_B(anion) shifts were to differ significantly from that of PC, other factors (β_{solv}, DN_{solv}, SB_{solv}, π^*_{solv}, and SPP_{solv}) may play a greater role than expected and should be further investigated. Additionally, solutes where the cation has been found to contain the lowest E_B within a system may be measured to probe $E_B(\mathrm{HOVS_{cation}})$ trends with Lewis basic solvent polarity descriptors, *i.e.*, β_{solv}, DN_{solv} and SB_{solv}.

3.5. References

1. A. D. McNaught and A. Wilkinson, *IUPAC Compendium of Chemical Terminology*, Blackwell Science, Oxford, 2nd edn., 1997.
2. J. Clayden, N. Greeves, S. Warren and P. Wothers, *Journal*, 2001.
3. W. J. Ong, L. L. Tan, S. P. Chai, S. T. Yong and A. R. Mohamed, *Nanoscale*, 2014, **6**, 1946-2008.
4. J. C. Hamill, J. Schwartz and Y. L. Loo, *ACS Energy Lett.*, 2018, **3**, 92-97.
5. L. Crowhurst, R. Falcone, N. L. Lancaster, V. Llopis-Mestre and T. Welton, *Journal of Organic Chemistry*, 2006, **71**, 8847-8853.
6. C. Reichardt, *Org. Process Res. Dev.*, 2007, **11**, 105-113.
7. C. Reichardt and T. Welton, *Solvents and Solvent Effects in Organic Chemistry*, Wiley, Weinheim, 4th edn., 2011.
8. J. P. Ceron-Carrasco, D. Jacquemin, C. Laurence, A. Planchat, C. Reichardt and K. Sraidi, *Journal of Physical Organic Chemistry*, 2014, **27**, 512-518.
9. M. J. Kamlet and R. W. Taft, *Journal of the American Chemical Society*, 1976, **98**, 377-383.
10. R. W. Taft and M. J. Kamlet, *Journal of the American Chemical Society*, 1976, **98**, 2886-2894.
11. M. J. Kamlet, J. L. Abboud and R. W. Taft, *Journal of the American Chemical Society*, 1977, **99**, 6027-6038.
12. R. W. Taft, J. L. M. Abboud and M. J. Kamlet, *Journal of the American Chemical Society*, 1981, **103**, 1080-1086.
13. J. Catalán, *The Journal of Physical Chemistry B*, 2009, **113**, 5951-5960.
14. C. Reichardt, *Chemical Reviews*, 1994, **94**, 2319-2358.
15. U. Mayer, V. Gutmann and W. Gerger, *Monatshefte Fur Chemie*, 1975, **106**, 1235-1257.
16. V. Gutmann, *The Donor-Acceptor Approach to Molecular Interactions*, Plenum Press, New York, 1978.
17. S. Spange, C. Lienert, N. Friebe and K. Schreiter, *Physical Chemistry Chemical Physics*, 2020, **22**, 9954-9966.
18. K. Fukui, *Science*, 1982, **218**, 747-754.
19. R. Seidel, M. N. Pohl, H. Ali, B. Winter and E. F. Aziz, *Review of Scientific Instruments*, 2017, **88**, 073107.
20. R. M. Fogarty, R. G. Palgrave, R. A. Bourne, K. Handrup, I. J. Villar-Garcia, D. J. Payne, P. A. Hunt and K. R. J. Lovelock, *Physical Chemistry Chemical Physics*, 2019, **21**, 18893-18910.

21. K. A. Perrine, M. H. C. Van Spyk, A. M. Margarella, B. Winter, M. Faubel, H. Bluhm and J. C. Hemminger, *J. Phys. Chem. C*, 2014, **118**, 29378-29388.
22. J. C. Vickerman and I. S. Gilmore, eds., *Surface Analysis: The Principal Techniques*, John Wiley & Sons, Chichester, 2009.
23. M. El Kazzi, I. Czekaj, E. J. Berg, P. Novak and M. A. Brown, *Topics in Catalysis*, 2016, **59**, 628-634.
24. I. J. Villar-Garcia, E. F. Smith, A. W. Taylor, F. L. Qiu, K. R. J. Lovelock, R. G. Jones and P. Licence, *Physical Chemistry Chemical Physics*, 2011, **13**, 2797-2808.
25. R. M. Fogarty, R. P. Matthews, C. R. Ashworth, A. Brandt-Talbot, R. G. Palgrave, R. A. Bourne, T. V. Hoogerstraete, P. A. Hunt and K. R. J. Lovelock, *Journal of Chemical Physics*, 2018, **148**, 193817.
26. N. Delgado-Mellado, J. García, F. Rodríguez and R. D. Rogers, *ChemPlusChem*, 2019, **84**, 872-881.
27. J. G. McDaniel and A. Verma, *Journal of Physical Chemistry B*, 2019, **123**, 5343-5356.
28. G. J. Puts, P. Crouse and B. M. Ameduri, *Chemical Reviews*, 2019, **119**, 1763-1805.
29. J. M. Seymour, E. Gousseva, A. Large, G. Held, D. Hein, G. Wartner, W. Quevedo, R. Seidel, C. Kolbeck, C. J. Clarke, R. Fogarty, R. Bourne, R. Bennett, R. Palgrave, P. A. Hunt and K. R. J. Lovelock, *Faraday Discussions*, 2022.
30. R. M. Fogarty, R. P. Matthews, M. T. Clough, C. R. Ashworth, A. Brandt-Talbot, P. J. Corbett, R. G. Palgrave, R. A. Bourne, T. W. Chamberlain, T. Vander Hoogerstraete, P. B. J. Thompson, P. A. Hunt, N. A. Besley and K. R. J. Lovelock, *Physical Chemistry Chemical Physics*, 2017, **19**, 31156-31167.
31. D. Ketenoglu, G. Spiekermann, M. Harder, E. Oz, C. Koz, M. C. Yagci, E. Yilmaz, Z. Yin, C. J. Sahle, B. Detlefs and H. Yavaş, *J. Synchrot. Radiat.*, 2018, **25**, 537-542.
32. N. Weiß, C. H. Schmidt, G. Thielemann, E. Heid, C. Schröder and S. Spange, *Physical Chemistry Chemical Physics*, 2021, **23**, 1616-1626.
33. J. Catalan, J. Gomez, A. Couto and J. Laynez, *Journal of the American Chemical Society*, 1990, **112**, 1678-1681.
34. Y. Marcus, *J. Chem. Soc.-Perkin Trans. 2*, 1994, 1751-1758.
35. R. Lungwitz, M. Friedrich, W. Linert and S. Spange, *New Journal of Chemistry*, 2008, **32**, 1493-1499.
36. R. Lungwitz, V. Strehmel and S. Spange, *New Journal of Chemistry*, 2010, **34**, 1135-1140.
37. W. R. Fawcett, *Journal of Physical Chemistry*, 1993, **97**, 9540-9546.
38. S. Thurmer, T. Shinno and T. Suzuki, *Journal of Physical Chemistry A*, 2021, **125**, 2492-2503.

39. P. A. Hunt, C. R. Ashworth and R. P. Matthews, *Chemical Society Reviews*, 2015, **44**, 1257-1288.

40. L. C. Brown, J. M. Hogg and M. Swadzba-Kwasny, *Top. Curr. Chem.*, 2017, **375**, 40.

41. M. D. Driver, M. J. Williamson, Joanne L. Cook and C. A. Hunter, *Chem. Sci.*, 2020, **11**, 4456-4466.

42. C. Yan, X. Huang, J. Chen, H. Guo and H. Shao, *Electroanalysis*, 2019, **31**, 2339-2346.

43. U. Hergenhahn, A. Rudel, K. Maier, A. M. Bradshaw, R. F. Fink and A. T. Wen, *Chemical Physics*, 2003, **289**, 57-67.

Chapter 4

Influence of anion identity and concentration on electronic structure

Abstract

Ions in solution feature across numerous branches of chemistry. Therefore, it is highly important to understand, and be able to make confident predictions, of the general behaviour of each component within solution. Interactions between each component within an electrolyte solution are closely related to their electronic structure. However, the fundamental properties that give rise to electronic structure variation of ionic species within molecular solution have not been well explored. In this chapter, an in-depth investigation into the influence of varying anionic identity and concentration on the electronic structure of all components within a liquid phase electrolyte system is reported. A combination of X-ray spectroscopic techniques were used to determine the energetic position of the occupied core orbitals and occupied valence states that make up the electronic structure of both, ions in H_2O and ions in ions, with the general formulae: 0.5 M ($[C_4C_1Im][anion]$)(H_2O) and $[C_nC_1Im][anion]$, respectively. Anionic occupied core orbital energy shifts, from aqueous solution to pure ionic liquid, were shown to be influenced by non-specific solvation effects, with the notable exception of fluorine core level energies. The magnitude of energy shifts due to solvation effects were shown to correlate with hydrogen bond donor/acceptor abilities of the anion, as well as the absolute electronegativity of the probed atomic species. In aqueous solution (0.5 M), anionic identity was shown not to have a significant effect on cationic electronic structure, enabling the direct influence of H_2O as a pseudo-counterion to the cation to be probed. The ability of H_2O to influence cationic electronic structure was shown to be greater than expected when compared to anionic species of a similar hydrogen bond acceptor ability. A lack of influence of anionic identity in aqueous solution on the solvent electronic structure was also shown, both covalently and electrostatically.

4.1. Introduction

The use of ions in solution features within vast topics of scientific discussion. Specific cation-anion interactions of various combinations are utilised within a range of different scientific applications: For example, in biology Na^+ and Cl^- ions are synergistically involved in the regulation of osmotic pressure, fluid levels and pH balance within the human body.[1, 2] In chemistry, redox catalysis[3] and battery systems[4] utilise cation-anion interactions to drive each relative process. Specific cation-anion combinations result in the unique physico-chemical properties displayed within a system, related to the electronic structure of each component.[5] Efforts to interpret relationships between cationic and anionic species in pure ionic liquids (ILs), which enable the observed physical and chemical properties have been vast.[5-14] However, for ions in aqueous solution the effect of the solvation environment on the electronic structure of ions is poorly understood.[15] The use of molecular solvent (MS), within which most of the above processes take place, can significantly alter the extent of cation-anion interactions in solution through enhanced solvent-solute interactions. Solvent polarity scales have been used to give insight into the strength and ability of interaction a solvent may display in solution.[16, 17] Additionally, Pearson absolute scales can be used to describe the interactions of both, individual atoms and molecular species.[18]

It is concurrent knowledge that ionic solutes are affected by solvent molecules, and interactions between ions and solvent molecules are closely related to their electronic structure.[5, 10, 19] However, an extensive study into the effect of varying anionic identity within extreme solvation environments (concentrated ions in ions compared to dilute ions in molecular solvent) on the electronic structure of each component in solution has never been carried out; especially using an information rich technique such as X-ray spectroscopy. Both, the non-bonding occupied core orbitals (OCOs) and the bonding occupied valence state (OVS) energies of an ionic system have been measured to gain a greater understanding of the electronic structure changes for each component within solution, in an effort to bridge the gap in knowledge between ion-ion interactions and ion-solvent interactions.

In this chapter, non-resonant X-ray photoelectron spectroscopy (NRXPS), X-ray absorption spectroscopy (XAS), and valence resonant XPS (RXPS) were used to measure samples of 0.5 M ($[C_4C_1Im][anion]$)(H_2O) and pure $[C_nC_1Im][anion]$, where anion = $[SCN]^-$, $[N(CN)_2]^-$, $[BF_4]^-$, $[TfO]^-$, Cl^-, and I^- (structures of each species used in this chapter shown in Figure 4.1). Anions were chosen with a range of size and basicity, according to Kamlet-Taft solvent polarity scales. Complementary X-ray spectroscopic techniques were used to determine the influence of anionic identity on the electronic structure of all liquid phase ions. Anionic and atomic physico-chemical properties were then related to the observed energetic trends. The role of H_2O as a pseudo-counterion was compared to common anionic species. The effect of varying the electrolyte concentration at both extremes of the concentration range, for all six samples with differing anion identities was investigated. Finally, the influence of anionic identity on the valence RXP spectra was explored and used to demonstrate the extent to which the anion influences cation-solvent interactions in aqueous solution.

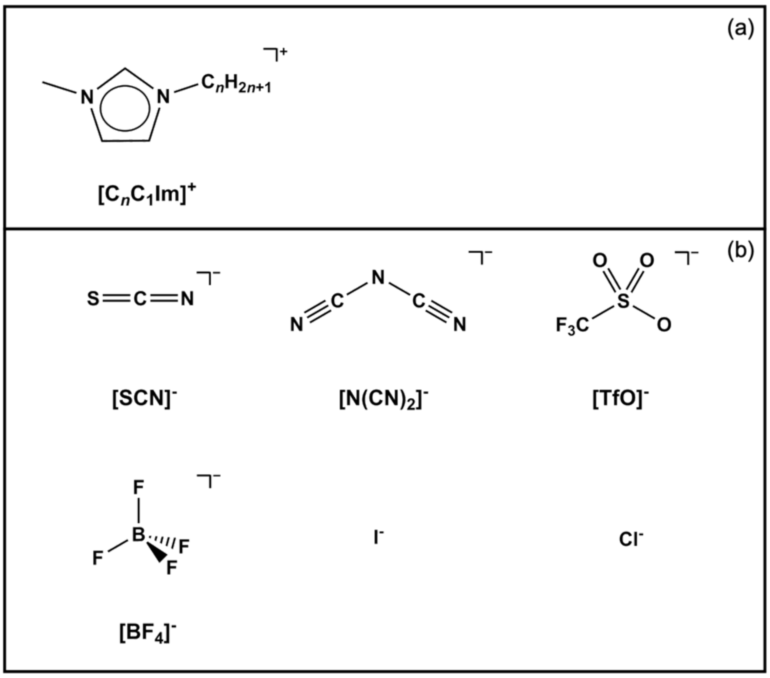

Figure 4.1. Names and structures of key ions and solvents studied within Chapter 4: (a) $[C_nC_1Im]^+$ cation studied within the current work, where n = 4 and 8. (b) Anions.

4.2. Spectroscopic methods

4.2.1. Sample preparation

Highly demineralised H_2O (conductivity ~0.2 $\mu S\ cm^{-1}$) was used within the formation of each aqueous solutions. All ILs were purchased from Iolitec, with no further purification or drying prior to use. ILs were weighed and mixed with a corresponding mass of H_2O to achieve a concentration of 0.5 M (Appendix Table 8.1). The corresponding mole fraction, concentration, and IL:solvent ratio for each sample was shown in Table 4.1.

Table 4.1. The six solutions and six pure ILs studied within Chapter 4. Concentrations were calculated using parameters listed in Appendix Tables 8.1 to 8.3.

	x_{IL}	x_{solv}	conc. IL/ M	conc. H_2O / M	IL:H_2O
$[C_4C_1Im][SCN]$	1	0	5.4	0	1:0
$([C_4C_1Im][SCN])(H_2O)$	0.01	0.99	0.5	50.3	1:99
$[C_4C_1Im][N(CN)_2]$	1	0	5.2	0	1:0
$([C_4C_1Im][N(CN)_2])(H_2O)$	0.01	0.99	0.5	50.1	1:99
$[C_4C_1Im][BF_4]$	1	0	5.75	0	1:0
$([C_4C_1Im][BF_4])(H_2O)$	0.01	0.99	0.5	50.6	1:99
$[C_8C_1Im]Cl$	1	0	4.4	0	1:0
$([C_4C_1Im]Cl)(H_2O)$	0.01	0.99	0.5	51.0	1:99
$[C_6C_1Im]I$	1	0	5.1	0	1:0
$([C_4C_1Im]I)(H_2O)$	0.01	0.99	0.5	50.5	1:99
$[C_4C_1Im][TfO]$	1	0	4.5	0	1:0
$([C_4C_1Im][TfO])(H_2O)$	0.01	0.99	0.5	49.4	1:99

4.2.2. Synchrotron XPS apparatus

The measurement of each 0.5 M $([C_nC_1Im][anion])(H_2O)$ solution, where anion = $[SCN]^-$, $[N(CN)_2]^-$, $[BF_4]^-$, $[TfO]^-$, Cl^-, and I^-, was performed on the U49/2-PGM 1 beamline with SOL^{3}PES end-station[20] at BESSY II (Germany) using liquid-jet apparatus.[20] XP and RXP spectra were acquired using a Scienta Omicron R4000 HIPP-2 hemispherical electron analyser. The analyser angle was 90.0° horizontal to the plane of polarised light.

4.2.3. Laboratory XPS apparatus

Laboratory–based XPS for each pure [C_nC_1Im][anion] IL, where anion = [SCN]$^-$, [N(CN)$_2$]$^-$, [BF_4]$^-$, [TfO]$^-$, Cl^-, and I^-, was carried out using a Thermo K–alpha spectrometer utilising Al Kα radiation ($h\nu$ = 1486.6 eV), as detailed in reference [21].

4.3. Results and discussion

4.3.1. Changes in anionic atomic charge with varying x_{IL} and anion identity

The anionic core level NRXP spectra were measured for $[C_nC_1Im]^+$ based ILs with differing anions: $[TfO]^-$, Cl^-, I^-, $[N(CN)_2]^-$, $[SCN]^-$, and $[BF_4]^-$ (Figure 4.2).

N_{anion} 1s NRXP spectra were measured for samples containing $[SCN]^-$ and $[N(CN)_2]^-$, which allowed for the comparison of the energetic behaviour between two different cyano anions, from dilute ions in molecular solvent to concentrated electrolyte (Figure 4.2a). For both 0.5 M $([C_4C_1Im][SCN])(H_2O)$ and pure $[C_4C_1Im][SCN]$, $[SCN]^-$ showed a single photoemission peak in the N_{anion} NRXP spectra due to a single nitrogen electronic environment on the anion. $E_B(N_{anion}\ 1s)$ was shown to be lower for pure $[C_4C_1Im][SCN]$ than that of 0.5 M $([C_4C_1Im][SCN])(H_2O)$. For both 0.5 M $([C_4C_1Im][N(CN)_2])(H_2O)$ and pure $[C_4C_1Im][N(CN)_2]$, $[N(CN)_2]^-$ showed two photoemission peaks in the N_{anion} NRXP spectra due to the presence of two nitrogen electronic environments on the anion, $[N^*(CN)_2]^-$ and $[N(CN^*)_2]^-$. Differing nitrogen environments within the anion, $[N(CN^*)_2]^-$ and $[N^*(CN)_2]^-$, were expected in a 2:1 area ratio respectively, which led to their assignment at lesser and greater $E_B(N_{anion}\ 1s)$, respectively. Both $E_B(N_{anion}\ 1s, [N^*(CN)_2]^-)$ and $E_B(N_{anion}\ 1s, [N(CN^*)_2]^-)$ were shown to be lower for pure $[C_4C_1Im][N(CN)_2]$ than that of 0.5 M $([C_4C_1Im][N(CN)_2])(H_2O)$. Therefore, for either cyano anion, $[SCN]^-$ or $[N(CN)_2]^-$, $E_B(\text{anion})$ decreased from aqueous solution to pure IL.

B 1s NRXP spectra were measured for $[C_4C_1Im][BF_4]$, within an aqueous solution, and for the pure IL (Figure 4.2b). For both 0.5 M $([C_4C_1Im][BF_4])(H_2O)$ and pure $[C_4C_1Im][BF_4]$, $[BF_4]^-$ showed a single photoemission peak in the B 1s NRXP spectra due to a single boron electronic environment on the anion. $E_B(B\ 1s)$ for pure $[C_4C_1Im][BF_4]$ was measured at lesser energy than that of 0.5 M $([C_4C_1Im][BF_4])(H_2O)$.

F 1s NRXP spectra were measured for two different samples containing fluorine atoms within their anion, $[C_4C_1Im][BF_4]$ and $[C_4C_1Im][TfO]$, both in aqueous solution and for the pure IL (Figure 4.2c). For either sample at either IL concentration, the F 1s NRXP spectra showed a single photoemission peak due to a single fluorine electronic environment on the anion. $E_B(F\ 1s)$ for pure $[C_4C_1Im][BF_4]$ was measured at lesser energy than that of 0.5 M $([C_4C_1Im][BF_4])(H_2O)$. Likewise, $E_B(F\ 1s)$ for pure $[C_4C_1Im][TfO]$ was measured at lesser energy than that of 0.5 M $([C_4C_1Im][TfO])(H_2O)$. Therefore,

E_B(F 1s) for fluorine atoms within two different anions, $[BF_4]^-$ and $[TfO]^-$, was shown to decrease in energy from aqueous solution to pure IL.

S 2p NRXP spectra were measured for two different samples containing sulphur atoms within their anion, $[C_4C_1Im][SCN]$ and $[C_4C_1Im][TfO]$ (Figure 4.2d). The S 2p NRXP spectra for either sample, within both aqueous solution and pure IL, showed a doublet of photoemission peaks due to a single sulphur electronic environment on the anion, which yielded two peaks due to spin orbit coupling. E_B(S $2p_{3/2}$) for pure $[C_4C_1Im][SCN]$ was measured at lesser energy than that of 0.5 M $([C_4C_1Im][SCN])(H_2O)$. Similarly, E_B(S $2p_{3/2}$) for pure $[C_4C_1Im][TfO]$ was measured at lesser energy than that of 0.5 M $([C_4C_1Im][TfO])(H_2O)$. Hence, E_B(S $2p_{3/2}$) for sulphur atoms within two different anionic environments, $[SCN]^-$ and $[TfO]^-$, was shown to decrease in energy from aqueous solution to pure IL.

Cl 2p NRXP spectra were measured for $[C_nC_1Im]Cl$, both within an aqueous solution, and for the pure IL, where n = 4 and 8, respectively (Figure 4.2e). For both 0.5 M $([C_4C_1Im]Cl)(H_2O)$ and pure $[C_8C_1Im]Cl$, Cl^- showed a doublet of photoemission peaks in the Cl 2p NRXP spectra due to a single chlorine electronic environment on the anion, which yielded two peaks due to spin orbit coupling. E_B(Cl $2p_{3/2}$) for pure $[C_8C_1Im]Cl$ was measured at lesser energy than that of 0.5 M $([C_4C_1Im]Cl)(H_2O)$.

I $3d_{5/2}$ NRXP spectra were measured for $[C_nC_1Im]I$, both within an aqueous solution, and for the pure IL, where n = 4 and 6, respectively (Figure 4.2f). For both 0.5 M $([C_4C_1Im]I)(H_2O)$ and pure $[C_6C_1Im]I$, I^- showed a doublet of photoemission peaks in the I 3d NRXP spectra due to a single iodine electronic environment on the anion, which yielded two peaks due to spin orbit coupling. However, as ΔE_B between E_B(I $3d_{5/2}$) and E_B(I $3d_{3/2}$) was so great (~11.5 eV), only the I $3d_{5/2}$ photoemission peak was shown. E_B(I $3d_{5/2}$) for pure $[C_6C_1Im]I$ was measured at lesser energy than that of 0.5 M $([C_4C_1Im]I)(H_2O)$.

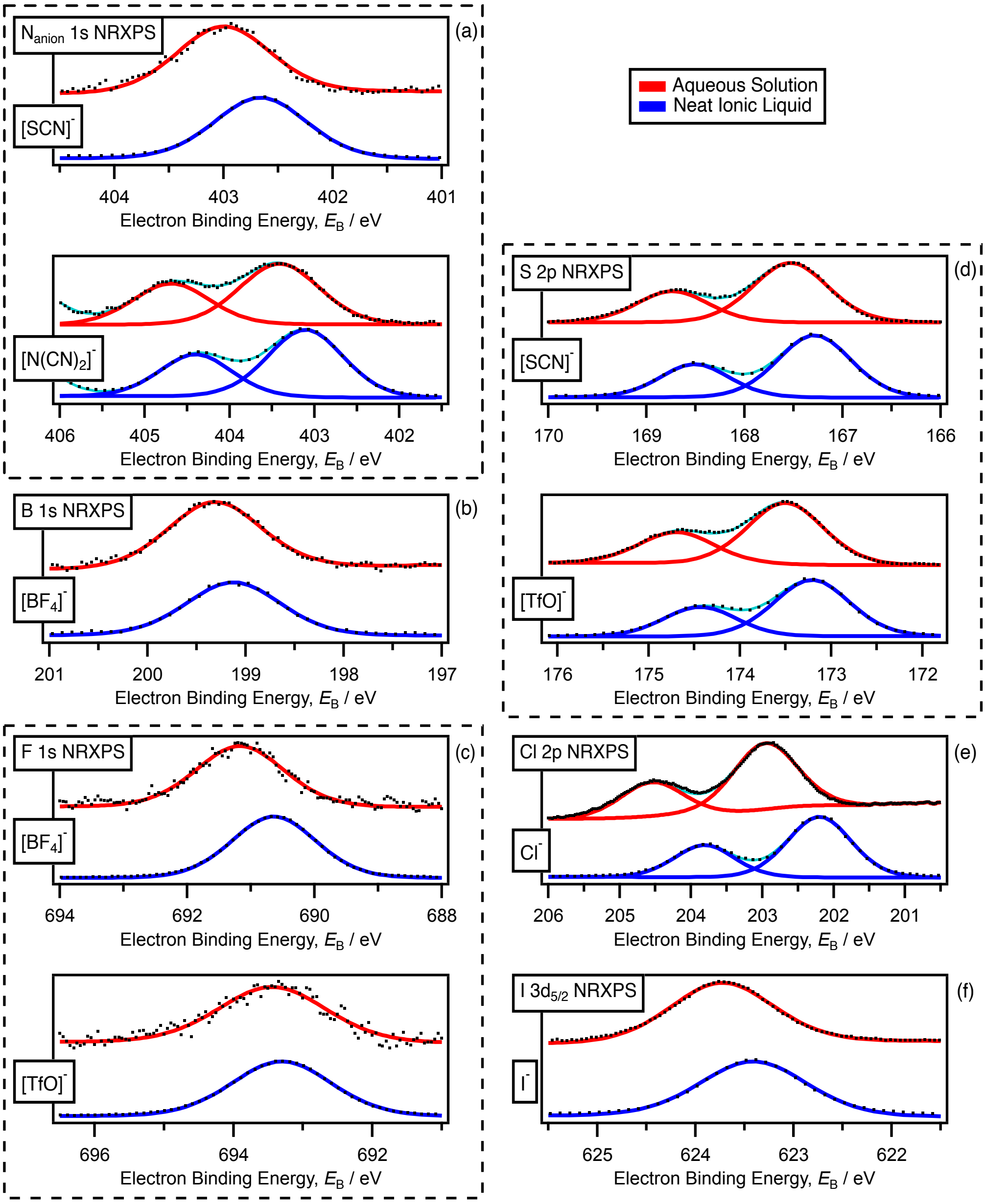

Figure 4.2. Anionic core level NRXP spectra for 0.5 M ([C$_n$C$_1$Im][anion])(H$_2$O) and pure [C$_n$C$_1$Im][anion], where anion = [SCN]$^-$, [N(CN)$_2$]$^-$, [BF$_4$]$^-$, [TfO]$^-$, Cl$^-$, and I$^-$: (a) N$_{anion}$ 1s. (b) B 1s. (c) F 1s. (d) S 2p. (e) Cl 2p. (f) I 3d$_{5/2}$. Spectra for samples in aqueous solution were measured at $h\nu$ = 700.0 eV; spectra for samples of pure IL were measured at $h\nu$ = 1486.6 eV. Spectra for aqueous solution and pure IL containing the same solute were vertically offset for clarity. All values were charge referenced using the methods detailed in Section 2.7.1.

For all examples of [C$_n$C$_1$Im][anion] shown, E_B(anion) decreased from dilute electrolyte (0.5 M aqueous solution) to concentrated electrolyte (pure IL) (Figure 4.2, Table 4.3). In 0.5 M aqueous solution, anions were assumed to exist within an infinite dilution of H$_2$O molecules, where many H$_2$O molecules were available for solvation of the anion in solution. Therefore, the ease in which anionic atomic charge was delocalised between many H$_2$O molecules was great (Chapter 5).

However, in pure IL, the lack of energetically stabilising H_2O molecules prevented the moderation of anionic atomic charge by solvent molecules. Hence, E_B(anion) decreased from 0.5 M aqueous solution to pure IL. The observed decrease in E_B(anion) from aqueous solution to pure IL was likely to be an electronic structure feature possessed by all $[C_4C_1Im]^+$-based ILs.

The extent of anionic binding energy shift from aqueous solution to pure IL, ΔE_B(anion), was shown to vary with differing anion identity. For example, $\Delta E_B(N_{anion}\ 1s)$ for $[SCN]^-$ and $[N(CN)_2]^-$, $\Delta E_B(S\ 2p_{3/2})$ for $[SCN]^-$ and $[TfO]^-$, and $\Delta E_B(I_{anion}\ 3d_{5/2})$ for I^-, were all shown to equal -0.3 eV. However, $\Delta E_B(B_{anion}\ 1s)$ for $[BF_4]^-$, and $\Delta E_B(Cl_{anion}\ 2p_{3/2})$ for Cl^-, were measured to be -0.2 eV and -0.8 eV, respectively (Table 4.3). The order of ΔE_B(anion) from aqueous solution to pure IL followed: $[BF_4]^- < [TfO]^- < [N(CN)_2]^- < I^- < [SCN]^- < Cl^-$ for the B 1s, S 2p, N 1s, I 3d, N 1s, and Cl 2p regions, respectively. Varying solvent-solute interactions for a single anion through changing of the solvent identity has previously been shown to influence E_B according to Kamlet-Taft (KT) Lewis basic solvent polarity descriptors, where a greater degree of solvent hydrogen bond donor, α_{solv}, resulted in an increased E_B(anion) (Chapter 3). The comparisons presented herein were also akin to varying both the anion identity ($[SCN]^-$, $[N(CN)_2]^-$, $[BF_4]^-$, $[TfO]^-$, Cl^-, or I^-), and the solvent identity (either H_2O or pure IL). Therefore, KT solvent polarity descriptors for pure $[C_4C_1Im]^+$-based ILs were compared to ΔE_B(anion) to determine the degree of solvent identity dependency on the observed energy shift (Figure 4.3, Table 4.2).

Table 4.2. KT α_{solv}, β_{solv}, and π^*_{solv} polarity scale descriptor and Pearson χ and η absolute scale descriptor values for pure [C_4C_1Im][anion] and H_2O included.

	$\alpha_{solv}{}^a$	$\beta_{solv}{}^a$	$\pi^*_{solv}{}^a$	χ^b	η^b
$[SCN]^-$	0.43	0.71	1.06		
$[N(CN)_2]^-$	0.44	0.64	0.98		
$[BF_4]^-$	0.52	0.55	0.96		
$[TfO]^-$	0.50	0.57	0.90		
Cl^-	0.32	0.95	1.13		
I^-	0.41	0.75	1.13		
H_2O	1.17[c]	0.47[c]	1.09[c]	3.10	9.50
N				7.30	7.23
B				4.29	4.01
F				10.41	7.01
S				6.22	4.14
Cl				8.30	4.68
I				6.76	3.69

[a] Obtained from reference [22, 23].

[b] Obtained from reference [18].

[c] Obtained from reference [17].

A linear correlation between ΔE_B(anion) and both, α_{solv} and β_{solv} polarity descriptors was observed, where a single linear line of best fit was drawn with $R^2 = 0.81$ and 0.86, respectively (Figure 4.3a and 4.3b, respectively). However, both polarity descriptors were shown to trend oppositely with ΔE_B(anion), where the greater the value of α_{solv} (β_{solv}) of the pure IL, the lesser (greater) ΔE_B(anion) was observed. α_{solv} and β_{solv} solvent polarity descriptors are known to describe opposite electron transfer processes, *i.e.*, Lewis acidity and Lewis basicity. As ILs are comprised of cationic and anionic species, they are capable of both, electron pair acceptance (Lewis acidity), and electron pair donation (Lewis basicity). For ions in aqueous solution, H_2O is known to provide a charge screening effect between the cation and the anion due to its high relative permittivity.[24] H_2O is also capable of acting as a strong Lewis acid ($\alpha_{solv} = 1.17$), providing electronic stabilisation of the anionic species. Therefore, the Lewis acid/base interactions between ions are negligible in aqueous solution, rendering overall ionic α_{solv} and β_{solv} irrelevant. However, within pure IL, ion-ion interactions dominate. As shown, species which are strongly Lewis basic but weakly Lewis acidic, *e.g.*, [C_4C_1Im]Cl, contain a high value of ΔE_B(anion), where the negative charge is heavily isolated on the anion with a lack of strong electron acceptor to aid in the stabilisation of the excess negative charge.

Contrastingly, species which are more strongly Lewis acidic but more weakly Lewis basic, *e.g.*, $[C_4C_1Im][BF_4]$, contain a low value of ΔE_B(anion), where the weaker electron donating ability of the anionic species is easily counterbalanced by the stronger electron acceptance ability. The stronger correlation between ΔE_B(anion) and β_{solv}, suggests that the extent of ΔE_B(anion) slightly favours the electron donor ability of the anionic species. The final KT solvent polarity descriptor, dipolarity-polarisability, π^*_{solv}, was compared to ΔE_B(anion), where a very weak linear correlation was observed with $R^2 = 0.39$ (Figure 4.3c). In general, the greater the dipolarity-polarisability, the lesser ΔE_B(anion) was observed, which as π^*_{solv} is known to correlate with the product of α_{solv} and β_{solv} supports the conclusion that the electron donor ability of the anionic species is favoured.[5]

While KT solvent polarity descriptors relate to the sum of all atomic contributions within a particular species, Pearson absolute scale descriptors can be used to describe the interactions of both, individual atoms and molecular species.[18] Pearson absolute scale descriptors, absolute electronegativity, χ, and absolute hardness, η, values were compared to measured ΔE_B(anion). A weak linear correlation between χ and ΔE_B(anion) was observed with $R^2 = 0.57$, where the greater the absolute electronegativity of the pure IL, the greater ΔE_B(anion) was observed (Figure 4.3d); this matched the trend shown between α_{solv} and ΔE_B(anion), which was unsurprising as a greater value of χ corresponds to a more Lewis acidic species, *i.e.*, electrons flow from that of lower to that of higher χ.[18] Absolute electronegativity would be described as a non-specific solvation effect. Therefore, non-specific solvation effects were shown to play an important role in determining ΔE_B(anion) through varying anion identity, similarly to that shown to impact upon E_B(anion) while varying concentration of IL in H_2O (Chapter 5) and varying solvent identity (Chapter 3). No correlation was observed between η and ΔE_B(anion) with $R^2 = 0$ (Figure 4.3e).

ΔE_B(anion) across N 1s and S 2p containing species were shown to be equal for different anion identities, *e.g.*, for $[SCN]^-$, $[N(CN)_2]^-$, and $[TfO]^-$. However, ΔE_B(anion) across F 1s containing species were shown to differ for different anion identities, *e.g.*, for $[TfO]^-$ and $[BF_4]^-$. One cause of this phenomena may be due to the strength of covalent bonding exhibited by fluorine atoms within different species. For example, the strong covalent bonding between carbon and fluorine in $[TfO]^-$ anions resulted in an uneasily oxidised fluorine atom compared to the weaker bonding between boron and fluorine in $[BF_4]^-$ anions; this is exemplified through the relative values of E_B(F 1s) for $[TfO]^-$ anions and $[BF_4]^-$ anions, which are higher and lower respectively. The strength of intramolecular covalent bonding determined the extent to which the atomic fluorine experiences external solvation effects.

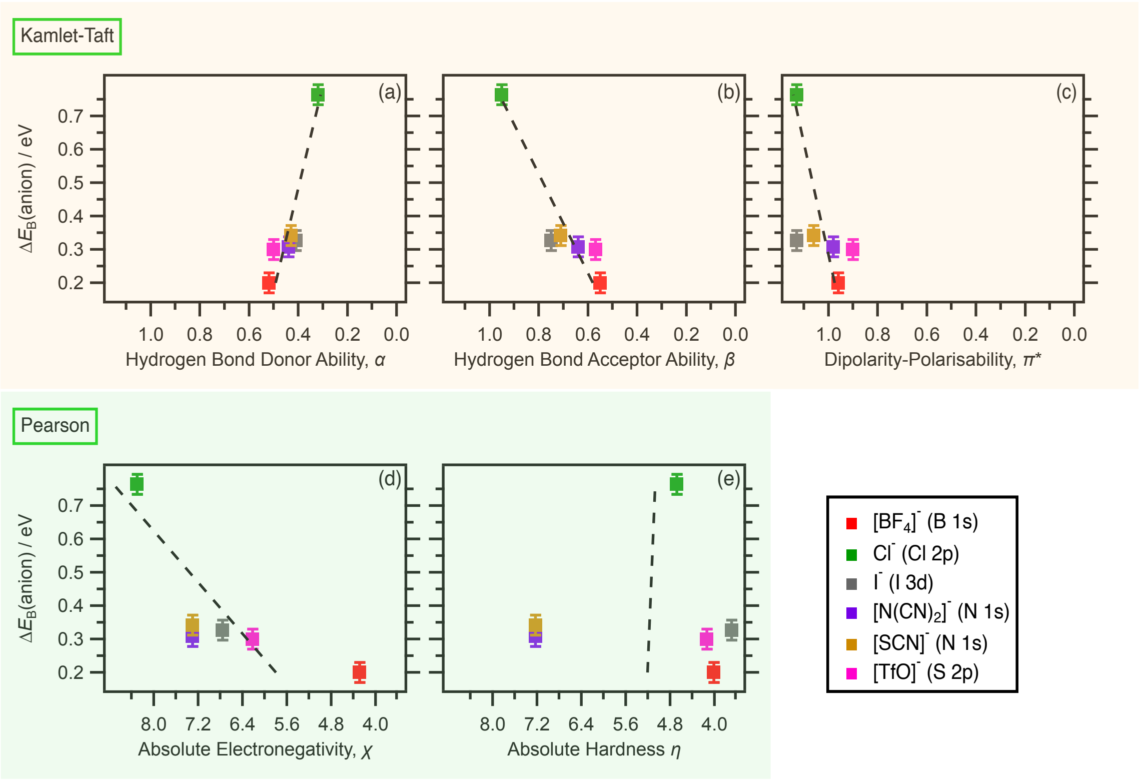

Figure 4.3. ΔE_B(anion) from 0.5 M ([C$_n$C$_1$Im][anion])(H$_2$O) to pure [C$_n$C$_1$Im][anion], against Kamlet-Taft polarity scale descriptors, and Pearson absolute scale descriptors, where anion = [BF$_4$]$^-$ (red), [N(CN)$_2$]$^-$ (purple), [TfO]$^-$ (pink), Cl$^-$ (green), I$^-$ (grey), and [SCN]$^-$ (orange): (a) ΔE_B(anion) against hydrogen bond donor, α_{solv}, $R^2 = 0.81$. (b) ΔE_B(anion) against hydrogen bond acceptor, β_{solv}, $R^2 = 0.86$. (c) ΔE_B(anion) against dipolarity-polarisability, π^*_{solv}, $R^2 = 0.39$. (d) ΔE_B(anion) against absolute electronegativity, χ, $R^2 = 0.57$. (e) ΔE_B(anion) against absolute hardness, η, $R^2 = 0$. ΔE_B(anion) values were calculated from E_B(anion) measured in aqueous solution minus E_B(anion) measured for the pure IL. KT solvent polarity descriptor values used were those of [C$_4$C$_1$Im][anion] species from references [22, 23]. Pearson absolute scale descriptor values pertain to those of the neutral atom within brackets on the legend, and were found in reference [18]. Dashed lines represented the linear line of best fit. ΔE_B(anion) values were charge referenced using the methods detailed in Section 2.7.1.

As previously discussed in relation to E_B(F 1s) values, relative E_B(anion) positions were shown to differ for the same atom within differing anions. For example, E_B(F 1s) for [BF$_4$]$^-$ appeared at lesser energy than shown for [TfO]$^-$, E_B(S 2p$_{3/2}$) for [SCN]$^-$ appeared at lesser energy than shown for [TfO]$^-$, and E_B(N$_{anion}$ 1s) for [SCN]$^-$ appeared at lesser energy than shown for [N(CN)$_2$]$^-$. E_B differences for the same atom can occur due to many factors relating to the nature of the probed atom, such as: the electronegativity of neighbouring atoms, the strength of intramolecular covalent bonding towards the probed species, and the oxidation state of the probed species. Therefore, the absolute differences in E_B(anion) for the same atomic species in differing anions were not due to solvation effects and were instead an artefact of covalent bonding within the species.

Table 4.3. Anionic experimental binding energies, E_B(anion), recorded by NRXPS for 0.5 M ([C_4C_1Im][anion])(H_2O) and pure [C_nC_1Im][anion], where anion = [SCN]$^-$, [N(CN)$_2$]$^-$, [BF_4]$^-$, [TfO]$^-$, Cl$^-$, and I$^-$. Spectra for samples in aqueous solution were measured at $h\nu$ = 700.0 eV; spectra for samples of pure IL were measured at $h\nu$ = 1486.6 eV. All values were charge referenced using the methods detailed in Section 2.7.1. All E_B values are reported to 2 decimal places.

		Electron binding energy / eV					
	x_{IL}	N$_{anion}$ 1s (± 0.03)	B 1s (± 0.03)	F 1s (± 0.03)	S 2p$_{3/2}$ (± 0.06)	Cl 2p$_{3/2}$ (± 0.06)	I 3d$_{5/2}$ (± 0.06)
[SCN]$^-$	0.01	403.00			167.53		
	1.00	402.66			167.20		
ΔE_B		-0.34			-0.33		
[N(CN)$_2$]$^-$	0.01	403.44[a]					
	1.00	403.11[a]					
ΔE_B		-0.33					
[BF_4]$^-$	0.01		199.32	691.17			
	1.00		199.12	690.64			
ΔE_B			-0.2	-0.53			
[TfO]$^-$	0.01			693.43	173.50		
	1.00			693.30	173.21		
ΔE_B				-0.13	-0.29		
Cl$^-$	0.01					202.96	
	1.00					202.20	
ΔE_B						-0.76	
I$^-$	0.01						623.74
	1.00						623.41
ΔE_B							-0.33

[a] [N(CN*)$_2$]$^-$.

[b] ΔE_B is the difference between 0.5 M (solute)(H_2O) and pure IL photoemission peak binding energies.

4.3.2. Changes in cationic atomic charge with varying x_{IL} and anion identity

N 1s NRXP spectra and C 1s NRXP spectra were measured for $[C_nC_1Im]^+$ based ILs with differing anions: $[TfO]^-$, Cl^-, I^-, $[N(CN)_2]^-$, $[SCN]^-$, and $[BF_4]^-$ (Figure 4.4). For ILs containing only cationic nitrogen atoms ($[TfO]^-$, Cl^-, I^-, and $[BF_4]^-$) a single photoemission peak was fitted within the N 1s NRXP spectra (Figure 4.4a), which contained electronic contributions from both N^1 and N^3 atoms located on the $[C_4C_1Im]^+$ cation (see Figure 4.1 for the structure of $[C_4C_1Im]^+$ and the position of the N^1 and N^3 atoms). N 1s NRXP spectra of ILs containing both cationic and one or more anionic nitrogen atoms ($[N(CN)_2]^-$ and $[SCN]^-$) display the corresponding number of fitted electronic environments, *e.g.*, $[C_4C_1Im]][N(CN)_2]$ spectra contain three N 1s photoemission peaks. $E_B(N_{cation}\ 1s)$ was shown at the greatest energy within the N 1s NRXP spectra at a fixed value of 406.75 eV. Hence, all photoemission peaks shown throughout this chapter were relative to a fixed $E_B(N_{cation}\ 1s)$. All C 1s NRXP spectra were fitted with three photoemission peaks, C_{alkyl} 1s, C_{hetero} 1s, and C^2, listed in increasing E_B respectively (Figure 4.4b). For ILs containing only cationic carbon atoms (Cl^-, I^-, and $[BF_4]^-$), the C 1s NRXP spectra was purely a representation of the cationic electronic contributions to the region. However, for samples also containing anionic carbon atoms, *e.g.*, $[N(CN)_2]^-$ and $[SCN]^-$, additional contributions were included within the C_{hetero} 1s photoemission peak, as anionic carbon atoms have been shown to appear at approximately the same E_B as carbon atoms within the heterocyclic ring structure.[25] The $[TfO]^-$ anion contains a single carbon atom bonded to three electronegative fluorine atoms, resulting in a positive shift of the C_{CF} 1s photoemission peak to higher E_B (297.6 eV). The C_{CF} 1s photoemission peak is therefore measured at energies above those shown within Figure 4.4b. Hence, the C 1s NRXP spectra shown for $[C_4C_1Im][TfO]$, in both aqueous solution and pure IL, were described as a representation of pure cationic contributions to the carbon region, absent of anionic OCOs.

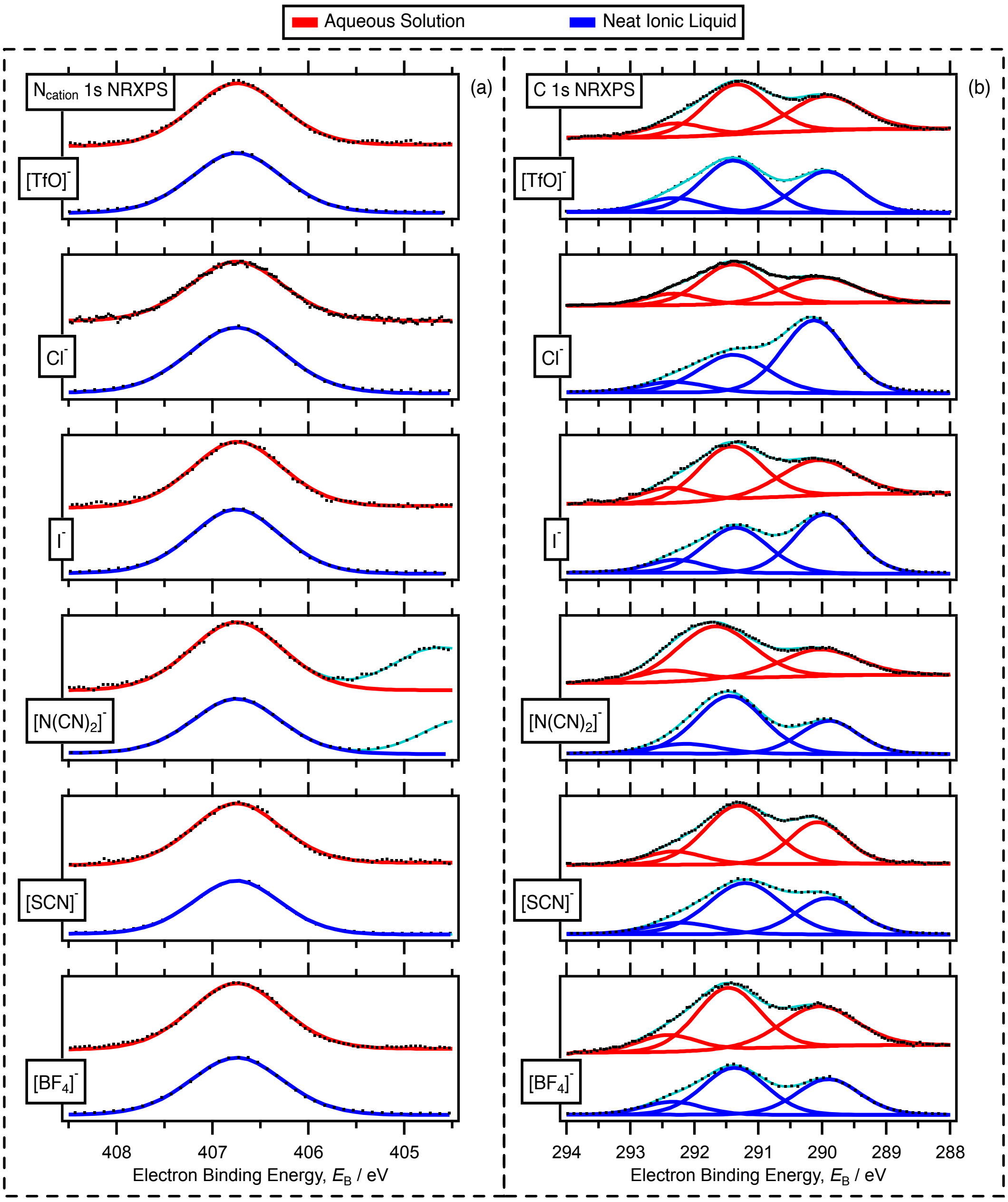

Figure 4.4. Cationic core level NRXP spectra for 0.5 M ([C_nC_1Im][anion])(H_2O) and pure [C_nC_1Im][anion], where anion = [SCN]$^-$, [N(CN)$_2$]$^-$, [BF$_4$]$^-$, [TfO]$^-$, Cl$^-$, and I$^-$: (a) N$_{cation}$ 1s. (b) C 1s. Spectra for samples in aqueous solution were measured at $h\nu$ = 700.0 eV; spectra for samples of pure IL were measured at $h\nu$ = 1486.6 eV. Spectra for aqueous solution and pure IL containing the same solute were vertically offset for clarity. All values were charge referenced using the methods detailed in Section 2.7.1.

When charge referenced to constant E_B(N$_{cation}$ 1s), E_B(C$_{alkyl}$ 1s) peaks were shown to remain at constant energies within experimental and fitting error (± 0.1 eV) for all samples of 0.5 M ([C_4C_1Im][anion])(H_2O) (Figures 4.4 and 4.5a). The lack of electronic influence from the counteranion, due to complete solvation of the [C_4C_1Im]$^+$ cation by H_2O molecules, resulted in the measurement of electronically identical $[C_4C_1Im]^+$ cations. Hence, the electronic structure of all cationic components were measured at the same E_B even whilst varying anionic identity within solution. Studying ILs in aqueous solution therefore provides a means of studying cationic species in the absence of the electronic influence of the counterion, affording the ability to study the electronic structure of pure ionic components (relative to the same solvation effect).

A comparison of $E_B(C_{alkyl}\ 1s)$ to $E_B(C_{hetero}\ 1s)$ with varying anion identity in aqueous solution was shown (Figure 4.5a). As discussed, $E_B(C_{alkyl}\ 1s)$ for 0.5 M $([C_4C_1Im][anion])(H_2O)$ species were shown to remain constant (within experimental error, ± 0.1 eV). However, for the same samples measured, $E_B(C_{hetero}\ 1s)$ was only shown to remain constant with varying anionic identity for species with no anionic carbon contribution towards the $E_B(C_{hetero}\ 1s)$ photoemission peak, *i.e.*, $E_B(C_{hetero}\ 1s)$ remained constant for $[BF_4]^-$, $[TfO]^-$, I^-, and Cl^- containing species. Both cyano anions measured, $[N(CN)_2]^-$ and $[SCN]^-$, contained carbon atoms that contributed towards the $E_B(C_{hetero}\ 1s)$ photoemission peak, whereby the anionic carbon atom on the $[SCN]^-$ anion acted to decrease $E_B(C_{hetero}\ 1s)$, whereas the anionic carbon atoms on the $[N(CN)_2]^-$ anion increased $E_B(C_{hetero}\ 1s)$, relative to their respective $E_B(C_{alkyl}\ 1s)$ values. The observed contrasting effect was due to the differing carbon electronic environments within $[SCN]^-$, where the carbon atom is bonded to two atoms with similar electronegativity values, and $[N(CN)_2]^-$, where each carbon atom within the anion is bonded to three highly electronegative fluorine atoms. Therefore, for samples where only cationic carbon atoms contributed to the C 1s NRXP spectra, $\Delta E_B(C_{hetero}\ 1s - C_{alkyl}\ 1s)$ remained constant (~1.4 ± 0.1 eV). Likewise, comparisons of $E_B(C_{alkyl}\ 1s)$ to $E_B(C_{hetero}\ 1s)$ with varying anion identity in corresponding pure ILs were shown (Figure 4.4b). The large variation in $E_B(C_{hetero}\ 1s)$ from aqueous solution to pure IL demonstrated the strong influence of the anion on the positive charge of the $[C_nC_1Im]^+$ cation, due to both, the size and coordinating strength of the anionic species.[5]

Within the literature, $E_B(N_{cation}\ 1s)$ and $E_B(C_{hetero}\ 1s)$ values have been used to demonstrate the effect of the counteranion on the electronic structure of the $[C_8C_1Im]^+$ cation, resulting in an established scale consisting of small, highly coordinating anions at low energies, and large, weakly coordinating anions at high energies.[5] Within each sample of 0.5 M $([C_4C_1Im][anion])(H_2O)$, where $[C_4C_1Im]^+$ was completely solvated by H_2O (rendering the effect of the anion to be negligible), the solvent could be considered to act as the counterion towards the cation. The effect of H_2O upon both $E_B(N_{cation}\ 1s)$ and $E_B(C_{hetero}\ 1s)$ was found to be similar to that of the small, highly coordinating Cl^- anion.[5] However, discrepancies were found between published $E_B(N_{cation}\ 1s)$ and $E_B(C_{hetero}\ 1s)$ values, and the data used within this chapter.[5] Differences may have arisen due to the use of a nonmonochromated X-ray source within the literature source, or due to the variation in alkyl chain length within pure IL data used within this chapter. The E_B difference between the C_{alkyl} 1s and the C_{hetero} 1s photoemission peaks, ΔE_B(C_{hetero} 1s – C_{alkyl} 1s), was shown to trend with the KT solvent polarity descriptor, β_{solv}, where an inverse relationship existed between E_B(C_{hetero} 1s – C_{alkyl} 1s) and β_{solv} (Figure 4.5c).[5] Aqueous solutions, denoted as H_2O within Figure 4.5c, was shown to exist as an outlier (additional to the cyano anions due to the C_{anion} contribution to E_B(C_{hetero} 1s)) within the observed ΔE_B(C_{hetero} 1s – C_{alkyl} 1s) against β_{solv} trend, where a lower ΔE_B(C_{hetero} 1s – C_{alkyl} 1s) than expected was measured relative to the low β_{solv} value reported for H_2O (Table 4.2). From the displayed linear line of best fit, two pieces of information would have been predicted:

1. From reported β_{solv} values, the predicted value of ΔE_B(C_{hetero} 1s – C_{alkyl} 1s) for 0.5 M ([C_4C_1Im][anion])(H_2O) should equal 1.51 eV.
2. From the measured value of ΔE_B(C_{hetero} 1s – C_{alkyl} 1s), the predicted value of β_{solv} for 0.5 M ([C_4C_1Im][anion])(H_2O) should equal 0.74 (like the I^- anion).

The most likely of the two suggestions would be for 0.5 M ([C_4C_1Im][anion])(H_2O) species to possess β_{solv} values unlike that of the pure solvent, but equally unlike those of either ion within solution. Alternatively, the unexpected ΔE_B(C_{hetero} 1s – C_{alkyl} 1s) value obtained for H_2O could instead be a reflection upon the hydrogen bond donor ability of the [C_4C_1Im]$^+$ cation towards the H_2O solvent molecules, as all 0.5 M ([C_4C_1Im][anion])(H_2O) species showed similar (± 0.06 eV) values of ΔE_B(C_{hetero} 1s – C_{alkyl} 1s), removing any likelihood of anionic dependency. On the other hand, one reasoning for the observed decrease in ΔE_B(C_{hetero} 1s – C_{alkyl} 1s) for H_2O may have been due to its small size and high coordinating ability through a very high hydrogen bond donor ability of H_2O, which is significantly greater than the similarly low α_{solv} values of measured pure ILs (Table 4.2). In each case, computational calculations of IL-H_2O combinations should be used to further investigate the interactions between [C_4C_1Im]$^+$ and H_2O.

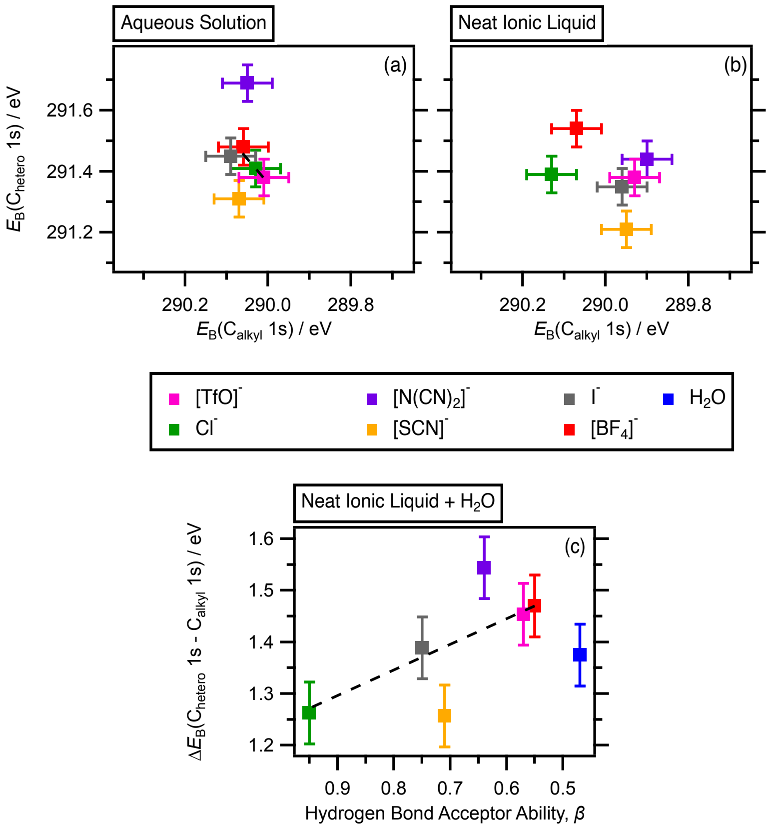

Figure 4.5. $E_B(C_{alkyl}$ 1s) against $E_B(C_{hetero}$ 1s) for 0.5 M ([C_nC_1Im][anion])(H_2O) and pure [C_nC_1Im][anion], and the comparison of $\Delta E_B(C_{hetero}$ 1s – C_{alkyl} 1s) against β_{solv} for pure [C_nC_1Im][anion] and [C_4C_1Im]$^+$ in H_2O, where anion = [SCN]$^-$, [N(CN)$_2$]$^-$, [BF$_4$]$^-$, [TfO]$^-$, Cl$^-$, and I$^-$: (a) Aqueous solution; the linear line of best fit displayed excluded data points for [SCN]$^-$ and [N(CN)$_2$]$^-$ and had an R^2 = 0.64. (b) Pure IL. (c) Pure IL excluding the data point for H_2O, where the data point for H_2O is obtained from ([C_4C_1Im]Cl)(H_2O); the linear line of best fit displayed excluded data points for [SCN]$^-$ and [N(CN)$_2$]$^-$ and had an R^2 = 0.98. Spectra for samples in aqueous solution were measured at $h\nu$ = 700.0 eV; spectra for samples of pure IL were measured at $h\nu$ = 1486.6 eV. All values were charge referenced using the methods detailed in Section 2.7.1.

A comparison of ΔE_B for $E_B(C_{alkyl}$ 1s), $E_B(C_{hetero}$ 1s), and $E_B(C^2$ 1s) were shown to vary by approximately ± 0.1 eV from aqueous solution to pure IL, except for the [N(CN)$_2$]$^-$ anion due to anionic contributions to the C_{hetero} 1s photoemission peak, which shift due to the charge referencing method employed. (Table 4.4). Furthermore, all C 1s photoemission peaks were shown to shift in the same direction (within experimental error). The monotonic trend of non-zero ΔE_B(carbon 1s) shifts demonstrated a non-specific solvation effect where all OCOs were affected equally with increasing concentration. Thus overall, cationic peaks were shown to remain constant within experimental error, while anionic peak energies varied significantly from aqueous solution to pure IL.

Additional to the E_B, measured photoelectron peaks contain two key parameters obtained through the fitting procedure, the peak area, and the peak full width at half maximum, FWHM. The area and FWHM ratio of the measured photoelectron peaks within the C 1s NRXP spectra, C_{alkyl} 1s: C_{hetero} 1s: C^2 1s, were compared for $[C_nC_1Im]$[anion] in both, aqueous solution, and pure IL. The area ratio between C_{alkyl} 1s: C_{hetero} 1s: C^2 1s was shown to be consistent for the same $[C_nC_1Im]$[anion] within aqueous solution and pure IL, due to the same photoelectron peak fitting parameters employed to provide a good overall fit (Appendix Table 8.4). However, the FWHM ratio between C_{alkyl} 1s: C_{hetero} 1s: C^2 1s was shown to vary for each $[C_nC_1Im]$[anion] within aqueous solution and pure IL (Figure 4.6). Relative to the measured C_{alkyl} 1s FWHM, the ratio of C_{hetero} 1s and C^2 1s were shown to be lesser in aqueous solution than those of pure IL, *i.e.*, the FWHM of the C_{hetero} 1s and C^2 1s peaks increased in relation to the C_{alkyl} 1s peak. As broadening of the peak can be indicative of a change in the number of chemical bonds contributing to the probed electronic environment, the subsequent FWHM variation may indicate that C_{hetero} and C^2 atoms participate in a greater number of interactions with ionic components in pure IL, than molecular solvent molecules in aqueous solution.

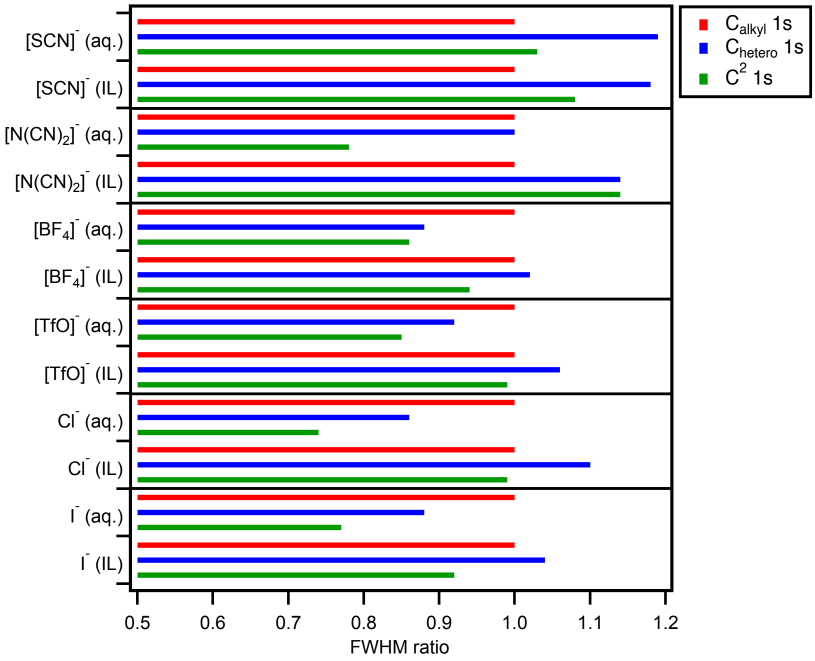

Figure 4.6. The ratio between measured photoelectron peak FWHM values within the C 1s region, C_{alkyl} 1s : C_{hetero} 1s : C^2 1s, for $[C_4C_1Im]$[anion] in aqueous solution (0.5 M) and pure IL, where anion = $[SCN]^-$, $[N(CN)_2]^-$, $[BF_4]^-$, $[TfO]^-$, Cl^-, and I^-.

Table 4.4. Experimental binding energies, E_B, recorded by C 1s NRXPS for 0.5 M ($[C_nC_1Im][anion]$)(H_2O) and pure $[C_nC_1Im][anion]$, where anion = $[SCN]^-$, $[N(CN)_2]^-$, $[BF_4]^-$, $[TfO]^-$, Cl^-, and I^-. Spectra for samples in aqueous solution were measured at $h\nu$ = 700.0 eV; spectra for samples of pure IL were measured at $h\nu$ = 1486.6 eV. All values were charge referenced using the methods detailed in Section 2.7.1. All E_B values are reported to 2 decimal places.

		Electron binding energy / eV		
	x_{IL}	C_{alkyl} 1s (± 0.06)	C_{hetero} 1s (± 0.06)	C^2 1s (± 0.06)
$[SCN]^-$	0.01	290.07	291.31	292.29
	1.00	289.95	291.21	292.21
ΔE_B		-0.12	-0.10	-0.08
$[N(CN)_2]^-$	0.01	290.04	291.69	292.42
	1.00	289.90	291.44	292.14
ΔE_B		-0.14	-0.25	-0.28
$[BF_4]^-$	0.01	290.06	291.48	292.42
	1.00	289.98	291.45	292.40
ΔE_B		-0.08	-0.03	-0.02
$[TfO]^-$	0.01	290.07	291.47	292.42
	1.00	289.93	291.38	292.32
ΔE_B		-0.14	-0.09	-0.10
Cl^-	0.01	290.07	291.41	292.33
	1.00	290.13	291.39	292.32
ΔE_B		0.06	-0.02	-0.01
I^-	0.01	290.09	291.45	292.40
	1.00	289.96	291.35	292.29
ΔE_B		-0.13	-0.10	-0.11

[a] ΔE_B is the difference between 0.5 M (solute)(H_2O) and pure IL photoemission peak binding energies.

4.3.3. Changes in solvent atomic charge with varying anion identity

O 1s NRXP spectra were measured for $[C_4C_1Im]^+$ based ILs with differing anions in H_2O, 0.5 M ($[C_4C_1Im][anion]$)(H_2O) (Figure 4.7a). For all ILs in aqueous solution, two photoemission peaks were fitted corresponding to the O_{gas} 1s peak at higher E_B, O_{liq} 1s peak at lower E_B. Most anions measured did not contain oxygen atomic environments ($[SCN]^-$, $[N(CN)_2]^-$, $[BF_4]^-$, Cl^-, I^-); Hence, O 1s NRXP spectra provided an electronic description of the H_2O oxygen core level electronic structure. However, the measured $[TfO]^-$ anion contained oxygen atoms which did contribute to the O 1s NRXP spectra. Domination of the spectra by the O_{liq} electronic environment meant oxygen contributions from the $[TfO]^-$ anion could not be reliably included within the fitted spectra. The presence of an additional anionic contribution to the O 1s NRXP spectra for $[TfO]^-$ was visually evident through comparison of the increased O_{liq} 1s FWHM.

Anion identity was shown to have a minimal effect on $E_B(O_{liq}$ 1s) at 0.5 M concentration (Figure 4.7b), due to the small IL:H_2O molecular ratio (Table 4.1). The large number of H_2O molecules, relative to the number of anions in solution, allowed for a greater ease of delocalisation of anionic atomic charge across all solvent molecules. Hence, $E_B(O_{liq}$ 1s) was shown to be unaffected within experimental error (± 0.1 eV). One notable exception to this trend was the $[TfO]^-$ anion, which contained anionic oxygen contributions to the O 1s NRXPS region that were unable to be fitted reliably due to the domination of the spectra by the solvent photoemission peak. Anionic oxygen contributions resulted in a visually broader, and decreased $E_B(O_{liq}$ 1s) fitted peak due to shifting to lower energies by the anionic oxygen contribution.

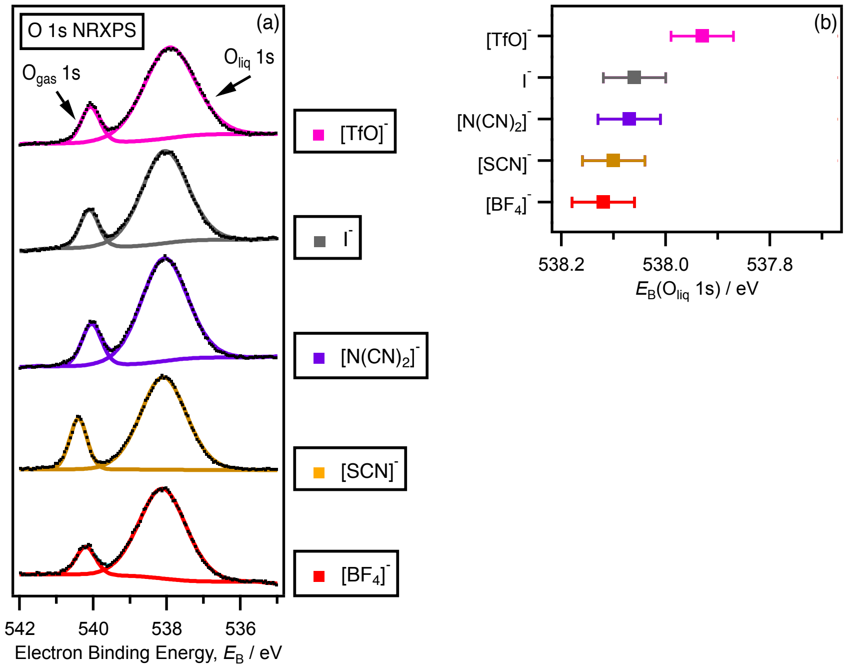

Figure 4.7. O 1s NRXP spectra and corresponding $E_B(O_{liq}$ 1s) against anion category plot for 0.5 M ($[C_4C_1Im][anion]$)(H_2O), where anion = $[SCN]^-$, $[N(CN)_2]^-$, $[BF_4]^-$, $[TfO]^-$, and I^-: (a) O 1s NRXP spectra; vertically offset for clarity. (b) $E_B(O_{liq}$ 1s) against anion; error bars = ± 0.06 eV. All spectra were measured at $h\nu$ = 700.0 eV. All values were charge referenced using the methods detailed in Section 2.7.1.

4.3.4. Probing OVSs through valence RXPS

The OVS and unoccupied molecular orbital (UMO) energies for a specific atom within a system were probed through the measurement of the valence RXPS heat map over the resonant edge energy.[26] For 0.5 M ([C_4C_1Im][anion])(H_2O), the N 1s valence RXPS heat map was shown (Figure 4.8a). The valence RXPS heat map was composed of valence spectra at differing values of $h\nu$, which allowed resonant features to be identified, with intensities shown on the colour scale. Varying the $h\nu$ allowed for specific OCO → UMO transitions to be probed, hence contributions to the valence region shown can be atom specific. In the case of Figure 4.8a, each resonant feature in the displayed heat map is a measure of the contribution of the nitrogen atom, located on the [C_4C_1Im]$^+$ cation, to the valence region. Subtracting a region below resonance allows for NRXPS features to be removed from the map, leaving only RXPS features. The N_{cation} 2p is highlighted as the lowest E_B feature on the heat map.

The vertical summation of the RXPS map gives partial electron yield XA spectra (Figure 4.8b). The N 1s XA spectra showed a single sharp peak (peak 1) due to the N_{cation} 1s → π* transition, which was shown to appear at equal energies for all samples of 0.5 M ([C_4C_1Im][anion])(H_2O), where $h\nu$(N_{cation} 1s → π*) = 402.1 eV. E_B(N_{cation} π*) for 0.5 M ([C_4C_1Im][anion])(H_2O) can be calculated from E_B(N_{cation} 1s) minus $h\nu$(N_{cation} 1s → π*) to give a value of 4.7 eV.

A horizontal summation of the RXPS map at selected resonant $h\nu$ was used to identify contributions to the valence region by each component, providing valence RXP spectra. For example, the trace at $h\nu$ = 402.1 eV yielded all contributions of the nitrogen atom of the [C_4C_1Im]$^+$ cation to the valence region, as $h\nu$(N_{cation} 1s → π*) = 402.1 eV for all samples compared (Figure 4.8c). The N_{cation} 2p was highlighted again as the lowest E_B feature to demonstrate the origin of each peak within the N 1s valence RXP spectra from the N 1s valence RXPS heat map. The high atomic selectivity of RXPS allows for the separation of differing OVS contributions to the valence region; therefore, enabling contributions which were otherwise obscured by other contributions from all OVSs to the valence region to be identified.

A visual comparison of the peak E_B separation and relative peak intensity of valence RXP spectra for all [C_4C_1Im]$^+$-based ILs at the cationic edge, $h\nu$ = 402.1 eV, showed a very good overall match, *i.e.*, all Auger emission peaks were measured at the same energy within all spectra. As the valence region contained OVSs associated with intermolecular bonding, one would expect to observe differences between RXP spectra if solvent-solute interactions varied within samples of 0.5 M ($[C_4C_1Im][anion])(H_2O)$. However, the spectral shape and relative energies matched even while anionic atoms were present ($[SCN]^-$, $[N(CN)_2]^-$). This further demonstrated the consistency of interaction between the $[C_4C_1Im]^+$ cation and H_2O when varying anionic identity, and additionally showed how the variation in the electronic structure of different cationic OVSs remained negligible at 0.5 M; hence, no anion dependency on solvent-cation interactions was observed.

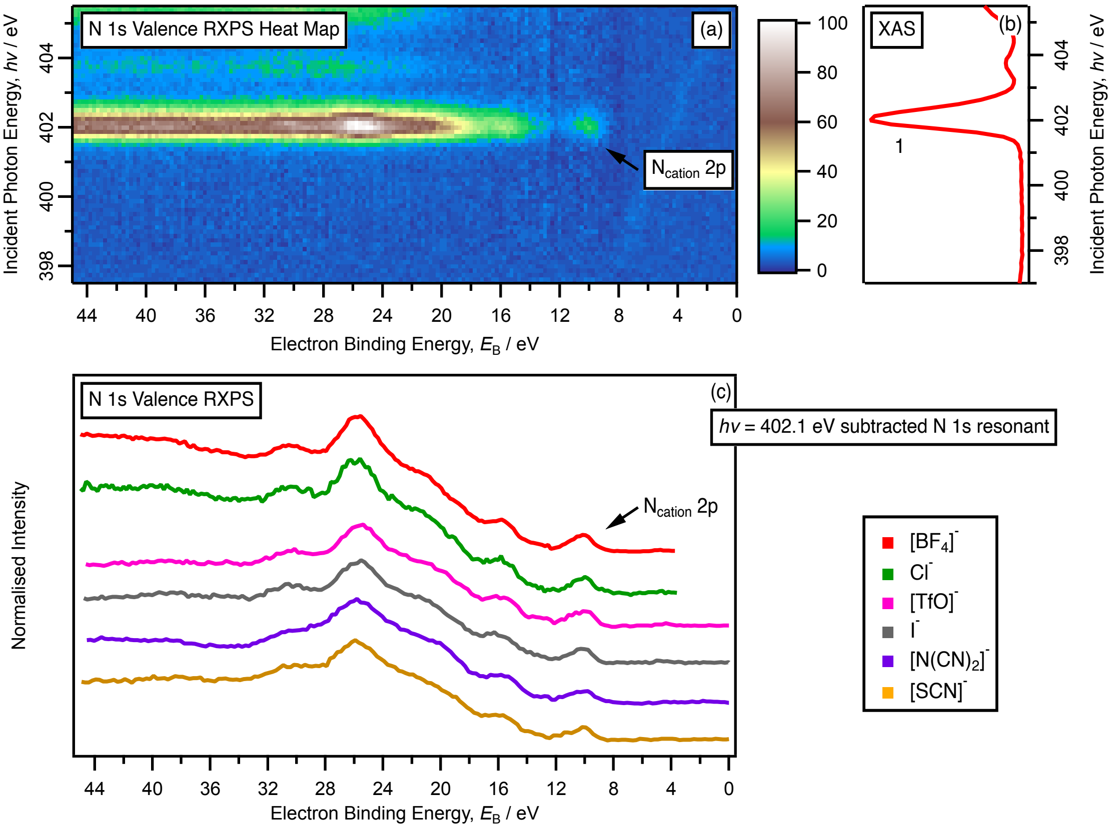

Figure 4.8. N 1s valence RXP heat map, XA spectra and valence RXP spectra for 0.5 M ($[C_4C_1Im][anion])(H_2O)$, where anion = $[SCN]^-$, $[N(CN)_2]^-$, $[BF_4]^-$, $[TfO]^-$, Cl^-, and I^-: (a) N 1s RXPS heat map. (b) N 1s partial electron yield XA spectra. (c) N 1s valence RXP spectra at $h\nu$ = 402.1 eV; vertically offset for clarity. N 1s valence RXPS heat map was subtracted using the procedure detailed in Section 8.2. N 1s valence RXPS heat map and N 1s valence RXP spectra were charge referenced using the methods detailed in Section 2.7.3. Remaining RXP spectra were shifted to match $E_B(N_{cation}$ 2p) to allow for a clearer visual comparison.

4.4. Conclusion and future work

Throughout this chapter, the influence of varying the anionic identity within samples of 0.5 M ($[C_4C_1Im][anion])(H_2O)$ and pure $[C_nC_1Im][anion]$ on the energies of key non-bonding (core level) OCOs was explored. Additionally, the effect of varying the concentration of an electrolyte solution on the electronic structure of each component (cation, anion, solvent) within the solution was probed.

Anionic OCO energies were shown to decrease from aqueous solution to pure IL for all anion identities measured. Anionic OCO energies were influenced by non-specific solvation effects as all E_B(anion) components for the same anion shifted equally with increasing electrolyte concentration, except for fluorine OCOs. The extent to which the binding energy shifted with increasing concentration was found to relate to the hydrogen bond donor and acceptor abilities of the anion present, as well as the absolute electronegativity, of the probed atomic species.

Anion identity was shown not to have a significant effect on the $[C_4C_1Im]^+$ cationic OCO energies within aqueous solution (dilute electrolytes). Through comparison to literature, the role of H_2O as a counterion to the $[C_4C_1Im]^+$ cation was found to act similarly to I^- despite a far lower hydrogen bond acceptor ability, which did not agree with the established $\Delta E_B(C_{hetero}\ 1s - C_{alkyl}\ 1s)$ against β_{solv} linear relationship. For this reason, it was determined that the position of H_2O was not straightforward in its interpretation with three possible conclusions proposed:

1. β_{solv} values resembled those of the 0.5 M $([C_4C_1Im][anion])(H_2O)$ solution, rather than pure H_2O.
2. $\Delta E_B(C_{hetero}\ 1s - C_{alkyl}\ 1s)$ values for H_2O were indicative of α_{solv} values for $[C_4C_1Im]^+$ in H_2O.
3. H_2O does not fit the observed relationship for $\Delta E_B(C_{hetero}\ 1s - C_{alkyl}\ 1s)$ against β_{solv} due to its small size and strong coordinating ability.

Anion identity was not shown to affect solvent component energies $E_B(O_{liq}\ 1s)$ in aqueous solution. The lack of influence of anion identity on solvent components at low electrolyte concentration was confirmed through N 1s RXP spectra, which were found to be identical in both, shape and relative peak energies.

In future, the influence of varying anion identity on the electronic structure of all components in solution should be carried out for different cation-based ILs, *e.g.*, $[P_{66614}]^+$, to confirm whether the general rules suggested within this chapter extend beyond $[C_nC_1Im]$ -based ILs. Additionally, varying the solvent identity for each [cation][anion] combination will allow for a comparative dataset to that of [C_4C_1Im][SCN], K[SCN], and Li[NTf_2], as previously discussed (Chapter 3). Finally, building upon the measurement of the same atomic OCOs within different anionic environments will aid in determining the anion dependency on ΔE_B(anion) trends, particularly for F 1s OCO species.

4.5. References

1. J. M. Hamlyn and M. P. Blaustein, *American Journal of Physiology-Renal Physiology*, 1986, **251**, F563-F575.
2. B. Eisenberg, *Physiology*, 2013, **28**, 28-38.
3. R. Francke and R. D. Little, *Chemical Society Reviews*, 2014, **43**, 2492-2521.
4. Y. Yamada, J. H. Wang, S. Ko, E. Watanabe and A. Yamada, *Nat. Energy*, 2019, **4**, 269-280.
5. T. Cremer, C. Kolbeck, K. R. J. Lovelock, N. Paape, R. Wölfel, P. S. Schulz, P. Wasserscheid, H. Weber, J. Thar, B. Kirchner, F. Maier and H. P. Steinrück, *Chem.-Eur. J.*, 2010, **16**, 9018-9033.
6. I. Krossing, J. M. Slattery, C. Daguenet, P. J. Dyson, A. Oleinikova and H. Weingärtner, *Journal of the American Chemical Society*, 2006, **128**, 13427-13434.
7. U. P. R. M. Preiss, J. M. Slattery and I. Krossing, *Ind. Eng. Chem. Res.*, 2009, **48**, 2290-2296.
8. R. J. Rees, G. H. Lane, A. F. Hollenkamp and A. S. Best, *Physical Chemistry Chemical Physics*, 2011, **13**, 10729-10740.
9. M. A. A. Rocha, C. F. R. A. C. Lima, L. R. Gomes, B. Schröder, J. A. P. Coutinho, I. M. Marrucho, J. M. S. S. Esperança, L. P. N. Rebelo, K. Shimizu, J. N. Canongia Lopes and L. M. N. B. F. Santos, *Journal of Physical Chemistry B*, 2011, **115**, 10919-10926.
10. M. Holzweber, R. Lungwitz, D. Doerfler, S. Spange, M. Koel, H. Hutter and W. Linert, *Chem.-Eur. J.*, 2013, **19**, 288-293.
11. Y. Zhang, C. J. Shi, J. F. Brennecke and E. J. Maginn, *Journal of Physical Chemistry B*, 2014, **118**, 6250-6255.
12. Y. V. Nelyubina, A. S. Shaplov, E. I. Lozinskaya, M. I. Buzin and Y. S. Vygodskii, *Journal of the American Chemical Society*, 2016, **138**, 10076-10079.
13. S. T. Keaveney, R. S. Haines and J. B. Harper, *Pure and Applied Chemistry*, 2017, **89**, 745-757.
14. M. H. Keshavarz, B. Nazari, M. Jafari and Z. Yazdani, *Journal of Thermal Analysis and Calorimetry*, 2018, **134**, 2383-2390.
15. R. Seidel, B. Winter and S. E. Bradforth, *Annual Review of Physical Chemistry*, 2016, **67**, 283-305.
16. N. Weiß, C. H. Schmidt, G. Thielemann, E. Heid, C. Schröder and S. Spange, *Physical Chemistry Chemical Physics*, 2021, **23**, 1616-1626.
17. C. Reichardt and T. Welton, *Solvents and Solvent Effects in Organic Chemistry*, Wiley, Weinheim, 4th edn., 2011.

18. R. G. Pearson, *Inorganic Chemistry*, 1988, **27**, 734-740.
19. B. A. Marekha, O. N. Kalugin, M. Bria, T. Takamuku, S. Gadzuric and A. Idrissi, *ChemPhysChem*, 2017, **18**, 718-721.
20. R. Seidel, M. N. Pohl, H. Ali, B. Winter and E. F. Aziz, *Review of Scientific Instruments*, 2017, **88**, 073107.
21. R. M. Fogarty, R. G. Palgrave, R. A. Bourne, K. Handrup, I. J. Villar-Garcia, D. J. Payne, P. A. Hunt and K. R. J. Lovelock, *Physical Chemistry Chemical Physics*, 2019, **21**, 18893-18910.
22. R. Lungwitz, M. Friedrich, W. Linert and S. Spange, *New Journal of Chemistry*, 2008, **32**, 1493-1499.
23. R. Lungwitz, V. Strehmel and S. Spange, *New Journal of Chemistry*, 2010, **34**, 1135-1140.
24. J. Wyman, *Journal of the American Chemical Society*, 1931, **53**, 3292-3301.
25. K. R. J. Lovelock, I. J. Villar-Garcia, F. Maier, H. P. Steinrück and P. Licence, *Chemical Reviews*, 2010, **110**, 5158-5190.
26. J. M. Seymour, E. Gousseva, A. Large, G. Held, D. Hein, G. Wartner, W. Quevedo, R. Seidel, C. Kolbeck, C. J. Clarke, R. Fogarty, R. Bourne, R. Bennett, R. Palgrave, P. A. Hunt and K. R. J. Lovelock, *Faraday Discussions*, 2022.

Chapter 5

Influence of aqueous electrolyte concentration on electronic structure

Abstract

Understanding the electronic structure of all components within an electrolyte solution is an important step towards predicting their suitability of implementation in a plethora of applications, *e.g.,* battery systems and heterogeneous catalysis reactions. This is especially necessary in a world that requires us to shift from non-renewable to renewable energy sources, where efficient, powerful, and environmentally safe battery systems are needed for a host of situations. The complete electronic structure of a species contains contributions from both, the non-bonding occupied core orbitals (OCOs), and the bonding valence states, where the energy of the highest occupied valence states (HOVSs) and lowest unoccupied molecular orbitals (LUMOs) reveal key information on the electronic and physico-chemical properties of each component within the system. The identity of the HOVS and LUMO of a solution can be tuned according to the electrolyte concentration, enabling different functionality depending upon the ratio of ions to molecular solvent molecules in solution. Moreover, OCO energies provide an indication of the effects of varying solvation environment on the energetic properties of each species in solution. Therefore, improved insight into the electronic structure of all components within solution will aid in better component choice within the design of new electrolyte systems. With this in mind, ions in aqueous solution across the entire concentration range were studied, utilising complementary X-ray spectroscopic techniques to probe the effect of changing solvation environment on the electronic structure of all components in solution. The directionality of all anionic and solvent energy level shifts were shown to be similarly influenced by the changing solvation environment, with solvent energy shifts found to be twice as large as anionic electronic states. Linear energetic relationships were found to exist between core and valence states for both, ionic, and solvent species. The recorded energy trends allowed for three key conclusions to be drawn.

5.1. Introduction

Ions in solution feature heavily within vast aspects of chemistry. Such solutions are termed electrolytes, and their constituent components can be summarised as cations, anions, and solvent molecules. Current applications of electrolytes include: advanced battery technologies,[1] dye-sensitised solar cells,[2, 3] thermo-electrochemical cells,[3] supercapacitors,[4] and sensors.[5] Rechargeable batteries, such as Li-ion batteries (LIBs), are at the forefront of the modern world's rapid transition away from non-renewables toward renewable energy sources, as we shift from vehicles running on petroleum to those powered by electricity. However, the basic formula for rechargeable LIBs (1 M $LiPF_6$ in ethylene carbonate) has not changed significantly since the early 1990s.[6] Consequently, current LIB systems are unable to keep up with the increasing ambitions of the developing world, which now go far beyond handheld devices. The need for batteries capable of supporting higher energy densities (voltage and capacity), while remaining safe, cost effective, and with a low environmental impact mean that new electrolyte systems must be developed.[7-10]

Research into new electrolytes include ionic liquids, which are considered concentrated electrolytes as they are liquids comprised only of mobile cations and anions.[11] Concentrated electrolytes are thought to allow new functionality, relative to currently employed dilute electrolyte systems, due to their unique coordination states.[6] For example, concentrated electrolytes enable higher voltage, capacity, and faster charge/discharge of battery systems.[6] On the contrasting position of the concentration scale, a current exciting area of interest is the incorporation of aqueous electrolyte systems, which offer far greater safety over their volatile, flammable, organic solvent counterparts.[6, 7, 10, 12-16] To better understand the fundamentals behind the possible new functions of electrolytes in aqueous solution, and to further optimise the processes in which they are employed, the entire concentration range must be probed, *i.e.*, from dilute electrolytes to concentrated electrolytes. One such way of furthering our understanding lies in electronic structure measurements for each component. Probing of the valence electronic structure can provide insight into the energetic states which control both electronic and physico-chemical interactions. Physico-chemical interactions include: chemical reactivity (*e.g*. thermal decomposition, homogeneous catalysis[17, 18]), electrochemistry (*e.g*. electrochemical window,[19] solute redox potentials[20]), and surface-ionic liquid interactions (*e.g.* heterogeneous catalysis[21, 22]). Electronic interactions (with light) include: radiolysis (*e.g*. excess electrons[23-27]), electronic absorption spectroscopy,[28] and photochemistry (*e.g*. nanoparticles dissolved in ionic liquids[29-31]). The most important valence states which govern these interactions are the highest occupied valence state (HOVS) and the lowest unoccupied molecular orbital (LUMO). The HOVS and LUMO of a system are most significant in relation to battery electrolyte oxidation and reduction.[32]

HOVS and LUMO energies have previously been linked to electronic stability of electrolytes.[33] Typically, the identity of the HOVS is associated with the anionic species, while the identity of the LUMO is synonymous with the cationic species.[34-36] However, in select circumstances the HOVS has instead been shown to originate from the cationic component.[26, 37, 38] Therefore, consideration of the HOVS and LUMO energies of both ionic species should be carefully considered when selecting an electrolyte solution. The identity of the HOVS and LUMO in solution has also been shown to vary between solute and solvent species according to the electrolyte concentration, demonstrating the important role of electrolyte concentration within electronic structure determination.[10, 39, 40] The valence electronic structure of both, dilute electrolyte solutions,[41-43] and concentrated electrolyte solutions,[34-36, 44, 45] for differing electrolyte systems have been measured extensively. However, the electronic structure of each component within dilute, intermediate, and concentrated, aqueous solutions for the same system have sparsely been compared.[46, 47] Therefore, knowledge of the energetic variations of the HOVSs and LUMOs of each component within an aqueous solution across the entire concentration range is currently lacking.[46, 47]

In this chapter, comprehensive electronic structure data for an electrolyte across the entire concentration range is reported, from an infinite dilution of ions in molecular solvent (dilute electrolyte), to ions in ions (concentrated electrolyte, Figure 5.1b). Four different concentrations of $([C_4C_1Im][SCN])_x(H_2O)_{1-x}$, where x_{IL} = 0.01, 0.10, 0.25 and 1.00 (see Figure 5.1a for the structure of $[C_4C_1Im][SCN]$), were measured. A range of complementary photoelectron spectroscopic techniques were utilised during this investigation: non-resonant X-ray photoelectron spectroscopy (NRXPS), X-ray absorption spectroscopy (XAS) and resonant X-ray photoelectron spectroscopy (RXPS, also known as resonant Auger electron spectroscopy, RAES). The identification of trends and relationships between system HOVS and LUMO energies were permitted, enabling discussion as to whether the observed energy shifts were due to ground state (initial state) or excited state (final state) effects. Lastly, a mechanism of interaction between ions and solvent molecules which rationalise these findings is examined.

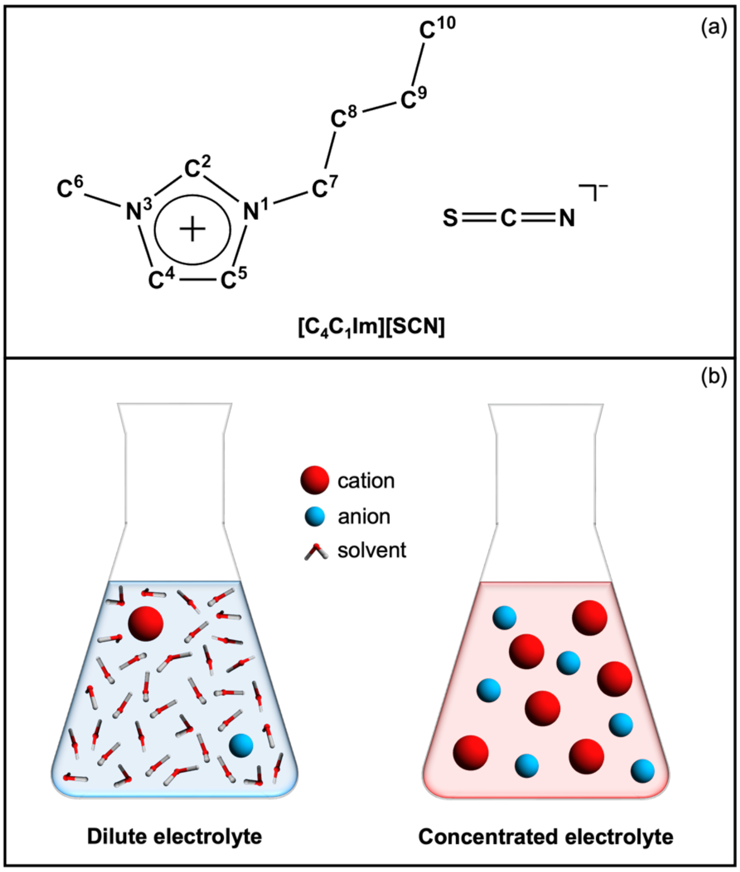

Figure 5.1. Samples measured within Chapter 5, where $([C_4C_1Im][SCN])_x(H_2O)_{1-x}$ was studied at various concentrations, from dilute electrolyte, to concentrated electrolyte. (a) The structure of $[C_4C_1Im][SCN]$, where atoms are numbered according to convention for reference within the current work. (b) A graphic depiction of a dilute electrolyte (left) and a concentrated electrolyte, which is not intended to represent the orientation or arrangement of ions or solvent molecules within solution; red = cation, blue = anion, and solvent (H_2O) = ball and stick structure.

5.2. Spectroscopic methods

5.2.1. Sample preparation

$[C_4C_1Im][SCN]$ was purchased from Iolitec, with no further purification prior to measurement. Highly demineralised water (conductivity ~0.2 μS cm^{-1}) was used for all aqueous solutions (Table 5.1). $[C_4C_1Im][SCN]$ was weighed and mixed with a corresponding mass of water to achieve the desired concentration (Appendix Table 8.1).

Table 5.1. The four solutions studied within Chapter 5. Concentrations were calculated using parameters listed in Appendix Tables 8.1 to 8.3.

	x_{IL}	x_{H2O}	conc. IL/ M	conc. H_2O/ M	IL:H_2O ratio
$[C_4C_1Im][SCN]$	100	0	5.4	0	1:0
$([C_4C_1Im][SCN])_{0.25}(H_2O)_{0.75}$	25	75	4.2	12.6	1:3
$([C_4C_1Im][SCN])_{0.10}(H_2O)_{0.90}$	10	90	2.9	26.0	1:9
$([C_4C_1Im][SCN])_{0.01}(H_2O)_{0.99}$	1	99	0.5	50.3	1:99

5.2.2. Synchrotron XPS apparatus

The measurement of $([C_4C_1Im][SCN])_x(H_2O)_{1-x}$, where x_{IL} = 0.01, 0.10 and 0.25 was performed on the U49/2-PGM 1 beamline with SOL^{3}PES end-station[48] at BESSY II (Germany). Liquid-jet apparatus was used.[48] XP and RXP spectra were acquired using a Scienta Omicron R4000 HIPP-2 hemispherical electron analyser. The analyser angle was 90.0° horizontal to the plane of polarised light.

RXPS measurements for $[C_4C_1Im][SCN]$ (x_{IL} = 1.00) was performed on the I311 beamline at MAX-lab (Sweden). The apparatus used at MAX-lab is explained in reference [36].

5.2.3. Laboratory XPS apparatus

Laboratory–based XPS for the IL $[C_4C_1Im][SCN]$ (x_{IL} = 1.00) was carried out using a Thermo K–alpha spectrometer utilising Al Kα radiation ($h\nu$ = 1486.6 eV), as detailed in reference [36].

5.3. Results and discussion

5.3.1. Changes in anionic and water atomic charge with varying x_{IL}

The occupied core orbital (OCO) E_B of the anionic components within $([C_4C_1Im][SCN])_x(H_2O)_{1-x}$ at varying x_{IL}, and the OCO E_B of the solvent, H_2O, were measured by NRXPS (Figure 5.2). The anionic components included the nitrogen 1s, $E_B(N_{anion}$ 1s), and sulfur 2p, E_B(S $2p_{3/2}$), states, which were readily identified using NRXPS (Figures 5.2a and 5.2b respectively). A single N_{anion} electronic environment from the $[SCN]^-$ anion resulted in a single Gaussian-like peak within the N 1s region (the N_{cation} peak was also present at higher E_B within the same region, Figure 5.2a). A single S_{anion} electronic environment, also from the $[SCN]^-$ anion, resulted in two peaks within the S 2p region at both high and low E_B due to spin-orbit-coupling, which were labelled the $2p_{1/2}$ and $2p_{3/2}$ peaks respectively. The O 1s OCO of the solvent, $E_B(O_{liq}$ 1s), was also measured (Figure 5.2c). For $0.01 \leq x_{IL} < 1.00$, a single O_{liq} electronic environment arising from the liquid-phase solvent, H_2O, resulted in a single gaussian-like peak in the O_{liq} 1s region (a sharp peak for O_{gas} 1s was also present at higher E_B, Appendix Figures 8.22 to 8.24).

A comparison between the OCO E_B values for the anionic and solvent components and electrolyte concentration showed that the E_B of each component decreased with increasing x_{IL} (Figure 5.3, Table 5.2). Therefore, anionic atomic charge was shown to be most positive at low values of x_{IL} (dilute electrolyte), while decreasing towards higher values of x_{IL} (concentrated electrolyte). At $x_{IL} = 0.01$, anions (and cations) were assumed to exist in an infinite dilution of H_2O molecules, where many H_2O molecules were available for solvation of the anion (and cation) in solution. Therefore, the ease with which anionic atomic charge was delocalised between many H_2O molecules was great. Anionic atomic charge was more positive at $x_{IL} = 0.01$ than $x_{IL} = 1.00$ due to the increased ability of charge delocalisation from the anion over a larger number of H_2O molecules. However, as x_{IL} increased, the ratio of IL:H_2O increased (Table 5.1) and the ability of the excess H_2O molecules to moderate the anionic atomic charge lessened. With increasing x_{IL}, the decreasing value of $E_B(O_{liq}$ 1s) reflected the dwindling ability of the solvent molecules to delocalise atomic charge amongst the decreasing number of neighbouring H_2O molecules in solution. Hence, both anionic and H_2O atomic charge decreased with increasing x_{IL}; anionic atomic charge decreased due to a lack of stabilising H_2O molecules and H_2O atomic charge decreased due to a lack of sufficient H_2O molecules in solution with which to share anionic atomic charge.

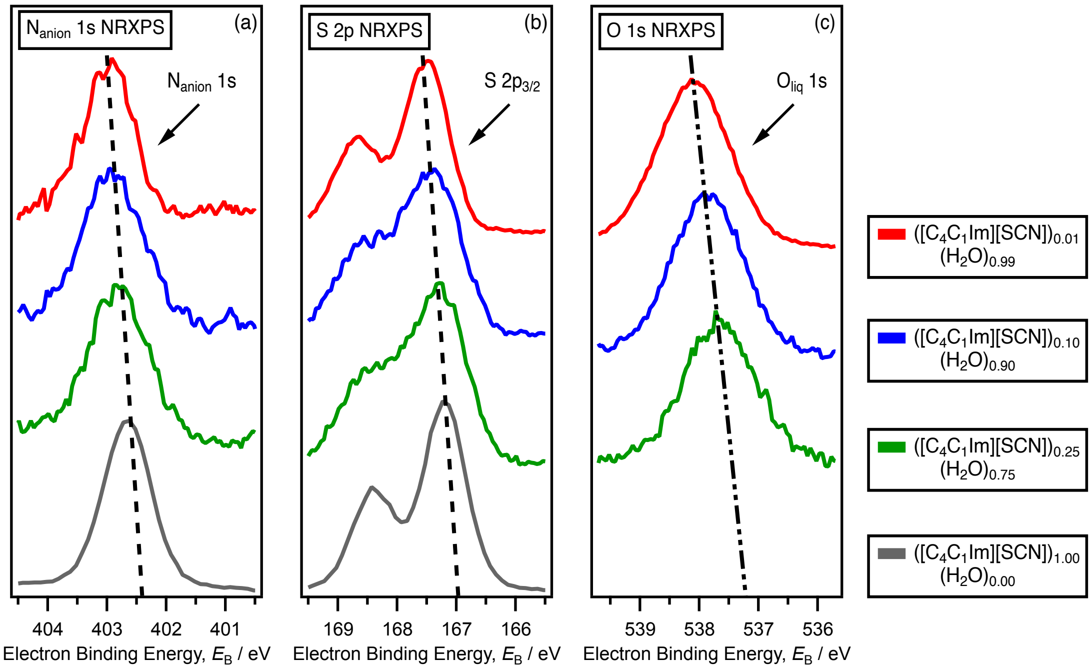

Figure 5.2. NRXPS spectra for $([C_4C_1Im][SCN])_x(H_2O)_{1-x}$, where x_{IL} = 0.01 (red), 0.10 (blue), 0.25 (green) and 1.00 (grey). (a) N_{anion} 1s NRXP spectra. (b) S 2p NRXP spectra. (c) O 1s NRXP spectra. All XP spectra for solutions of $([C_4C_1Im][SCN])_x(H_2O)_{1-x}$, where x_{IL} = 0.01, 0.10, and 0.25, were measured at $h\nu$ = 700.0 eV; pure $[C_4C_1Im][SCN]$ XP spectra were measured at $h\nu$ = 1486.6 eV. Dashed lines are intended as a visual aid of the changes in E_B that occur with varying x_{IL}, where lines of the same type have the same gradient. All values were charge referenced using the methods detailed in Section 2.7.1.

Table 5.2. Experimental binding energies, E_B, recorded by NRXPS for $([C_4C_1Im][SCN])_x(H_2O)_{1-x}$, where x = 0.01, 0.10, 0.25 and 1.00. All values were charge referenced using the methods detailed in Section 2.7.1.

		Electron Binding Energy / eV		
	x_{IL}	$E_B(N_{anion}$ 1s) (± 0.03 eV)	$E_B(S\ 2p_{3/2})$ (± 0.06 eV)	$E_B(O_{liq}$ 1s) (± 0.06 eV)
$([C_4C_1Im][SCN])_{0.01}(H_2O)_{0.99}$	0.01	403.00	167.53	538.10
$([C_4C_1Im][SCN])_{0.10}(H_2O)_{0.90}$	0.10	402.92	167.37	537.94
$([C_4C_1Im][SCN])_{0.25}(H_2O)_{0.75}$	0.25	402.82	167.30	537.73
$([C_4C_1Im][SCN])_{1.00}(H_2O)_{0.00}$	1.00	402.66	167.20	

The measured anionic OCO energies, $E_B(N_{anion}\ 1s)$ and $E_B(S\ 2p_{3/2})$, were shown to trend in the same direction by the same magnitude with increasing x_{IL}, whereas $E_B(O_{liq}\ 1s)$ was shown to trend in the same direction as each OCO energy but by a greater magnitude with increasing x_{IL}. The differing magnitude of OCO E_B shifts were reflected in the type of each visual aid shown in Figures 5.2a, 5.2b compared to Figure 5.2c. As shown, $E_B(N_{anion}\ 1s)$ and $E_B(S\ 2p_{3/2})$ followed a monotonic (always decreasing) exponential curve shape when plotted against x_{IL} (Figure 5.3a and 3.3b). When viewed in conjunction with Table 5.2 the anionic components were shown to decrease by approximately 0.1 eV between each measured x_{IL} increase. $E_B(O_{liq}\ 1s)$ was also found to decrease with increasing x_{IL} but the trend looked far more linear than the trend in anionic components (although this may be due to lack of measured datapoints, Figure 5.3c); one can assume that this trend would also become exponential with a greater number of datapoints due to the need to balance atomic charge within in the system. For the solvent component, E_B decreased by approximately 0.2 eV with each measured x_{IL} increment. Consequently, $E_B(O_{liq}\ 1s)$ was found to decrease at twice the rate of $E_B(N_{anion}\ 1s)$ and $E_B(S\ 2p_{3/2})$ at the same values of x_{IL}. The more greatly decreasing E_B(solvent) relative to E_B(anion) had previously been observed (although not explicitly mentioned) for NaI in water.[47] The cause of this phenomena is explained in a two-fold and cumulative manner:

1. Bulk effects

As previously discussed, anionic atomic charge was delocalised across solvent molecules, driving $E_B(O_{liq}\ 1s)$ to lower energies with increasing electrolyte concentration. Additionally, as the ratio of IL:H_2O increased, the number of H_2O molecules within the solvent bonding network was fewer. A reduced number of solvent molecules forced H_2O from its preferred tetrahedral structure, as it is known to exist in the bulk, to a crystalline-like phase.[46, 47] However, this would have eventually resulted in a stabilisation (shift to positive E_B) of the solvent OCOs with increasing x_{IL}, whereas destabilisation (shift to negative E_B) of the solvent OCOs with increasing x_{IL} was observed. Therefore, perhaps the solution containing the highest H_2O content (x_{IL} = 0.25) was not great enough to permit such an observation.

2. Surface effects

The surface electrical potential of an electrolyte solution (ions in water in this case) relies upon both, the surface dipole formation and the distribution of ions in solution.[49, 50] The surface potential of pure water is low due to one O-H (non-hydrogen bonding) pointing towards the continuum, and another O-H (hydrogen bonding) pointing toward the bulk liquid, resulting in a permanent dipole along the solution surface.[51] However, upon addition of IL to water, a negative change in surface potential (the change from surface to bulk) with increasing x_{IL} is expected, as $[C_4C_1Im]^+$ is shown to lay flat on the liquid-gas interface with alkyl chains pointing towards the gas phase, and $[SCN]^-$ is shown to be either, not present, or poorly orientated at the interface.[52, 53] Therefore, an ionic double layer is created near the surface with its negative side pointed towards the bulk liquid.[54] This may lead to destabilisation of solvent OCOs as they interact with the positively charged cations at the surface, which are capable of accepting electron density, resulting in a more negative $E_B(O_{liq}\ 1s)$.

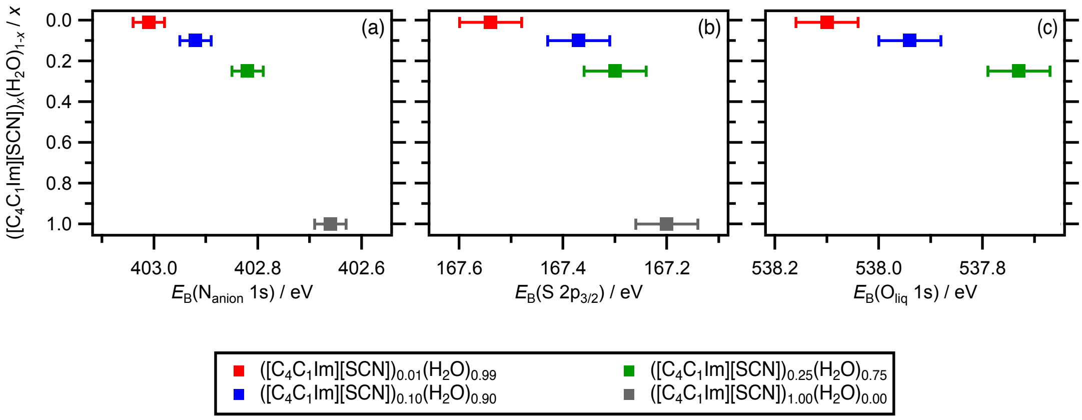

Figure 5.3. Photoemission peak binding energies, E_B, against $([C_4C_1Im][SCN])_x(H_2O)_{1-x}$, where x_{IL} = 0.01 (red), 0.10 (blue), 0.25 (green) and 1.00 (grey). (a) $E_B(N_{anion}\ 1s)$ against x_{IL}. (b) $E_B(S\ 2p_{3/2})$ against x_{IL}. (c) $E_B(O_{liq}\ 1s)$ against x_{IL}. All XP spectra for solutions of $([C_4C_1Im][SCN])_x(H_2O)_{1-x}$, where x_{IL} = 0.01, 0.10, and 0.25, were measured at $h\nu$ = 700.0 eV; pure $[C_4C_1Im][SCN]$ XP spectra were measured at $h\nu$ = 1486.6 eV. All values were charge referenced using the methods detailed in Section 2.7.1.

Depth profile experiments were carried out for the solution of $([C_4C_1Im][SCN])_{0.01}(H_2O)_{0.99}$ by monitoring $E_B(N_{anion}\ 1s)$ within the N 1s NRXPS spectra at various $h\nu$ (Figure 5.4a). According to the universal inelastic mean free path (IMFP) curve (Figure 2.1), the chosen $h\nu$ range enabled the probing of the solution at multiple depths (at 95 % signal intensity) between 1.29 nm ($h\nu$ = 450 eV) to 4.56 nm ($h\nu$ = 1200 eV). The measured $E_B(N_{anion}\ 1s)$ shift with varying $h\nu$ was found to be negligible and within the error of the experiment for the measured range of $h\nu$ = 450 eV to 1200 eV (Figure 5.4b). As the E_B shifts caused by surface versus bulk measurements were relatively small in comparison to E_B shifts measured as a function of concentration, energetic variations for OCOs with varying electrolyte concentration observed within this work were evidently not an artefact of surface versus bulk effects and were instead a reflection of solvent-solute interactions in solution. The measured E_B values have previously been shown not to be influenced by interfacial and bulk-solution structure differences.[46]

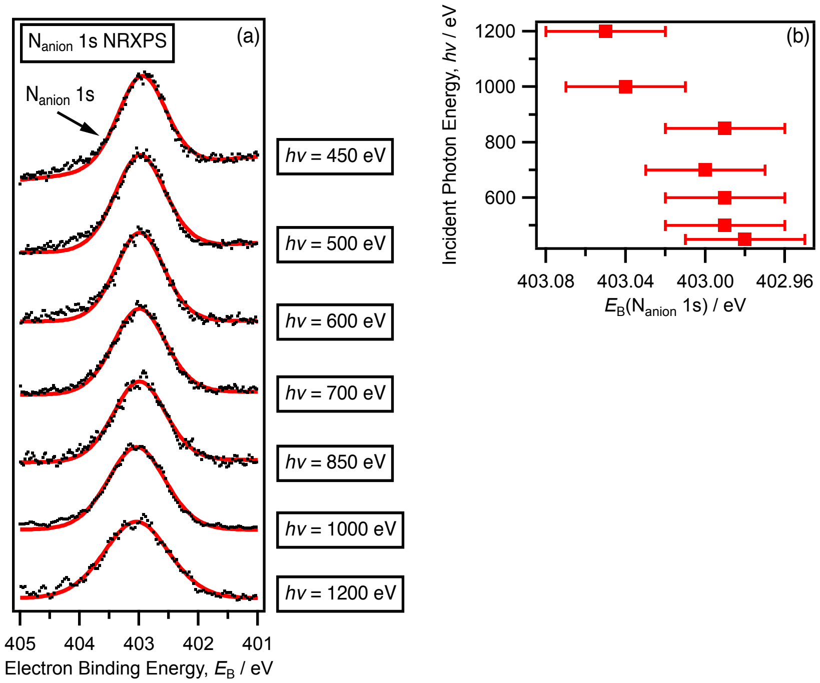

Figure 5.4. Depth profile experiments for E_B(N$_{anion}$ 1s) at varying *hν* (450.0 eV, 500.0 eV, 600.0 eV, 700.0 eV, 850.0 eV, 1000.0 eV, and 1200.0 eV) for a solution of ([C$_4$C$_1$Im][SCN])$_{0.01}$(H$_2$O)$_{0.99}$: (a) N$_{anion}$ 1s NRXP spectra at varying *hν*. (b) E_B(N$_{anion}$ 1s) against *hν*. All values were charge referenced using the methods detailed in Section 2.7.1.

Table 5.3. Experimental area and FWHM ratios of (N$_{cation}$ 1s/N$_{anion}$ 1s) and (S 2p$_{3/2}$/S 2p$_{1/2}$) recorded by NRXPS for ([C$_4$C$_1$Im][SCN])$_x$(H$_2$O)$_{1-x}$, where x_{IL} = 0.01, 0.10, 0.25, and 1.00. All XP spectra for solutions of ([C$_4$C$_1$Im][SCN])$_x$(H$_2$O)$_{1-x}$, where x_{IL} = 0.01, 0.10, and 0.25, were measured at *hν* = 700.0 eV; pure [C$_4$C$_1$Im][SCN] XP spectra were measured at *hν* = 1486.6 eV.

	(N$_{cation}$ 1s / N$_{anion}$ 1s)	
	Area	FWHM / eV
([C$_4$C$_1$Im][SCN])$_{0.01}$(H$_2$O)$_{0.99}$	2.27	1.06
([C$_4$C$_1$Im][SCN])$_{0.10}$(H$_2$O)$_{0.90}$	2.18	0.98
([C$_4$C$_1$Im][SCN])$_{0.25}$(H$_2$O)$_{0.75}$	2.18	1.00
([C$_4$C$_1$Im][SCN])$_{1.00}$(H$_2$O)$_{0.00}$	2.21	1.08

The photoelectron peak area ratio and full width at half maximum (FWHM) ratio for measured peaks within the N 1s NRXP spectra, (N_{cation} 1s/N_{anion} 1s) were compared for all solutions of $([C_4C_1Im][SCN])_x(H_2O)_{1-x}$ (Table 5.3.). The values used to calculate area ratio reflected the total intensity of electrons within the measurement, due to reported peaks being the sole photoelectron peaks within the region. Therefore, area ratios presented in Table 5.3. were to be considered percentage atomic concentration measurements. Hence, small changes in experimental conditions did not influence relative comparisons between samples.

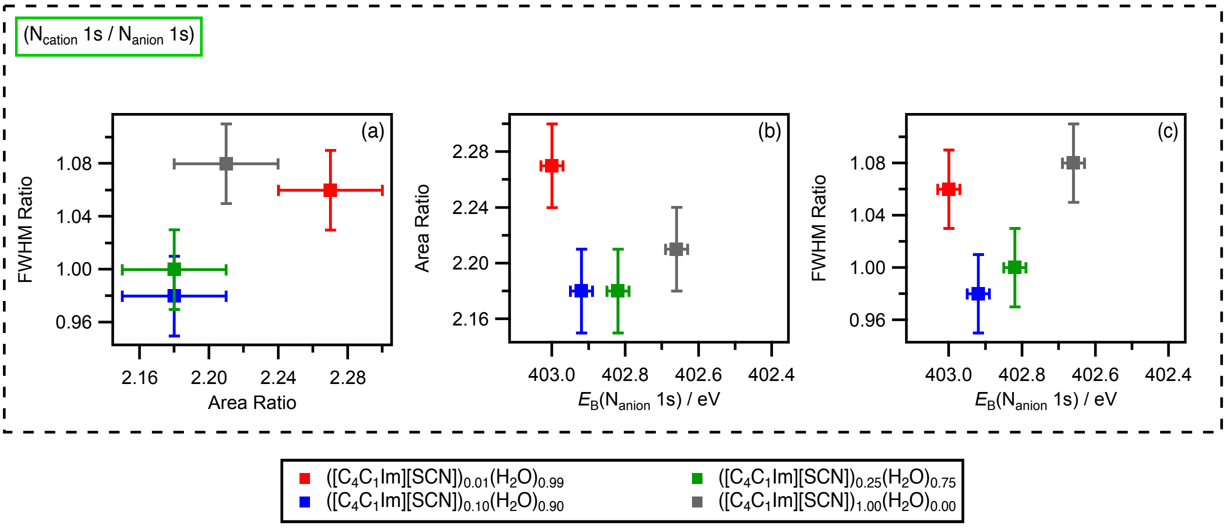

Figure 5.5. Comparisons between E_B(anion), area ratio, and FWHM ratio for (N_{cation} 1s/N_{anion} 1s): (a) FWHM ratio against area ratio for (N_{cation} 1s/N_{anion} 1s). (b) Area ratio against E_B(N_{anion} 1s) for (N_{cation} 1s/N_{anion} 1s). (c) FWHM ratio against E_B(N_{anion} 1s) for (N_{cation} 1s/N_{anion} 1s). All XP spectra for solutions of $([C_4C_1Im][SCN])_x(H_2O)_{1-x}$, where x_{IL} = 0.01, 0.10, and 0.25, were measured at $h\nu$ = 700.0 eV; pure $[C_4C_1Im][SCN]$ XP spectra were measured at $h\nu$ = 1486.6 eV. All values were charge referenced using the methods detailed in Section 2.7.1.

The relationship between (N_{cation} 1s/N_{anion} 1s) area ratio and FWHM ratio was explored, with no significant correlation observed between the two (Figure 5.5a). Photoelectron peak area and FWHM ratios for (N_{cation} 1s/N_{anion} 1s) were also compared to E_B(N_{anion} 1s) (Figures 5.5b and 5.5c, respectively). Again, no significant correlation was observed between either, area ratio, or FWHM ratio, when compared to E_B(N_{anion} 1s). A greater FWHM value for measured photoelectron peaks is usually associated with the presence of additional electronic environment contributions with similar energies for the same atomic species.[55] Therefore, a lack of measured FWHM deviation as a function of concentration within this work suggested little to no variation of solvent-solute interactions within solution, at least in relation to the involvement of the cationic and anionic nitrogen atoms. The occurrence of separate specific solvent-solute interactions with varying electrolyte concentration was therefore not supported within the current analysis, even while the solvation regime changed from dilute ions in MS to concentrated ions in ions. Hence, the hypothesis that non-specific solvation effects were responsible for the measured E_B shift upon varying electrolyte concentration was supported.

5.3.2. Changes in cationic atomic charge with varying x_{IL}

The cationic components of $([C_4C_1Im][SCN])_x(H_2O)_{1-x}$ at varying x_{IL} were measured using NRXPS (Figure 5.6). The OCOs of the cationic components included the nitrogen 1s, $E_B(N_{cation}$ 1s), and carbon 1s, $E_B(C_{hetero}$ 1s) and $E_B(C_{alkyl}$ 1s), states, which were readily identified using NRXPS (Figures 5.6a, 5.6b respectively). A single N_{cation} electronic environment from the $[C_4C_1Im]^+$ cation resulted in a single gaussian-like peak within the N 1s region (the N_{anion} peak was also present at lower E_B within the same region at half the intensity due to half as many nitrogen atoms in the anion as in the cation, Figure 5.2a, Appendix Figures 8.22 to 8.24). There were three different carbon electronic environments in the C 1s NRXP spectra for solutions of $([C_4C_1Im][SCN])_x(H_2O)_{1-x}$, located on both the $[C_4C_1Im]^+$ cation and the $[SCN]^-$ anion. The carbon energetic electronic environments were labelled $E_B(C^2$ 1s), $E_B(C_{hetero}$ 1s) and $E_B(C_{alkyl}$ 1s). $E_B(C^2$ 1s) (atom 2, Figure 5.1) and $E_B(C_{alkyl}$ 1s) (atoms 7-10, Figure 5.1) carbon environments were located exclusively on the $[C_4C_1Im]^+$ cation. The $E_B(C_{hetero}$ 1s) included contributions from both the $[C_4C_1Im]^+$ cation (atom 4 and 5, Figure 5.1) and the $[SCN]^-$ anion (atom 12, Figure 5.1). Fitting parameters for the C 1s region were shown in Appendix Table 8.4 and have been described elsewhere.[36]

As $E_B(N_{cation}$ 1s) = 406.75 eV was used as a charge reference for all photoemission peaks, it was unsurprising that N_{cation} 1s peaks match in E_B. However, interestingly $E_B(C^2$ 1s), $E_B(C_{hetero}$ 1s) and $E_B(C_{alkyl}$ 1s) energies also matched with varying x_{IL} (same E_B at every electrolyte concentration). Therefore, it was evident that the E_B of cationic core level components shifted together with varying x_{IL}. The E_B shifts for all cationic photoemission peaks were shown to match with varying x_{IL} by NRXPS measurements, as they also were for anionic photoemission peaks (Section 5.3.1). Therefore, all NRXPS shifts matched in terms of size and direction in energy within each component, greatly suggesting that the electronic structure of ions in solution were influenced by non-specific solvation effects.

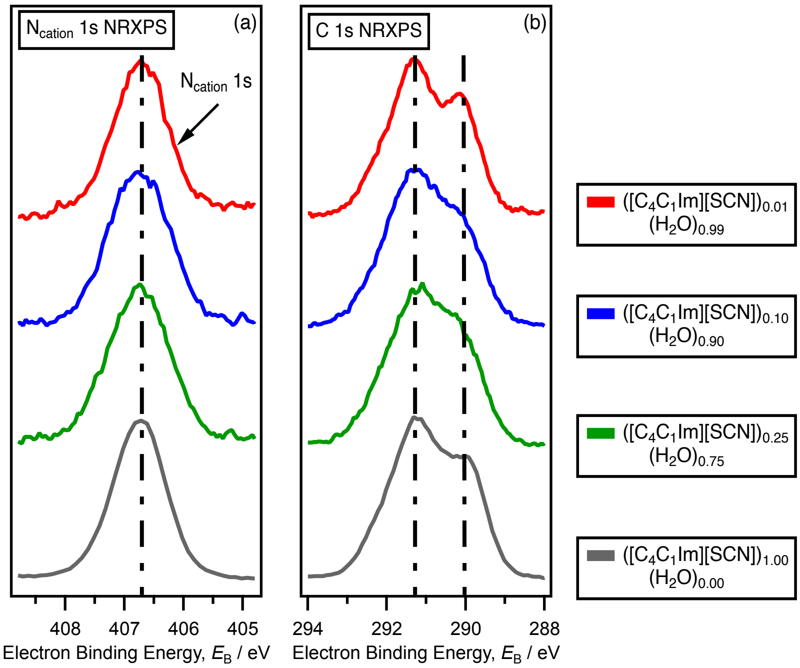

Figure 5.6. NRXPS spectra for $([C_4C_1Im][SCN])_x(H_2O)_{1-x}$, where x_{IL} = 0.01 (red), 0.10 (blue), 0.25 (green) and 1.00 (grey). (a) N_{cation} 1s NRXP spectra. (b) C 1s NRXP spectra. All spectra were measured at $h\nu$ = 700.0 eV. Dashed lines are intended as a visual aid of the changes in E_B that occur with varying x_{IL}. All XP spectra for solutions of $([C_4C_1Im][SCN])_x(H_2O)_{1-x}$, where x_{IL} = 0.01, 0.10, and 0.25, were measured at $h\nu$ = 700.0 eV; pure $[C_4C_1Im][SCN]$ XP spectra were measured at $h\nu$ = 1486.6 eV. All values were charge referenced using the methods detailed in Section 2.7.1.

5.3.3. HOVS and LUMO level shifts with varying x_{IL}

The valence electronic structure determines the potential of each species to participate within Lewis acidic or Lewis basic solvent-solute interactions. Of particular interest within the valence electronic structure are the highest occupied valence state (HOVS) and the lowest unoccupied molecular orbital (LUMO) of a system, which were measured using a combination of valence NRXPS and XAS (Figure 5.7).

The HOVS was probed using valence NRXPS (Figure 5.7a). The non-resonant valence state XP spectra, containing electronic contributions from all components from the entire system, was measured and the HOVS assigned to anionic N 2p and S 2p contributions.[36] As the HOVS contained multiple valence state contributions, its E_B position was labelled E_B(HOVS). E_B(HOVS) was shown to decrease with increasing values of x_{IL}.

The LUMO was indirectly probed using XAS, which yielded information on the energy of an electron transition from an OCO to an UMO, $h\nu(\text{OCO} \rightarrow \text{UMO})$. Through varying the incident photon energy, $h\nu$, it is possible to select for specific OCO → UMO transitions and therefore, XAS is considered an atom specific/selective technique.[35, 36] The N 1s edge (also known as the N K-edge) was probed and yielded two sharp peaks in the XA spectra (Appendix Figure 8.34). For both transitions, the excited electron originated from either the N_{anion} OCO ($h\nu$ = 399.7 eV) or the N_{cation} OCO ($h\nu$ = 402.1 eV), assigned to the N_{anion} 1s → π^* and N_{cation} 1s → π^* transitions respectively. The final state of each transition resulted in the occupancy of the π^* UMO, as both the $[C_4C_1\text{Im}]^+$ cation and the $[\text{SCN}]^-$ anion contain π-systems (involving the N atoms), which have high absorption intensities due to a large absorption cross-section.[35] As the HOVS contained purely anionic components, only the N_{anion} 1s → π^* transition was shown for clarity of comparison (Figure 5.7b). $h\nu(N_{\text{anion}}\ 1s \rightarrow \pi^*)$ probed the $\text{LUMO}_{\text{anion}}$ and was measured to be constant, $h\nu$ = 399.7 ± 0.06 eV, at all values of x_{IL}.

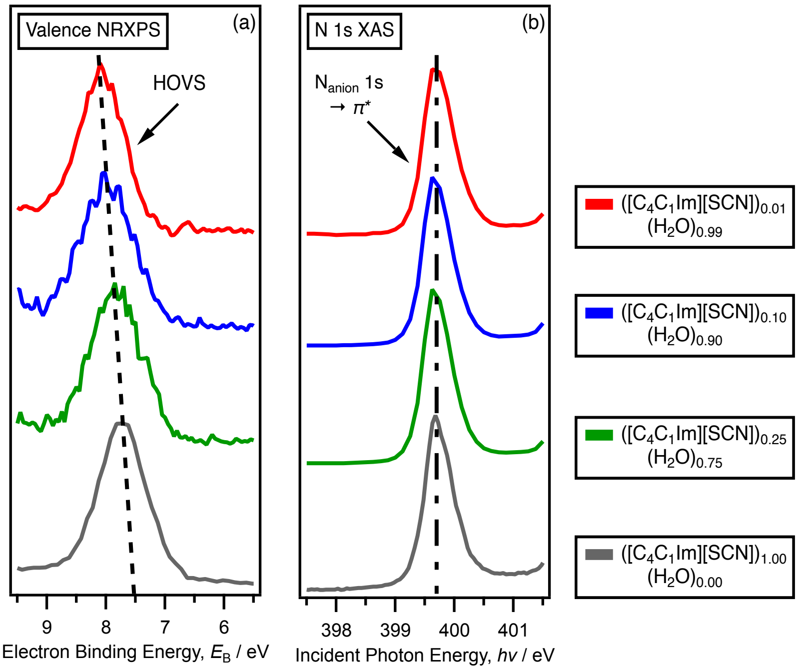

Figure 5.7. XAS spectra for $([C_4C_1\text{Im}][\text{SCN}])_x(H_2O)_{1-x}$, where x_{IL} = 0.01 (red), 0.10 (blue), 0.25 (green) and 1.00 (grey). (a) Valence NRXPS for solutions of $([C_4C_1\text{Im}][\text{SCN}])_x(H_2O)_{1-x}$, where x_{IL} = 0.01, 0.10, and 0.25, were measured at $h\nu$ = 700.0 eV; pure $[C_4C_1\text{Im}][\text{SCN}]$ XP spectra were measured at $h\nu$ = 1486.6 eV. (b) N_{anion} 1s → π^* XAS. Dashed lines are intended as a visual aid of the changes in E_B that occur with varying x_{IL}, where lines of the same type have the same gradient. Valence NRXPS values were charge referenced using the methods detailed in Section 2.7.1.

Plotting E_B against x_{IL} enabled a greater visual comparison of the change in both $h\nu$ and E_B across varying x_{IL} (Figure 5.8). E_B(HOVS) was shown to decrease, while $h\nu$(N_{anion} 1s → π*) did not change with varying x_{IL} (Figure 5.8a and Figure 5.8b, respectively). As $h\nu$(N_{anion} 1s → π*) was an energy transition, no observed change in $h\nu$ indicated that the energy gap between the OCO and the UMO was consistent across all x_{IL}. As E_B(N_{anion} 1s) had previously been shown to decrease with increasing x_{IL} (Figures 5.2a and 5.3a, Table 5.2), it could be deduced that the corresponding π* UMO trended in the same direction by the same magnitude, as little to no $h\nu$(N_{anion} 1s → π*) shift was observed with varying x_{IL}. Furthermore, as E_B(N_{anion} 1s) and E_B(HOVS) trended very similarly in energy (Figure 5.3a and Figure 5.8a, respectively), HOVS and $LUMO_{anion}$ level shifts were shown to be equal (within experimental error) with varying x_{IL}. Consequently, it was easier to remove an electron from the $[SCN]^-$ anion HOVS but harder to add an electron to the $[SCN]^-$ $LUMO_{anion}$, with increasing x_{IL}. Additionally, this indicated that the energy gap between the $LUMO_{anion}$ and $LUMO_{cation}$ increased with increasing electrolyte concentration. Similarly, the energy gap between the $HOVS_{anion}$ and $HOVS_{cation}$ increased with increasing electrolyte concentration. Hence, through careful control of electrolyte concentration, HOVS/LUMO energies can be tailored to favour specific requirements.

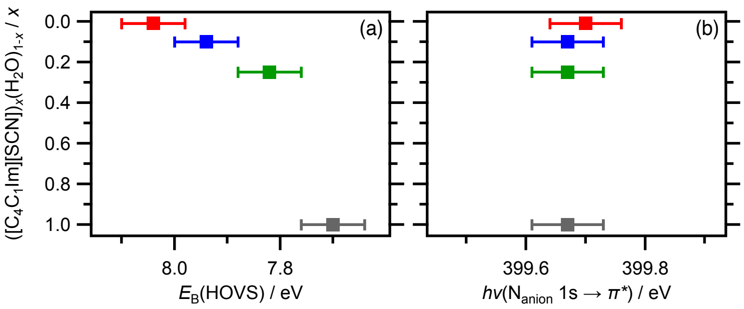

Figure 5.8. Photoemission peak binding energies, E_B, against $([C_4C_1Im][SCN])_x(H_2O)_{1-x}$, where x_{IL} = 0.01 (red), 0.10 (blue), 0.25 (green) and 1.00 (grey). (a) E_B(HOVS) against x_{IL}. (b) $h\nu$(N_{anion} 1s → π*) against x_{IL}. All values were charge referenced using the methods detailed in Section 2.7.1.

The implications of a tuneable HOVS/LUMO energy are great. For example, during the Diels-Alder reaction, some interactions are known to proceed at a much faster rate in water relative to other solvents; perhaps due to the increased accessibility of the LUMO of the species at low concentration in water versus in other solvents.[56-58] Greater understanding and control over solute LUMO energies may aid in greater control over the rates of these reactions. In addition, during condensed phase photodissociation reactions a more readily accessible LUMO may allow the dilute species to become more photoactive.[59] Lastly, susceptibility to nucleophilic attack is influenced by the energetic position of the LUMO; conversely, the ability of a successful nucleophile is influenced by the energetic position of the HOVS.[60]

5.3.4. Core and valence state atomic charge correlations with varying x_{IL}

Resonant X-ray photoelectron spectroscopy (RXPS) is a photoelectron technique which takes advantage of inherent resonant energies of atoms to enhance their photoionisation intensity signal.[36, 61, 62] RXPS can be described by two distinct processes: spectator Auger (SA) emission and participator Auger (PA) emission (Section 2.3). The resonant nature of the PA process is useful for identification of valence state contributions, especially for peaks hidden by solvent/surfaces. Therefore, within the current work, PA valence RXPS was used to separate cation, anion, and solvent contributions to the valence electronic structure.

Cationic valence states were probed using RXPS (from N 1s valence RXPS heat map, Appendix Figures 8.26 to 8.29). N 1s RXPS at the $h\nu$($\mathrm{N_{cation}}$ 1s → π^*) energy ($h\nu$ = 402.1 eV) revealed the position of the $\mathrm{N_{cation}}$ 2p valence state within the valence state (E_{B} = ~10.3 eV, Figure 5.9a). The E_{B}($\mathrm{N_{cation}}$ 2p) was impractical to measure with conventional NRXPS due to dominance and obstruction of the valence spectra by solvent photoemission peaks, *e.g.*, the $1\mathrm{b}_1$ valence state. The E_{B}($\mathrm{N_{cation}}$ 2p) remained at a fixed energy across all x_{IL}, similarly to E_{B}($\mathrm{N_{cation}}$ 1s). Additional cationic peaks, such as E_{B}($\mathrm{C_{alkyl}}$ 1s) (Figure 5.6b) were also measured to be at a fixed energy across all x_{IL}. Therefore, cationic core and valence state atomic charges were shown to correlate with varying x_{IL}.

Anionic valence states were probed using RXPS (from N 1s valence RXPS heat map, Appendix Figures 8.26 to 8.29). Relative to a fixed E_{B}($\mathrm{N_{cation}}$ 1s), E_{B}($\mathrm{N_{anion}}$ 1s), E_{B}(S $2\mathrm{p}_{3/2}$) and E_{B}(HOVS) shifted to lower energy with increasing x_{IL} (Figures 5.2a, 5.2b, 5.7a, respectively). N 1s RXPS at the $h\nu$($\mathrm{N_{anion}}$ 1s → π^*) edge revealed the position of the $\mathrm{N_{anion}}$ 2p valence state within the valence region (8.0 eV $\geq E_{\mathrm{B}} \geq$ 7.7 eV, Figure 5.9b). The $\mathrm{N_{anion}}$ 2p valence state had previously been shown to contribute to the HOVS peak using experimental RXPS.[36] E_{B}($\mathrm{N_{anion}}$ 2p) shifted to lower energy with increasing x_{IL}, similarly to E_{B}($\mathrm{N_{anion}}$ 1s), E_{B}(S $2\mathrm{p}_{3/2}$) and E_{B}(HOVS). It had not previously been reported that OCOs shift comparably to valence states (for the corresponding atom) in energy, when influenced by electrolyte concentration. Anionic core and valence state atomic charges therefore correlated with varying x_{IL}; atomic charge was more negative with increasing x_{IL}. Additionally, this would indicate that the energy gap between the $\mathrm{N_{anion}}$ 2p ($\mathrm{HOVS_{anion}}$) and $\mathrm{N_{cation}}$ 2p ($\mathrm{HOVS_{cation}}$) increased with increasing electrolyte concentration.

H_2O valence states were probed using RXPS (from O 1s valence RXPS heat map, Appendix Figures 8.31 to 8.33). Relative to a fixed E_B(N_{cation} 1s), E_B(O_{liq} 1s) shifted to lower energy with increasing x_{IL} (Figure 5.2c). O 1s RXPS at the $h\nu$(O_{liq} 1s → $4a_1$) edge revealed the position of the O_{liq} $1b_1$ valence state (11.3 eV $\geq E_B \geq$ 10.9 eV, Figure 5.9c). E_B($1b_1$) shifted to lower energy with increasing x_{IL} (11.3 eV $\geq E_B \geq$ 10.9 eV), similarly to E_B(O_{liq} 1s). Therefore, H_2O OCO and valence state atomic charges correlated with varying x_{IL}; atomic charge was more negative with increasing x_{IL}. As the $1b_1$ valence state was the H_2O HOVS, H_2O molecules were shown to be more reactive at low concentrations within a highly concentrated electrolyte solution.

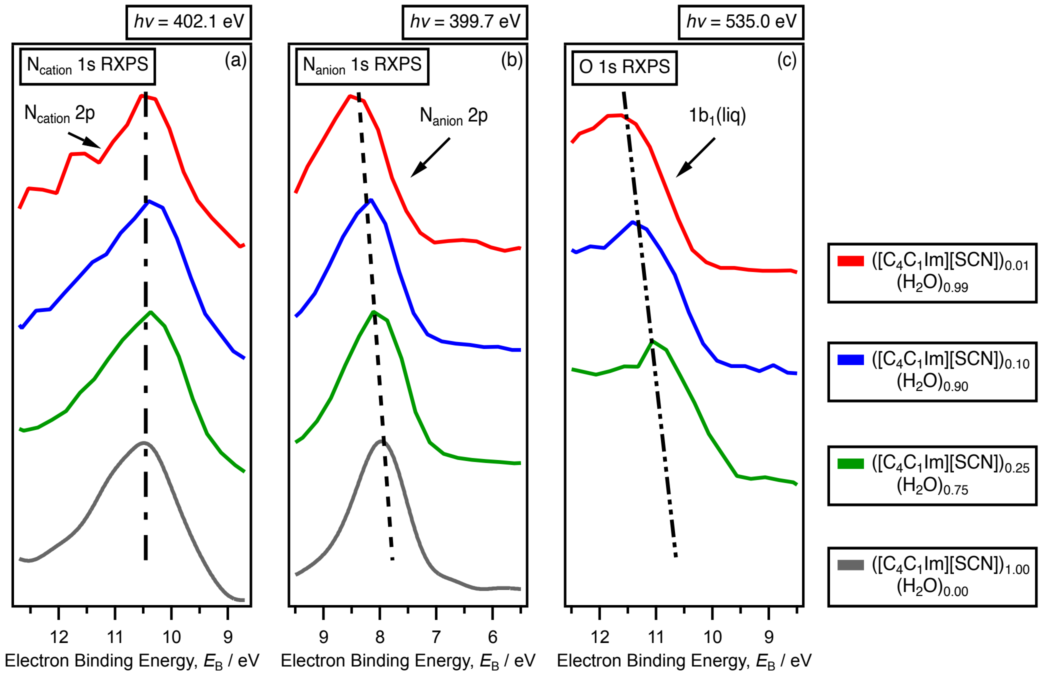

Figure 5.9. RXPS spectra for $([C_4C_1Im][SCN])_x(H_2O)_{1-x}$, where x = 0.01 (red), 0.10 (blue), 0.25 (green) and 1.00 (grey). (a) N_{cation} 1s at $h\nu$ = 402.1 eV. (b) N_{anion} 1s at $h\nu$ = 399.7 eV. (c) O_{liq} 1s RXPS at $h\nu$ = 535.0 eV. Dashed lines are intended as a visual aid of the changes in E_B that occur with varying x_{IL}, where lines of the same type have the same gradient. All values were charge referenced using the methods detailed in Section 2.7.3.

5.3.5. Experimental energy level diagram

Using data collected from a combination of complementary photoelectron spectroscopic methods allowed for the construction of an energy level diagram showing core, valence, and unoccupied energies (Figure 5.10). This allowed for easier visual comparison and a summary of the energetic trends within the system. NRXPS yielded values for both, E_B(N_{anion} 1s) and E_B(HOVS). XAS yields a transition energy rather than directly measuring the UMO energetic position. As E_B(N_{anion} 1s) is known from NRXPS measurements, E_B(N_{anion} 1s) minus $h\nu$ (N_{anion} 1s → π*) results in E_B(N_{anion} π*), enabling the determination of all core, valence, and unoccupied energies.

The energetic behaviour of each anionic component within the system was shown to follow the same trend: E_B decreased by approximately 0.1 eV for each successive measurement of increasing x_{IL}. The correlation between E_B and x_{IL} was not linear in nature. The fact that all OCO and OVS energy levels shifted by the same amount at each x_{IL} meant that no specific solvent-solute interactions or variation in covalent bonding occurred. This was supported by the identical overall shape of the N 1s RXP spectra with varying x_{IL} (Appendix Figure 8.36). As stated previously, the interactions taking place which resulted in a decrease in anionic component E_B with increasing electrolyte concentration were said to be non-specific solvation effects.

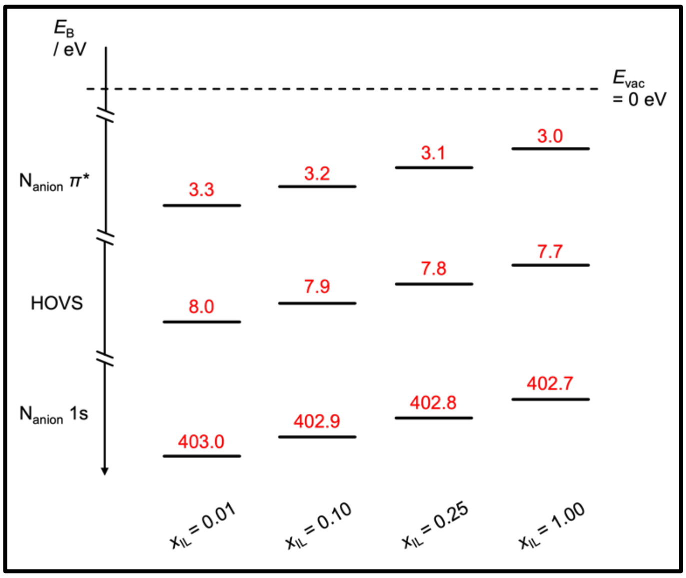

Figure 5.10. An energy level diagram for $([C_4C_1Im][SCN])_x(H_2O)_{1-x}$, where x_{IL} = 0.01, 0.10, 0.25 and 1.00, constructed from spectroscopic data measured using NRXPS and partial electron yield XAS. All values were charge referenced using the methods detailed in Section 2.7.1 (NRXPS) and Section 2.7.3 (RXPS).

An equivalent energy level diagram for the E_B shifts that occurred for the solvent component would have shown E_B for all OCO and UMO levels to trend similarly to Figure 5.10 between $0.01 < x_{IL} < 0.25$, but with E_B shifts twice as large. However, an equivalent energy level diagram for the shifts that occurred for the cationic component would have shown E_B for all OCO and UMO levels to be equal across x_{IL}; *i.e.*, E_B(N_{cation} 2p) would be equal between $0.01 < x_{IL} < 1.00$. Again, this demonstrated the influence and role of initial state solvation effects on OCO and UMO levels for all components in $([C_4C_1Im][SCN])_x(H_2O)_{1-x}$.

5.3.6. Evidence for initial state versus final state effects

Determining whether initial state or final state effects are responsible for measured E_B shifts is an important distinction to make, which point towards the type of interaction that take place between each component in solution. Initial state effects relate to chemical/bonding environment, whereas final state effects relate to screening effects after photoemission, when a core hole exists.[55]

Core versus valence level XPS contributions

Valence XPS has very little contribution from the final state due to the low relaxation energies involved in the filling of the core hole post- photoemission.[55] Core level and valence states showed the same E_B shifts. Therefore, it can be assumed that the same influence affected both, core and valence state energy shifts. Hence, initial state effects were shown to dominate.

***Ab initio* molecular dynamics**

Ab initio molecular dynamics calculations for $[C_4C_1Im][SCN]$ were shown to match experimental binding energies.[35, 63] The computational calculations carried out did not consider the influence of final state effects, yet still achieved a satisfactory match to experimental data. Therefore, initial state effects were shown to provide an accurate representation of the experimental phenomena.

Varying the molecular solvent identity

OCO and HOVS energies for solutions of 0.5 M ($[C_4C_1Im][SCN]$)(solvent), where solvent = H_2O, H_2O/EtOH, MeCN, and PC, were shown to strongly correlate with solvent polarity scale descriptors, which indicated the strength of solvent Lewis acidity (Chapter 3). The Lewis acidity of the solvent described its ability to accept an electron pair from a solute species; hence, involving a specific solvent-solute interaction, which would be categorised as an initial state effect.

XPS versus XAS contribution

XAS involves the indirect measurement of absorption through the monitoring of secondary processes, which result in core hole filling. Therefore, final state effects were expected to determine (or at least play a significant role in determining) the measured edge energy. As the N 1s XA spectra showed no energetic peak shifts with varying electrolyte concentration, final state influences were thought to be negligible.

5.4. Conclusion and future work

The current work demonstrated the effect of varying electrolyte concentration on the bonding HOVS and LUMO energies, and non-bonding OCO energies. Three main conclusions were reached:

1. Atomic charge variation of the anion and water molecules with changing x_{IL} were deemed to be the result of non-specific solvation effects.
2. OCO and valence state energies were both shown to correlate with varying x_{IL} for all components in solution, *i.e.*, cationic OCO shifted energetically in the same direction and by the same magnitude as the cationic valence states.
3. Initial state effects dominated at all values of x_{IL}.

Excluding the cation, the OCO and OVSs for all components in solution were shown to shift to lower E_{B} with increasing x_{IL}. From these relationships it was concluded that the interaction between ions and H_2O in solution were non-specific in nature. The lack of contrasting E_{B} shifts supported this conclusion and the reasoning for the observed effect was suggested to be due to electrostatic effects. Hence, it is expected that experimental $E_{\mathrm{B}}(\mathrm{N_{anion}}\ 1s)$, $E_{\mathrm{B}}(\mathrm{N_{anion}}\ 2p)$, $E_{\mathrm{B}}(\mathrm{O_{liq}}\ 1s)$, and $E_{\mathrm{B}}(1b_{1_{\mathrm{liq}}})$ states correlate strongly with the relative permittivity of solution at each value of x_{IL}.[63] Of course, the linear relationship between E_{B}(anion) and solvent polarity scale descriptor values, such as those measured by Kamlet-Taft[58, 64-67] can point to specific solvation effects, such as hydrogen-bonding (Chapter 3), but the strong correlation between E_{B}(anion) and relative permittivity would be an indication of non-specific solvation effects.

Valence RXPS PA peak and valence NRXPS peak binding energies were shown to match well, Demonstrating the feasibility of new experiments which would otherwise have involved difficult measurements due to low photoionisation cross sections and photoemission peaks obscured by dominant solvent peaks. Resonant techniques can also aid with analysis due to the selective nature of the spectroscopy, *e.g.*, during the analysis of components within catalytic systems with complex valence band assignment.

Whilst the electronic structure of the full concentration range of $([C_4C_1Im][SCN])_x(H_2O)_{1-x}$ has been studied by three different spectroscopic techniques, further variation of solution parameters are needed to achieve a more complete understanding of the behaviour of ions in molecular solvent. For example, is the same effect observed in less polar solvents? The assumption that the cation was unaffected due to its existence as a large, organic ion has been made throughout the current work. Hence, what is the effect, if any, of instead using a smaller, monatomic cation? Contrastingly, what is the effect of changing to a larger anion, such as bis(trifluoromethanesulfonyl)imide ($[NTf_2]^-$)? Are the binding energy differences between pure IL and infinitely dilute IL consistent across these different factors? Once these questions have been addressed, we can begin to gain a more complete understanding of the behaviour of ions in solution and how this pertains to electronic structure of each component.

5.5. References

1. Q. Wang, H. C. Wang, J. Y. Wu, M. Y. Zhou, W. Liu and H. H. Zhou, *Nano Energy*, 2021, **80**.
2. J. M. Pringle and V. Armel, *International Reviews in Physical Chemistry*, 2011, **30**, 371-407.
3. D. R. MacFarlane, M. Forsyth, P. C. Howlett, M. Kar, S. Passerini, J. M. Pringle, H. Ohno, M. Watanabe, F. Yan, W. J. Zheng, S. G. Zhang and J. Zhang, *Nat. Rev. Mater.*, 2016, **1**.
4. A. Muzaffar, M. B. Ahamed, K. Deshmukh and J. Thirumalai, *Renew. Sust. Energ. Rev.*, 2019, **101**, 123-145.
5. T. Hübert, L. Boon-Brett, G. Black and U. Banach, *Sensors and Actuators B: Chemical*, 2011, **157**, 329-352.
6. Y. Yamada, *Bulletin of the Chemical Society of Japan*, 2020, **93**, 109-118.
7. L. M. Suo, O. Borodin, T. Gao, M. Olguin, J. Ho, X. L. Fan, C. Luo, C. S. Wang and K. Xu, *Science*, 2015, **350**, 938-943.
8. D. R. MacFarlane, N. Tachikawa, M. Forsyth, J. M. Pringle, P. C. Howlett, G. D. Elliott, J. H. Davis, M. Watanabe, P. Simon and C. A. Angell, *Energy Environ. Sci.*, 2014, **7**, 232-250.
9. H. Zhang, X. Liu, H. H. Li, I. Hasa and S. Passerini, *Angew. Chem.-Int. Edit.*, 2021, **60**, 598-616.
10. Y. Yamada, J. H. Wang, S. Ko, E. Watanabe and A. Yamada, *Nat. Energy*, 2019, **4**, 269-280.
11. M. Watanabe, M. L. Thomas, S. Zhang, K. Ueno, T. Yasuda and K. Dokko, *Chemical Reviews*, 2017, **117**, 7190-7239.
12. L. M. Suo, Y. S. Hu, H. Li, M. Armand and L. Q. Chen, *Nat. Commun.*, 2013, **4**, 9.
13. L. M. Suo, O. Borodin, Y. S. Wang, X. H. Rong, W. Sun, X. L. Fan, S. Y. Xu, M. A. Schroeder, A. V. Cresce, F. Wang, C. Y. Yang, Y. S. Hu, K. Xu and C. S. Wang, *Adv. Energy Mater.*, 2017, **7**, 10.
14. X. J. Yan, X. L. Zhao, C. C. Liu, S. P. Wang, Y. J. Zhang, M. Guo, Y. Y. Wang, L. Y. Dai and X. W. Yang, *Journal of Power Sources*, 2019, **423**, 331-338.
15. X. Y. Wu, Y. K. Xu, C. Zhang, D. P. Leonard, A. Markir, J. Lu and X. L. Ji, *Journal of the American Chemical Society*, 2019, **141**, 6338-6344.
16. M. M. Zhang, H. X. Hao, D. X. Zhou, Y. Y. Duan, Y. Wang and H. T. Bian, *J. Phys. Chem. C*, 2020, **124**, 8594-8604.
17. C. Lagrost, S. Gmouh, M. Vaultier and P. Hapiot, *Journal of Physical Chemistry A*, 2004, **108**, 6175-6182.
18. X. Y. Zhu, P. Cui, D. J. Zhang and C. B. Liu, *Journal of Physical Chemistry A*, 2011, **115**, 8255-8263.

19. P. Ballone and R. Cortes-Huerto, *Faraday Discussions*, 2012, **154**, 373-389.

20. L. H. J. Xiong, A. M. Fletcher, S. G. Davies, S. E. Norman, C. Hardacre and R. G. Compton, *Chemical Communications*, 2012, **48**, 5784-5786.

21. D. Wagle, G. Kamath and G. A. Baker, *J. Phys. Chem. C*, 2013, **117**, 4521-4532.

22. M. H. Ghatee and F. Moosavi, *J. Phys. Chem. C*, 2011, **115**, 5626-5636.

23. I. A. Shkrob and J. F. Wishart, *Journal of Physical Chemistry B*, 2009, **113**, 5582-5592.

24. Z. P. Wang, L. Zhang, X. H. Chen, R. I. Cukier and Y. X. Bu, *Journal of Physical Chemistry B*, 2009, **113**, 8222-8226.

25. Z. P. Wang, L. Zhang, R. I. Cukier and Y. X. Bu, *Physical Chemistry Chemical Physics*, 2010, **12**, 1854-1861.

26. C. J. Margulis, H. V. R. Annapureddy, P. M. De Biase, D. Coker, J. Kohanoff and M. G. Del Popolo, *Journal of the American Chemical Society*, 2011, **133**, 20186-20193.

27. C. H. Xu, A. Durumeric, H. K. Kashyap, J. Kohanoff and C. J. Margulis, *Journal of the American Chemical Society*, 2013, **135**, 17528-17536.

28. R. P. Morco, A. Y. Musa and J. C. Wren, *Solid State Ionics*, 2014, **258**, 74-81.

29. S. Z. Hu, A. J. Wang, X. Li, Y. Wang and H. Lowe, *Chem.-Asian J.*, 2010, **5**, 1171-1177.

30. Y. N. Wang, K. J. Deng and L. Z. Zhang, *J. Phys. Chem. C*, 2011, **115**, 14300-14308.

31. J. J. Liu, S. Q. Han, J. Li and J. Lin, *Rsc Advances*, 2014, **4**, 37556-37562.

32. S. S. Manna, P. Bhauriyal and B. Pathak, *Materials Advances*, 2020, **1**, 1354-1363.

33. J. B. Goodenough and K. S. Park, *Journal of the American Chemical Society*, 2013, **135**, 1167-1176.

34. J. M. Seymour, E. Gousseva, A. Large, C. J. Clarke, P. Licence, R. M. Fogarty, D. Duncan, P. Ferrer, F. Venturini, R. A. Bennett, R. G. Palgrave and K. R. J. Lovelock, *Physical Chemistry Chemical Physics*, 2021, **23**, 20957 - 20973.

35. J. M. Seymour, E. Gousseva, A. Large, G. Held, D. Hein, G. Wartner, W. Quevedo, R. Seidel, C. Kolbeck, C. J. Clarke, R. Fogarty, R. Bourne, R. Bennett, R. Palgrave, P. A. Hunt and K. R. J. Lovelock, *Faraday Discussions*, 2022.

36. R. M. Fogarty, R. G. Palgrave, R. A. Bourne, K. Handrup, I. J. Villar-Garcia, D. J. Payne, P. A. Hunt and K. R. J. Lovelock, *Physical Chemistry Chemical Physics*, 2019, **21**, 18893-18910.

37. M. Kar, Z. Ma, L. M. Azofra, K. Chen, M. Forsyth and D. R. MacFarlane, *Chemical Communications*, 2016, **52**, 4033-4036.

38. K. Fujii, H. Wakamatsu, Y. Todorov, N. Yoshimoto and M. Morita, *J. Phys. Chem. C*, 2016, **120**, 17196-17204.

39. X. Shen, P. Li, X. Liu, S. Chen, X. Ai, H. Yang and Y. Cao, *Chem. Sci.*, 2021, **12**, 9037-9041.

40. X. Chen and Q. Zhang, *Accounts of Chemical Research*, 2020, **53**, 1992-2002.

41. A. P. Gaiduk, M. Govoni, R. Seidel, J. H. Skone, B. Winter and G. Galli, *Journal of the American Chemical Society*, 2016, **138**, 6912-6915.

42. A. P. Gaiduk and G. Galli, *J. Phys. Chem. Lett.*, 2017, **8**, 1496-1502.

43. B. Jagoda-Cwiklik, P. Slavíček, D. Nolting, B. Winter and P. Jungwirth, *Journal of Physical Chemistry B*, 2008, **112**, 7355-7358.

44. K. R. J. Lovelock, I. J. Villar-Garcia, F. Maier, H. P. Steinrück and P. Licence, *Chemical Reviews*, 2010, **110**, 5158-5190.

45. R. M. Fogarty, R. P. Matthews, C. R. Ashworth, A. Brandt-Talbot, R. G. Palgrave, R. A. Bourne, T. V. Hoogerstraete, P. A. Hunt and K. R. J. Lovelock, *Journal of Chemical Physics*, 2018, **148**, 193817.

46. M. N. Pohl, E. Muchova, R. Seidel, H. Ali, S. Srsen, I. Wilkinson, B. Winter and P. Slavicek, *Chem. Sci.*, 2019, **10**, 848-865.

47. B. Credidio, M. Pugini, S. Malerz, F. Trinter, U. Hergenhahn, I. Wilkinson, S. Thurmer and B. Winter, *Physical Chemistry Chemical Physics*, 2021.

48. R. Seidel, M. N. Pohl, H. Ali, B. Winter and E. F. Aziz, *Review of Scientific Instruments*, 2017, **88**, 073107.

49. P. B. Petersen and R. J. Saykally, *Annual Review of Physical Chemistry*, 2006, **57**, 333-364.

50. H. J. Lee, A. C. Jamison and T. R. Lee, *Accounts of Chemical Research*, 2015, **48**, 3007-3015.

51. B. Winter and M. Faubel, *Chemical Reviews*, 2006, **106**, 1176-1211.

52. E. Clavero and J. Rodriguez, *Journal of Molecular Liquids*, 2011, **163**, 64-69.

53. F. Huo, J. Ding, J. Tong and H. He, *Mol. Simul.*, 2021, **47**, 1-11.

54. J. E. B. Randles, *Phys. Chem. Liq.*, 1977, **7**, 107-179.

55. J. C. Vickerman and I. S. Gilmore, eds., *Surface Analysis: The Principal Techniques*, John Wiley & Sons, Chichester, 2009.

56. D. C. Rideout and R. Breslow, *Journal of the American Chemical Society*, 1980, **102**, 7816-7817.

57. J. B. F. N. Engberts, *Abstr. Pap. Am. Chem. Soc.*, 1994, **207**, 110-Phys.

58. C. Reichardt and T. Welton, *Solvents and Solvent Effects in Organic Chemistry*, Wiley, Weinheim, 4th edn., 2011.

59. K. Ledbetter, E. Biasin, J. P. F. Nunes, M. Centurion, K. J. Gaffney, M. Kozina, M. F. Lin, X. Shen, J. Yang, X. J. Wang, T. J. A. Wolf and A. A. Cordones, *Structural Dynamics*, 2020, **7**, 064901.

60. N. T. Anh, in *Organic Chemistry Syntheses and Reactivity*, Springer, 1980, pp. 145-162.

61. T. Miteva, N. V. Kryzhevoi, N. Sisourat, C. Nicolas, W. Pokapanich, T. Saisopa, P. Songsiriritthigul, Y. Rattanachai, A. Dreuw, J. Wenzel, J. Palaudoux, G. Öhrwall, R. Püttner, L. S. Cederbaum, J. P. Rueff and D. Céolin, *J. Phys. Chem. Lett.*, 2018, **9**, 4457-4462.
62. P. A. Brühwiler, O. Karis and N. Mårtensson, *Rev. Mod. Phys.*, 2002, **74**, 703-740.
63. R. M. Fogarty, PhD thesis, Imperial College London, 2018.
64. M. J. Kamlet and R. W. Taft, *Journal of the American Chemical Society*, 1976, **98**, 377-383.
65. R. W. Taft and M. J. Kamlet, *Journal of the American Chemical Society*, 1976, **98**, 2886-2894.
66. M. J. Kamlet, J. L. Abboud and R. W. Taft, *Journal of the American Chemical Society*, 1977, **99**, 6027-6038.
67. R. W. Taft, J. L. M. Abboud and M. J. Kamlet, *Journal of the American Chemical Society*, 1981, **103**, 1080-1086.

Chapter 6

Influence of solvent identity on cationic electronic structure

Abstract

The electronic structure of the cationic components within a solution is an equally important property of a solvated system to that of the anionic or molecular solvent components. Cationic interactions, usually associated with Lewis acidity, drive many chemical processes such as heterogenous catalysis and more recently, frustrated Lewis pairs. However, knowledge of the influence of solvent identity on the cationic electronic structure, including the non-bonding occupied core orbital energies, remain sparse. Within this work, a combination of complementary X-ray spectroscopic techniques coupled with liquid jet apparatus allowed for the measurement of the electronic structure of liquid phase cationic species. The energetic position of the occupied core orbitals (OCOs) for each cationic species, $[C_4C_1Im]^+$, K^+, and Li^+, was determined within both, H_2O, and propylene carbonate (PC). The cationic electronic structure was shown to be least influenced by varying solvation identity for very strongly coordinating cations, such as Li^+, even at low electrolyte concentration. Li^+ was shown to act as a strong Lewis acid equally within in aqueous or organic solution. The effect of varying solvent identity was found to be more important for weakly coordinating cations, such as K^+ and $[C_4C_1Im]^+$, where the chemical structure of each ion affected the extent of electronic structure variation. The extent of the binding energy shift for cationic OCOs, from H_2O solvation to PC solvation, was related to the Lewis acidic solvent polarity descriptors. The ability to detect small energy shifts for targeted atoms within key battery electrolytes was successfully demonstrated.

6.1. Introduction

When considering the reactivity of a chemical system, the donation of electron density, *i.e.*, Lewis basicity, is usually the first property that comes to mind. Therefore, reactivity is normally associated with anionic components within a system. However, when exploring the energetic relationships between each component, Lewis acidic species (those that accept electron density) must also be carefully considered. Lewis acidity involves the acceptance of a pair of electrons into the lowest unoccupied molecular orbital (LUMO), or acceptor orbital, of a species.[1] Consequently, Lewis acids are most commonly electron poor cationic species, which are utilised within a wide range of research areas such as catalysis[2, 3], organic synthesis[4, 5], frustrated Lewis pairs[6, 7], and halometallate ionic liquids (ILs)[8, 9]. Lewis acid/base interactions also feature heavily within battery technologies, where most processes take place within the liquid phase of the solvent electrolyte. Solvent-solute interactions must therefore not only be considered for the anionic species, but also the cation, within an electrolyte system. Greater understanding of the influence of the solvent identity on the cationic electronic structure will therefore aid in the design and implementation of better systems for these processes.

Solvents are known to possess varying electron donor abilities, which are key to the strength of specific solvent-cation interactions.[10] Therefore, by measuring cationic species in solvents with differing electron donor abilities, the influence of charge transfer on the electronic structure of cationic species can be determined. Additionally, each cationic species contains an inherent ability to accept electron density, leading to classes of both, weakly, and strongly coordinating cations. Within this work, solvents across the Kamlet-Taft[10-14] hydrogen bond acceptor, β_{solv}, and Gutmann-Beckett[15, 16] donor number, DN_{solv}, solvent polarity scales were chosen to reflect the difference in electron donation of the solvent to the cationic species. Therefore, cationic species with varying tendency to strongly, or weakly, coordinate to solvent species were chosen. This chapter focusses on the influence of the solvent identity on the cationic electronic structure.

In this chapter, non-resonant X-ray photoelectron spectroscopy (NRXPS) was used to probe the energetic position of the occupied core orbitals (OCOs) within samples of 0.5 M (solute)(H_2O) and 0.5 M (solute)(PC), where solute = [C_4C_1Im][SCN], K[SCN], and Li[NTf_2] (Figure 6.1). Cationic OCO energetic shifts, ΔE_{B}(cation), from 0.5 M (solute)(H_2O) to 0.5 M (solute)(PC) were compared and the subsequent observed solvation effects discussed. ΔE_{B}(cation) from 0.5 M (Li[NTf_2])(H_2O) to 0.5 M (Li[NTf_2])(PC) was used to exemplify the varying degree of influence the cation may have on the electronic structure of a key battery electrolyte system. The comparison between $[C_4C_1Im][SCN]$ and K[SCN] allowed for an investigation of the effect of varying both, solvent, and cation identity, due to the presence of the same ionic species within each solution. Full width at half maximum (FWHM) measurements were discussed to provide a spectroscopic understanding of the extent and variation of solvent-solute interactions taking place in solution.

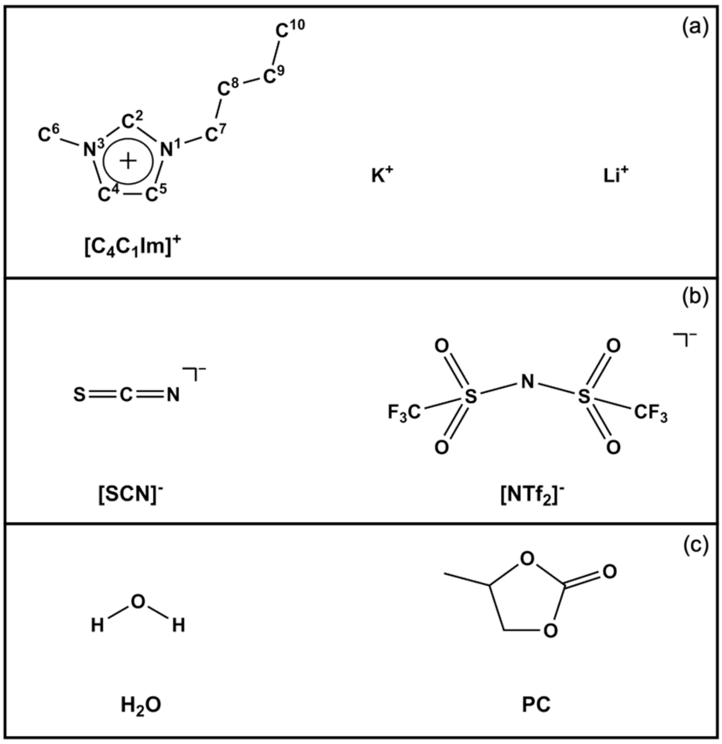

Figure 6.1. Names and structures of key ions and solvents studied within Chapter 6: (a) Cations, where atoms within $[C_4C_1Im]^+$ are numbered according to convention for reference within the current work. (b) Anions. (c) Solvents.

6.2. Spectroscopic methods

6.2.1. Sample preparation

PC was purchased from Sigma-Aldrich, with no further purification or drying prior to use. Highly demineralised H_2O (conductivity ~0.2 μS cm^{-1}) was used for 0.5 M solutions of K[SCN], $[C_4C_1Im][SCN]$ and $Li[NTf_2]$ in H_2O. $[C_4C_1Im][SCN]$ was purchased from Iolitec, with no further purification or drying prior to use. $[C_4C_1Im][SCN]$ was weighed and mixed with a corresponding mass of solvent to achieve a concentration of 0.5 M. The corresponding mole fraction, concentration, and solute:solvent ratio for each sample is shown in Table 6.1.

Table 6.1. The six solutions studied within Chapter 6. Concentrations were calculated using parameters listed in Appendix Tables 8.1 to 8.3.

	x_{solute}	x_{solv}	conc. solute/ M	conc. solv / M	solute:solv
$([C_4C_1Im][SCN])(H_2O)$	1	99	0.5	50.3	1:99
$([C_4C_1Im][SCN])(PC)$	4	96	0.5	10.8	1:24
$(K[SCN])(H_2O)$	1	99	0.5	54.1	1:109
(K[SCN])(PC)	4	96	0.5	11.5	1:23
$(Li[NTf_2])(H_2O)$	1	99	0.5	49.6	1:99
$(Li[NTf_2])(PC)$	4	96	0.5	10.5	1:21

6.2.2. Synchrotron XPS apparatus

The measurement of all samples in Table 6.1 were performed on the U49/2-PGM 1 beamline with SOL^3PES end-station[17] at BESSY II (Germany). Liquid-jet apparatus was used.[17] XP and RXP spectra were acquired using a Scienta Omicron R4000 HIPP-2 hemispherical electron analyser. The analyser angle was 90.0° horizontal to the plane of polarised light.

6.3. Results and discussion

6.3.1. Changes in cationic atomic charge with varying solvent identity

The cationic occupied core orbital (OCO) energies for 0.5 M (solute)(H_2O) and 0.5 M (solute)(PC), where solute = [C_4C_1Im][SCN], K[SCN], and Li[NTf_2], were measured by NRXPS (Figure 6.2). N 1s NRXP spectra for 0.5 M ([C_4C_1Im][SCN])(H_2O) and 0.5 M ([C_4C_1Im][SCN])(PC) both showed one photoelectron peak due to single N_{cation} electronic environment on [C_4C_1Im]$^+$ cation (Figure 6.2a). The measured binding energy for the N_{cation} 1s OCO, E_B(N_{cation} 1s), was shown to be greater when solvated by H_2O than solvated by PC (Table 6.2). K 2p NRXP spectra for 0.5 M (K[SCN])(H_2O) and 0.5 M (K[SCN])(PC) both contained two photoelectron peaks with an area ratio of 2:1, due to spin orbit coupling of a single K 2p electronic environment on K^+ cation (Figure 6.2b). E_B(K $2p_{3/2}$) was also found to be greater for 0.5 M (K[SCN])(H_2O) than 0.5 M (K[SCN])(PC) but to a lesser extent. Li 1s NRXP spectra for 0.5 M (Li[NTf_2])(H_2O) and 0.5 M (Li[NTf_2])(PC) both showed one photoelectron peak due to single Li_{cation} electronic environment on Li^+ cation (Figure 6.2c). ΔE_B(Li_{cation} 1s) was shown to be zero (within experimental error) from solvation in H_2O to solvation in PC.

Table 6.2. Experimental binding energies, E_B, recorded by NRXPS for 0.5 M (solute)(H_2O) and 0.5 M (solute)(PC), where solute = [C_4C_1Im][SCN], K[SCN], and Li[NTf_2], and the E_B difference between each sample, ΔE_B. All spectra were measured at $h\nu$ = 700.0 eV. All values charge referenced using the methods detailed in Section 2.7.2. All E_B values are reported to 2 decimal places.

	Electron binding energy / eV		
	N_{cation} 1s (± 0.03)	K $2p_{3/2}$ (± 0.06)	Li 1s (± 0.06)
0.5 M ([C_4C_1Im][SCN])(H_2O)	406.75		
0.5 M ([C_4C_1Im][SCN])(PC)	406.28		
ΔE_B[a]	-0.47		
0.5 M (K[SCN])(H_2O)		298.05	
0.5 M (K[SCN])(PC)		297.76	
ΔE_B[a]		-0.29	
0.5 M (Li[NTf_2])(H_2O)			60.56
0.5 M (Li[NTf_2])(PC)			60.55
ΔE_B[a]			-0.01

[a] ΔE_B is the difference between 0.5 M (solute)(H_2O) and 0.5 M (solute)(PC) peak binding energies.

Through measurement of NRXPS photoemission peaks for three different cations, $[C_4C_1Im]^+$, K^+, and Li^+, the identity of the cation was shown to play a key role in determining the magnitude and direction of the cationic binding energy shift, ΔE_B(cation), from solvation in H_2O to solvation in PC. The relatively large negative value of ΔE_B(cation) from 0.5 M ($[C_4C_1Im][SCN]$)(H_2O) to 0.5 M ($[C_4C_1Im][SCN]$)(PC) indicated that the cationic N^1 and N^3 atoms possessed a greater electron density when solvated by PC than solvated by H_2O (see Figure 6.1a for the position of the N^1 and N^3 nitrogen atoms). Similarly, ΔE_B(cation) was shown to be negative from 0.5 M (K[SCN])(H_2O) to 0.5 M (K[SCN])(PC), although the magnitude of the negative shift was smaller than that of $[C_4C_1Im]^+$. The large variation in ΔE_B(cation) for $[C_4C_1Im]^+$ and K^+ suggested that the cation OCO energies were greatly affected by the change in solvation environment. Solvent polarity descriptors, *e.g.*, Kamlet-Taft (KT),[10-14] and Gutmann-Beckett,[15, 16] currently provide the greatest indicator of the strength of solvent-solute interactions within solution. In particular, those which describe solvent Lewis basicity, the solvent hydrogen bond acceptor ability, β_{solv}, and solvent electron donor number, DN_{solv}, relate to the role of the solvent within solvent-cation interactions. DN_{solv} is known to be greater for H_2O than for PC (Table 6.3), demonstrating an increased electron pair donor ability of H_2O over PC. Moreover, $[C_4C_1Im]^+$ has been shown to readily accept electron density through the C^2 carbon on the imidazolium ring (see Figure 6.1a for the position of the C^2 carbon atom).[18] Despite the increased ability of H_2O to donate electron density to the cationic species, E_B(cation) of the solute while solvated by H_2O was greater than while solvated by PC. The observed trend in ΔE_B(cation) was therefore the inverse of the expected result. As the identity of both, the solvent, and the anion, were identical within solutions of 0.5 M ($[C_4C_1Im][SCN]$)(H_2O) and (K[SCN])(H_2O), and solutions of 0.5 M ($[C_4C_1Im][SCN]$)(PC) and (K[SCN])(PC), the measured differences in E_B(cation) must solely lie with properties of the cationic identity. A likely cationic property which can influence the magnitude of ΔE_B(cation) is the ability of the cation to accept electron density from the solvating species, *i.e.*, Lewis acidity. The chemical structure of each cation may also provide reasoning for the observed ΔE_B(cation) values. As $[C_4C_1Im]^+$ is a large organic molecule and K^+ is a smaller inorganic atom, there is likely a wider range of solvent-solute bonding interactions available for $[C_4C_1Im]^+$ than are likely accessible to K^+. Therefore, it is more feasible that the $[C_4C_1Im]^+$ cation can capitalise on the electron density donation from the solvent with the greatest DN_{solv}, resulting in a greater ΔE_B(cation). ΔE_B(cation) for both, $[C_4C_1Im][SCN]$, and K[SCN] were however still considerably low when compared with the relatively large (-1.01 eV) shift observed for the anionic OCO energies between the same solutions (using the same charge referencing method, Chapter 3). Therefore, the solvation environment was concluded to have a strong effect on the cationic OCO energies for weakly coordinating ions such as $[C_4C_1Im]^+$ and K^+ (but not as strong as the effect on the counteranions).

Table 6.3. KT and Gutmann-Beckett solvent polarity scale descriptor values for H_2O, and PC. Values for β_{solv} were obtained from reference [10]; values for DN_{solv} were obtained from reference [19].

	H_2O	PC
β_{solv}	0.47	0.40
DN_{solv}	18.0	15.10

The negligible value of ΔE_B(cation) from 0.5 M $(Li[NTf_2])(H_2O)$ to 0.5 M $(Li[NTf_2])(PC)$ indicated that the cationic Li^+ atom possessed a similar electron density when solvated by H_2O or PC. ΔE_B(cation) from 0.5 M $(Li[NTf_2])(H_2O)$ to 0.5 M $(Li[NTf_2])(PC)$ differed to that of both $[C_4C_1Im][SCN]$ and K[SCN], which both showed strong negative ΔE_B(cation) values. Li^+ cations have previously been described as good Lewis acids due to their high absolute electronegativities, and 'hard' due to a large HOVS-LUMO energy gap.[20] For this reason, Li^+ cations are good at accepting electron density from their corresponding anion and solvent molecules in solution.[21] However, in a dilute electrolyte solution (0.5 M) cation-anion interactions were expected to be negligible, suggesting solvent-cation interactions were the dominant cause for the observed ΔE_B(cation) shift. It has previously been found that the oxidative stability of solvents such as PC are increased as a result of the electron withdrawing strength of Li^+ cations, demonstrating the capability of Li^+ as a Lewis acid in solution.[22-24] Consequently, it may be argued that Li^+ cations perform as Lewis acids equally as well in H_2O. The comparative Lewis acidity of Li^+ in each solvent is supported by the equal stable coordination number of Li^+ in H_2O[25] and PC[26-28], of 4 to 5 molecules. The increased ability of H_2O to donate electron density to the Li^+ cation compared to the lesser ability of PC (according to solvated basicity values, Table 6.3), was shown not to result in any variation of $E_B(Li_{cation}$ 1s) when solvated by either solvent. Therefore, the solvation environment was concluded to have a weak effect on the cationic OCO energies for strongly coordinating ions such as Li^+.

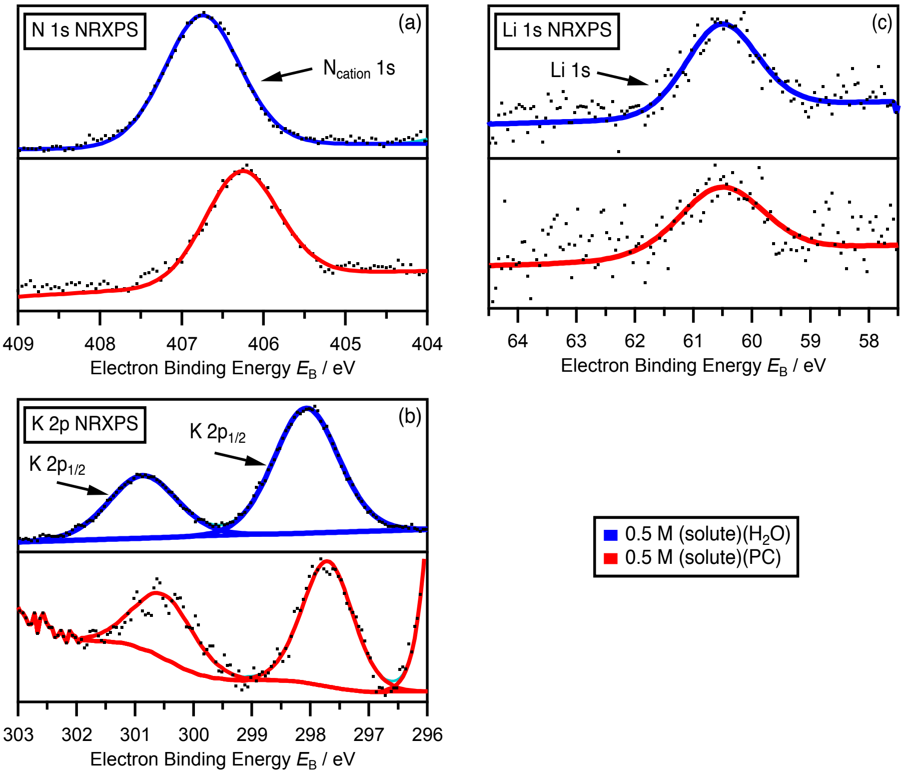

Figure 6.2. Cationic NRXP spectra for 0.5 M (solute)(H_2O) and 0.5 M (solute])(PC), where solute = [C_4C_1Im][SCN], K[SCN], and Li[NTf_2]: (a) N 1s comparison between 0.5 M ([C_4C_1Im][SCN])(H_2O) and 0.5 M ([C_4C_1Im][SCN])(PC). (b) K 2p comparison between 0.5 M (K[SCN])(H_2O) and 0.5 M (K[SCN])(PC). (c) Li 1s comparison between 0.5 M (Li[NTf_2])(H_2O) and 0.5 M (Li[NTf_2])(PC). All spectra were measured at $h\nu$ = 700.0 eV and vertically offset for clarity. All values charge referenced using the methods detailed in Section 2.7.2.

Table 6.4. Experimental K $2p_{1/2}$ and K $2p_{3/2}$ FWHM values and area ratios of (K $2p_{3/2}$/K $2p_{1/2}$) recorded by NRXPS for 0.5 M (K[SCN])(H_2O) and 0.5 M (K[SCN])(PC). All 0.5 M spectra were measured at $h\nu$ = 700.0 eV.

	FWHM / eV		Area
	K $2p_{3/2}$	K $2p_{1/2}$	(K $2p_{3/2}$ / K $2p_{1/2}$)
0.5 M (K[SCN])(H_2O)	1.30	1.37	1.90
0.5 M (K[SCN])(PC)	0.96	1.09	1.52

The measured FWHM values of both, K $2p_{3/2}$, K $2p_{1/2}$, from 0.5 M (K[SCN])(H_2O) to 0.5 M (K[SCN])(PC) were found to differ greatly (Table 6.4). The FWHM for the K $2p_{1/2}$ photoemission peak was greater than the K $2p_{3/2}$ in either solvent. Photoemission peaks arising due to spin orbit coupling interactions are normally expected to contain equal FWHM values. Hence, the observed peak broadening of approximately 0.1 eV was suggested to be the margin of experimental error.

Varying solvation environment through the change of solvent identity was shown to influence FWHM values, where photoemission peaks arising from K^+ cations solvated by H_2O had greater FWHM values than K^+ solvated by PC. FWHM can be an indicator of the evolution of solvation shells around the cation, where variation within the short-range bonding networks were shown to broaden photoemission peaks through change of the local electrostatic potential energy.[29] At 0.5 M concentration, ion-ion interactions were thought to be negligible, and solvent-ion interactions likely dominate. The observed FWHM difference was therefore due to an increased variation in solvent-solute bonding interactions when K^+ cations were solvated by H_2O compared to solvation by PC molecules.

The area ratio between (K $2p_{3/2}$ / K $2p_{1/2}$) was shown to be greater for K^+ cations solvated by H_2O compared to solvation by PC molecules. A greater area ratio indicated the K $2p_{3/2}$ was larger relative to the K $2p_{1/2}$ when solvated by H_2O. Photoemission peaks arising due to spin orbit coupling interactions for p-type orbitals are expected to exhibit an area ratio of 2:1, for K $2p_{3/2}$ and K $2p_{1/2}$ peaks respectively. Therefore, (K $2p_{3/2}$ / K $2p_{1/2}$) for K^+ cations solvated by H_2O were as expected, whereas (K $2p_{3/2}$ / K $2p_{1/2}$) for K^+ cations solvated by PC was shown to be unusually low. From comparison of the K 2p spectra for 0.5 M (K[SCN])(PC) and C 1s spectra for pure PC, it was evident that the energetic position of the K 2p photoemission peaks coincided with the energy at which the intensity of the background increased within the C 1s region for pure PC (Appendix Figure 8.4).[30] Thus, the (K $2p_{3/2}$ / K $2p_{1/2}$) area ratio for 0.5 M (K[SCN])(PC) was shown to be lower than expected due to the increased background intensity.

6.4. Conclusion and future work

In this chapter, the effect of varying the solvent identity on E_B(cation) was measured through non-resonant X-ray photoelectron spectroscopy.

ΔE_B(cation) was used to quantify the influence of the solvation environment on the energetic positions of the cationic OCOs, from solvation by H_2O to solvation by PC molecules. Due to the variation in Lewis basic solvent polarity descriptor values for H_2O and PC, the solvated cationic species were expected to yield a positive ΔE_B(cation) from solvation in H_2O to solvation in PC. However, ΔE_B(cation) for the weakly coordinating $[C_4C_1Im]^+$ and K^+ cations were shown to shift negatively, suggesting that solvation environment yielded a large effect on the cationic OCO energies for weakly coordinating ions.

In contrast to $[C_4C_1Im]^+$ and K^+ cationic OCOs, Li^+ cationic OCOs (Li 1s) yielded zero ΔE_B(cation). The lack of observed ΔE_B(cation) from $(Li[NTf_2])(H_2O)$ to $(Li[NTf_2])(PC)$ was due to the high electron withdrawing strength of Li^+ cations. The ability of Li^+ cations to act as equally strong Lewis acids allowed Li^+ to accept electron density similarly from both, H_2O, and PC, resulting in an equal E_B(Li 1s). Therefore, ΔE_B(cation) for the strongly coordinating Li^+ cation was shown not to vary, suggesting that solvation environment yielded a negligible effect on the cationic OCO energies for strongly coordinating ions.

Spectral FWHM values for cationic photoemission peaks were shown to decrease from solvation by H_2O to solvation by PC molecules. The decrease in measured cationic FWHM was due to a decreased variation within the short-range cation-solvent bonding networks when solvated by H_2O, relative to solvation by PC. An increased number of solvent-cation interactions were described as broadening photoemission peaks through changing of the local electrostatic potential energy.

The implications for the observed OCO energetic differences for $Li[NTf_2]$ versus X[SCN] were:

1. The role of the cation was related to the Lewis acidity of very strongly coordinating cations, such as Li^+, even at low electrolyte concentration in solvents of differing Lewis basicities.
2. The role of the cation was related to the chemical structure and size of more weakly coordinating cations, such as K^+ and $[C_4C_1Im]^+$, where anionic identity was likely to dictate electronic interactions with the solvent.

In future, it is important to further test the hypotheses presented within this chapter around the influence of solvent identity on cationic electronic structure. Therefore, additional $[SCN]^-$ containing species with a variety of cations, *e.g.*, Li[SCN] and Na[SCN], should be explored. Additionally investigated $[SCN]^-$ containing species should be measured in a wide range of molecular solvents, *e.g.*, ethanol, acetonitrile and triethylphosphate, which will provide better insight into the relationship between E_B(cation) and Lewis basic solvent polarity descriptors. Furthermore, a comparison between species containing the same anion will allow for the elimination of solvent-anion effects, providing a comprehensive investigation of how solvent identity affects cationic OCO and OVSs. As $Li[NTf_2]$ is a key battery electrolyte, it would be beneficial to observe the energetic relationships of both, E_B(cation) and E_B(anion), within a range of solvents, *e.g.*, EtOH and MeCN (Chapter 3). Moreover, through the experimental methods demonstrated in this chapter and others, it is shown to be highly feasible to measure most solute stable battery electrolytes, such as $Li[PF_6]$, in this manner.

6.5. References

1. W. B. Jensen, *Chemical Reviews*, 1978, **78**, 1-22.
2. A. Corma and H. García, *Chemical Reviews*, 2003, **103**, 4307-4366.
3. G. Busca, *Chemical Reviews*, 2007, **107**, 5366-5410.
4. H. Yamamoto, *Lewis Acids in Organic Synthesis*, Wiley, New York, 2000.
5. P. Latos, A. Culkin, N. Barteczko, S. Boncel, S. Jurczyk, L. C. Brown, P. Nockemann, A. Chrobok and M. Swadźba-Kwaśny, *Front. Chem.*, 2018, **6**, 15.
6. D. W. Stephan and G. Erker, *Angew. Chem. Int. Ed.*, 2015, **54**, 6400-6441.
7. L. C. Brown, J. M. Hogg, M. Gilmore, L. Moura, S. Imberti, S. Gärtner, H. Q. N. Gunaratne, R. J. O'Donnell, N. Artioli, J. D. Holbrey and M. Swadźba-Kwaśny, *Chemical Communications*, 2018, **54**, 8689-8692.
8. J. Estager, J. D. Holbrey and M. Swadźba-Kwaśny, *Chemical Society Reviews*, 2014, **43**, 847-886.
9. L. C. Brown, J. M. Hogg and M. Swadzba-Kwasny, *Top. Curr. Chem.*, 2017, **375**, 40.
10. C. Reichardt and T. Welton, *Solvents and Solvent Effects in Organic Chemistry*, Wiley, Weinheim, 4th edn., 2011.
11. M. J. Kamlet and R. W. Taft, *Journal of the American Chemical Society*, 1976, **98**, 377-383.
12. R. W. Taft and M. J. Kamlet, *Journal of the American Chemical Society*, 1976, **98**, 2886-2894.
13. M. J. Kamlet, J. L. Abboud and R. W. Taft, *Journal of the American Chemical Society*, 1977, **99**, 6027-6038.
14. R. W. Taft, J. L. M. Abboud and M. J. Kamlet, *Journal of the American Chemical Society*, 1981, **103**, 1080-1086.
15. U. Mayer, V. Gutmann and W. Gerger, *Monatshefte Fur Chemie*, 1975, **106**, 1235-1257.
16. V. Gutmann, *The Donor-Acceptor Approach to Molecular Interactions*, Plenum Press, New York, 1978.
17. R. Seidel, M. N. Pohl, H. Ali, B. Winter and E. F. Aziz, *Review of Scientific Instruments*, 2017, **88**, 073107.
18. P. A. Hunt, C. R. Ashworth and R. P. Matthews, *Chemical Society Reviews*, 2015, **44**, 1257-1288.
19. W. R. Fawcett, *Journal of Physical Chemistry*, 1993, **97**, 9540-9546.
20. R. G. Pearson, *Inorganic Chemistry*, 1988, **27**, 734-740.
21. S. P. Beltran, X. Cao, J. G. Zhang and P. B. Balbuena, *Chemistry of Materials*, 2020, **32**, 5973-5984.

22. K. Yoshida, M. Nakamura, Y. Kazue, N. Tachikawa, S. Tsuzuki, S. Seki, K. Dokko and M. Watanabe, *Journal of the American Chemical Society*, 2011, **133**, 13121-13129.
23. X. Chen, H. R. Li, X. Shen and Q. Zhang, *Angew. Chem.-Int. Edit.*, 2018, **57**, 16643-16647.
24. T. Doi, R. Masuhara, M. Hashinokuchi, Y. Shimizu and M. Inaba, *Electrochimica Acta*, 2016, **209**, 219-224.
25. L. M. Suo, O. Borodin, T. Gao, M. Olguin, J. Ho, X. L. Fan, C. Luo, C. S. Wang and K. Xu, *Science*, 2015, **350**, 938-943.
26. Z. Wang, W. Gao, X. Huang, Y. Mo and L. Chen, *J. Raman Spectrosc.*, 2001, **32**, 900-905.
27. H. Jiang, Q. Zhang, Y. Zhang, L. Sui, G. Wu, K. Yuan and X. Yang, *Physical Chemistry Chemical Physics*, 2019, **21**, 10417-10422.
28. Y. Yamada, *Bulletin of the Chemical Society of Japan*, 2020, **93**, 109-118.
29. J. Liu, H. Zhang, Y. M. Li and Z. Liu, *Journal of Physical Chemistry B*, 2018, **122**, 10600-10606.
30. W. Stickle and T. Stickle, *Surf. Sci. Spectra*, 2014, **21**, 28-34.

Chapter 7

Conclusion

Experimental X-ray spectroscopic studies on ions in solution often feature both, solely aqueous solvent, and two differing states of matter, the liquid (solution) and solid phase (ionic crystal structure).[1-7] Whilst such studies are useful for exploring the properties of dilute and medium concentrated ions, they neglect the impact upon highly concentrated solutions where ions effectively act as the solvent and molecular solvent as the solute. Crucially, such studies also neglect the vast majority of solvents utilised within common applications of ions in solution. Therefore, knowledge of the governing factors, which control the electronic structure of each liquid phase component, is heavily lacking. To attempt to fill the void of information surrounding how the electronic structure of each component within solution is influenced by changing solvation effects, complementary X-ray spectroscopic methods, such as XPS, XAS, and RXPS, were employed. Each technique allowed for the measurement of the electronic structure of all components within an ionic solution, including the cation, anion, and solvent species, which has enabled the identification of energetic trends upon changing solvation environment.

The electronic structure of ionic species in varying molecular solvent (MS) identity were shown to possess a strong relationship with the solvent Gutmann AN_{solv} descriptor, with slightly weaker relationships additionally observed with Kamlet-Taft α_{solv} and Catalán SA_{solv} (Chapter 3). It was shown that when solvated by more effective hydrogen bond donating solvents (high values of α_{solv}, AN_{solv}, and SA_{solv}), *e.g.*, H_2O and EtOH, the energy of the highest occupied valence state (HOVS) of the anion, $E_B(\text{HOVS}_{\text{anion}})$, was high in comparison to those solvated by less effective hydrogen bond donating solvents (low values of α_{solv}, AN_{solv}, and SA_{solv}), *e.g.*, MeCN and PC. As each of the correlating solvent polarity descriptors indicate a measure of Lewis acidity, it was concluded that highly Lewis acidic solvents provide an energetically stabilising effect on the anionic electronic structure. Moreover, the anionic occupied core orbital (OCO) and OVS energies were shown to be equally influenced by changing solvation environment. Therefore, two additional pieces of information were gained:

1. The anionic OCO energies were also correlated with α_{solv}, AN_{solv}, and SA_{solv}.
2. The measured OCO and OVS energy shifts were deemed a result of non-specific solvation effects.

Differing anion identities in both, aqueous solution, and pure IL, were shown to have no effect on the direction of the anionic energy level shifts, where an equal decrease in OCO and OVS energies were observed, from solutions containing ions in molecular solvent to those consisting of ions in ions, for all anion identities measured (Chapter 4). Anionic MO energies were therefore influenced by non-specific solvation effects as all E_{B}(anion) components for the same anion shifted equally with increasing electrolyte concentration, except for fluorine OCOs. However, the extent to which energies shifted with increasing concentration was found to correlate to the hydrogen bond donor and hydrogen bond acceptor abilities of the anion present, as well as the absolute electronegativity of the probed atomic species. Additionally, anion identity was shown not to have a significant effect on the $[C_4C_1Im]^+$ cationic OCO energies within low concentration (0.5 M) aqueous solution. The role of H_2O as a counterion to the $[C_4C_1Im]^+$ cation was unpredictably shown to act similarly to I^- despite a far lower hydrogen bond acceptor ability. For this reason, it was determined that the influence of H_2O on the electronic structure of the cation was not straightforward in its interpretation, with the most likely explanation due to the small size and strong coordinating ability of H_2O. Anion identity was not shown to significantly affect solvent component energies $E_{\text{B}}(\text{O}_{\text{liq}}\ 1s)$ in aqueous solution; an expected result due to the very low concentration (0.5 M) of the measured solution.

The OCO and OVS energies of ionic species at varying concentration within aqueous solution was measured, where the use of an ionic liquid (IL) as a source of ions allowed for the determination of the electronic structure at both concentration extremes: highly dilute (ions in MS), and highly concentrated (ions in ions) solution (Chapter 5). The OCO and OVS energies for anionic and solvent species were both shown to decrease with increasing electrolyte concentration, explained through the changing solvation environment regime, which accompanied concentration changes within solution.[8] The measured energetic trends were deemed to be the result of non-specific solvation effects due to the monotonic shift of OCO and OVS energies for the same component and lack of contrasting shift within other component energies. Electrostatic effects were concluded to be dominant in the determination of OCO and OVS energetic changes, which was in agreement with previous assessments of a similar system where it was found that $E_{\text{B}}(\text{HOVS}_{\text{anion}})$ correlated with the relative permittivity of the solution.[9] In addition, cationic OCO and OVS energies were shown to correlate with varying electrolyte concentration, shifting by the same energetic value relative to the concentration of the solution; anionic and solvent OCO and OVS energies were found to act likewise.

The electronic structure of ionic species with varying cation identity were measured in both, aqueous solution, and solvated by PC, where trends for the Lewis basic solvent polarity descriptors, β_{solv} and DN_{solv}, were found to be irrelevant with respect to the observed ΔE_{B}(cation) for [C_4C_1Im][SCN], K[SCN], and Li[NTf_2] species (Chapter 6). In contrast to the negative ΔE_{B}(cation) values observed for [C_4C_1Im]$^+$ and K^+, Li^+ cationic OCO (Li 1s) energies yielded no change from solvation in H_2O to PC. The implications for the observed OCO energetic differences for Li^+ versus [C_4C_1Im]$^+$ were:

1. The cationic molecular structure was important for weakly coordinating species, such as [C_4C_1Im]$^+$ and K^+, in the determination of the extent of solvation effects on the energy of the cationic OCOs.
2. The Lewis acidity of the cationic species was significant for very strongly coordinating cations, such as Li^+, where the high Lewis acidity of the cationic species enables equal abstraction of electron density from the solvent molecules irrespective of the DN_{solv} of the solvent.

In summary, it has been shown that non-specific solvation effects provide the dominant reasoning for electronic structure variation due to a multitude of differing parameters in solution. Solvent polarity descriptors relating to Lewis basicity have been shown to aid in the interpretation of the observed energetic shifts when varying the anion identity, whereas Lewis acidity has been found to correlate strongly with energetic shifts caused by varying solvent but not for varying cation identity. Exceptions to these rules were shown to occur for strongly coordinating species, such as Li^+ and F^-.

This work aims to lay the foundations for the use of complementary X-ray spectroscopic techniques within the investigation of the electronic structure of every component within solution, leading to the better understanding, choice, and design, of systems which rely upon ion-solvent interactions. This is enabled through the demonstration of the feasibility of measuring highly volatile pure solvents, and their corresponding ionic solutions, by liquid jet XPS. Additionally, the use of X-ray spectroscopy as a tool for the verification and prediction of Lewis acid and base trends has been discussed. The prediction of the electronic structure of unmeasured solvent and solute species can be achieved simply from widely available solvent polarity descriptor values, and vice versa. This new ability will lead to a more targeted design of new ion in solvent systems, as the acquired electronic structures give indication of the expected behaviours and interactions within a solution.

Future work should aim to build upon the range of solvent, anion, and cation species investigated within this work.

7.1. References

1. A. P. Gaiduk, M. Govoni, R. Seidel, J. H. Skone, B. Winter and G. Galli, *Journal of the American Chemical Society*, 2016, **138**, 6912-6915.
2. A. P. Gaiduk and G. Galli, *J. Phys. Chem. Lett.*, 2017, **8**, 1496-1502.
3. M. N. Pohl, E. Muchova, R. Seidel, H. Ali, S. Srsen, I. Wilkinson, B. Winter and P. Slavicek, *Chem. Sci.*, 2019, **10**, 848-865.
4. B. Credidio, M. Pugini, S. Malerz, F. Trinter, U. Hergenhahn, I. Wilkinson, S. Thurmer and B. Winter, *Physical Chemistry Chemical Physics*, 2021.
5. B. Jagoda-Cwiklik, P. Slavíček, D. Nolting, B. Winter and P. Jungwirth, *Journal of Physical Chemistry B*, 2008, **112**, 7355-7358.
6. D. Nolting, N. Ottosson, M. Faubel, I. V. Hertel and B. Winter, *Journal of the American Chemical Society*, 2008, **130**, 8150-8151.
7. B. Jagoda-Cwiklik, P. Slavíček, L. Cwiklik, D. Nolting, B. Winter and P. Jungwirth, *Journal of Physical Chemistry A*, 2008, **112**, 3499-3505.
8. O. Borodin, J. Self, K. A. Persson, C. S. Wang and K. Xu, *Joule*, 2020, **4**, 69-100.
9. R. M. Fogarty, PhD thesis, Imperial College London, 2018.

Appendix

8.1. Solution formation parameters

Appendix Table 8.1. Solute and solvent masses used to produce 100 mL of each solution at the required concentration, measured within the current work.

Solution	Conc. / mol dm^{-3}	Solute mass / g	Solvent mass / g
$([C_4C_1Im][SCN])_{0.01}(H_2O)_{0.99}$	0.50	10.03	90.62
$([C_4C_1Im][SCN])_{0.10}(H_2O)_{0.90}$	2.89	56.96	46.77
$([C_4C_1Im][SCN])_{0.25}(H_2O)_{0.75}$	4.19	82.76	22.65
$([C_4C_1Im][N(CN)_2])(H_2O)$	0.50	10.39	90.20
$([C_4C_1Im][TfO])(H_2O)$	0.50	14.39	88.93
$([C_4C_1Im][BF_4])(H_2O)$	0.50	11.56	91.11
$([C_4C_1Im]I)(H_2O)$	0.50	13.57	90.83
$([C_4C_1Im]Cl)(H_2O)$	0.50	8.99	91.72
$(K[SCN])(H_2O)$	0.50	4.83	97.44
$(Li[NTf_2])(H_2O)$	0.50	14.37	89.19
$([C_4C_1Im][SCN])(H_2O/EtOH)$	0.50	4.96	22.42[a] / 57.37[b]
$([C_4C_1Im][SCN])(EtOH)$	0.50	9.52	71.88
$([C_4C_1Im][SCN])(MeCN)$	0.50	10.53	70.86
$([C_4C_1Im][SCN])(PC)$	0.50	9.71	109.12
$(K[SCN])(PC)$	0.50	4.88	116.90
$(Li[NTf_2])(PC)$	0.50	14.21	107.18

[a] values refer to H_2O in solution.

[b] values refer to EtOH in solution.

Appendix Table 8.2. Solute molar mass (M_r) and density (ρ) used to produce each solution measured within the current work.

Solute	M_r / g mol^{-1}	ρ / g cm^{-3}
$[C_4C_1Im][SCN]$	197.30	1.07
$[C_4C_1Im][N(CN)_2]$	205.26	1.06
$[C_4C_1Im][TfO]$	288.29	1.30
$[C_4C_1Im][BF_4]$	226.02	1.30
$[C_4C_1Im]I$	266.12	1.48
$[C_4C_1Im]Cl$	174.67	1.09
K[SCN]	97.18	1.89
$Li[NTf_2]$	287.19	1.33

Appendix Table 8.3. Solvent molar mass (M_r) and density (ρ) used to produce each solution measured within the current work.

Solvent	M_r / g mol^{-1}	ρ / g cm^{-3}
H_2O	18.00	1.00
EtOH	46.07	0.79
MeCN	41.05	0.79
PC	102.09	1.20

8.2. Photoemission peak fitting parameters and subtraction methods

Photoemission peak fitting parameters

Throughout this thesis, CasaXPS software[1] was used to fit photoelectron peaks, which arise from the non-resonant X-ray spectroscopic process. The software was used to fit each photoelectron peak using a Shirley background and GL(30) line shape. The fitting constraints and parameters employed to fit photoelectron peaks within this work are outlined in Appendix Table 8.4.

Appendix Table 8.4. Constraints used within the peak fitting models for core level X-ray photoelectron spectroscopy (XPS) employed within the current work.

Solvent/solute	Core level	Fitting constraints used
EtOH	C 1s	1:1 for C_{methyl}:$C_{methylene}$
MeCN	C 1s	1:1 for C_{methyl}:C_{cyano} FWHM(C_{methyl}) = FWHM(C_{cyano})
$[C_4C_1Im][SCN]$	C 1s	1:5:3 for C^2:C_{hetero}:C_{alkyl}
	S 2p	1:2 for $2p_{1/2}$:$2p_{3/2}$
$[C_4C_1Im][N(CN)_2]$	C 1s	1:6:3 for C^2:C_{hetero}:C_{alkyl}
$[C_4C_1Im][TfO]$	C 1s	1:4:3 for C^2:C_{hetero}:C_{alkyl}
$[C_4C_1Im][BF_4]$	C 1s	1:4:3 for C^2:C_{hetero}:C_{alkyl}
$[C_4C_1Im]I$	C 1s	1:4:3 for C^2:C_{hetero}:C_{alkyl}
	I 3d	2:3 for $3d_{3/2}$:$3d_{5/2}$
$[C_6C_1Im]I$	C 1s	1:4:5 for C^2:C_{hetero}:C_{alkyl}
	I 3d	2:3 for $3d_{3/2}$:$3d_{5/2}$
$[C_4C_1Im]Cl$	C 1s	1:4:3 for C^2:C_{hetero}:C_{alkyl}
	Cl 2p	1:2 for $2p_{1/2}$:$2p_{3/2}$
$[C_8C_1Im]Cl$	C 1s	1:4:7 for C^2:C_{hetero}:C_{alkyl}
	Cl 2p	1:2 for $2p_{1/2}$:$2p_{3/2}$
K[SCN]	K 2p	1:2 for $2p_{1/2}$:$2p_{3/2}$
	S 2p	1:2 for $2p_{1/2}$:$2p_{3/2}$
$Li[NTf_2]$	S 2p	1:2 for $2p_{1/2}$:$2p_{3/2}$

Valence RXPS heat map subtraction methods

Within the non-subtracted valence resonant X-ray photoelectron spectroscopy (RXPS) heat map, the RXP spectra at specific values of $h\nu$ contained contributions from both, the resonant Auger electron processes, and the valence non-RXP processes. To remove the non-resonant contributions, resulting in a heat map containing purely (or mostly) RXP, a method of NRXP subtraction was devised, as reported in the literature.[2] Subtraction was achieved at consistent values of $h\nu$, corresponding to NRXP spectra just below resonant $h\nu$ (Table 8.5). This method also served to reduce the intensity of any second order light features present within each valence RXPS heat map.

Appendix Table 8.5. The photoemission peak identity and $h\nu$ value of the NRXP spectra used for subtraction of the valence RXPS heat map.

Absorption edge	Valence NRXP energy / $h\nu$
N 1s	398.0
O 1s	532.5
C 1s	284.0
F 1s	686.0

8.3. Supplementary information for Chapter 3

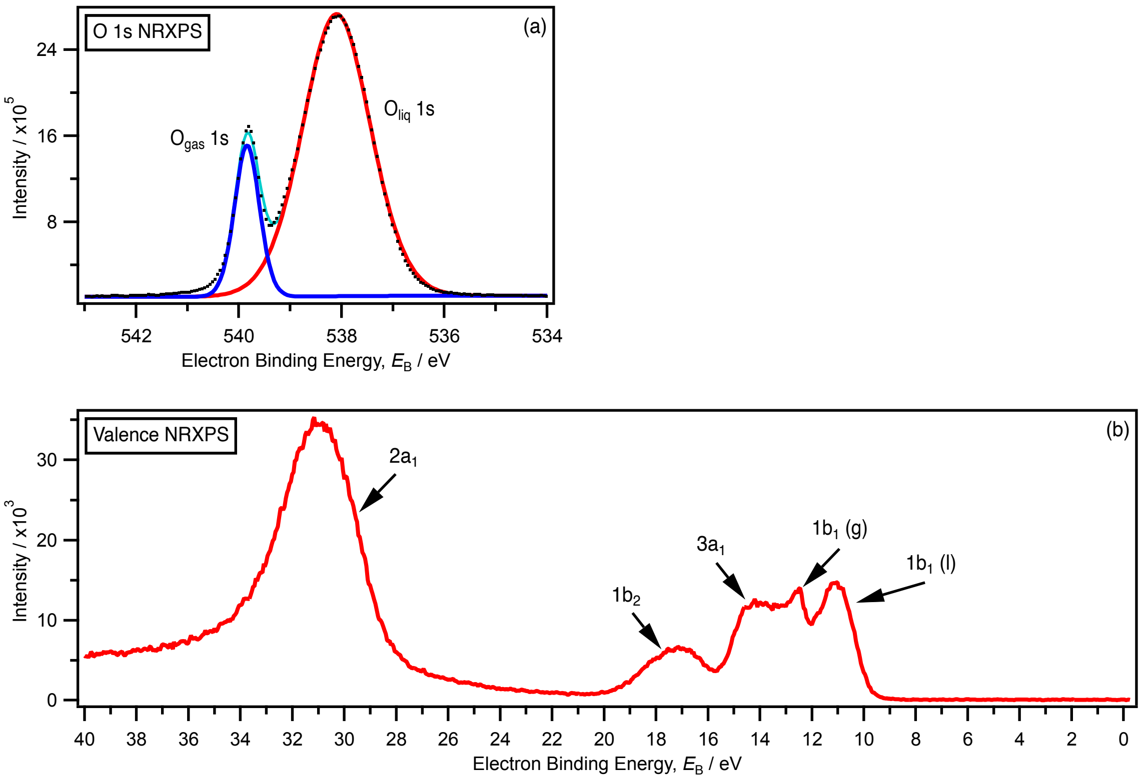

Appendix Figure 8.1. Core and valence state NRXP spectra for pure H_2O (plus 20 mM NaI): (a) O 1s. (b) Valence. All XP spectra were measured at *hν* = 700.0 eV. All XP spectra were charge referenced using the methods detailed in Section 2.7.2.

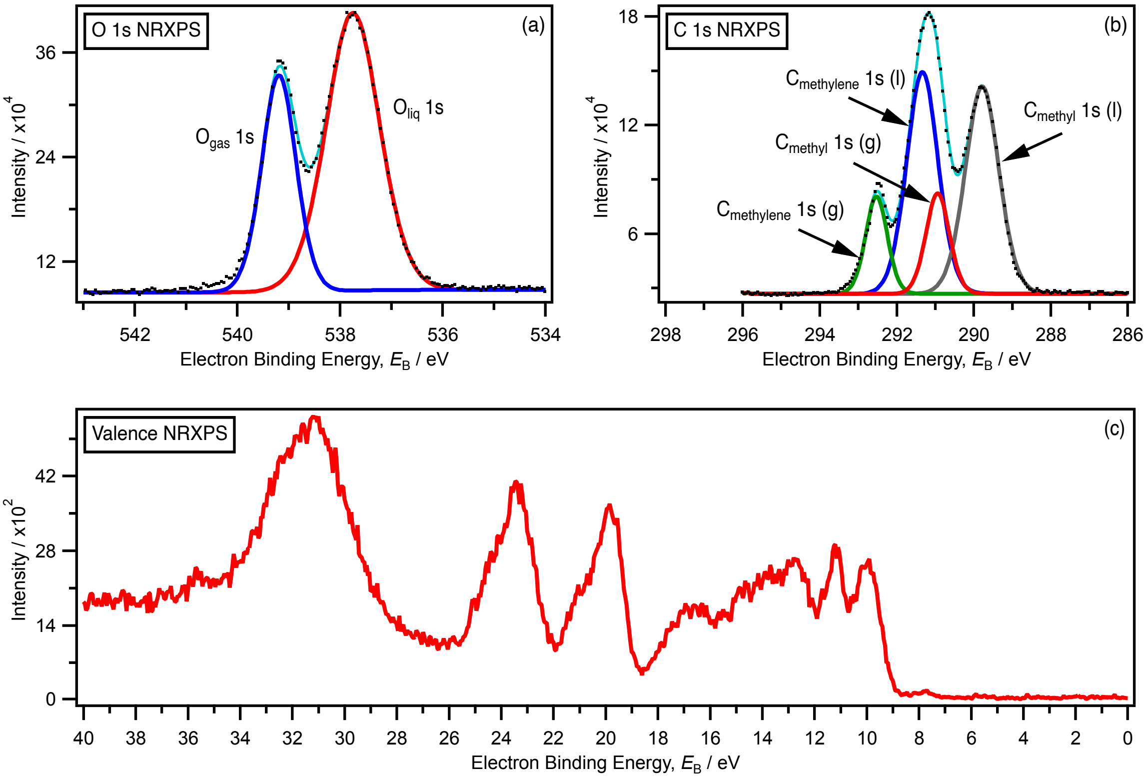

Appendix Figure 8.2. Core and valence state NRXP spectra for pure EtOH (plus 20 mM NaI): (a) O 1s. (b) C 1s. (c) Valence. All XP spectra were measured at *hν* = 700.0 eV. No charge referencing methods were applied to the NRXP spectra for pure EtOH.

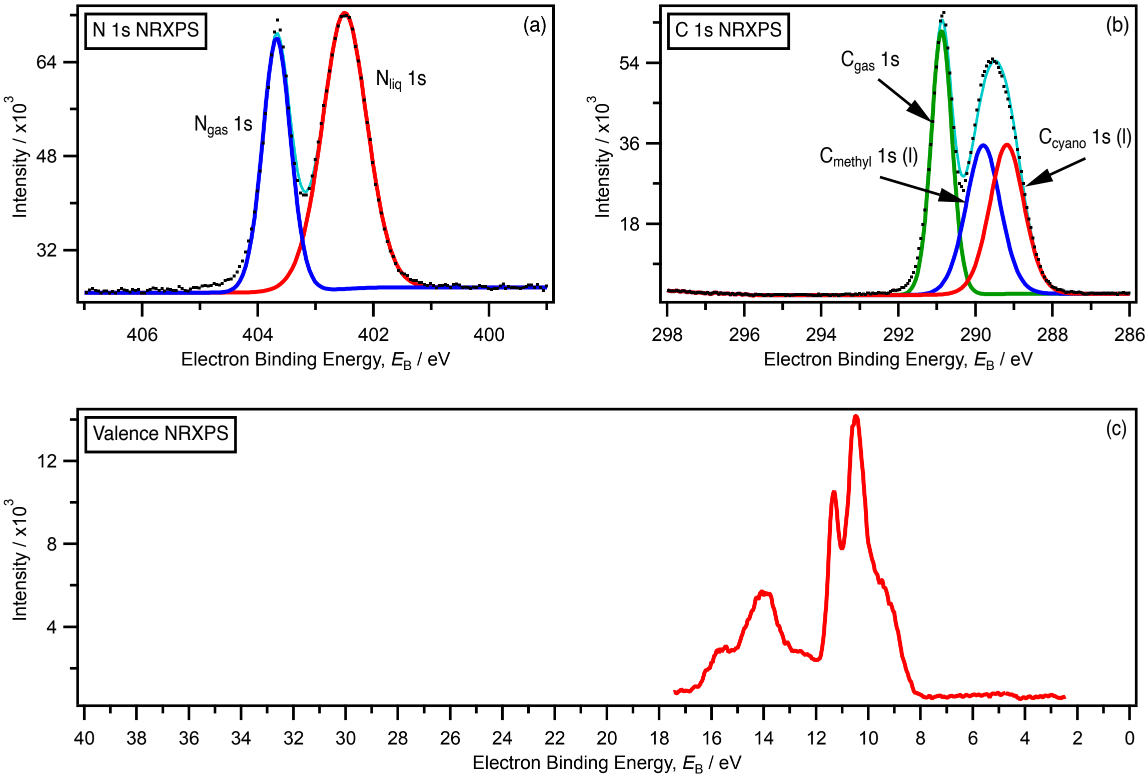

Appendix Figure 8.3. Core and valence state NRXP spectra for pure MeCN (plus 20 mM NaI): (a) N 1s. (b) C 1s. (c) Valence. All XP spectra were measured at *hν* = 700.0 eV. No charge referencing methods were applied to the NRXP spectra for pure MeCN.

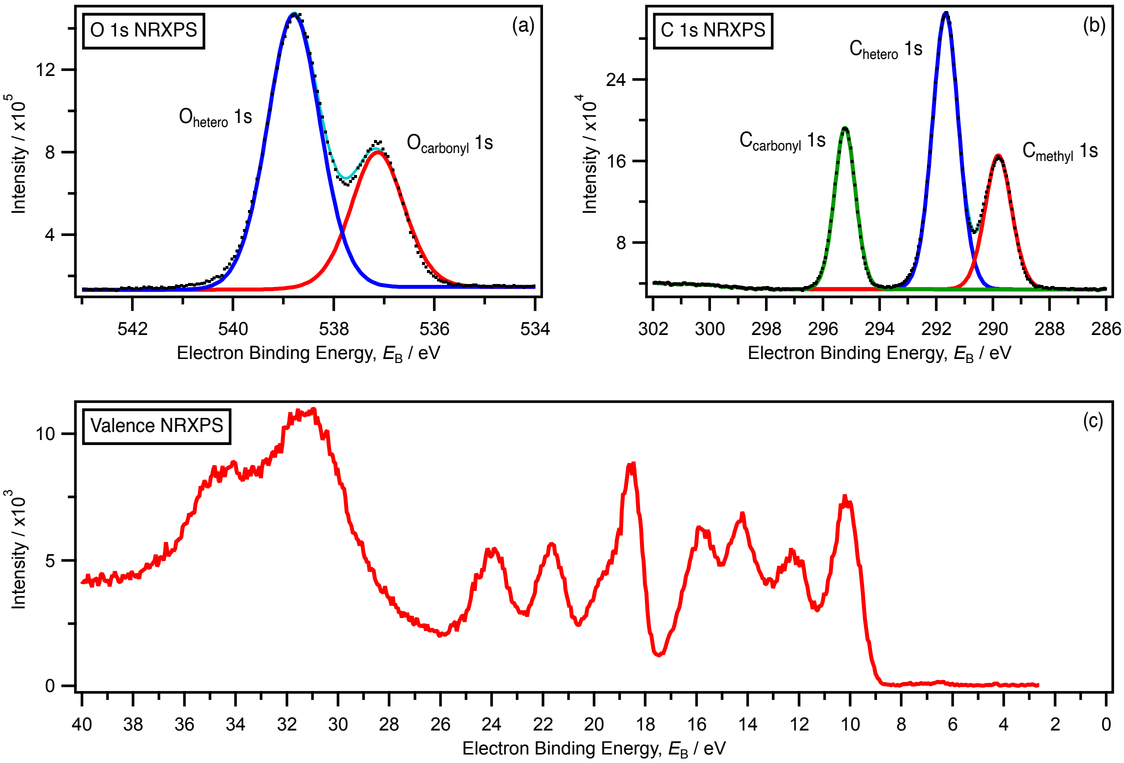

Appendix Figure 8.4. Core and valence state NRXP spectra for pure PC (plus 20 mM NaI): (a) O 1s. (b) C 1s. (c) Valence. All XP spectra were measured at *hν* = 700.0 eV. All XP spectra were charge referenced using the methods detailed in Section 2.7.2.

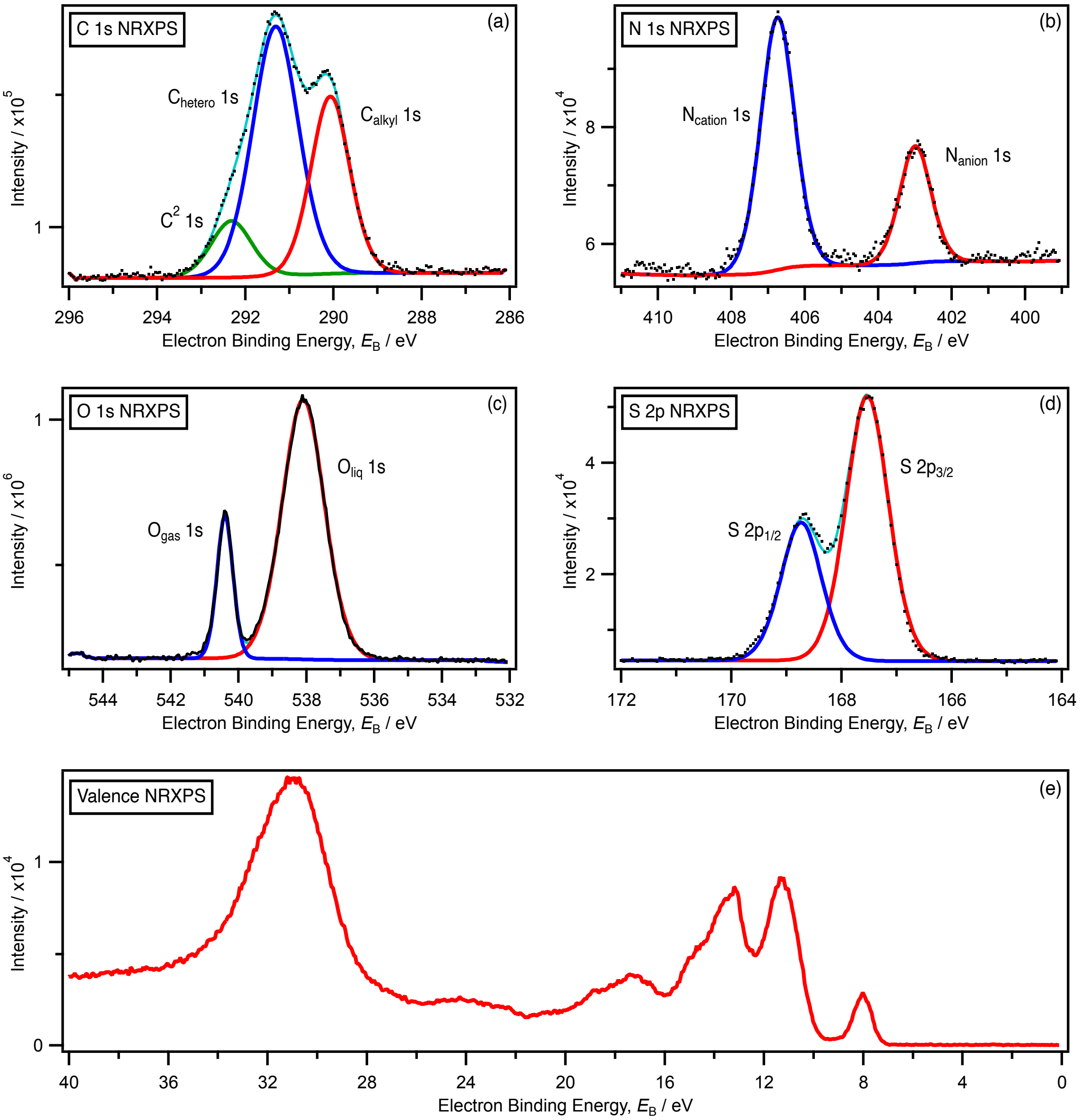

Appendix Figure 8.5. Core and valence state NRXP spectra for 0.5 M ([C_4C_1Im][SCN])(H_2O): (a) C 1s. (b) N 1s. (c) O 1s. (d) S 2p. (e) Valence. All XP spectra were measured at *hν* = 700.0 eV. All XP spectra were charge referenced using the methods detailed in Section 2.7.1.

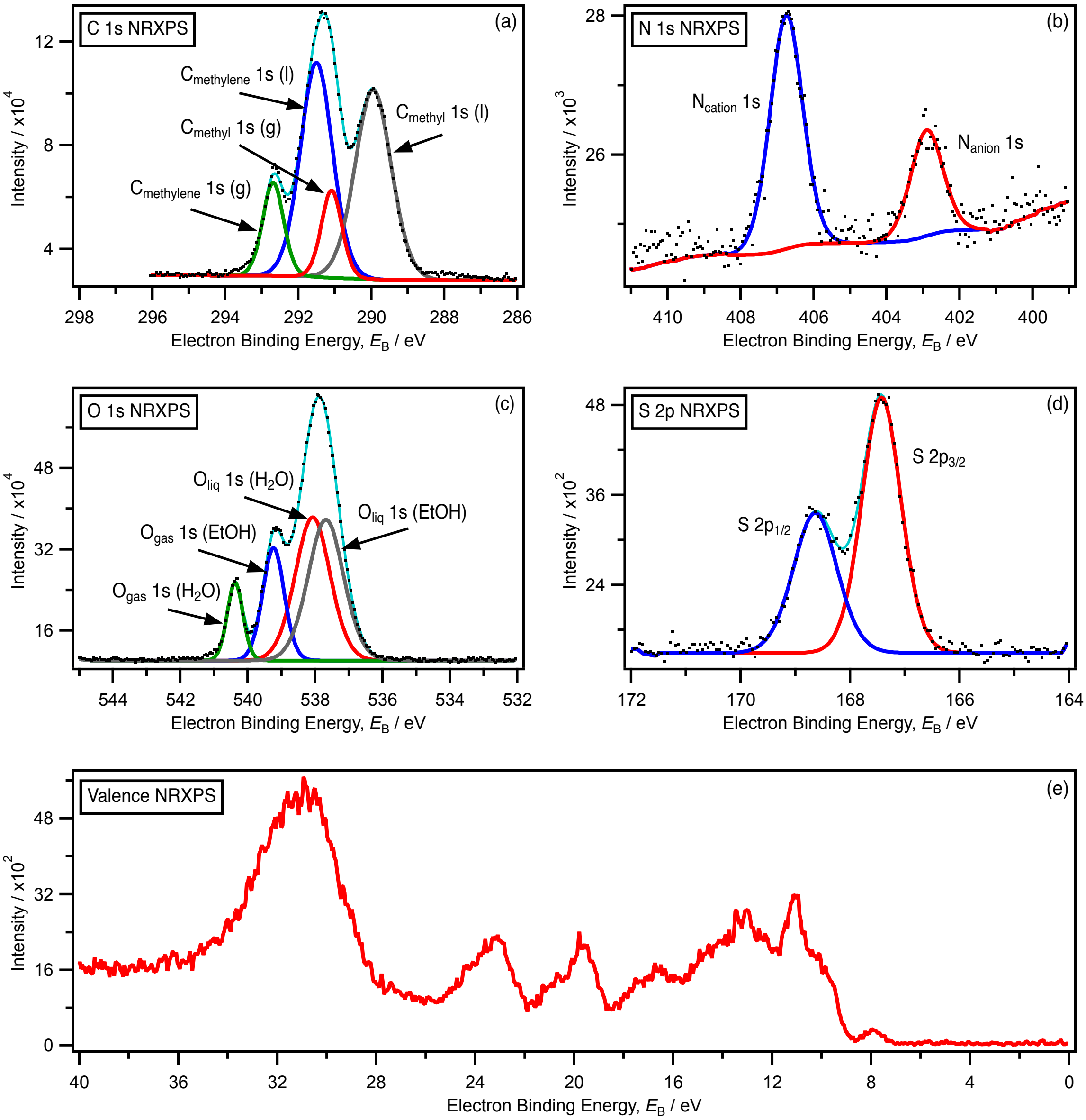

Appendix Figure 8.6. Core and valence state NRXP spectra for 0.5 M ($[C_4C_1Im][SCN]$)(H_2O/EtOH): (a) C 1s. (b) N 1s. (c) O 1s. (d) S 2p. (e) Valence. All XP spectra were measured at $h\nu$ = 700.0 eV. All XP spectra were charge referenced using the methods detailed in Section 2.7.1.

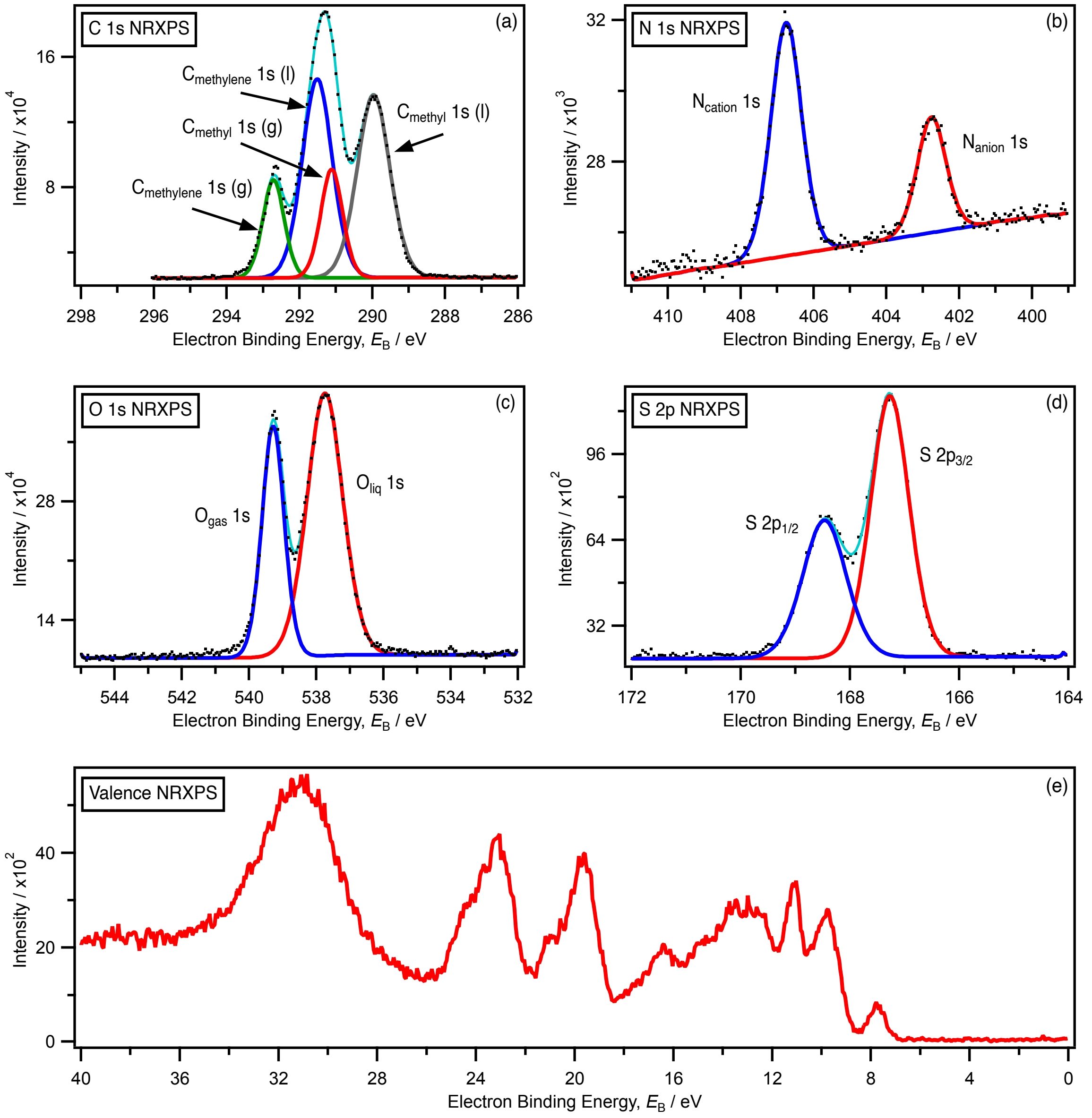

Appendix Figure 8.7. Core and valence state NRXP spectra for 0.5 M ($[C_4C_1Im][SCN]$)(EtOH): (a) C 1s. (b) N 1s. (c) O 1s. (d) S 2p. (e) Valence. All XP spectra were measured at *hν* = 700.0 eV. All XP spectra were charge referenced using the methods detailed in Section 2.7.1.

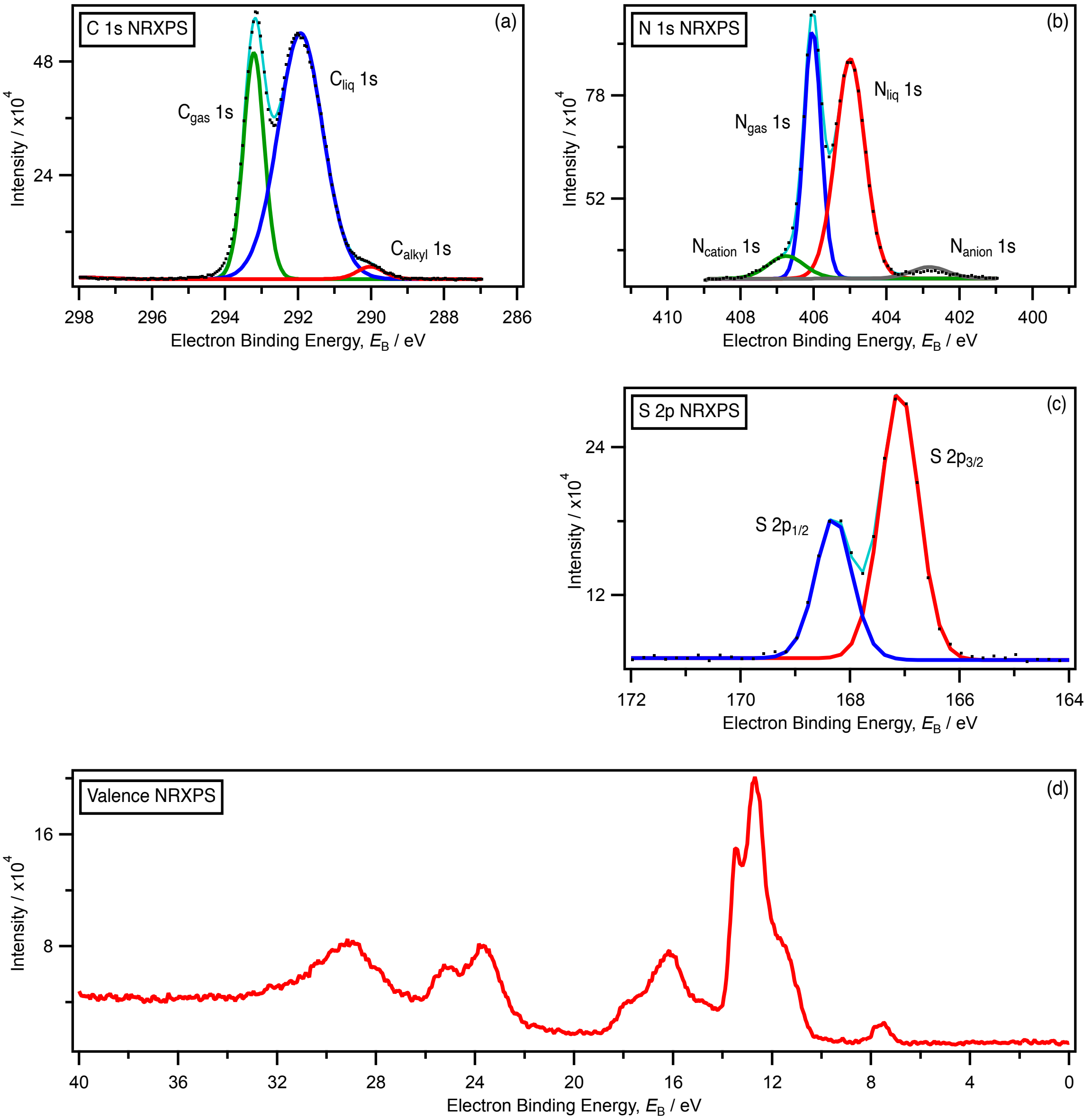

Appendix Figure 8.8. Core and valence state NRXP spectra for 0.5 M ([C_4C_1Im][SCN])(MeCN): (a) C 1s. (b) N 1s, where the N_{cation} 1s and N_{anion} 1s photoemission peaks were not reliably fitted without heavy constraints. (c) S 2p. (d) Valence. All XP spectra were measured at *hν* = 700.0 eV. All XP spectra were charge referenced using the methods detailed in Section 2.7.1.

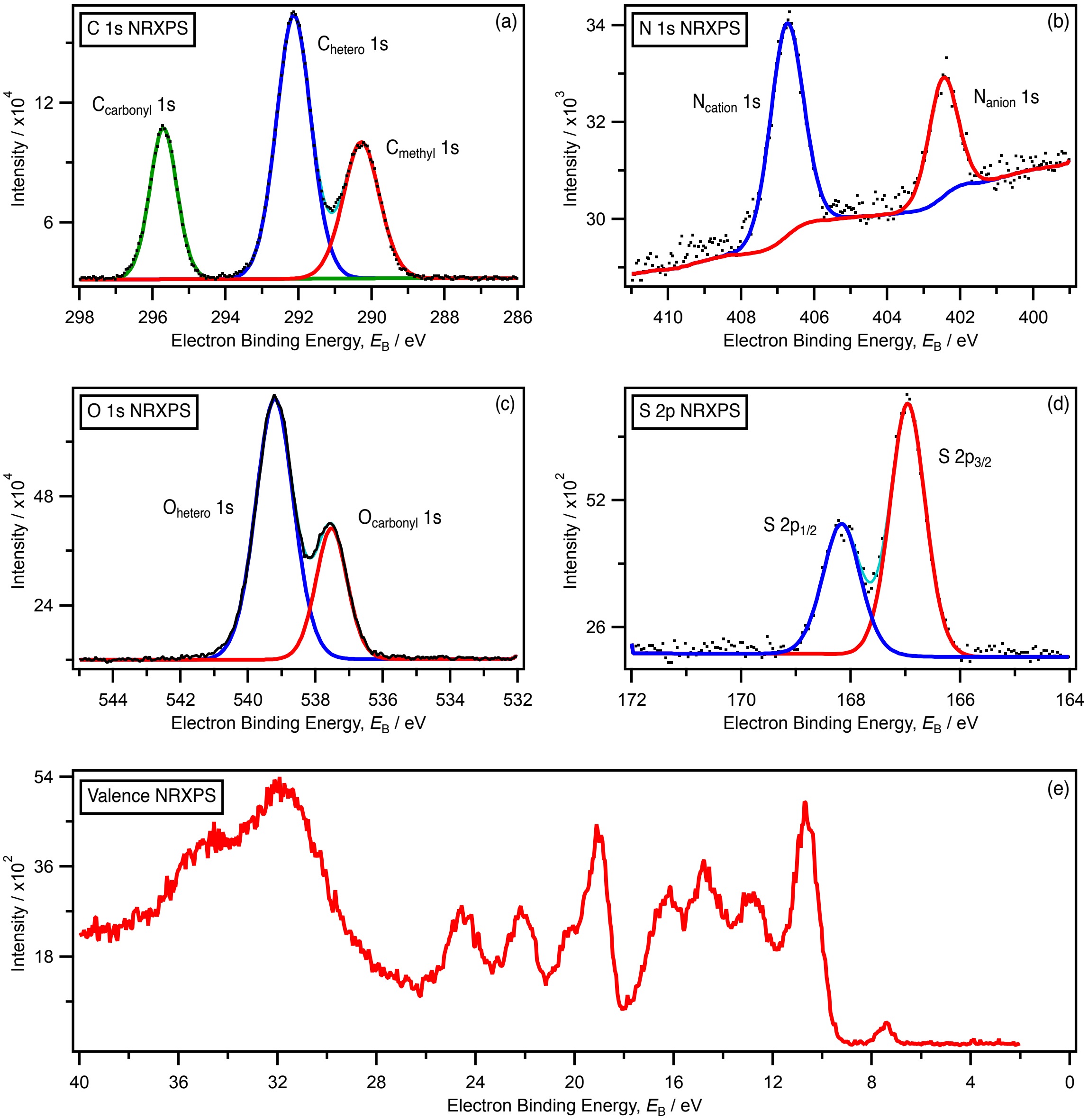

Appendix Figure 8.9. Core and valence state NRXP spectra for 0.5 M ($[C_4C_1Im][SCN]$)(PC): (a) C 1s. (b) N 1s. (c) O 1s. (d) S 2p. (e) Valence. All XP spectra were measured at $h\nu$ = 700.0 eV. All XP spectra were charge referenced using the methods detailed in Section 2.7.1.

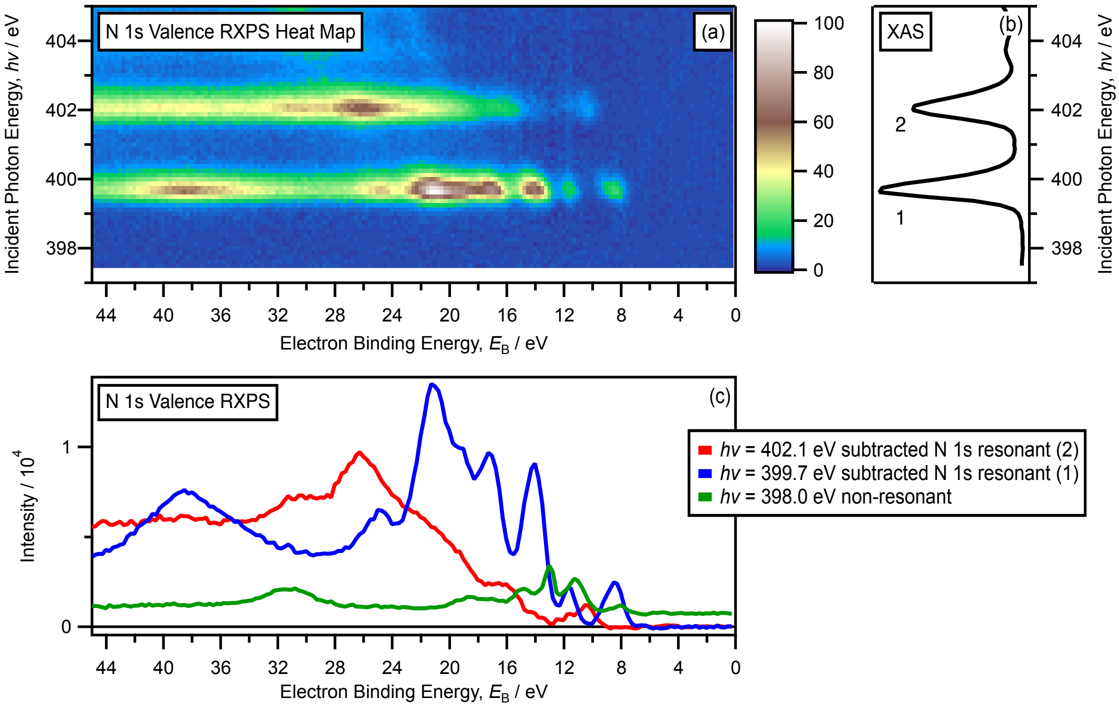

Appendix Figure 8.10. N 1s valence RXPS map and spectra for 0.5 M ([C_4C_1Im][SCN])(H_2O): (a) N 1s valence RXPS heat map for 0.5 M ([C_4C_1Im][SCN])(H_2O). (b) Partial electron yield N 1s XA spectra. (c) N 1s valence NRXP spectrum (*hν* = 398.0 eV) and N 1s valence RXP spectra (*hν* = 402.1 eV and *hν* = 399.7 eV), with the valence NRXP contributions subtracted. The NRXPS contributions were subtracted using the procedure detailed in Section 8.2. All RXP spectra were charge referenced using the methods detailed in Section 2.7.3.

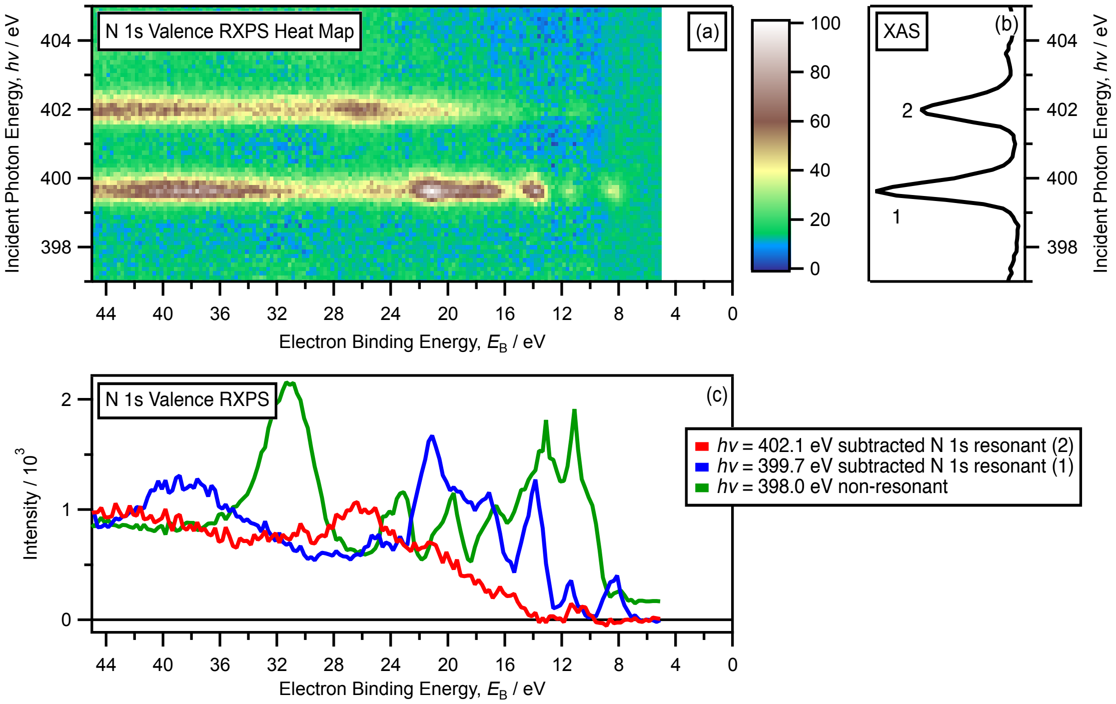

Appendix Figure 8.11. N 1s valence RXPS map and spectra for 0.5 M ($[C_4C_1Im][SCN]$)(H_2O/EtOH): (a) N 1s valence RXPS heat map for 0.5 M ($[C_4C_1Im][SCN]$)(H_2O/EtOH). (b) Partial electron yield N 1s XA spectra. (c) N 1s valence NRXP spectrum (*hν* = 398.0 eV) and N 1s valence RXP spectra (*hν* = 402.1 eV and *hν* = 399.7 eV), with the valence NRXP contributions subtracted. The NRXPS contributions were subtracted using the procedure detailed in Section 8.2. All RXP spectra were charge referenced using the methods detailed in Section 2.7.3.

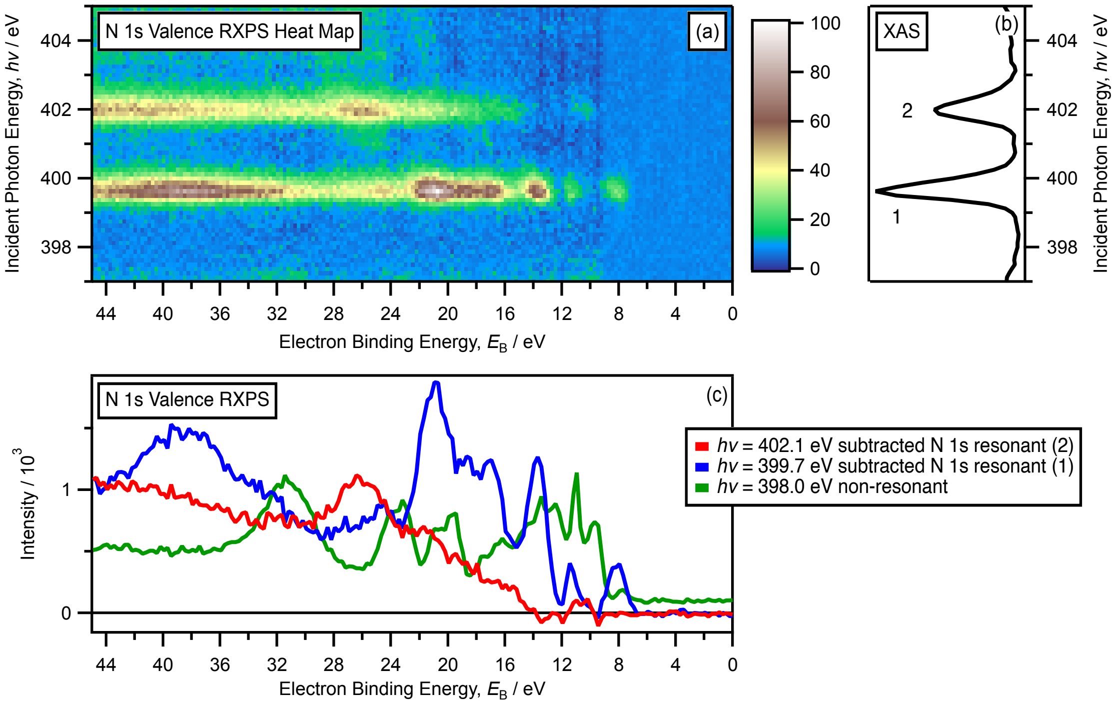

Appendix Figure 8.12. N 1s valence RXPS map and spectra for 0.5 M ([C$_4$C$_1$Im][SCN])(EtOH): (a) N 1s valence RXPS heat map for 0.5 M ([C$_4$C$_1$Im][SCN])(EtOH). (b) Partial electron yield N 1s XA spectra. (c) N 1s valence NRXP spectrum (*hν* = 398.0 eV) and N 1s valence RXP spectra (*hν* = 402.1 eV and *hν* = 399.7 eV), with the valence NRXP contributions subtracted. The NRXPS contributions were subtracted using the procedure detailed in Section 8.2. All RXP spectra were charge referenced using the methods detailed in Section 2.7.3.

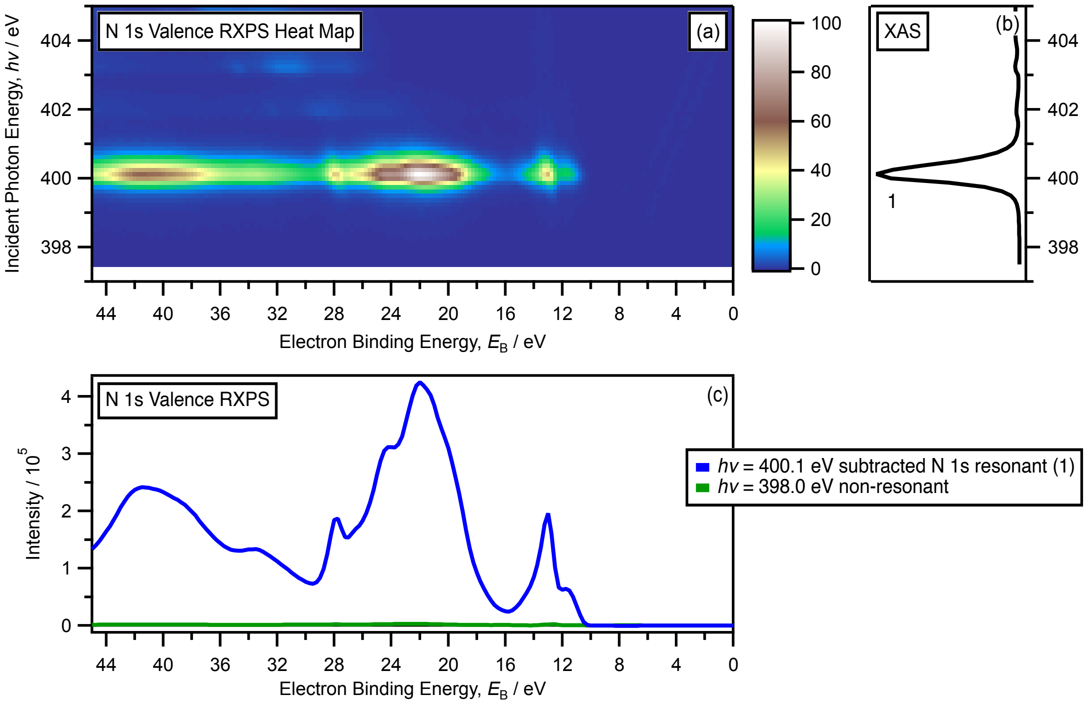

Appendix Figure 8.13. N 1s valence RXPS map and spectra for 0.5 M ([C_4C_1Im][SCN])(MeCN): (a) N 1s valence RXPS heat map for 0.5 M ([C_4C_1Im][SCN])(MeCN). (b) Partial electron yield N 1s XA spectra. (c) N 1s valence NRXP spectrum (*hν* = 398.0 eV) and N 1s valence RXP spectra (*hν* = 400.1 eV), with the valence NRXP contributions subtracted. The NRXPS contributions were subtracted using the procedure detailed in Section 8.2. All RXP spectra were charge referenced using the methods detailed in Section 2.7.3.

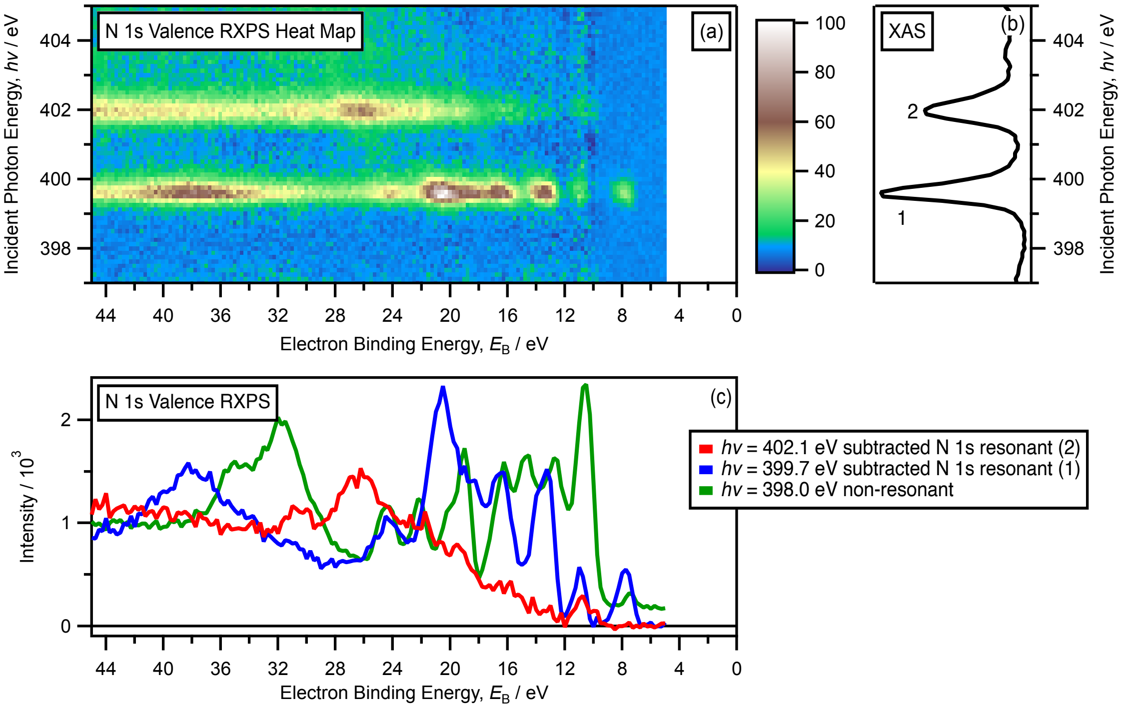

Appendix Figure 8.14. N 1s valence RXPS map and spectra for 0.5 M ([C_4C_1Im][SCN])(PC): (a) N 1s valence RXPS heat map for 0.5 M ([C_4C_1Im][SCN])(PC). (b) Partial electron yield N 1s XA spectra. (c) N 1s valence NRXP spectrum (*hν* = 398.0 eV) and N 1s valence RXP spectra (*hν* = 402.1 eV and *hν* = 399.7 eV), with the valence NRXP contributions subtracted. The NRXPS contributions were subtracted using the procedure detailed in Section 8.2. All RXP spectra were charge referenced using the methods detailed in Section 2.7.3.

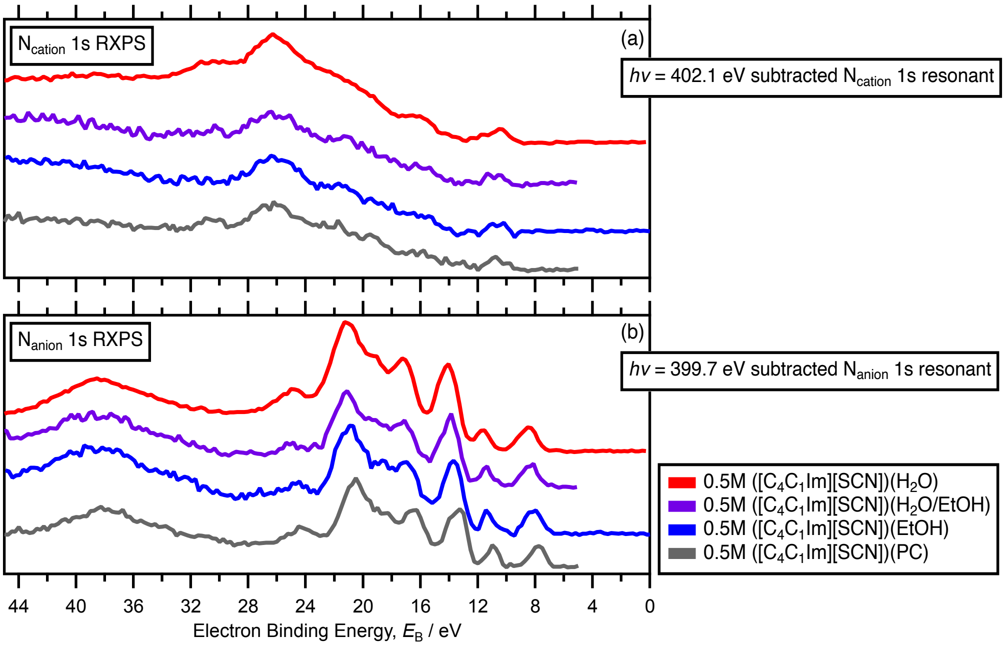

Appendix Figure 8.15. N 1s valence RXP spectra comparison for 0.5 M ([C_4C_1Im][SCN])(solvent), where solvent = H_2O, H_2O/EtOH, EtOH, MeCN, and PC. (a) N$_{cation}$ 1s valence RXP spectra ($h\nu$ = 402.1 eV), with the valence NRXP contributions subtracted. (b) N$_{anion}$ 1s valence RXP spectra ($h\nu$ = 399.7 eV), with the valence NRXP contributions subtracted. Spectra are vertically offset for clarity. All NRXP spectra were charge referenced using the methods detailed in Section 2.7.3.

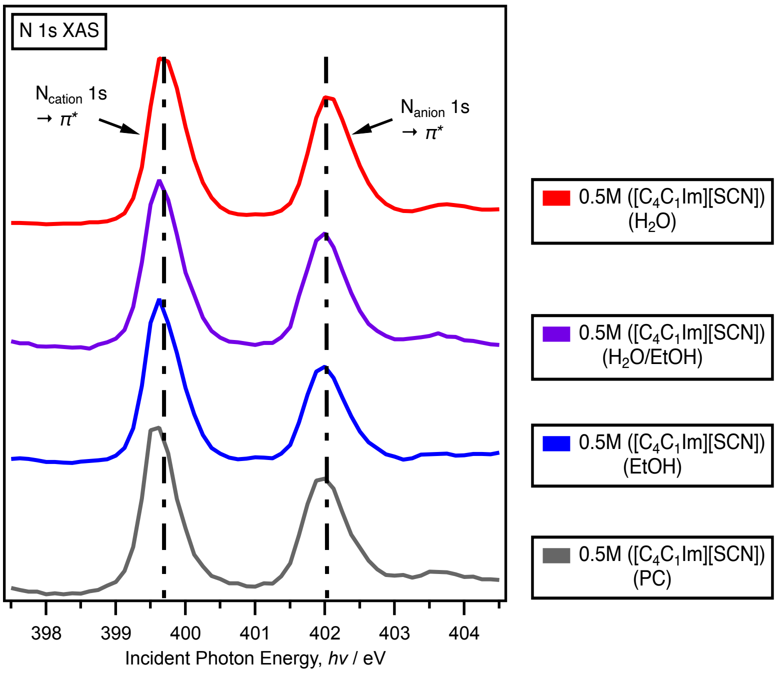

Appendix Figure 8.16. N 1s XA spectra comparison for 0.5 M ([C_4C_1Im][SCN])(solvent), where solvent = H_2O, H_2O/EtOH, EtOH, MeCN, and PC. Spectra are vertically offset for clarity and dashed lines are added as a visual aid.

8.4. Supplementary information for Chapter 4

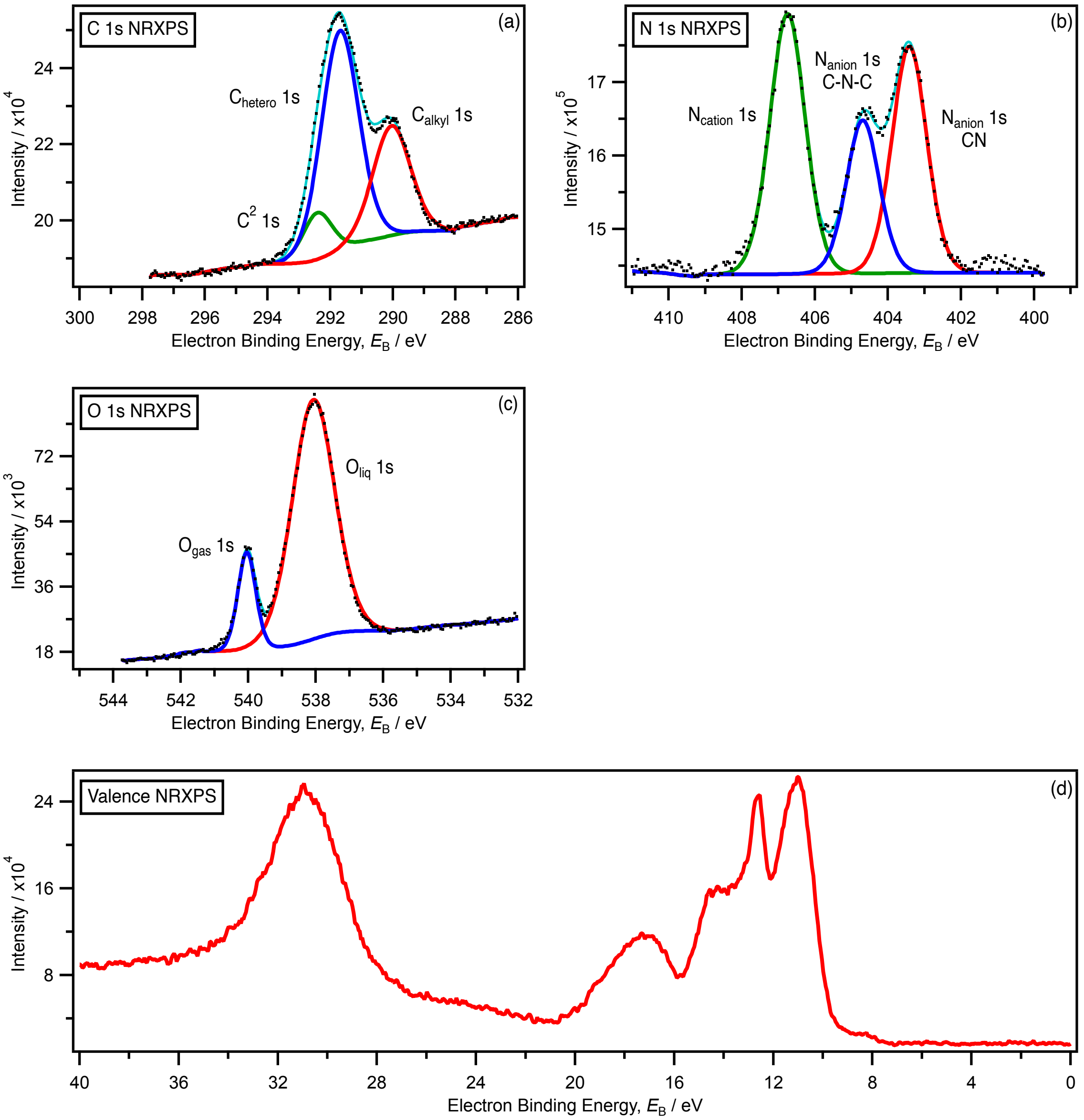

Appendix Figure 8.17. Core and valence state NRXP spectra for 0.5 M ($[C_4C_1Im][N(CN)_2]$)(H_2O): (a) C 1s. (b) N 1s. (c) O 1s. (d) Valence. All XP spectra were measured at $h\nu$ = 700.0 eV. All XP spectra were charge referenced using the methods detailed in Section 2.7.1.

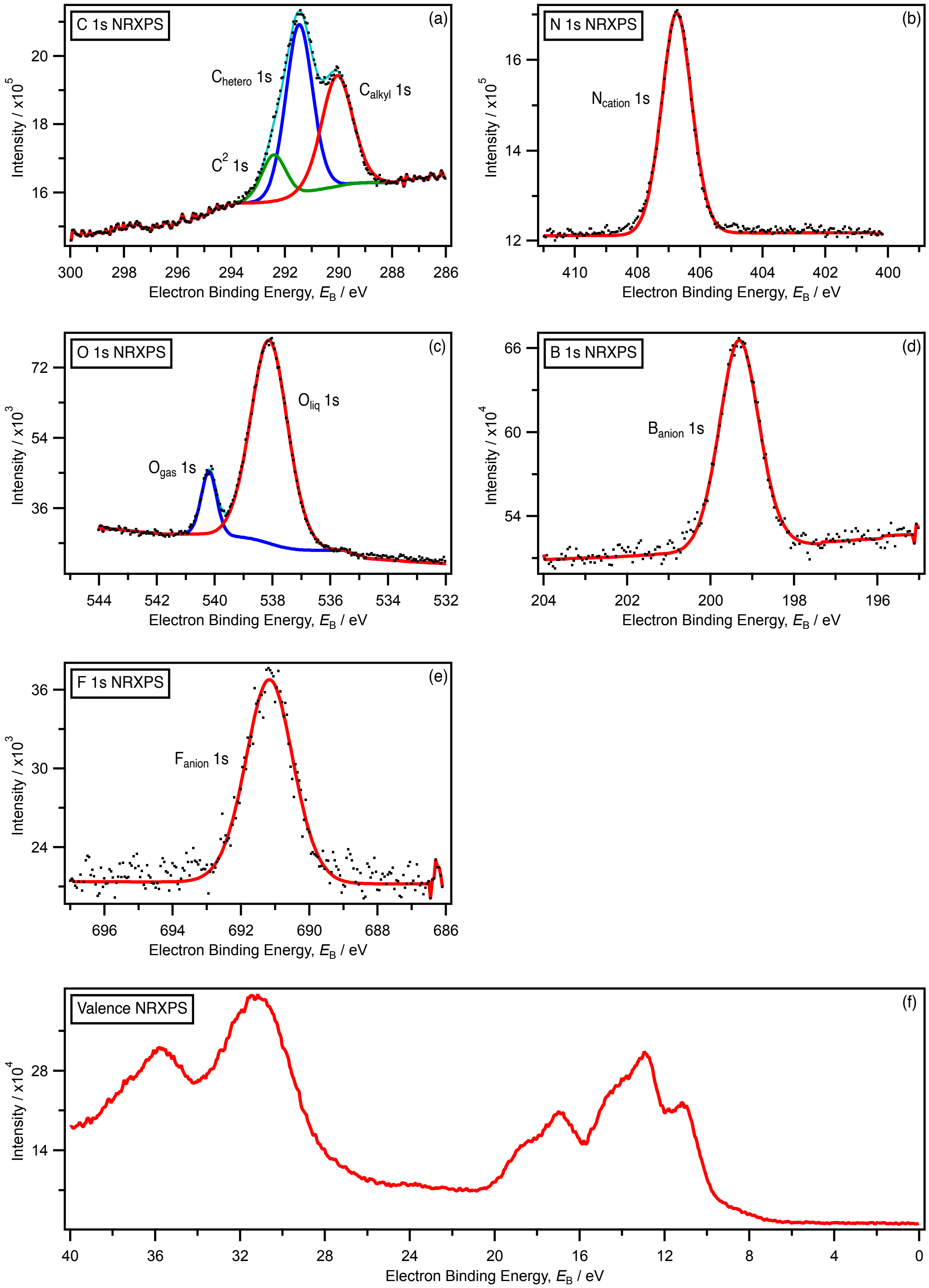

Appendix Figure 8.18. Core and valence state NRXP spectra for 0.5 M ([C_4C_1Im][BF_4])(H_2O): (a) C 1s. (b) N 1s. (c) O 1s. (d) B 1s. (e) F 1s. (f) Valence. All XP spectra were measured at $h\nu$ = 700.0 eV. All XP spectra were charge referenced using the methods detailed in Section 2.7.1.

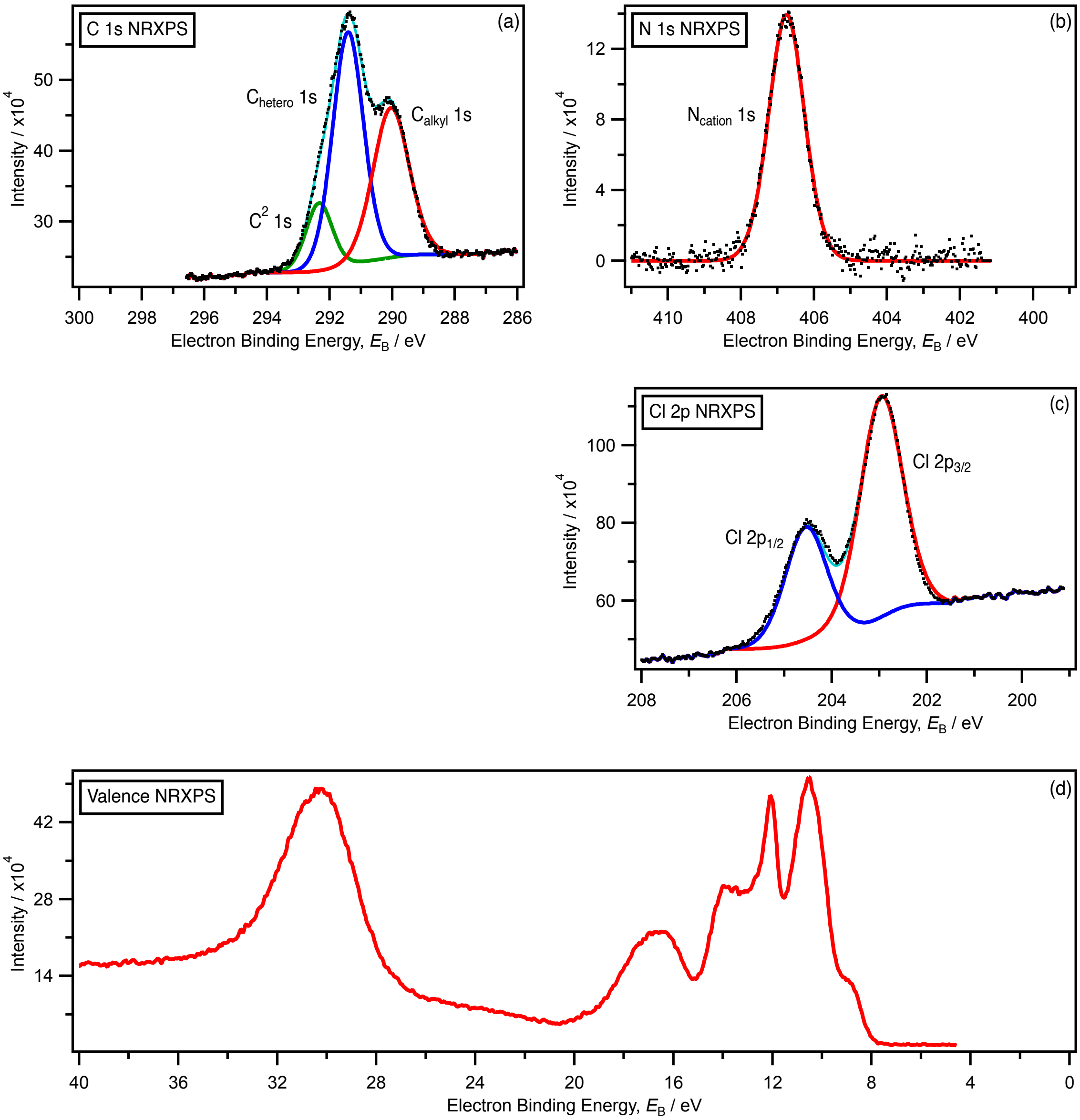

Appendix Figure 8.19. Core and valence state NRXP spectra for 0.5 M ([C_4C_1Im]Cl)(H_2O): (a) C 1s. (b) N 1s. (c) Cl 2p. (d) Valence. All XP spectra were measured at $h\nu$ = 700.0 eV. All XP spectra were charge referenced using the methods detailed in Section 2.7.1.

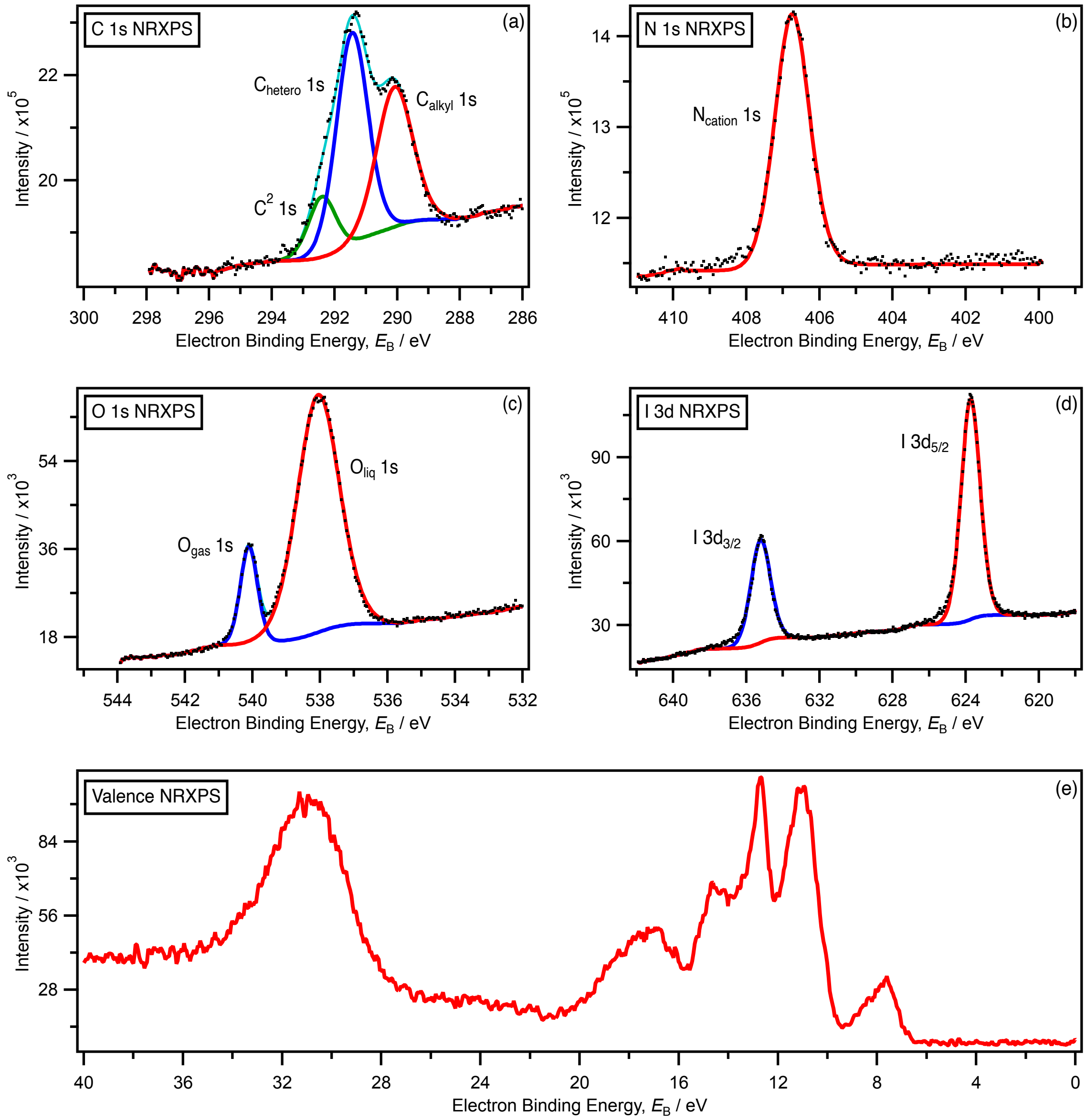

Appendix Figure 8.20. Core and valence state NRXP spectra for 0.5 M ($[C_4C_1Im]I$)(H_2O): (a) C 1s. (b) N 1s. (c) O 1s. (d) I 3d. (e) Valence. All XP spectra were measured at $h\nu$ = 700.0 eV. All XP spectra were charge referenced using the methods detailed in Section 2.7.1.

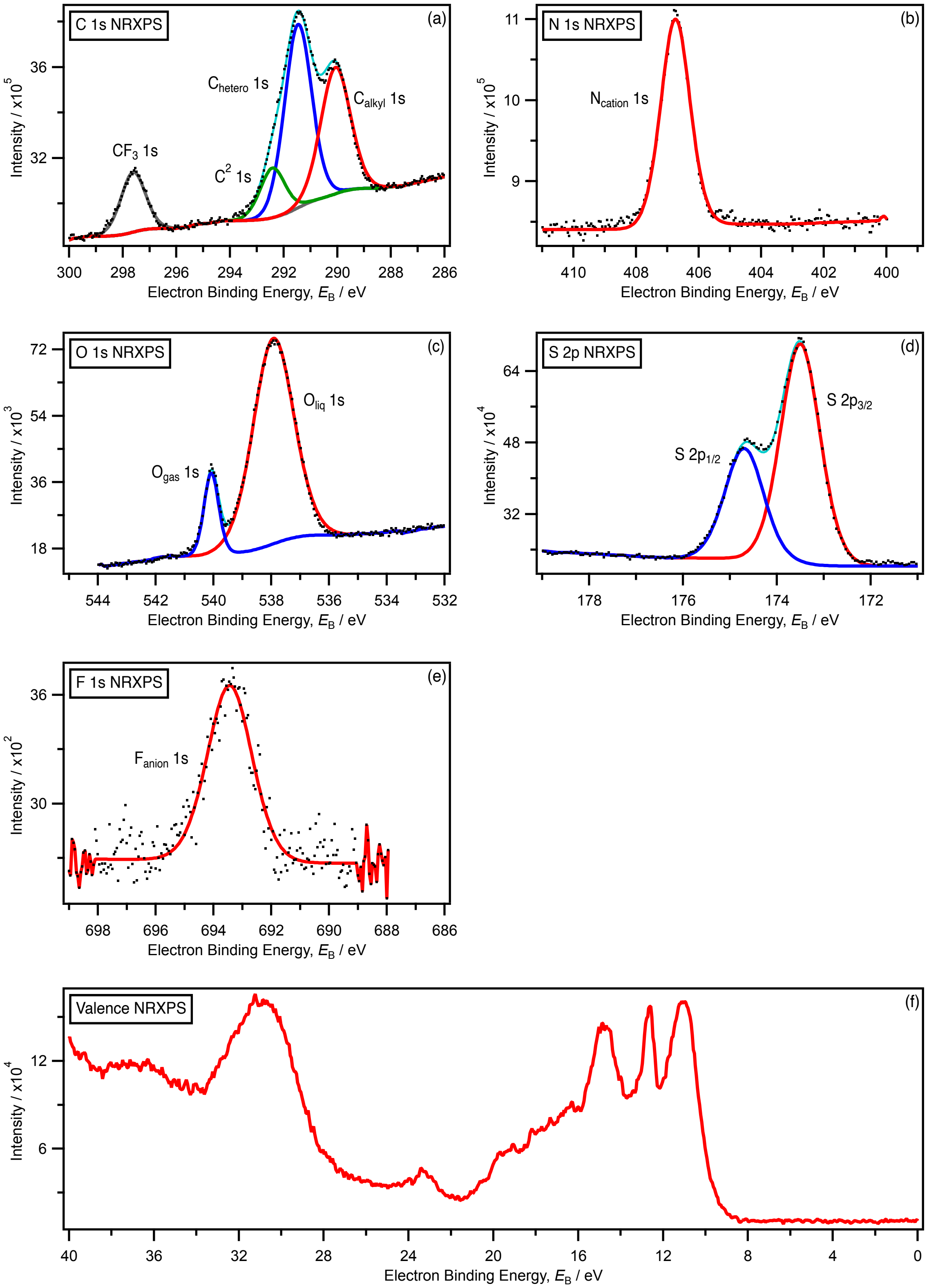

Appendix Figure 8.21. Core and valence state NRXP spectra for 0.5 M ([C_4C_1Im][TfO])(H_2O): (a) C 1s. (b) N 1s. (c) O 1s. (d) S 2p. (e) F 1s. (f) Valence. All XP spectra were measured at *hν* = 700.0 eV. All XP spectra were charge referenced using the methods detailed in Section 2.7.1.

8.5. Supplementary information for Chapter 5

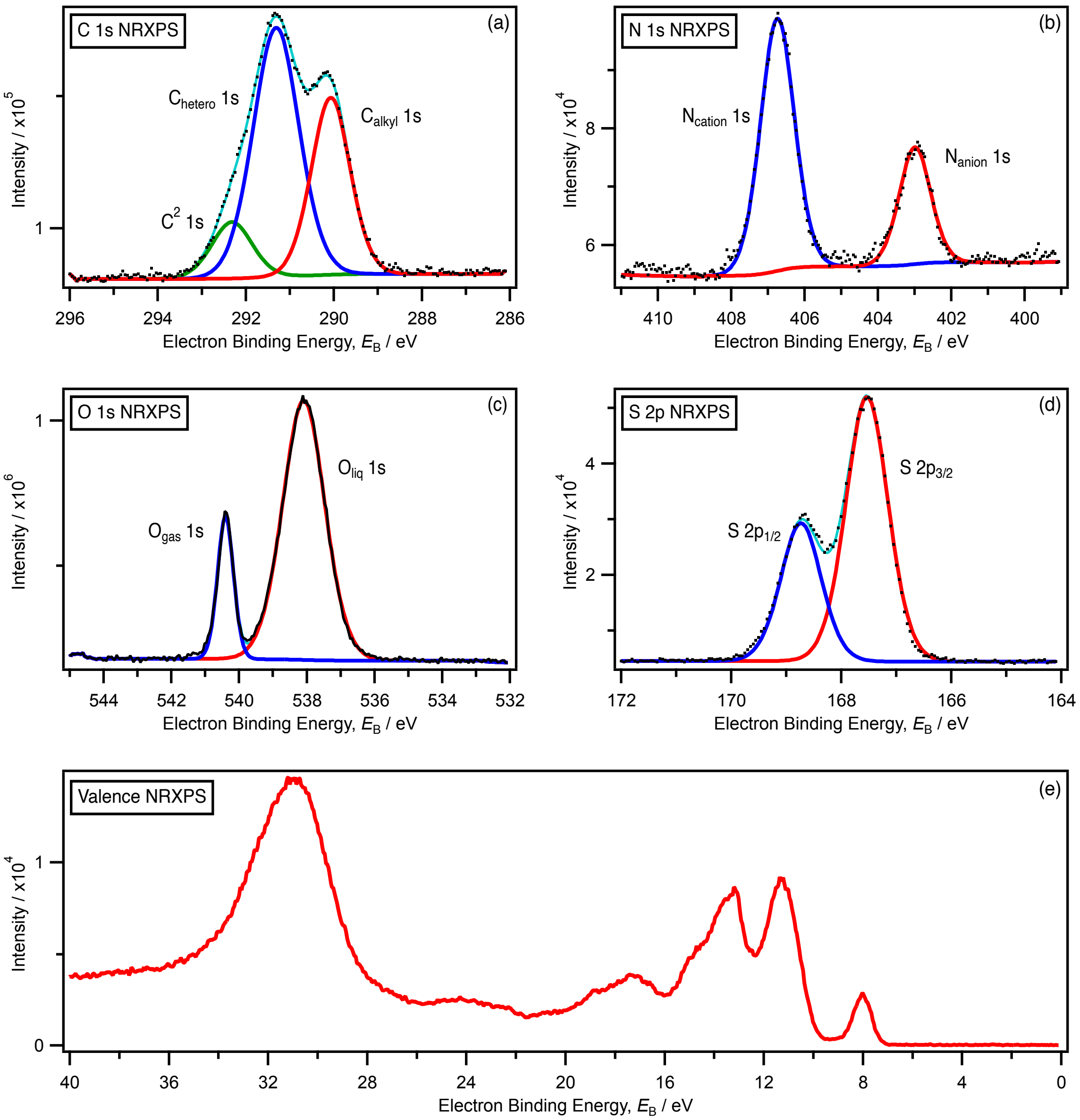

Appendix Figure 8.22. Core and valence state NRXP spectra for $([C_4C_1Im][SCN])_{0.01}(H_2O)_{0.99}$: (a) C 1s. (b) N 1s. (c) O 1s. (d) S 2p. (e) Valence. All XP spectra were measured at $h\nu$ = 700.0 eV. All XP spectra were charge referenced using the methods detailed in Section 2.7.1.

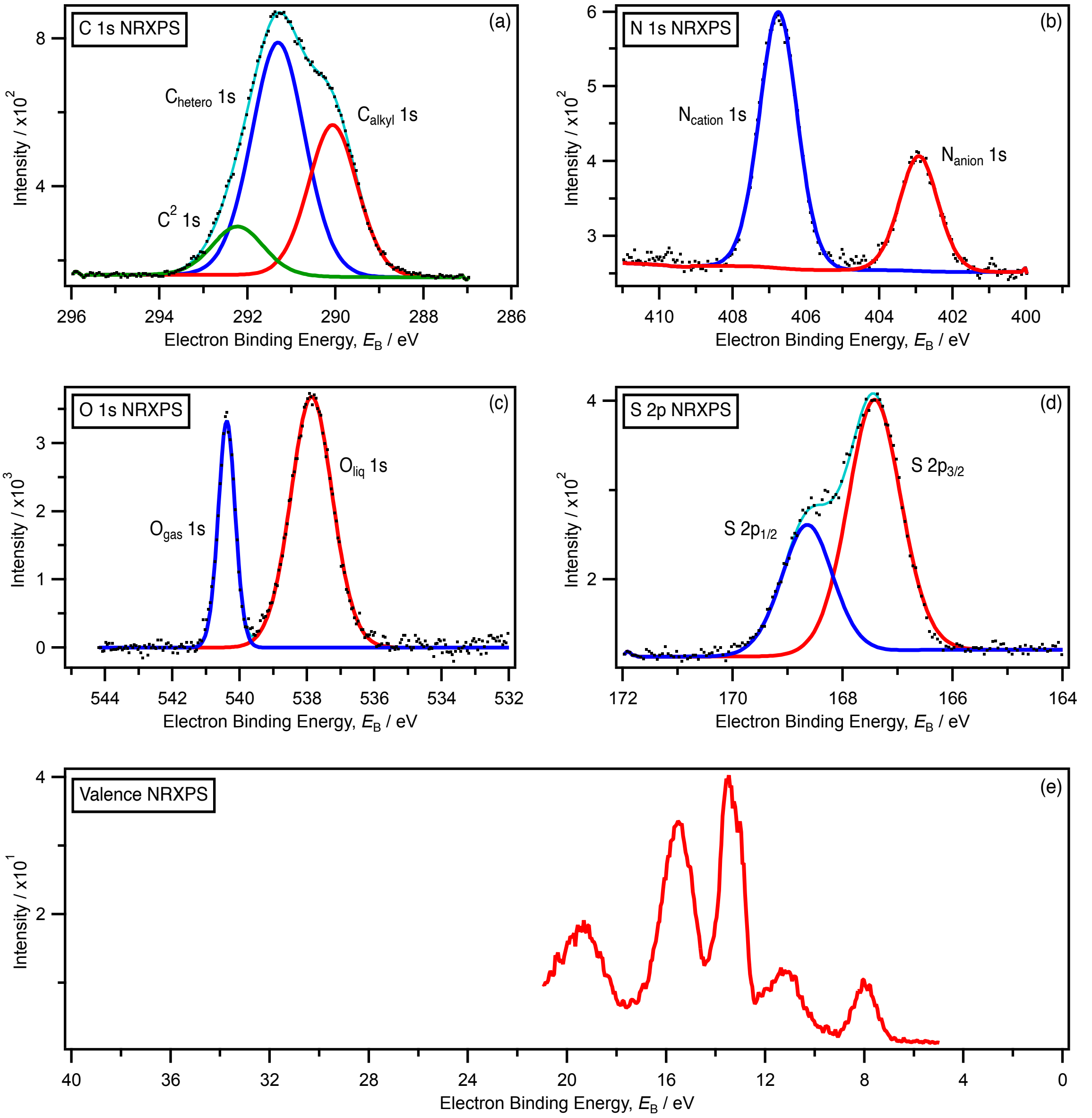

Appendix Figure 8.23. Core and valence state NRXP spectra for $([C_4C_1Im][SCN])_{0.10}(H_2O)_{0.90}$: (a) C 1s. (b) N 1s. (c) O 1s. (d) S 2p. (e) Valence. All XP spectra were measured at $h\nu$ = 700.0 eV. All XP spectra were charge referenced using the methods detailed in Section 2.7.1.

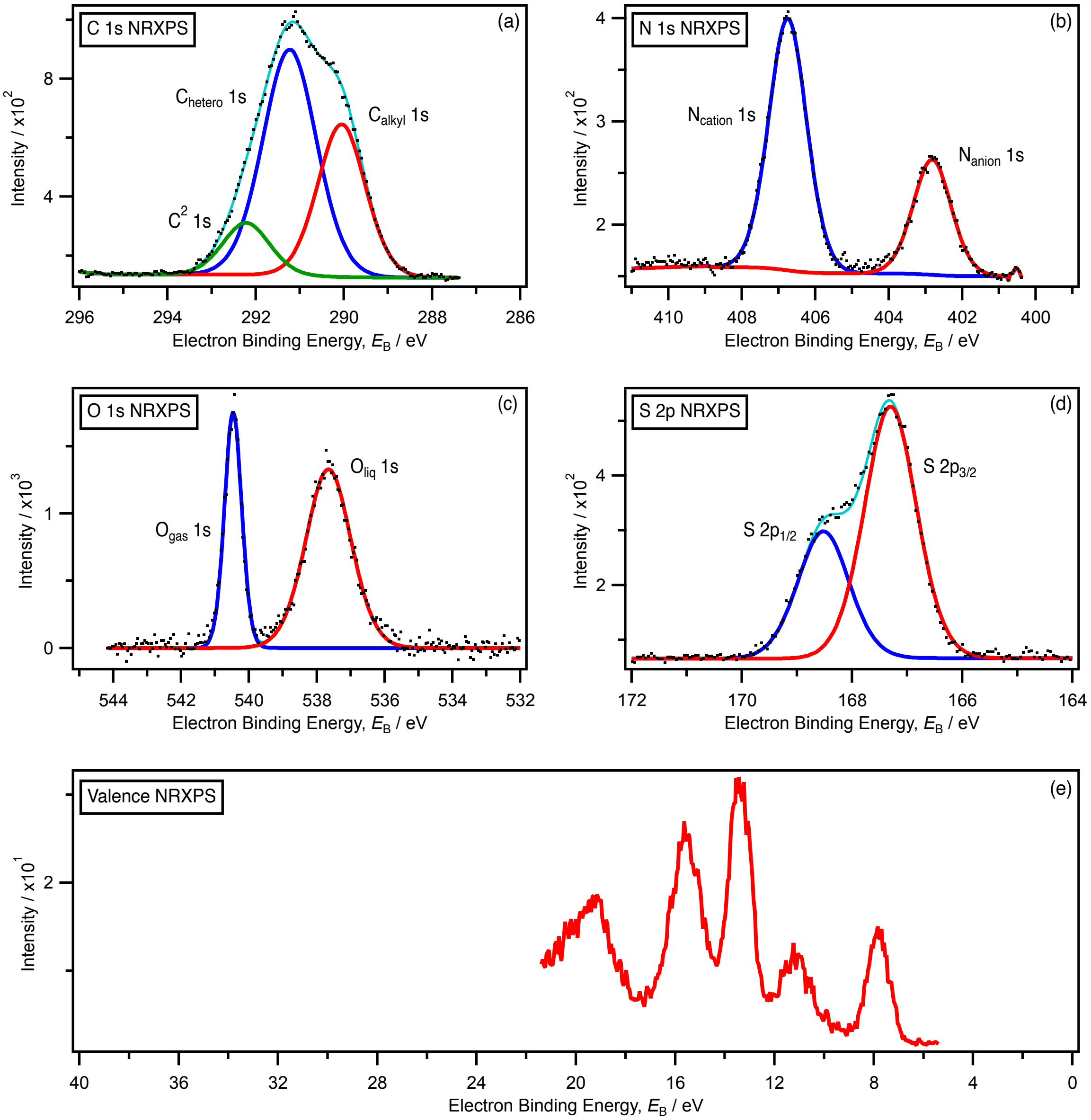

Appendix Figure 8.24. Core and valence state NRXP spectra for $([C_4C_1Im][SCN])_{0.25}(H_2O)_{0.75}$: (a) C 1s. (b) N 1s. (c) O 1s. (d) S 2p. (e) Valence. All XP spectra were measured at *hν* = 700.0 eV. All XP spectra were charge referenced using the methods detailed in Section 2.7.1.

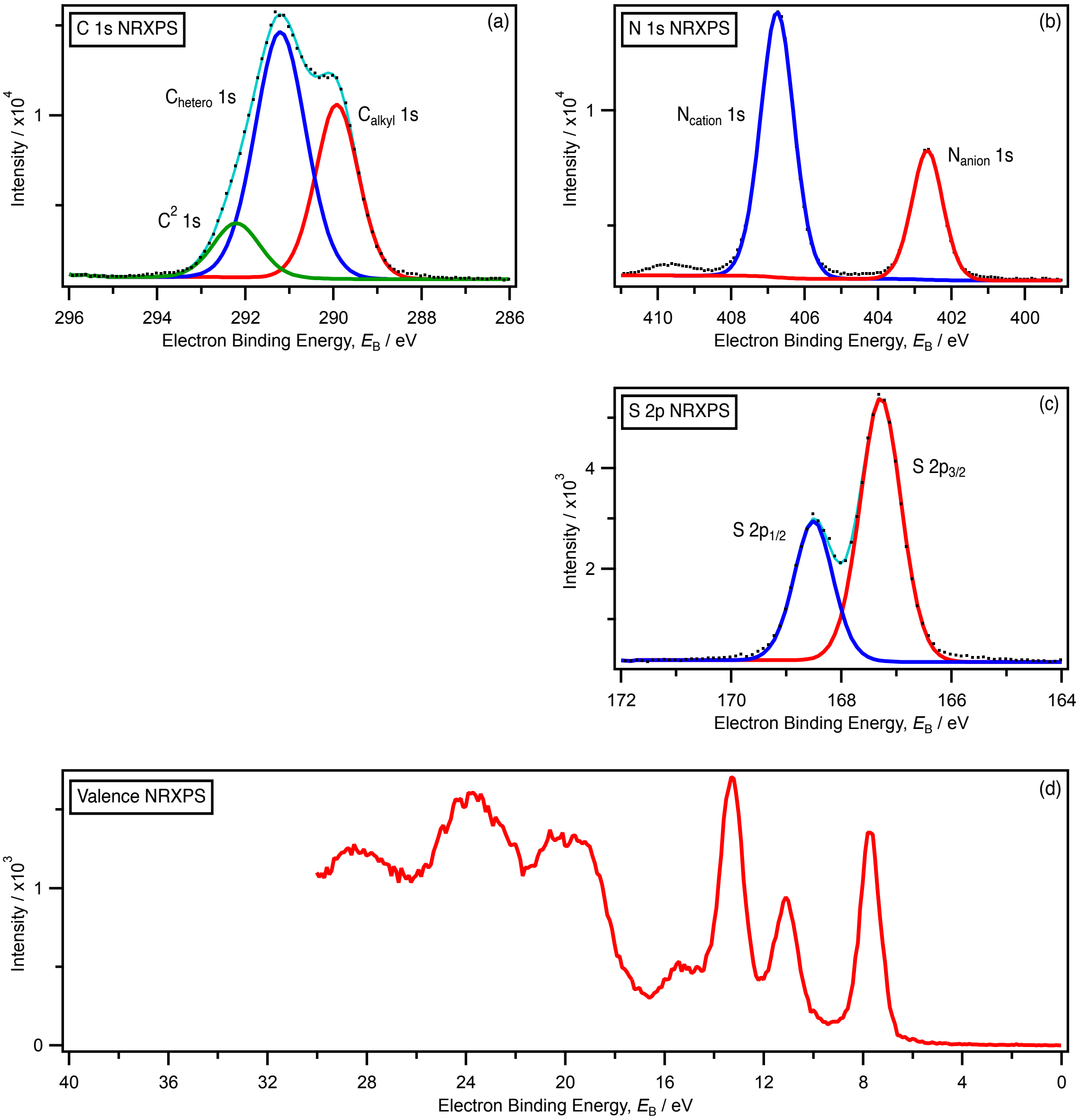

Appendix Figure 8.25. Core and valence state NRXP spectra for $([C_4C_1Im][SCN])_{1.00}(H_2O)_{0.00}$: (a) C 1s. (b) N 1s. (c) S 2p. (d) Valence. All XP spectra were measured at *hν* = 700.0 eV. All XP spectra were charge referenced using the methods detailed in Section 2.7.1.

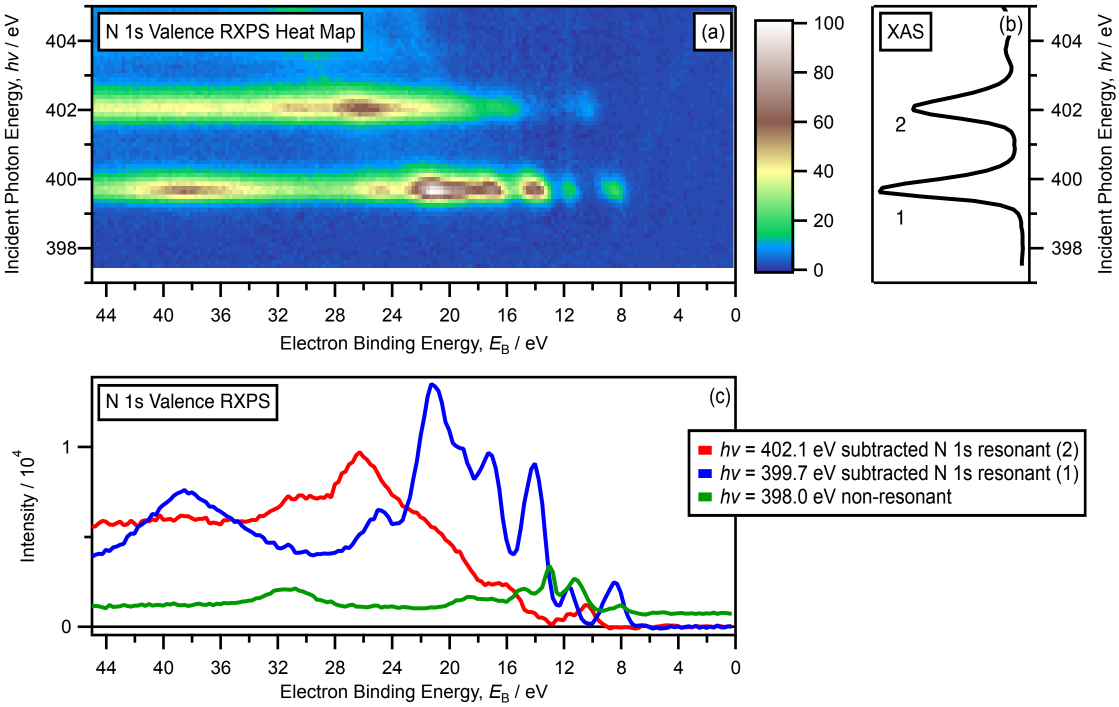

Appendix Figure 8.26. N 1s valence RXPS map and spectra for $([C_4C_1Im][SCN])_{0.01}(H_2O)_{0.99}$: (a) N 1s valence RXPS heat map for $([C_4C_1Im][SCN])_{0.01}(H_2O)_{0.99}$. (b) Partial electron yield N 1s XA spectra. (c) N 1s valence NRXP spectrum (*hν* = 398.0 eV) and N 1s valence RXP spectra (*hν* = 402.1 eV and *hν* = 399.7 eV), with the valence NRXP contributions subtracted. The NRXPS contributions were subtracted using the procedure detailed in Section 8.2. All RXP spectra were charge referenced using the methods detailed in Section 2.7.3.

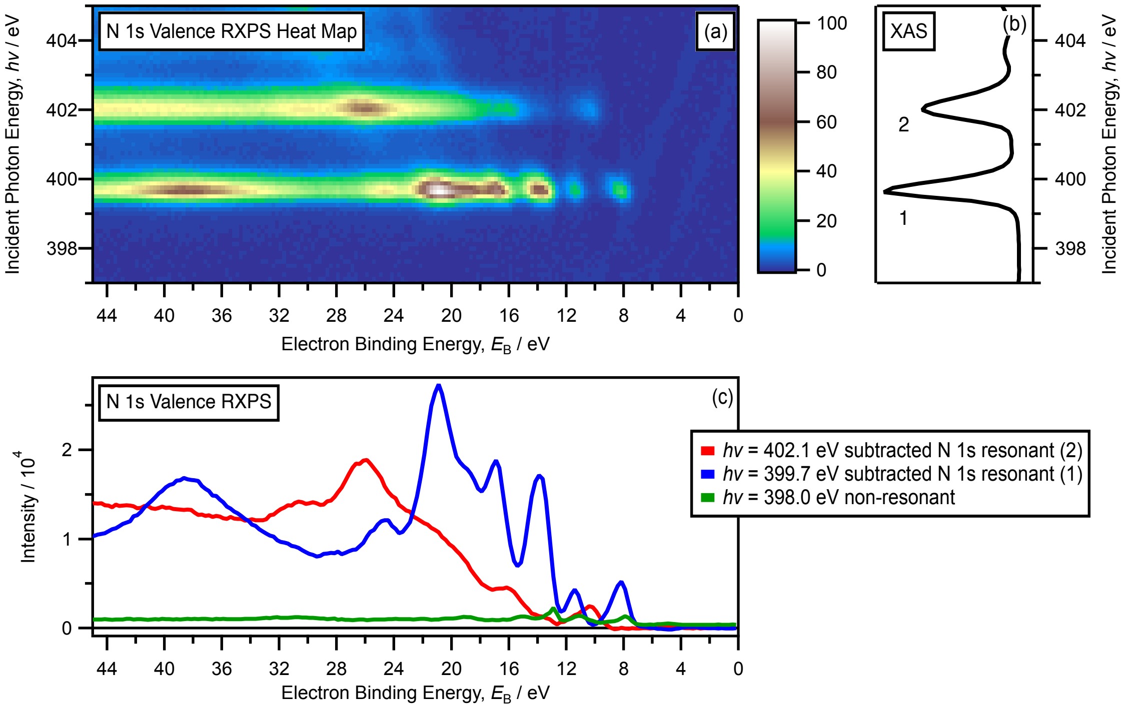

Appendix Figure 8.27. N 1s valence RXPS map and spectra for ([C_4C_1Im][SCN])$_{0.10}$(H_2O)$_{0.90}$: (a) N 1s valence RXPS heat map for ([C_4C_1Im][SCN])$_{0.10}$(H_2O)$_{0.90}$. (b) Partial electron yield N 1s XA spectra. (c) N 1s valence NRXP spectrum (*hν* = 398.0 eV) and N 1s valence RXP spectra (*hν* = 402.1 eV and *hν* = 399.7 eV), with the valence NRXP contributions subtracted. The NRXPS contributions were subtracted using the procedure detailed in Section 8.2. All RXP spectra were charge referenced using the methods detailed in Section 2.7.3.

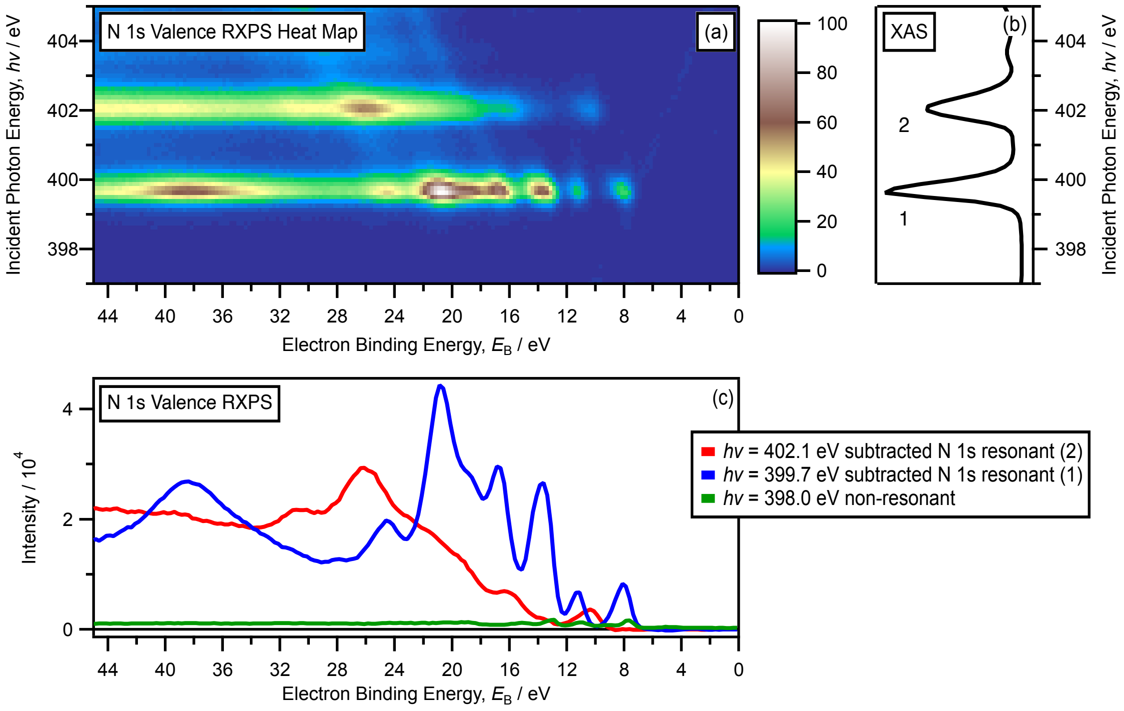

Appendix Figure 8.28. N 1s valence RXPS map and spectra for ($[C_4C_1Im][SCN])_{0.25}(H_2O)_{0.75}$: (a) N 1s valence RXPS heat map for ($[C_4C_1Im][SCN])_{0.25}(H_2O)_{0.75}$. (b) Partial electron yield N 1s XA spectra. (c) N 1s valence NRXP spectrum (*hν* = 398.0 eV) and N 1s valence RXP spectra (*hν* = 402.1 eV and *hν* = 399.7 eV), with the valence NRXP contributions subtracted. The NRXPS contributions were subtracted using the procedure detailed in Section 8.2. All RXP spectra were charge referenced using the methods detailed in Section 2.7.3.

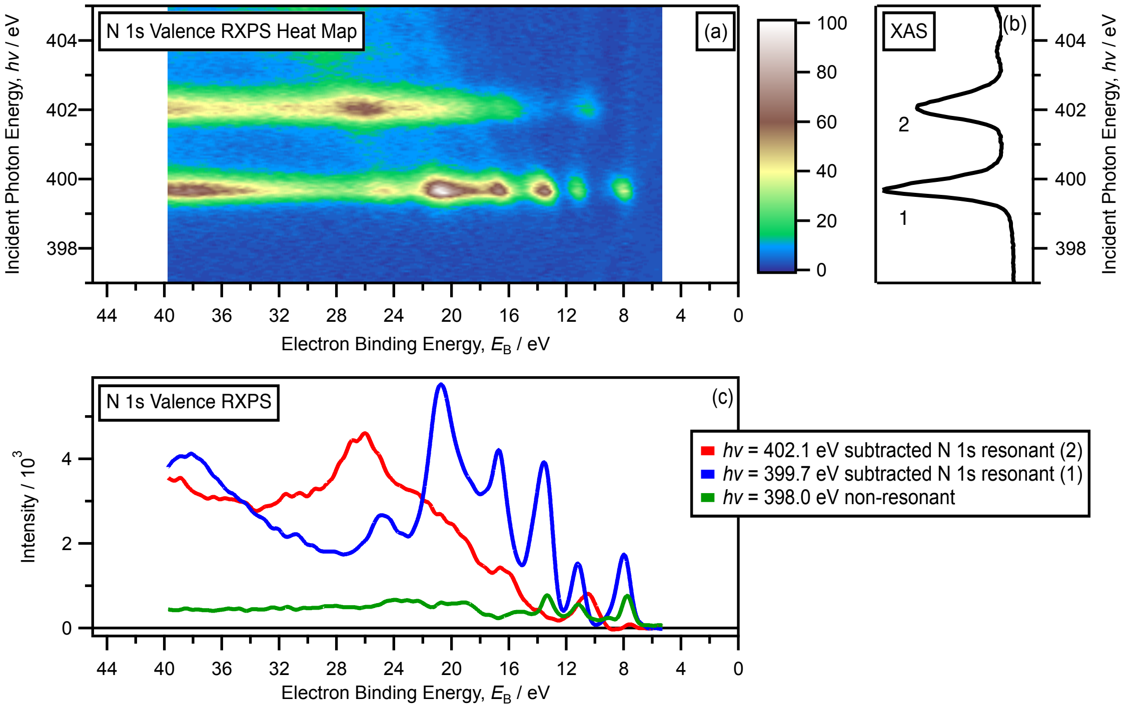

Appendix Figure 8.29. N 1s valence RXPS map and spectra for $([C_4C_1Im][SCN])_{1.00}(H_2O)_{0.00}$: (a) N 1s valence RXPS heat map for $([C_4C_1Im][SCN])_{1.00}(H_2O)_{0.00}$. (b) Partial electron yield N 1s XA spectra. (c) N 1s valence NRXP spectrum (*hν* = 398.0 eV) and N 1s valence RXP spectra (*hν* = 402.1 eV and *hν* = 399.7 eV), with the valence NRXP contributions subtracted. The NRXPS contributions were subtracted using the procedure detailed in Section 8.2. All RXP spectra were charge referenced using the methods detailed in Section 2.7.3.

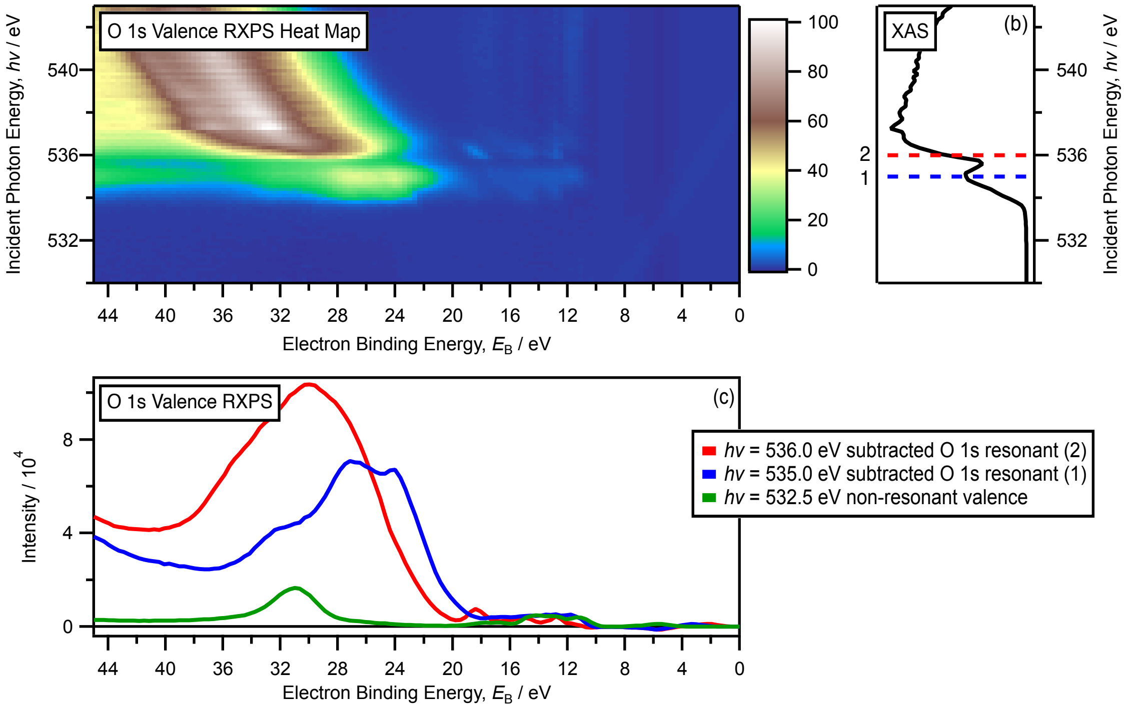

Appendix Figure 8.30. O 1s valence RXPS map and spectra for pure H_2O: (a) O 1s valence RXPS heat map for pure H_2O. (b) Partial electron yield O 1s XA spectra. (c) O 1s valence NRXP spectrum (*hν* = 532.5 eV) and O 1s valence RXP spectra (*hν* = 536.0 eV and *hν* = 535.0 eV), with the valence NRXP contributions subtracted. The NRXPS contributions were subtracted using the procedure detailed in Section 8.2. All RXP spectra were charge referenced using the methods detailed in Section 2.7.3.

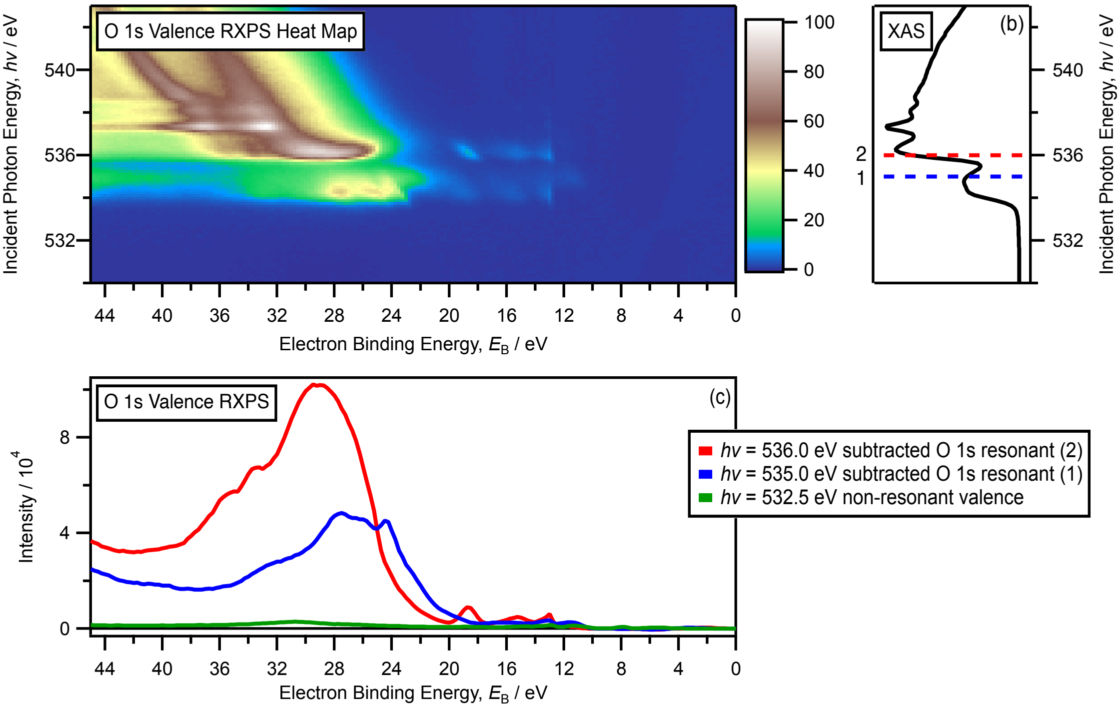

Appendix Figure 8.31. O 1s valence RXPS map and spectra for ([C_4C_1Im][SCN])$_{0.01}$(H_2O)$_{0.99}$: (a) O 1s valence RXPS heat map for ([C_4C_1Im][SCN])$_{0.01}$(H_2O)$_{0.99}$. (b) Partial electron yield O 1s XA spectra. (c) O 1s valence NRXP spectrum (*hν* = 532.5 eV) and O 1s valence RXP spectra (*hν* = 536.0 eV and *hν* = 535.0 eV), with the valence NRXP contributions subtracted. The NRXPS contributions were subtracted using the procedure detailed in Section 8.2. All RXP spectra were charge referenced using the methods detailed in Section 2.7.3.

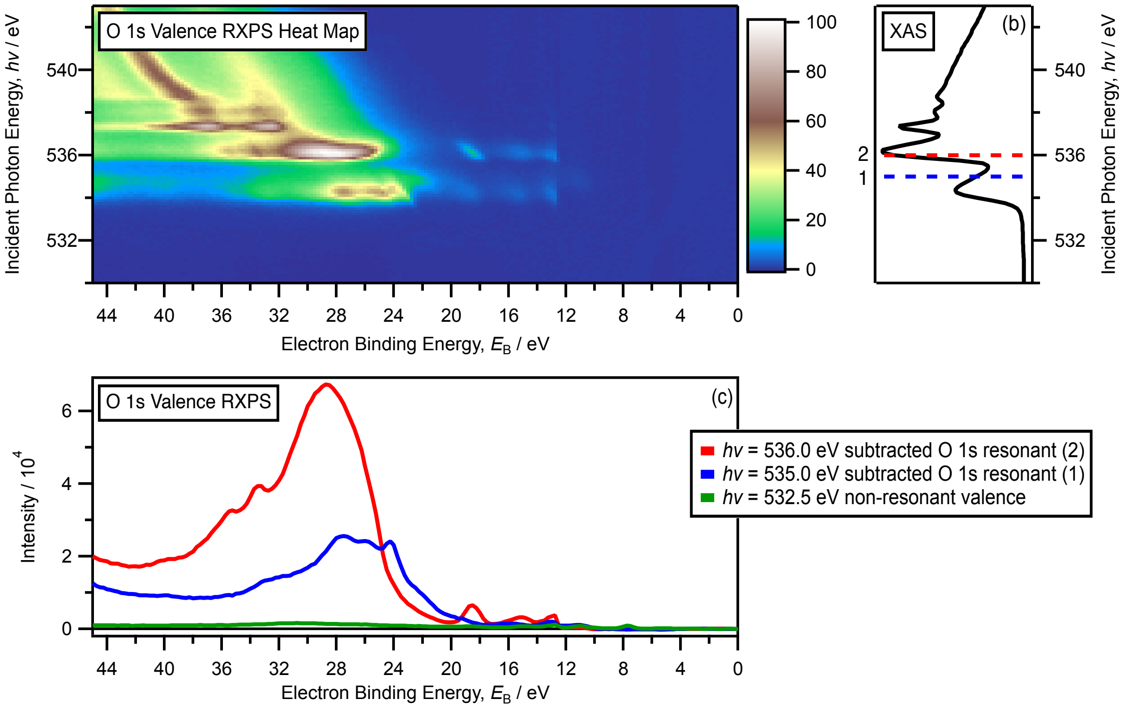

Appendix Figure 8.32. O 1s valence RXPS map and spectra for $([C_4C_1Im][SCN])_{0.10}(H_2O)_{0.90}$: (a) O 1s valence RXPS heat map for $([C_4C_1Im][SCN])_{0.10}(H_2O)_{0.90}$. (b) Partial electron yield O 1s XA spectra. (c) O 1s valence NRXP spectrum (*hν* = 532.5 eV) and O 1s valence RXP spectra (*hν* = 536.0 eV and *hν* = 535.0 eV), with the valence NRXP contributions subtracted. The NRXPS contributions were subtracted using the procedure detailed in Section 8.2. All RXP spectra were charge referenced using the methods detailed in Section 2.7.3.

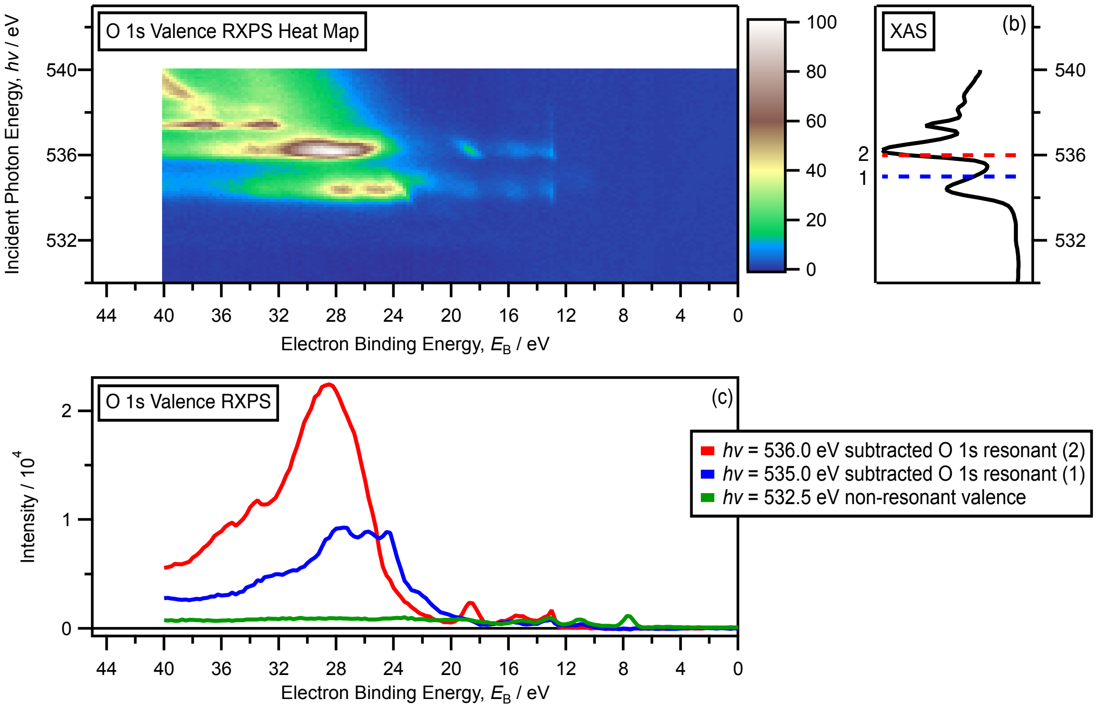

Appendix Figure 8.33. O 1s valence RXPS map and spectra for $([C_4C_1Im][SCN])_{0.25}(H_2O)_{0.75}$: (a) O 1s valence RXPS heat map for $([C_4C_1Im][SCN])_{0.25}(H_2O)_{0.75}$. (b) Partial electron yield O 1s XA spectra. (c) O 1s valence NRXP spectrum (*hν* = 532.5 eV) and O 1s valence RXP spectra (*hν* = 536.0 eV and *hν* = 535.0 eV), with the valence NRXP contributions subtracted. The NRXPS contributions were subtracted using the procedure detailed in Section 8.2. All RXP spectra were charge referenced using the methods detailed in Section 2.7.3.

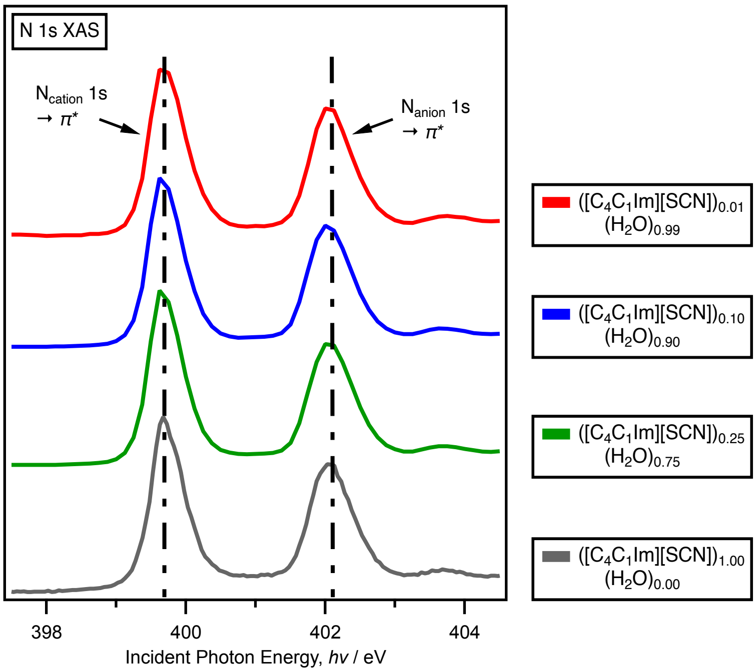

Appendix Figure 8.34. Full N 1s XA spectra comparison for $([C_4C_1Im][SCN])_x(H_2O)_{1-x}$, where x_{IL} = 0.01, 0.10, and 0.25. Spectra are vertically offset for clarity and dashed lines are added as a visual aid.

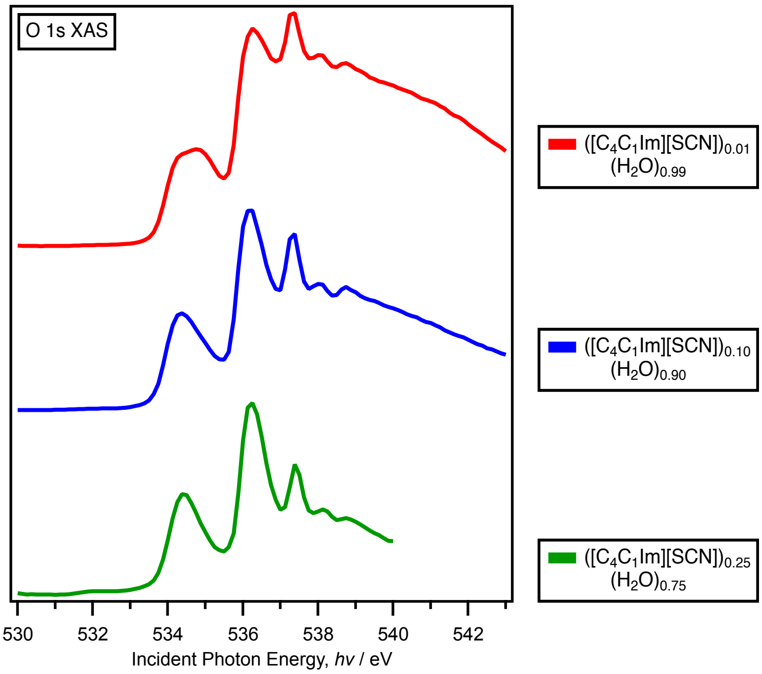

Appendix Figure 8.35. Full O 1s XA spectra comparison for $([C_4C_1Im][SCN])_x(H_2O)_{1-x}$, where x_{IL} = 0.01, 0.10, and 0.25. Spectra are vertically offset for clarity and dashed lines are added as a visual aid.

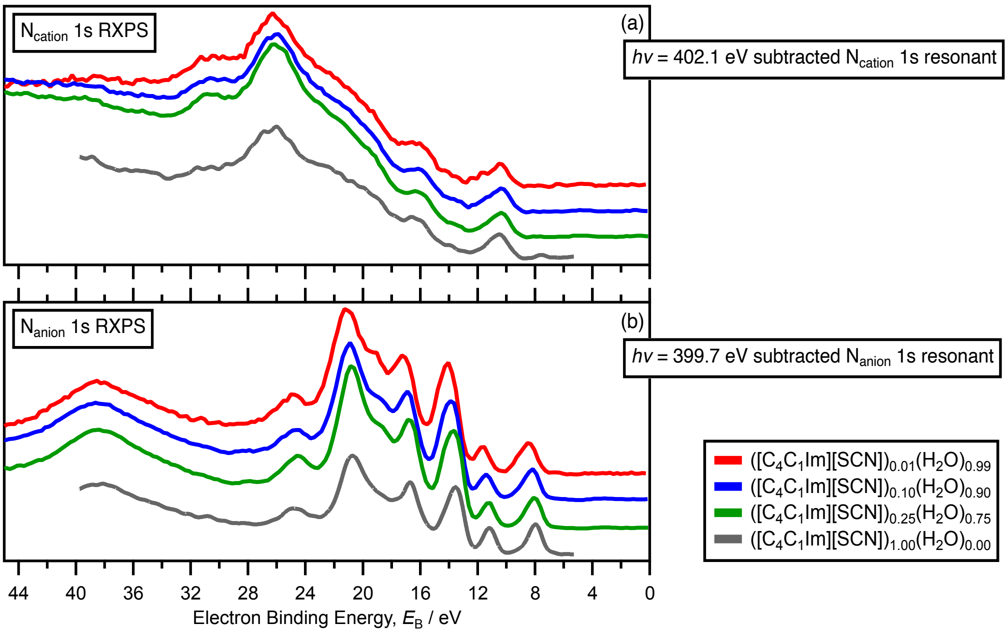

Appendix Figure 8.36. N 1s valence RXP spectra comparison for ([C_4C_1Im][SCN])$_x$(H_2O)$_{1-x}$, where x_{IL} = 0.01, 0.10, 0.25, and 1.00. (a) N$_{cation}$ 1s valence RXP spectra (*hν* = 402.1 eV), with the valence NRXP contributions subtracted. (b) N$_{anion}$ 1s valence RXP spectra (*hν* = 399.7 eV), with the valence NRXP contributions subtracted. Spectra are vertically offset for clarity. All NRXP spectra were charge referenced using the methods detailed in Section 2.7.3.

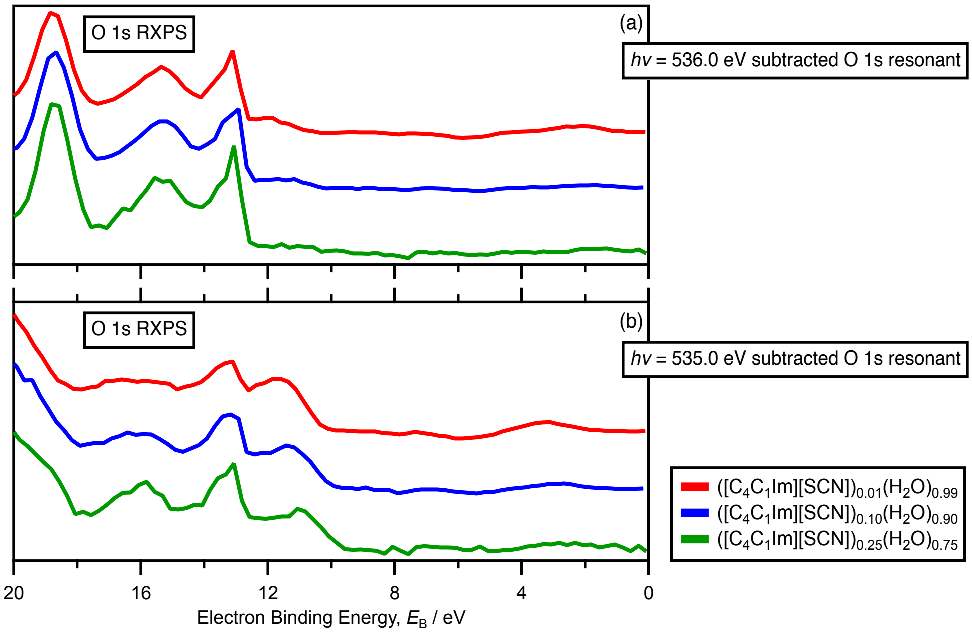

Appendix Figure 8.37. O 1s valence RXP spectra comparison within the participator Auger region for $([C_4C_1Im][SCN])_x(H_2O)_{1-x}$, where x_{IL} = 0.01, 0.10, and 0.25: (a) O 1s valence RXP spectra ($h\nu$ = 536.0 eV), with the valence NRXP contributions subtracted. (b) O 1s valence RXP spectra ($h\nu$ = 535.0 eV), with the valence NRXP contributions subtracted. The NRXPS contributions were subtracted using the procedure detailed in Section 8.2. All RXP spectra were charge referenced using the methods detailed in Section 2.7.3.

8.6. Supplementary information for Chapter 6

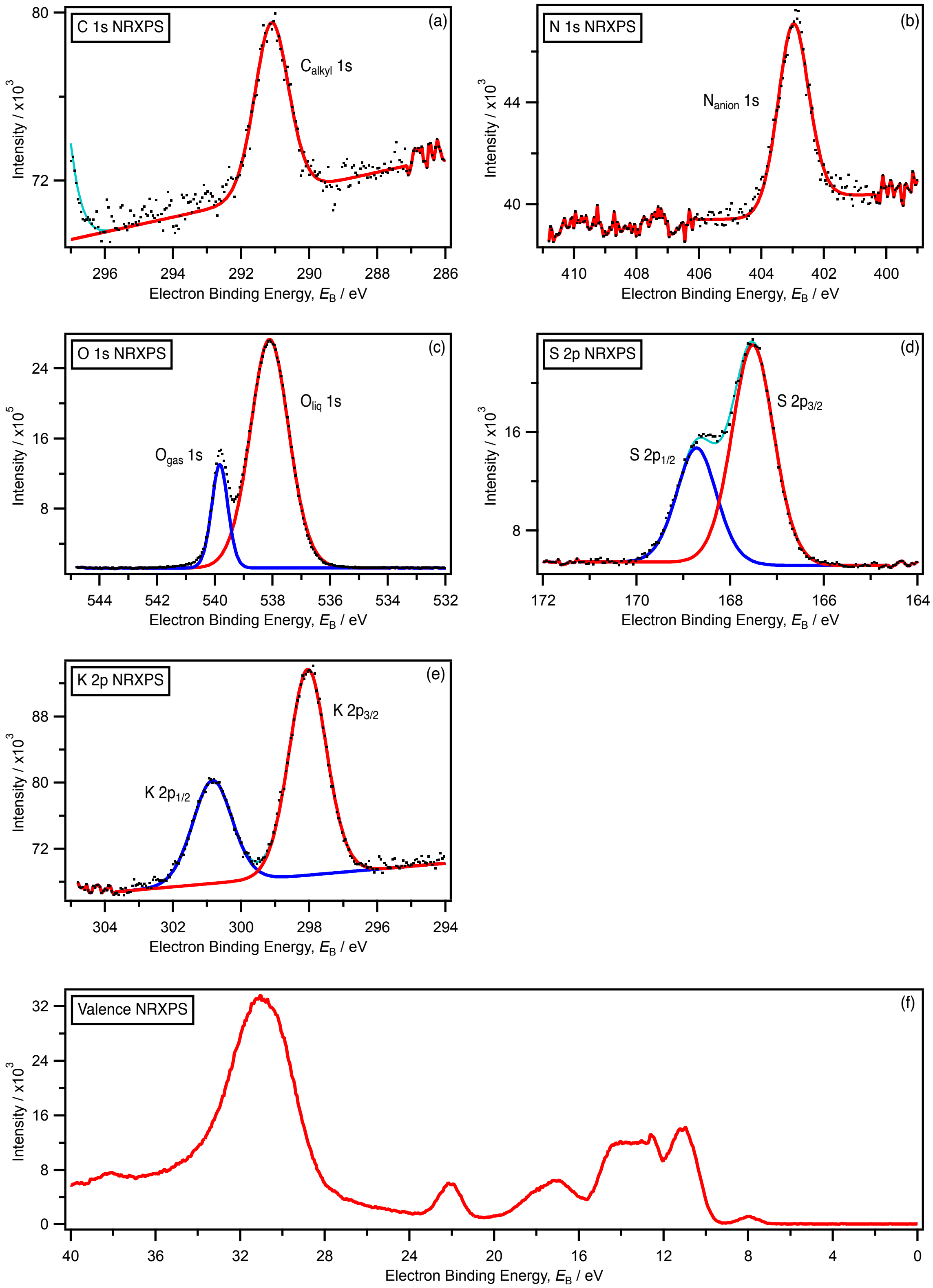

Appendix Figure 8.38. Core and valence state NRXP spectra for 0.5 M (K[SCN])(H_2O): (a) C 1s. (b) N 1s. (c) O 1s. (d) S 2p. (e) K 2p. (f) Valence. All XP spectra were measured at $h\nu$ = 700.0 eV. All XP spectra were charge referenced using the methods detailed in Section 2.7.2.

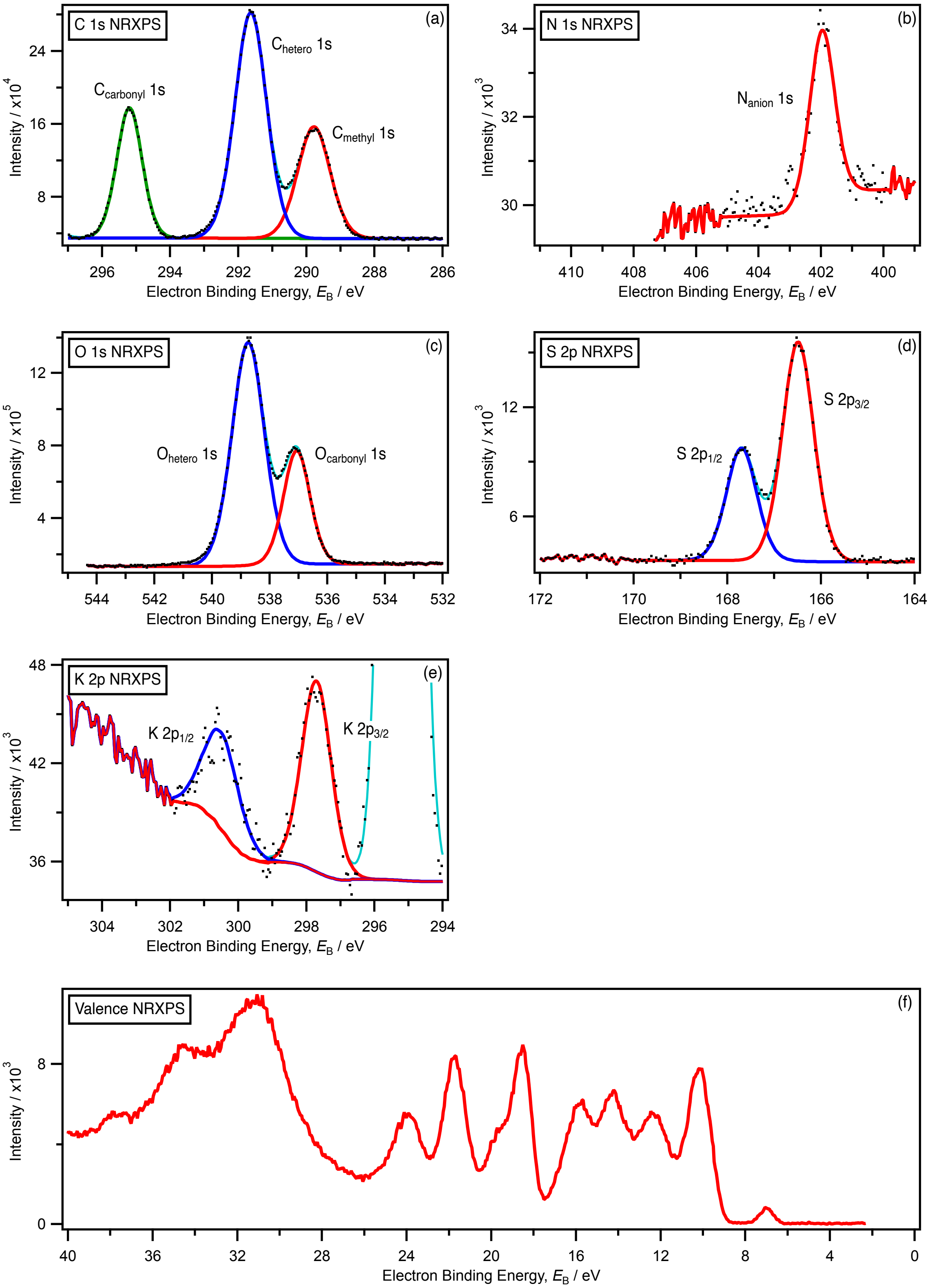

Appendix Figure 8.39. Core and valence state NRXP spectra for 0.5 M (K[SCN])(PC): (a) C 1s. (b) N 1s. (c) O 1s. (d) S 2p. (e) K 2p. (f) Valence. All XP spectra were measured at *hν* = 700.0 eV. All XP spectra were charge referenced using the methods detailed in Section 2.7.2.

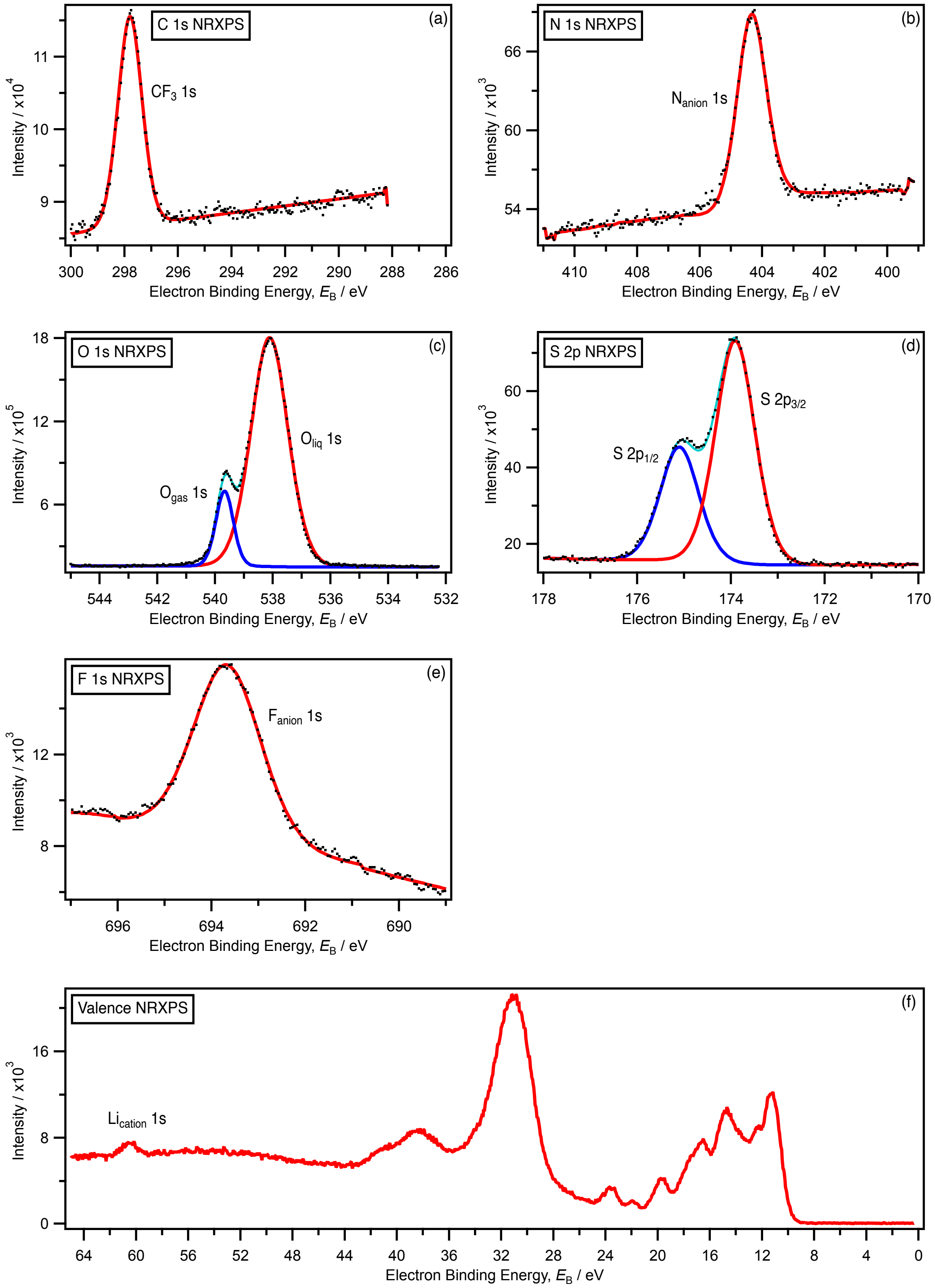

Appendix Figure 8.40. Core and valence state NRXP spectra for 0.5 M (Li[NTf$_2$])(H$_2$O): (a) C 1s. (b) N 1s. (c) O 1s. (d) S 2p. (e) F 1s. (f) Valence. All XP spectra were measured at *hν* = 700.0 eV. All XP spectra were charge referenced using the methods detailed in Section 2.7.2.

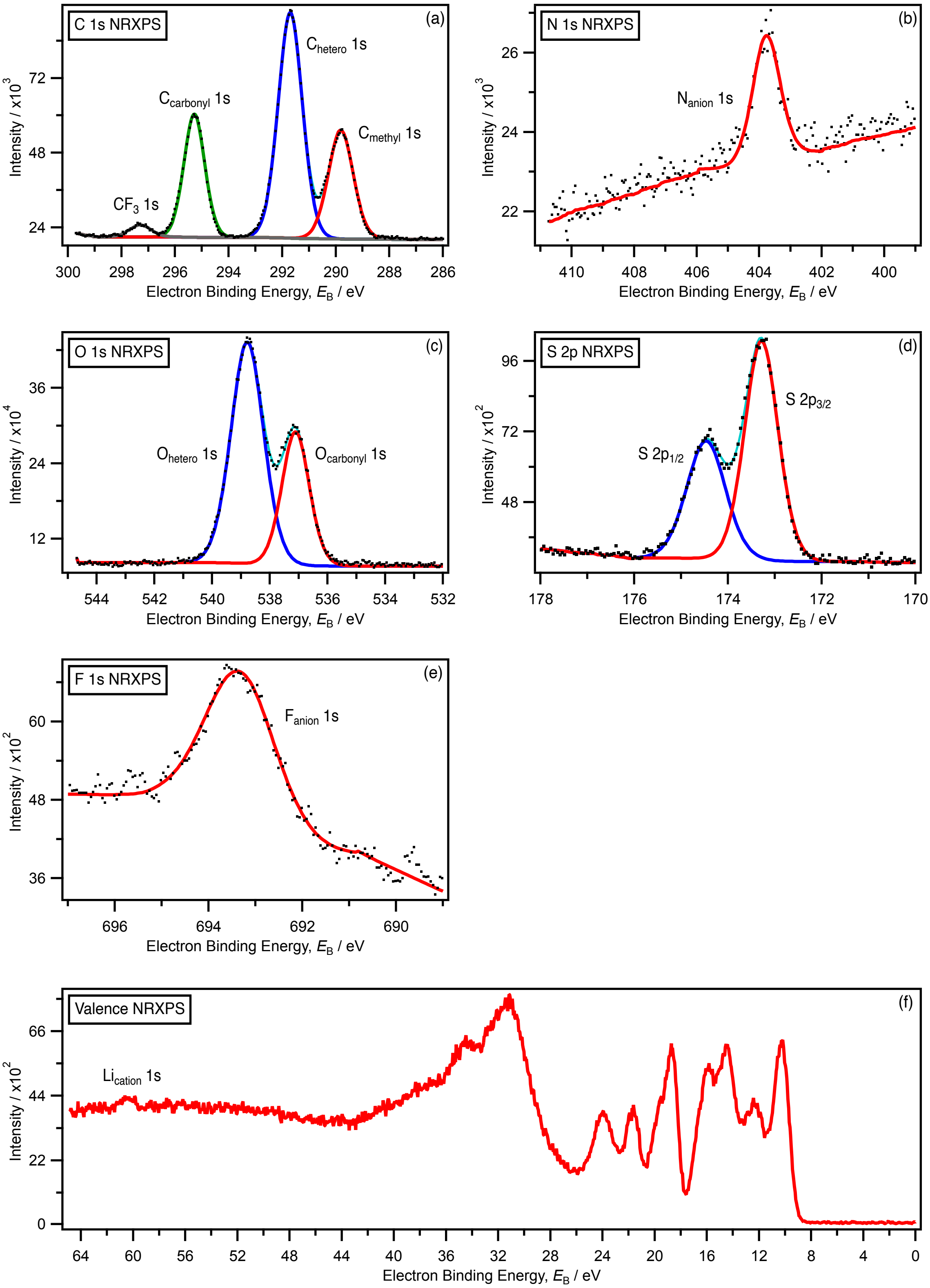

Appendix Figure 8.41. Core and valence state NRXP spectra for 0.5 M (Li[NTf$_2$])(PC): (a) C 1s. (b) N 1s. (c) O 1s. (d) S 2p. (e) F 1s. (f) Valence. All XP spectra were measured at $h\nu$ = 700.0 eV. All XP spectra were charge referenced using the methods detailed in Section 2.7.2.

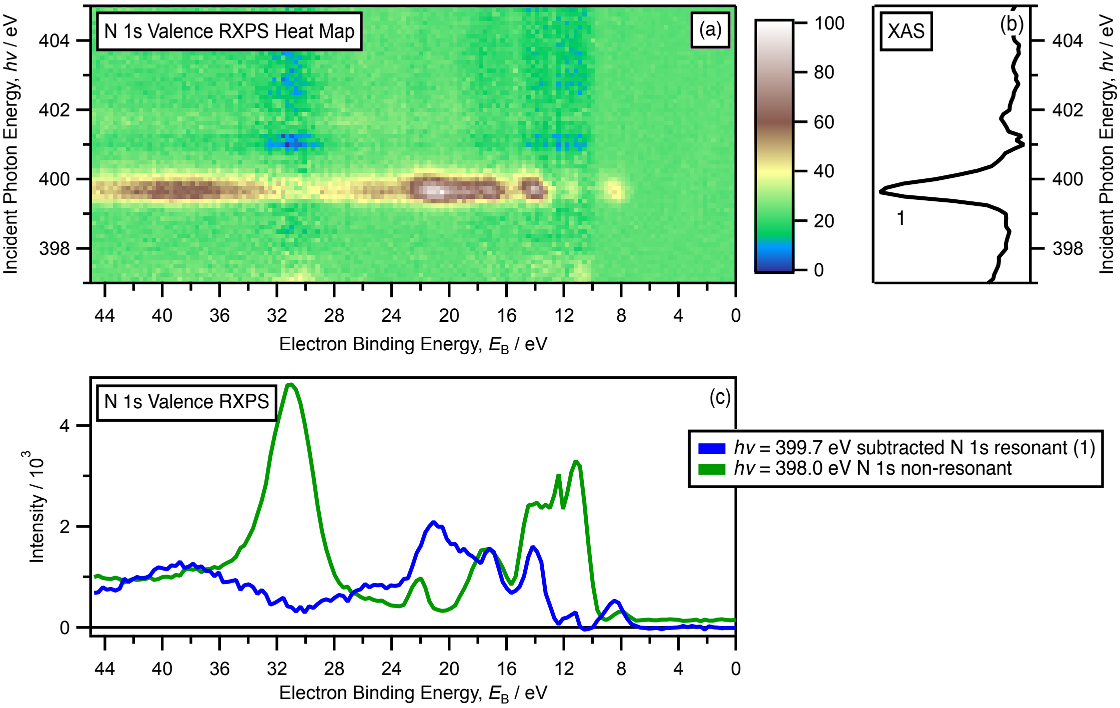

Appendix Figure 8.42. N 1s valence RXPS map and spectra for 0.5 M (K[SCN])(H_2O): (a) N 1s valence RXPS heat map for 0.5 M (K[SCN])(H_2O). (b) Partial electron yield N 1s XA spectra. (c) N 1s valence NRXP spectrum (*hν* = 398.0 eV) and N 1s valence RXP spectra (*hν* = 399.7 eV), with the valence NRXP contributions subtracted. The NRXPS contributions were subtracted using the procedure detailed in Section 8.2. All RXP spectra were charge referenced using the methods detailed in Section 2.7.3.

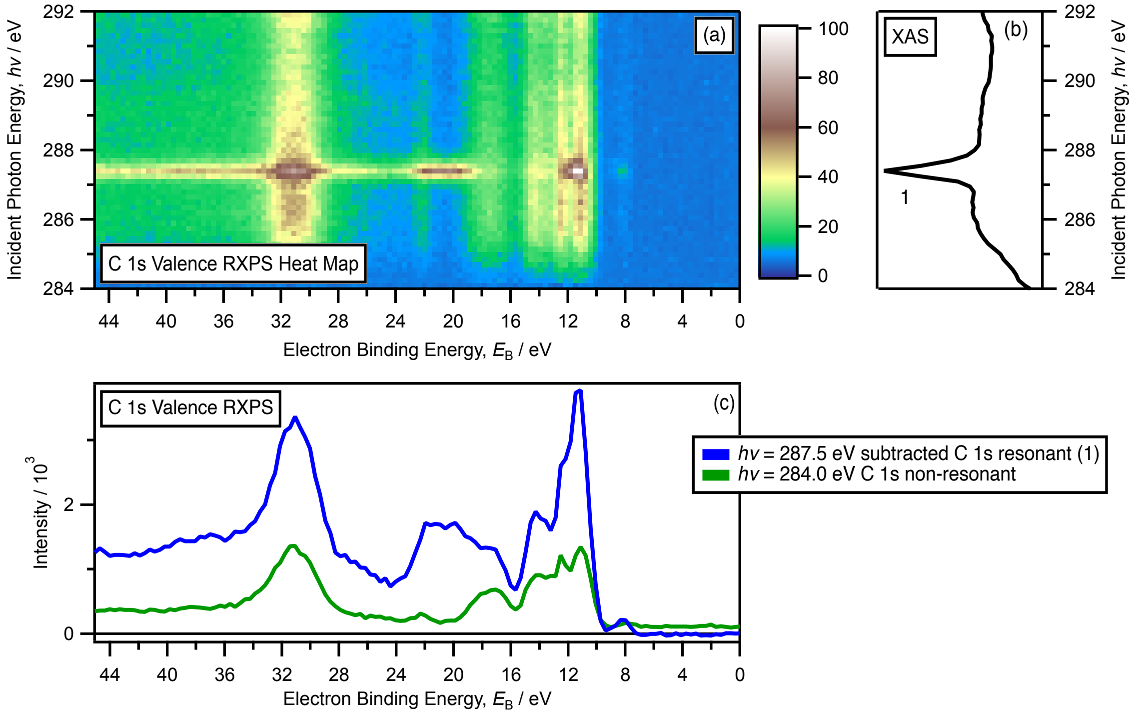

Appendix Figure 8.43. C 1s valence RXPS map and spectra for 0.5 M (K[SCN])(H_2O): (a) C 1s valence RXPS heat map for 0.5 M (K[SCN])(H_2O). (b) Partial electron yield C 1s XA spectra. (c) C 1s valence NRXP spectrum (*hν* = 284.0 eV) and C 1s valence RXP spectra (*hν* = 287.5 eV), with the valence NRXP contributions subtracted. The NRXPS contributions were subtracted using the procedure detailed in Section 8.2. All RXP spectra were charge referenced using the methods detailed in Section 2.7.3.

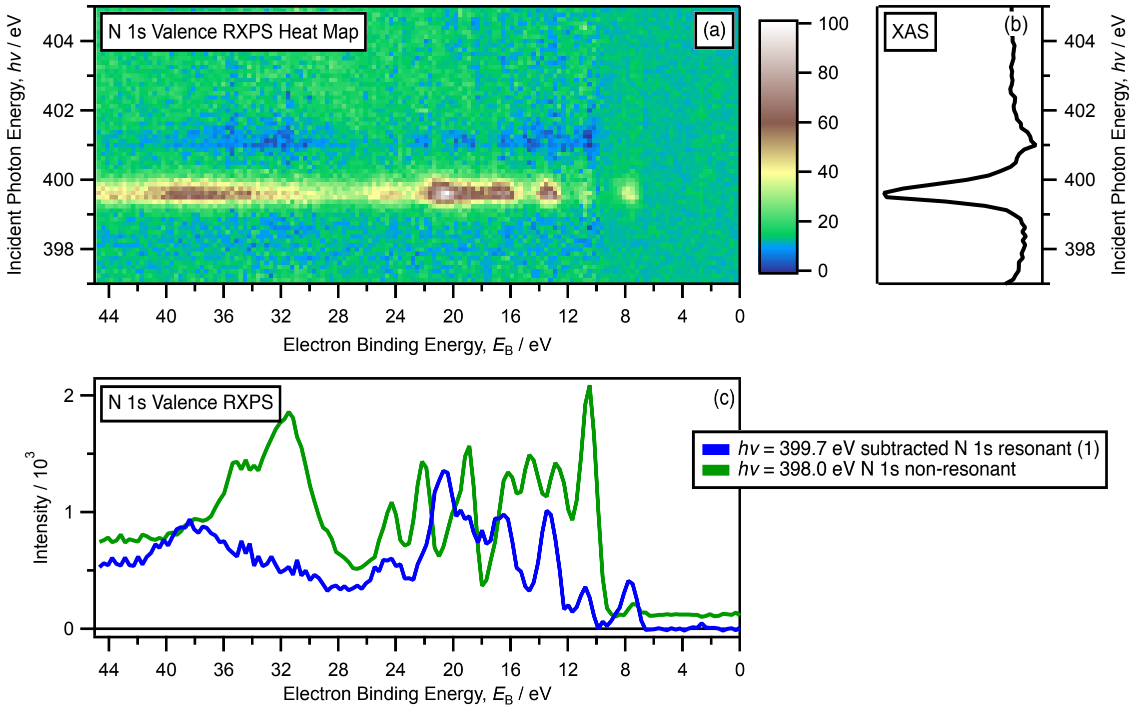

Appendix Figure 8.44. N 1s valence RXPS map and spectra for 0.5 M (K[SCN])(PC): (a) N 1s valence RXPS heat map for 0.5 M (K[SCN])(PC). (b) Partial electron yield N 1s XA spectra. (c) N 1s valence NRXP spectrum (*hν* = 398.0 eV) and N 1s valence RXP spectra (*hν* = 399.7 eV), with the valence NRXP contributions subtracted. The NRXPS contributions were subtracted using the procedure detailed in Section 8.2. All RXP spectra were charge referenced using the methods detailed in Section 2.7.3.

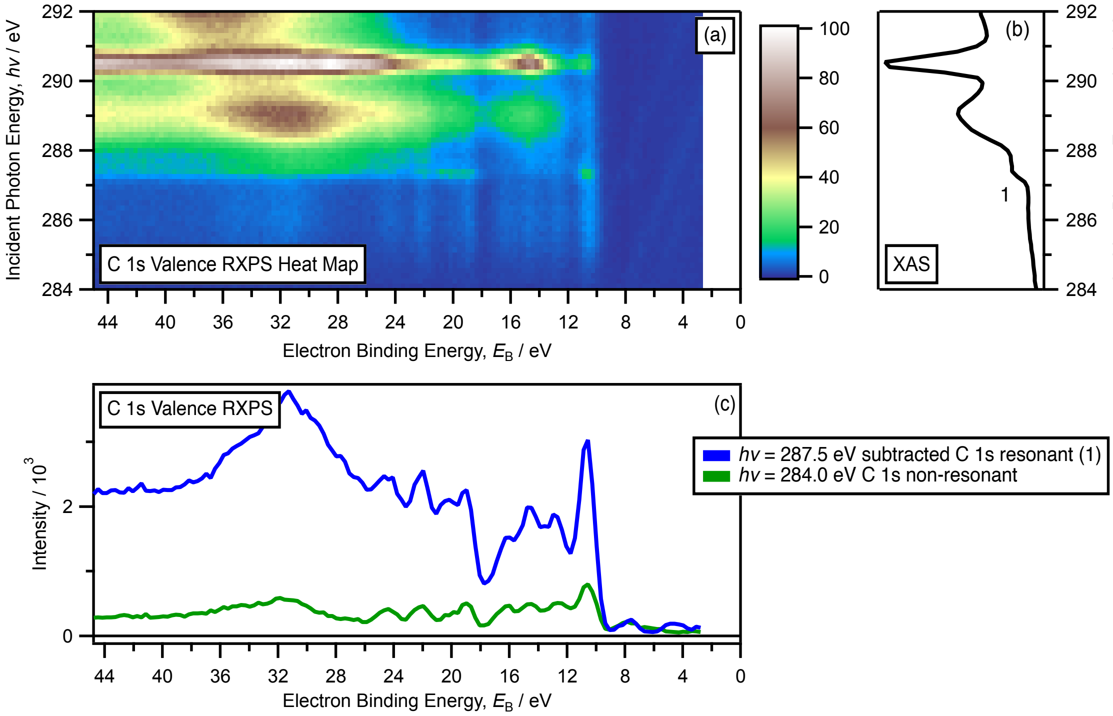

Appendix Figure 8.45. C 1s valence RXPS map and spectra for 0.5 M (K[SCN])(PC): (a) C 1s valence RXPS heat map for 0.5 M (K[SCN])(PC). (b) Partial electron yield C 1s XA spectra. (c) C 1s valence NRXP spectrum (*hν* = 284.0 eV) and C 1s valence RXP spectra (*hν* = 287.5 eV), with the valence NRXP contributions subtracted. The NRXPS contributions were subtracted using the procedure detailed in Section 8.2. All RXP spectra were charge referenced using the methods detailed in Section 2.7.3.

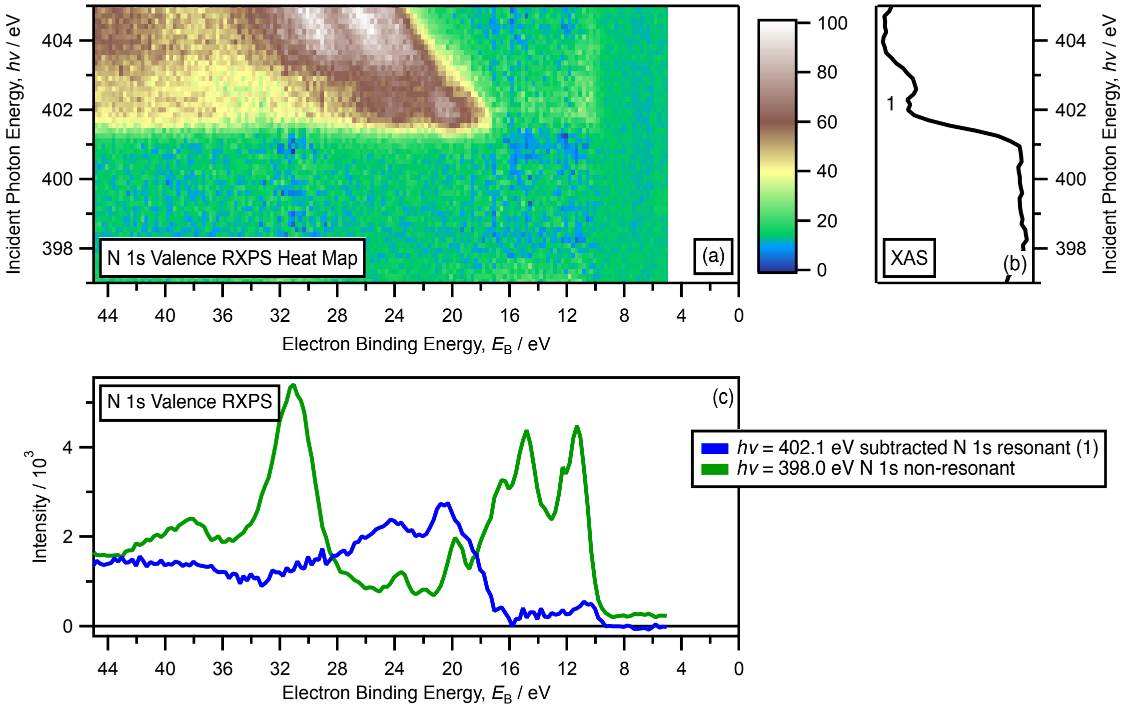

Appendix Figure 8.46. N 1s valence RXPS map and spectra for 0.5 M (Li[NTf$_2$])(H$_2$O): (a) N 1s valence RXPS heat map for 0.5 M (Li[NTf$_2$])(H$_2$O). (b) Partial electron yield N 1s XA spectra. (c) N 1s valence NRXP spectrum (*hν* = 398.0 eV) and N 1s valence RXP spectra (*hν* = 402.1 eV), with the valence NRXP contributions subtracted. The NRXPS contributions were subtracted using the procedure detailed in Section 8.2. All RXP spectra were charge referenced using the methods detailed in Section 2.7.3.

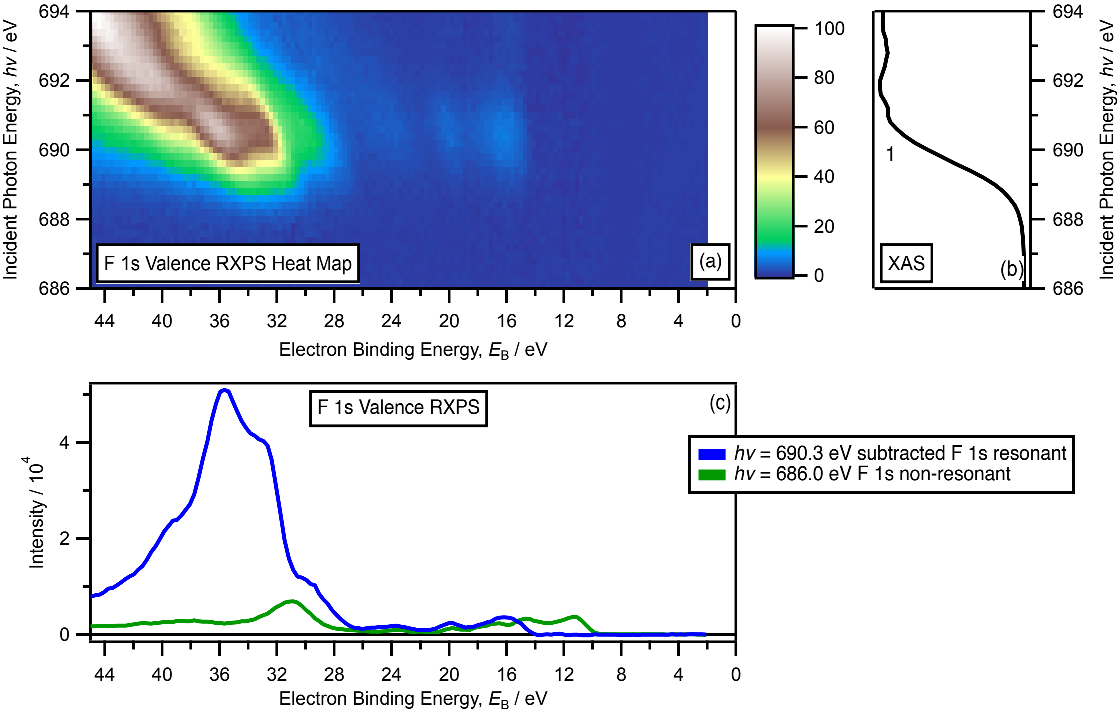

Appendix Figure 8.47. F 1s valence RXPS map and spectra for 0.5 M (Li[NTf$_2$])(H$_2$O): (a) F 1s valence RXPS heat map for 0.5 M (Li[NTf$_2$])(H$_2$O). (b) Partial electron yield F 1s XA spectra. (c) F 1s valence NRXP spectrum (*hν* = 686.0 eV) and F 1s valence RXP spectra (*hν* = 690.3 eV), with the valence NRXP contributions subtracted. The NRXPS contributions were subtracted using the procedure detailed in Section 8.2. All RXP spectra were charge referenced using the methods detailed in Section 2.7.3.

8.7. References

1. J. Walton, P. Wincott, N. Fairley and A. Carrick, *Peak Fitting with CasaXPS: A Casa Pocket Book*, Accolyte Science, Knutsford, UK, 2010.
2. R. M. Fogarty, R. G. Palgrave, R. A. Bourne, K. Handrup, I. J. Villar-Garcia, D. J. Payne, P. A. Hunt and K. R. J. Lovelock, *Physical Chemistry Chemical Physics*, 2019, **21**, 18893-18910.